Conception, modeling, and control of a convertible mini-drone

Duc Kien Phung

Thèse

présentée à

L'Université Pierre et Marie Curie

par

Duc Kien PHUNG

pour obtenir le grade de

Docteur de l'Université Pierre et Marie Curie

Spécialité : Robotique

Conception, modélisation et commande d'un mini-drone convertible

---

Soutenue le 28-01-2015

JURY

M.	Tarek HAMEL	Rapporteur
M.	Jean-Marc MOSCHETTA	Rapporteur
M.	Faïz BEN AMAR	Examinateur
M.	Philippe MARTIN	Examinateur
Mme.	Alexandra MOUTINHO	Examinatrice
M.	Pascal MORIN	Directeur de thèse
M.	Stéphane DONCIEUX	Co-Directeur de thèse

Duc Kien PHUNG

Conception, Modeling, and Control of a Convertible Mini-Drone

---

Abstract

The family of aircraft essentially consists of two classes of systems: fixed-wing and VTOL (Vertical Take-Off and Landing) aircraft. Due to their streamline shapes inducing high lift/drag ratio, fixed-wing airplanes are efficient in cruising flight. However, most of them require runways or catapult/net systems for take-off and landing. As for VTOL aircraft, thanks to their hover ability, they are particularly suitable for many applications including observation and structures inspection, but their efficiency in horizontal flight is generally mediocre. There is therefore an interest in designing so-called "convertible" vehicles, that combine the advantages of these two types of aircraft: efficient cruising flight and VTOL capability. This thesis is devoted to the conception, modeling, and control of such a convertible mini-UAV (Unmanned Aerial Vehicle).

The main contributions of this work are threefold. Firstly, we design a novel UAV structure by adding to each side of a quadrotor one wing that can rotate around an axis belonging to the propellers' plane. Our prototype has many advantages over existing convertible structures: simple mechanical concept since inspired by a classical quadrotor, flexibility for selecting different components (wings, propellers) and payload placement, flexibility for the control design, etc. Secondly, we provide an energy modeling of this type of convertible UAVs, taking into account their characteristics as compared to full-scale helicopters (large variation of aerodynamic forces, performance degradation at low Reynolds number, etc.). This modeling relies on momentum and blade element theories for the propellers and an aerodynamic coefficient model for full range of angle of attack for the wings. The ultimate objective is to optimize the wings' inclination with respect to the propellers' plane so as to achieve energy-efficient flight. In addition, the impact of various parameters (choice of propellers, wings' area, mass of UAV) is analyzed. The energy modeling provides useful guidelines for UAV presizing and control design - which is also the third contribution of this thesis. The degrees of freedom of the wings permit the decoupling between propellers and wings' orientations. This greatly enhances the control flexibility as compared to traditional aircraft. Relying on this feature, several control approaches are proposed. In particular, using a specific geometrical design, we show that an efficient control of our UAV can be obtained without air-velocity measurements. This strategy is well suited to small aerial vehicles for which such measurements are difficult to acquire. Simulation results confirm the soundness of our control design even in the presence of strong and varying wind.

En route to validate the theory, a mechanical prototype of the UAV was constructed in our laboratory and preliminary flight tests were performed. This is reported in the last chapter of the thesis.

Keywords: VTOL UAV, Convertible UAV, Energy Modeling, Aerodynamics, Feedback Control

Résumé

La famille des véhicules aériens est essentiellement constituée de deux classes de systèmes: les voilures-fixes et les systèmes à décollage et atterrissage vertical (VTOL en anglais, pour "Vertical Take-Off and Landing"). En raison de leur forme profilée, induisant un rapport portance/traînée élevé, les voilures-fixes ont l'avantage d'une bonne efficacité énergétique. Cependant, la plupart d'entre eux nécessitent des pistes ou des systèmes catapulte/filet pour le décollage et l'atterrissage. Quant aux VTOL, grâce à leur capacité au vol stationnaire, ils sont particulièrement bien adaptés aux applications d'observation et d'inspection de structures, mais leur efficacité énergétique en vol "de croisière" est généralement médiocre. Il y a donc un intérêt à concevoir des véhicules appelés "convertibles", qui combinent les avantages de ces deux types de structures : bonne efficacité énergétique en vol de croisière et capacité au vol stationnaire. Cette thèse est consacrée à la conception, la modélisation et la commande d'un tel mini-drone convertible.

Les principales contributions de ce travail comportent trois volets. Tout d'abord, nous concevons une nouvelle structure de drone en ajoutant de chaque côté d'un quadrirotor une aile qui peut pivoter autour d'un axe appartenant au plan des hélices. Notre prototype a de nombreux avantages par rapport aux structures convertibles existantes: conception mécanique simple car dérivée d'un quadrirotor classique, flexibilité pour le montage de différents composants (ailes, hélices) et le placement de la charge utile, flexibilité de la conception de commande, etc. Deuxièmement, nous proposons une modélisation énergétique de ce type de drone convertible, en tenant compte de ses caractéristiques par rapport aux hélicoptères avec pilote à bord (grande variation des forces aérodynamiques, dégradation des performances à faible nombre de Reynolds, etc.). Cette modélisation s'appuie sur les théories de la quantité de mouvement et de l'élément de pale pour les hélices et un modèle de coefficient aérodynamique couvrant la gamme complète des angles d'attaque pour les ailes. L'objectif ultime est d'optimiser l'inclinaison des ailes par rapport au plan des hélices afin d'obtenir la meilleure efficacité énergétique. En outre, l'impact de divers paramètres (choix des hélices, des aile(s), masse de drone) est analysé. La modélisation énergétique fournit des informations utiles pour la conception mécanique et la conception de la commande; ce dernier aspect constituant la troisième contribution de cette thèse. Les degrés de liberté des ailes permettent le découplage entre les orientations des hélices et celle des ailes. Cela augmente considérablement les possibilités de contrôle par rapport aux aéronefs traditionnels. S'appuyant sur cette caractéristique, plusieurs approches de contrôle sont proposées. En particulier, en utilisant une conception géométrique spécifique, nous montrons qu'un contrôle efficace peut être obtenu sans mesures de la vitesse air. Cette stratégie est bien adaptée aux petits véhicules aériens pour lesquels ces mesures sont difficiles à acquérir. Les résultats de simulation confortent cette stratégie de contrôle, même en présence de vent fort et variable.

Afin de valider la théorie, un prototype mécanique du drone a été construit dans notre laboratoire et des essais en vol préliminaires ont été effectués. Ces aspects sont décrits dans le dernier chapitre de la thèse.

Mots-clés: Véhicule à décollage et atterrissage vertical, Drone convertible, Modélisation énergétique, Aérodynamique, Commande par retour d'état

Acknowledgments

This thesis could not be successful without the help of many people. I owe my sincere gratitude to my Ph.D. supervisor Dr. Pascal Morin for his guidance and support all along the thesis. Initially when I came to ISIR, there was almost nothing in the UAV team. Pascal has been building the team with great determination. In addition, he taught me to bring forward the principal ideas and to write the documents in professional manner. I would like to show my great appreciation for my Ph.D. co-supervisor Dr. Stéphane Doncieux. The discussions on the evolutionary algorithm for UAV trajectory planning are always interesting. Although I did not have enough time to fully implement the algorithms, these ideas will be certainly helpful in the future.

I would like to acknowledge all the members of my Ph.D. jury for evaluating the present work. In particular, I am grateful to Dr. Jean-Marc Moschetta and Dr. Tarek Hamel for reviewing the manuscript and for their constructive criticism. My thanks go to Dr. Faïz Ben Amar for chairing the jury. I am also thankful to Dr. Alexandra Moutinho and Dr. Philippe Martin for examining the present work.

In our drone team, I want to express my special recognition to Mr. Olivier Gasté for the helps in the construction and assembly of the convertible UAV. I want to extend my gratitude to Dr. Alexandre Eudes for developing the embedded code and for the tutorial on ROS. I want to show my appreciation to Dr. Tiago Gonçalves - a specialist in aerodynamic - for all the fruitful discussions on aircraft, aerodynamic, or any general subject in the lab or over a cup of coffee.

I deeply indebted to my whole family for everything I am and everything I have achieved. My grandmothers always take care of me even for the smallest details. My father Phung Quang Toan teaches me to dream big and inspires me to pursue science. My mother Tran Thu Hoa always concerns about and takes great care of me. My sister Phung Thanh Thuy is perpetually confident in her brother. Last but not least, I want to express my deepest love to my soul-mate Do Hong Trang. Without her, I could never finish the thesis on time. It was a very difficult period with the late nights and crazy hours. She always encourages me and I am forever grateful.

Contents

Nomenclature

Abbreviations

nD	n-dimensional, e.g. 2D: two-dimensional, 3D: three-dimensional
CAN	Controller Area Network
CoM	Center of Mass
DoF	Degree of Freedom
ESC	Electronic Speed Controller
GPS	Global Positioning System
I2C	Inter-Integrated Circuit
IDE	Integrated Development Environment
IMU	Inertial Measurement Unit
PID	Proportional Integral Derivative
PPM	Pulse Position Modulation
PVTOL	Planar Vertical Take-Off and Landing
PWM	Pulse Width Modulation
RC	Radio Control
ROS	Robot Operating System
RPM	Revolution per minute
SPI	Serial Peripheral Interface
UAV	Unmanned Aerial Vehicle
USB	Universal Serial Bus
VTOL	Vertical Take-Off and Landing

Frames and Matrices

$\mathcal{S}(\cdot)$	Skew-symmetric matrix for cross product $\mathcal{S}(u)v = u \times v, \forall u, v \in \mathbb{R}^3$
$\mathcal{B} = \{G; \boldsymbol{i}; \boldsymbol{j}; \boldsymbol{k}\}$	Body frame

$\mathcal{E} = \{M, \boldsymbol{i_\Psi}, \boldsymbol{j_\Psi}, \boldsymbol{k_\Psi}\}$	Frame attached to a blade element
$\mathcal{I} = \{O; \boldsymbol{i_0}; \boldsymbol{j_0}; \boldsymbol{k_0}\}$	Inertial frame
$\mathcal{R}$	Rotation matrix from frame $\mathcal{B}$ to frame $\mathcal{I}$

Symbols

α	Angle of attack of the wing
$\alpha_0(\mathrm{Re})$	Angle where the stall zone starts for the airfoil at Reynolds number Re
$\alpha_{0\mathrm{ref}}$	Angle where the stall zone starts for the airfoil at reference Reynolds number $\mathrm{Re}_{\mathrm{ref}}$
α_e	Angle of attack at equilibrium
α_P	Blade element angle of attack
$\beta_1,\ \beta_2,\ \beta_3$	Blade aerodynamic constants, see Eq. (2.61)
$\eta = \mathcal{R}e_3$	Thrust direction unit vector in inertial frame $\mathcal{I}$
$\eta_P = J_a \dfrac{C'_T}{C'_P}$	Propeller efficiency
$\gamma = \mathcal{R}^\top e_3$	Gravitational vector's direction in body frame $\mathcal{B}$
κ_Q	Constant to relate propeller torque Q with its rotational speed ϖ
κ_T	Constant to relate propeller thrust T with its rotational speed ϖ
μ	Inclination angle between the wing and the propellers' plane
μ_{vis}	Air viscosity
$\boldsymbol{\nu} = -\boldsymbol{v_a}$	Air flow velocity
$\boldsymbol{\nu_D}$	Downstream wake velocity
$\boldsymbol{\nu_{\mathrm{ind}}}$	Induced velocity
$\boldsymbol{\nu_{\mathrm{ind,0}}}$	Induced velocity at hover
$\nu_T = \varpi R$	Rotor tip velocity
φ	Inflow angle to the propeller blade
Ψ	Azimuthal angle
ρ	Air density
Σ	Wing(s) area
Σ_{para}	Parasite drag effective area
Θ	Any minimal parametrization of $SO(3)$ around the identity matrix (e.g., the vector of Euler angles θ_1: roll, θ_2: pitch, θ_3: yaw)

θ	UAV's orientation angle in 2D representation, equivalent to θ_1 in 3D representation
θ_P	Mean pitch angle of the propeller blade at 75% radius
θ_1, θ_2, θ_3	Three parametrization Euler angles of $SO(3)$ around axes $\boldsymbol{i_0}, \boldsymbol{j_0}, \boldsymbol{k_0}$ to pass from frame $\mathcal{I}$ to $\mathcal{B}$
ϖ	Propeller rotor angular speed
a	Blade lift curve slope
$A = \pi R^2$	Area swept by the propeller blades
$a_\nu \triangleq k_a v^2/(mg)$	Ratio of aerodynamic force and the gravity force
$a_s = \mathcal{R}^\top(\dot{v} - ge_3)$	UAV specific acceleration in the body frame $\mathcal{B}$
$b_0,\ b_1,\ b_2$	Blade drag coefficient constants
c	Wing chord length
c_1	Drag constant
c_2	Average lift constant
c_{2T}	High lift constant
$c_D(\alpha, \mathrm{Re})$	Wing drag coefficient
$C_{DP}(\alpha_P)$	Blade drag coefficient at angle of attack α_P
$C_H \triangleq \dfrac{H}{\frac{1}{2}\rho A \nu_T^2}$	Drag coefficient for in-plane H force
$c_L(\alpha, \mathrm{Re})$	Wing lift coefficient
C_{L0}	Blade lift coefficient at zero angle of attack
$C_{LP}(\alpha_P)$	Blade lift coefficient at angle of attack α_P
C_{Lt}	Blade lift coefficient at angle of attack θ_P
$C_P \triangleq \dfrac{P}{\frac{1}{2}\rho A \nu_T^3}$	Propeller power coefficient
c_P	Chord of the propeller blade at 75% radius
$C_P^{'} = \dfrac{\pi^4}{8} C_P$	Scaled propeller power coefficient
c_{para}	Parasite drag coefficient
$C_Q \triangleq \dfrac{Q}{\frac{1}{2}\rho A R \nu_T^2}$	Propeller torque coefficient
$C_T \triangleq \dfrac{T}{\frac{1}{2}\rho A \nu_T^2}$	Propeller thrust coefficient

$C_T' = \frac{\pi^3}{8} C_T$	Scaled propeller thrust coefficient
d	Distance between the wing pivot and the aerodynamic center of the wing
d_A	Distance between the wing pivot and wing's CoM
$\mathbf{d}\boldsymbol{D}$	Drag force on the blade element
$\mathbf{d}\boldsymbol{H}$	In-plane drag force on the blade element
$\mathbf{d}\boldsymbol{L}$	Lift force on the blade element
$\mathbf{d}\boldsymbol{Q}$	Torque on the blade element around the propeller axis
$\mathbf{d}\boldsymbol{T}$	Thrust force on the blade element
E	Specific energy consumption
e_1, e_2, e_3	Vectors of the canonical basis of $\mathbb{R}^3$
$\boldsymbol{F_a}$	Aerodynamic forces acting on the wing(s)
FM	Figure of Merit
g	Gravity constant
GR	Glide Ratio
$\boldsymbol{H}$	In-plane drag force on the propeller
J	Moment of inertia of the UAV
J_A	Moment of inertia of the wing
J_B	Moment of inertia of the UAV structure except the wing
$k_a = \frac{1}{2}\rho\Sigma$	Characteristic constant for the wing
$k_{\text{para}} = \frac{1}{2}\rho\Sigma_{\text{para}}$	Parasite characteristic constant
L	Distance between the wing pivot and UAV's CoM
l	Distance between UAV's CoM and each propeller center
m	Mass of the UAV
m_A	Mass of the wing
m_B	Mass of the UAV structure except the wing
M_{FLOW}	Air mass flow along the wake
N	Number of propellers on the UAV
N_P	Number of blades in a propeller
P	Propeller power

p_∞	Atmospheric static pressure
p_l	Atmospheric pressure below the propeller disk
p_u	Atmospheric pressure above the propeller disk
Q	Torque acting on the propeller around its axis
R	Propeller radius
r	Distance from the blade element to the rotor hub
$\bar{r} = r/R$	Ratio of distance from the blade element to the rotor hub over the propeller radius
Re	Reynolds number
$\mathrm{Re}_{\mathrm{exp}}$	Exponential scaling constant for Reynolds number
$\mathrm{Re}_{\mathrm{ref}}$	Reference Reynolds number
$s = N_P c_P R/A$	Solidity of the propeller
$\boldsymbol{T}$	Thrust force generated by the propeller
$\boldsymbol{U}$	Total flow velocity over the blade section
$\boldsymbol{U_P}$	Velocity component perpendicular to the rotor plane
$\boldsymbol{U_T}$	Velocity component normal to the blade span in the rotor plane
$\boldsymbol{v_a}$	UAV linear air-velocity
$\boldsymbol{v_r}$	UAV reference velocity

List of Figures

List of Tables

Introduction

Unmanned Aerial Vehicles (UAVs) are becoming omnipresent in military, industries, and academia around the world. UAVs first appeared in the military as remote-control aircraft,[1] and nowadays they are increasingly popular in the battlefield for diverse missions such as real-time video reconnaissance, surveillance, electronic decoys and jammers, air-to-ground and air-to-air attacks, etc. [2, Chap. 2]. The expansion of the UAV market in recent years, however, mainly concerns the civil domain with small multi-rotor systems that can be easily deployed for various applications such as aerial video shooting for the media industry, inspection of plants, electricity networks, railways, etc. This fast-growing UAV industry impacts the global economy. According to Teal Group (tealgroup.com), worldwide UAV Market will total $91 billion in the next ten years. Based on the report in 2013 by AUVSI, 70,000 new jobs in the UAV sector will be created by 2017 in the USA (auvsi.org). Presently, progress in embarked electronics, light-weight cameras, and wireless communication has now made UAV technology affordable for general use. Indeed, myriad prototypes, especially small UAVs, have been constructed in the last two decades. One can mention some examples: fixed-wing UAVs such as the BATCAM [3] or the Trimble UX5 (trimble.com); helicopters such as the Raptor 90 [4] or the coaxial PetiteLion [5]; quadrotors such as the X4-flyer [6], the OS4 [7], or the experimental platform STARMAC II [8].

These UAVs are traditionally classified into fixed-wing and Vertical Take-Off & Landing (VTOL). For fixed-wing UAVs, the flight is primarily based on the use of the aerodynamic lift on the wings to compensate for the weight of the vehicle and the thrust to cancel the drag induced by air movement. Due to their streamlined shapes, inducing a high lift-to-drag ratio, these aerial vehicles have the advantage of energy efficiency. The disadvantage, however, is the need of runways for take-off and landing. As for VTOL UAVs, thanks to their ability to hover, they are particularly suitable for applications like observation and inspection of structures (power lines, bridges, etc.), but their efficiency in cruising flight is generally poor.

For many applications, however, both capacities of vertical take-off and efficient cruising flight are required. For example, a typical scenario requires the UAV to inspect an electricity pylon/wind turbine, and then to fly rapidly for examining another pylon/turbine that is hundreds meters away from the initial position. Clearly, fixed-wing UAVs are unsuitable for these types of missions whereas VTOL UAVs are not very efficient in the cruising flight phase. Given the requirements of these missions, convertible UAVs that have both the abilities of VTOL and efficient cruising flight, become interesting alternatives to both fixed-wing and VTOL UAVs. In fact, convertible aerial vehicles are not new. Throughout the late 1950s and early 1960s, the U.S. military began to examine the most effective approach to improve the speed of VTOL prototypes that include tilt-rotors, tilt-jets, tilt-wings, tilt-ducts, tail-sitters, and deflected thrust systems (see the website of the Smithsonian Air and Space Museum). However, these manned prototypes suffered from mechanical complexity, and some other specific problems like high angle of attack

[1] After World War I, three Standard E-1 fighter aircraft were converted as remote-control prototypes [1, p. 854].

stall in transition phases (e.g. tilt-wings), pilots' awkward sitting position (e.g. tail-sitters), etc. Till date, the arguably most successful convertible full-scale aircraft are tilt-rotors, e.g. Bell Boeing V22 Osprey. These types of convertible aerial vehicles, nevertheless, are designed not to sustain hover flight for a long time but to change quickly to forward flight mode.

Unmanned aerial vehicles usually possess less mechanical complexity and less payload constraints than manned vehicles with similar sizes. These facts, coupled with the improvement in efficiency of electrical motors and recent minimization of electronic components, have rekindled the interest in small convertible prototypes, as exemplified by the tail-sitters HoverEye [9] and Hediasyc [10], the tilt-rotor Wingcopter (wingcopter.com), the tilt-body Quadshot (transition-robotics.com), the tilt-body biplane quadrotor from University of Maryland [11], or the tilt-wing from Aachen University [12].

The objective of this work is to design, model, and control a new convertible UAV here proposed.

Simple mechanical concept:

The idea starts from a classical structure of quadrotor. The principal advantage of quadrotors is the simplicity of conception, as compared to helicopters which for a long time have been dominating the class of full-scale VTOL aerial vehicles. Our proposed structure, represented by figure 1, consists in adding to a quadrotor structure two wings that have axes very close to the propellers' plane, and that are joined with the quadrotor by several bars. Moreover, each wing is connected with the structure by a pivot articulation. This articulation is actuated, for example by one or several servo-motor(s), as represented in figure 1, in order to modify the wing pitch angle with respect to the propellers' plane. Another advantage of this structure is its flexibility. Indeed, we can easily replace the wings by different wings (in terms of profile or chord length for instance), without impacting the rest of the structure, knowing that different wings are more or less adapted to flight conditions, flight velocity, and payload.

Motivations for this structure:

- Autonomy for high speed flight: As mentioned above, one severe limitation of classical VTOL structures including quadrotor is their low energy efficiency. The addition of the wings to the quadrotor structure improves the energy efficiency in high speed cruising flight, while keeping the system's capacity for stationary flight.
- Flexibility for control design: The articulations of the wings provide the control for their inclination angles. This offers a grand flexibility for the control of the convertible aerial vehicle. Specifically, in cruising flight, the UAV's pitch angle can be controlled by either modifying the propeller thrust force, or the inclination angle of the wings, or both at the same time. The fact that the wings' pitch angles can be completely decoupled from the UAV's pitch angle is also an important aspect from the control point of view. This will be explained later in the thesis.
- Flexibility for the placement of payload: This type of UAV is typically utilized for inspection and surveillance tasks. For these goals, the UAV is required to embark some payload (e.g. a camera). Since inspired by a classical quadrotor structure, the proposed UAV is endowed with the same flexibility of payload placement, which is not generally the case for other structures with multi-rotors and wings.

Throughout this thesis, we attempt to find the right balance between simple design and accurate enough modeling to capture the physical behaviors of the system. For example, in aerodynamic modeling of propellers, analytical calculations based on momentum and blade element

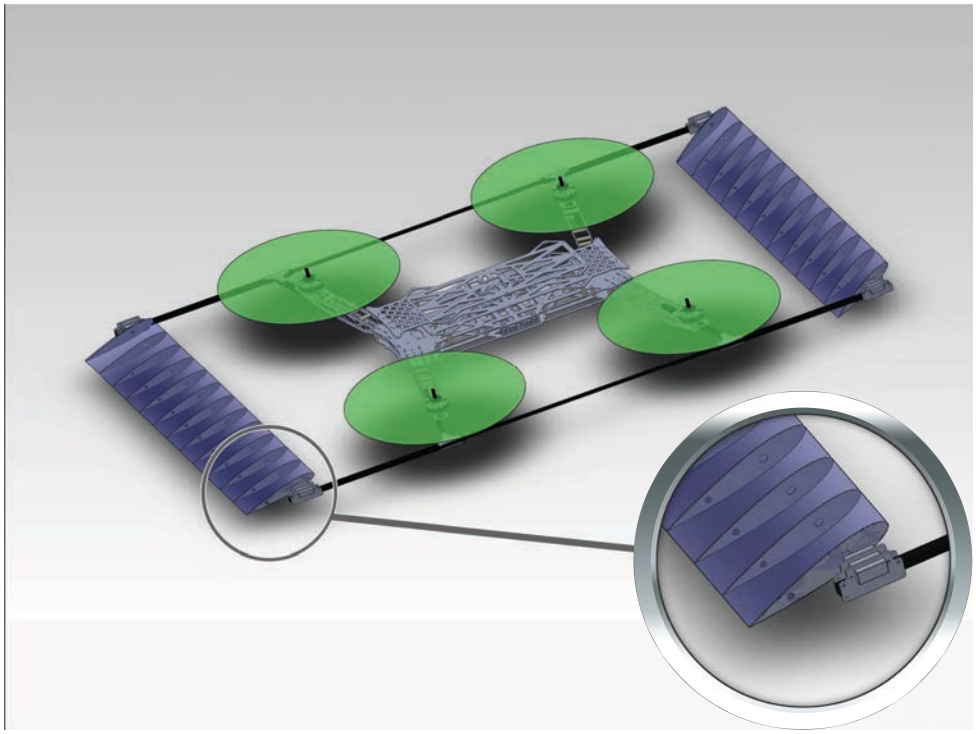

Figure 1: 3D SolidWorks model of our convertible mini-UAV

theories are favored over sophisticated computational fluid dynamics (CFD) numerical analysis. In addition, whenever sufficient to present the principal ideas, we focus on the planar (i.e. two-dimensional) movements of the UAV, which comprise the most common operating trajectories such as hover, VTOL, and forward cruising flight.

This work has been carried out during my Ph.D. at the *Institut des Systèmes Intelligents et de Robotique* (ISIR), *Université Pierre et Marie Curie* (UPMC). My research was funded by the *Chaire d'excellence en Robotique RTE*[2] *-UPMC* . This manuscript is organized in four chapters:

- **Chapter 1 - A Short Introduction to Aerial Vehicles:** This chapter introduces the main types of aerial vehicles, thereby provides the readers with basic information on the principal components of fixed-wing, VTOL, and convertible aircraft. At the same time, this chapter describes how the force and torque controls are generated in these aerial vehicles. Finally, we recall some performance indicators, which characterize the efficiency of each type of aerial vehicles in important flight phases such as hover or cruising flight.

- **Chapter 2 - Energy Modeling:** This chapter concerns the energy modeling approach for aerial vehicles with coplanar propellers and wing(s). The ultimate goal is to optimize the wings' inclination with respect to the propellers' plane so as to achieve energy-efficient flight. Standard momentum and blade element theories are the main ingredients for modeling of propeller aerodynamics. In order to obtain simple closed-form expressions, modeling simplifications are made and an eight-parameter-analytical model is proposed. The model parameters are identified from the experimental data reported in the literature. As for the wings, a simple NACA profile is selected and an approximate model of lift and drag coefficients over the entire flight domain is defined. Based on these models, the calculation

[2]The French company *Réseau de transport d'électricité*

of energy consumption reduces to solving a minimization problem in two variables. As an application, we compare the energy consumption of different UAV structures in the horizontal-flight range of $[0, 20]$ m/s. Concerning UAV design, the impact of various parameters (choice of propellers, wing(s) area, mass of UAV) is analyzed. This chapter also provides useful guidelines for the control design.

- **Chapter 3 - Control Design:** Before detailing the control design of our convertible UAV, a brief review of the control techniques for fixed-wing, VTOL, and convertible aerial vehicles in the literature is presented. Next, three approaches to the control design of our convertible system are introduced. The objective is to develop control strategies with minimal sensor suite. The first approach concerns teleoperation without velocity measurement. In this case only the Inertial Measurement Unit (IMU) (gyrometer, accelerometer) and barometer data are used for the control design. The second approach makes use of the same measurements. However, we consider the presence of strong varying wind that cannot be directly measured. The proposed solution relies on a slightly modified mechanical design and a spring-damper feedback control. By taking advantage of the additional degrees of freedom of the wings, we show that efficient control of the vehicle can be obtained without air-velocity measurements. This proposed strategy is particularly suited to small UAVs for which such measurements are difficult to obtain. Finally, the third approach benefits from velocity measurements in addition to the IMU data. The effect of propellers' downwash on the wings is analyzed, and a simple torque compensation strategy is proposed to reduce this undesirable effect. Simulation results support these above control strategies.

- **Chapter 4 - Conception and Preliminary Experiments:** This chapter presents the mechanical prototype of our convertible UAV. The fabrication process of the UAV is briefly described. The system architecture consists of a high level control and a low level control. Most of the components in these levels are described in detail. Finally, we present the experiments conducted on the platform and discuss the results.

Some of the results reported in this thesis have been published in research papers. The principal parts of chapter 2 appeared in [13, 14]. The second control approach in chapter 3 can be found in [15].

Chapter 1

A Short Introduction to Aerial Vehicles

1.1 Aerial Vehicles Introduction

Ever since the Wright brothers made the first flight by means of a vehicle heavier than air in 1903, many aerial vehicles have been constructed and developed with the aim to fly farther, faster, and more efficiently. The family of aerial vehicles can be roughly divided into three main classes: fixed-wing aircraft, Vertical Take-Off and Landing (VTOL) aircraft, and convertible aircraft.[1] We will discuss each class in detail.

1.1.1 Fixed-Wing Aircraft

A fixed-wing aircraft uses its wings to generate lift force to compensate for the weight of the vehicle. The thrust force generated by the aircraft engines compensates for the drag force acting on the aircraft body. Since the lift force is normally much larger than the drag force, fixed-wing aircraft is energy efficient. Figure 1.1 shows the principal components of the aircraft.

- The fuselage is the central main body of the aircraft.
- The wings are airfoils which mainly provide the lift force. The principal movable surfaces on the wings are ailerons, which are shown in figure 1.2.
- The empennage is the tail group that consists of stabilizers, elevators, and rudders.
- The powerplant is an assembling group of turbines and propellers to generate the thrust force.

The aircraft is controlled precisely thanks to its control surfaces: elevator, aileron, and rudder (figure 1.2). The movements of these surfaces change the airflow and pressure distribution on the wings and tail, thereby modifying the aircraft three-dimensional orientations: roll, pitch, and yaw. Figure 1.3 illustrates these orientations with associated axes and conventional types of stability. The elevators help balancing the aircraft since the latter is traditionally nose-heavy. In addition, the elevators are used for pitch control. The ailerons usually locate on the wings, one on each side. Moving the pilot control stick to the left causes the right aileron to deflect downward and the left aileron to deflect upward, as shown in figure 1.4. The downward deflection

[1] This classification is not perfect, since one can always find some counter-examples. Indeed, some high thrust-to-weight ratio fixed-wing aircraft can take off vertically, e.g. indoor single-propeller airplanes [16,17], so that they can be considered convertibles. In this thesis, fixed-wing aircraft refer to airplanes with fixed wing(s) uniquely designed for horizontal flight mode. In addition, this thesis does not consider flapping-wing prototypes.

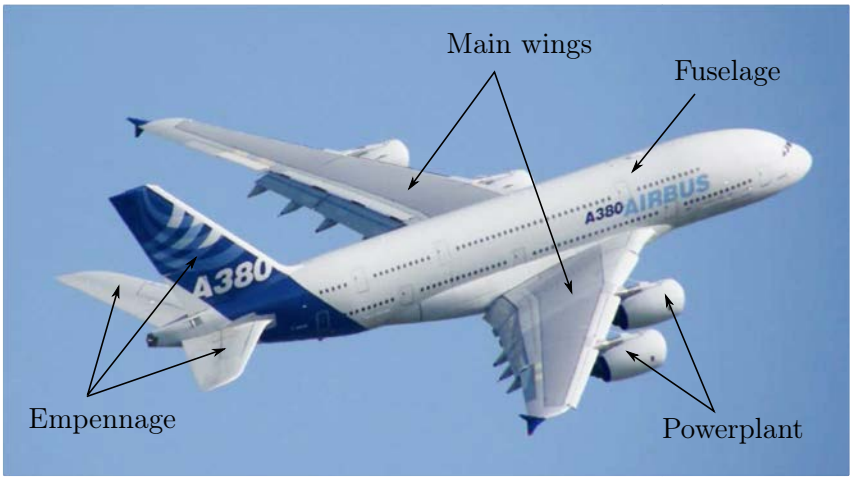

Figure 1.1: Main components of a fixed-wing airplane (Airbus A380, adapted image from Wikipedia)

of the right aileron increases the effective camber of the wing, thereby increasing the lift on the right wing. The reverse effect is produced on the left wing, decreasing its lift. The difference in the lift on the two wings causes the airplane to roll to the left. In addition, a secondary effect of aileron deflections is that the drag force on the right wing is greater than the one on the left wing. Consequently, an adverse yaw is produced as shown in figure 1.4. This effect is counteracted by the rudder. At this point, we call for a few remarks on airplane control:

- The control action of control surfaces depends on the aircraft speed. At low speed, the aerodynamic pressure on the control surfaces is low, hence larger control inputs, i.e. larger control surface angle deflections are required. By contrast, at high speed, the forces acting on the surfaces (proportional to the square of speed) are high even at small deflection of the control surfaces.

- The rotational and translational movements of the airplane are coupled, e.g. if an airplane inclines nose down, it flies forward at the same time and vice versa. This is due to the *underactuated* nature of standard airplanes: for six DoFs parameterizing the airplane position/orientation in space, there are only four independent control inputs: thrust intensity, elevator, aileron, and rudder deflections.

In the early days of aviation, mechanical systems with pulleys, linkages, etc. were used to control the airplane (figure 1.5(a)). These systems were often heavy and complex. To overcome these shortcomings, they were replaced by hydromechanical designs (figure 1.5(b)). These designs usually consisted of mechanical circuits and hydraulic circuits. Nowadays, with the advancement of electronics and computers, most airplanes are controlled by digital signals.

1.1.2 Vertical Take-Off and Landing (VTOL) Aircraft

VTOL aircraft, as its name implies, can take off or land vertically. It also has the ability to hover. There are many different types of VTOL aircraft as shown in figure 1.6[2]. Generally, VTOL design requires answering three basic questions [21]

[2]Note that convertible aircraft belong to a subset of VTOL aircraft. Therefore in figure 1.6, convertible aircraft like Bell Boeing V22 Osprey or Boeing X-50 are presented. They will be discussed in more detail in section 1.1.3.

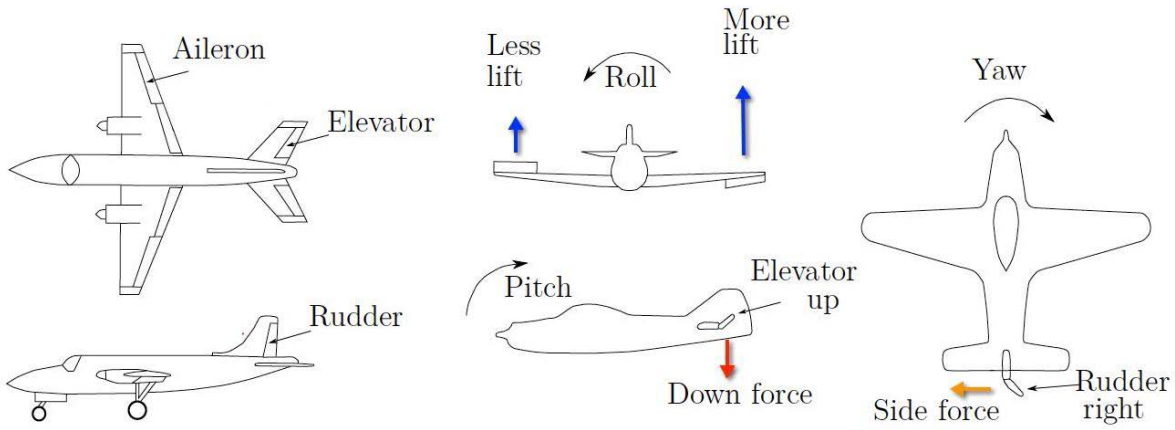

Figure 1.2: Control surfaces and their effects (aerospaceweb.org and [18])

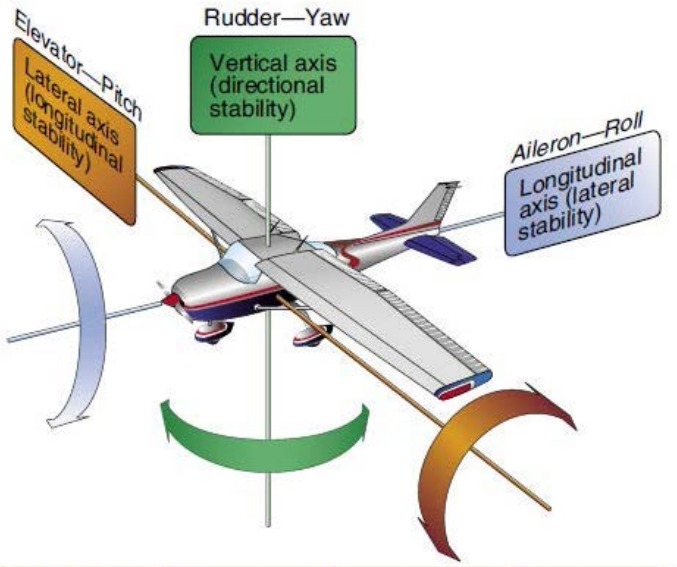

Primary Control Surface	Airplane Movement	Axes of Rotation	Type of Stability
Aileron	Roll	Longitudinal	Lateral
Elevator/ Stabilator	Pitch	Lateral	Longitudinal
Rudder	Yaw	Vertical	Directional

Figure 1.3: Overview of airplane control with control surfaces, control axes, and types of stability [19]

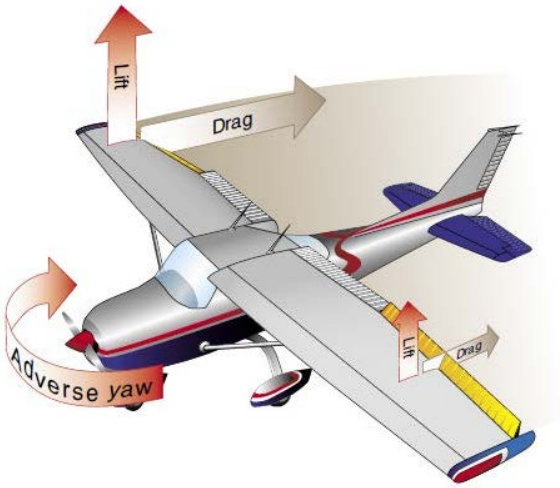

Figure 1.4: Lift and drag forces acting on wings and the adverse yaw due to deflection of ailerons [19]

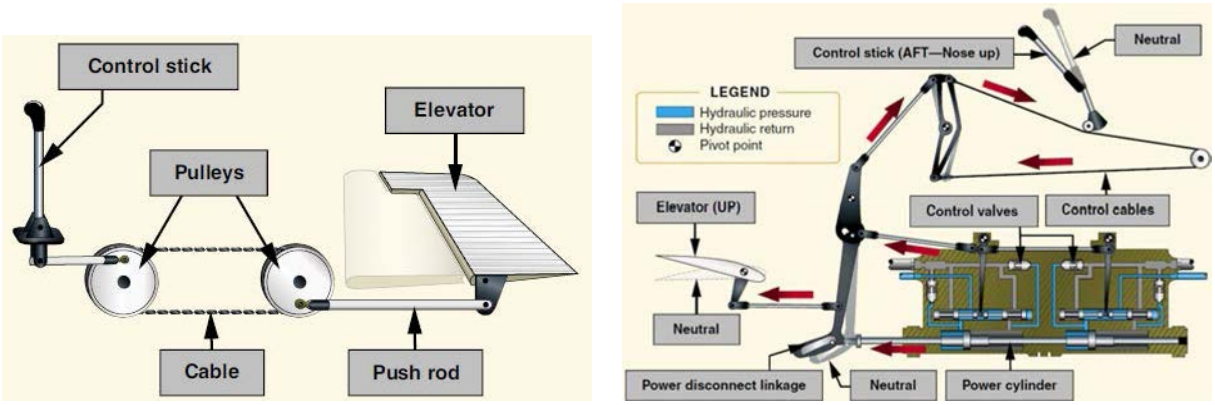

(a) (b)

Figure 1.5: Airplane (a) mechanical control system and (b) hydromechanical control system [19]

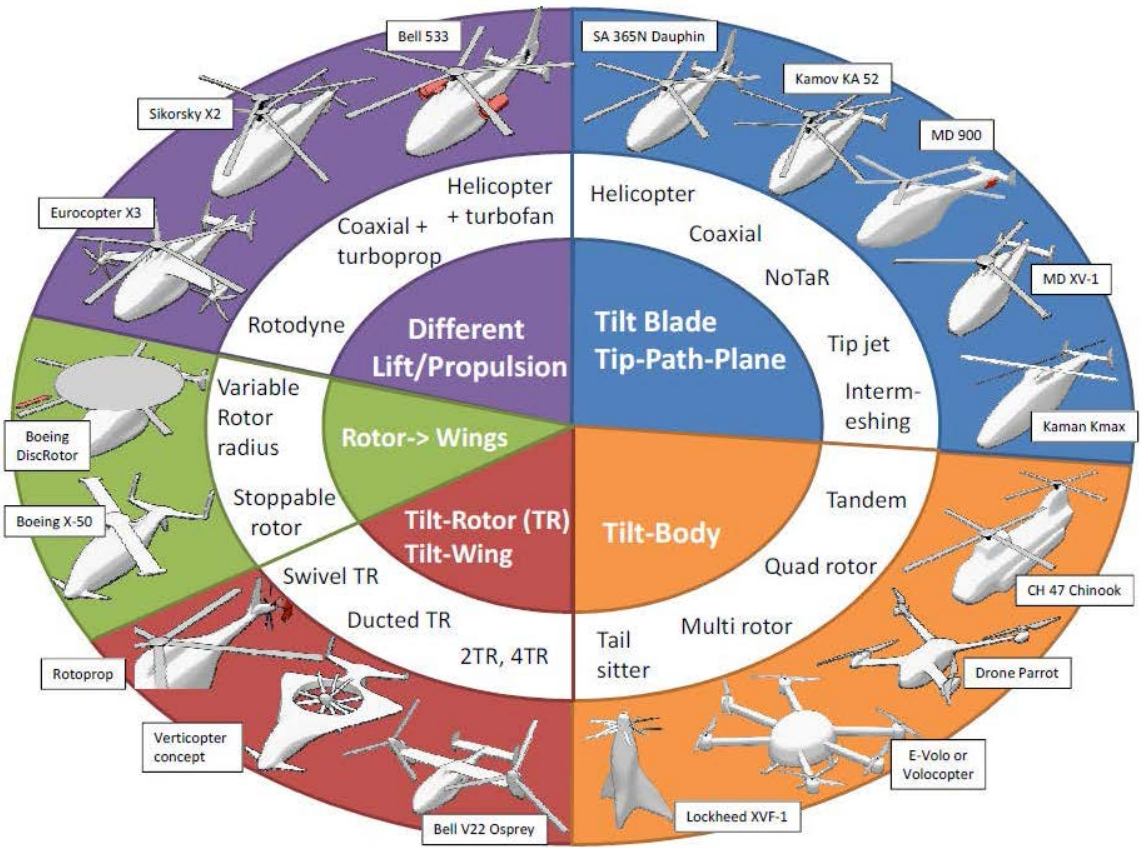

Figure 1.6: Non-exhaustive overview list of different types of VTOL concepts [20]

1. How to generate and regulate the thrust force?
2. How to generate the torques to control the VTOL orientation in three-dimensional space?
3. How to counter parasite torques generated by drag forces?

Due to the flexibility of designing mechanisms and the diversity of VTOL applications, there are countless VTOL prototypes built over the years. For these prototypes, the thrust force is generally generated by one or several main rotor(s). Following [20], VTOL aircraft can be roughly classified into five categories:

1. "Tilt Blade Tip-Path-Plane" is the most common category, which includes classical helicopters. The control torque for roll and pitch is obtained by changing the blade angle of attack over the rotor disk, thereby changing the lift distribution over this disk. The counter torque (yaw control) can be obtained in different ways: using one tail rotor like SA 365N Dauphin, two tail rotors like MD XV-1, contra-rotating main rotors like Kamov KA 52, intermeshing counter-rotating rotors like Kaman Kmax, air flow generated from a fan like MD 900.
2. "Tilt-Body": most tilt-body vehicles are multi-rotor systems (quadrotor, tandem, etc.) and roll/pitch control torque is achieved by generating different lift forces on the different rotors. For tail-sitter, torque control is accomplished by changing the orientations of control surfaces. In general, tilt-body usually use contra-rotating or counter-rotating rotors for counter-torque and yaw control.
3. "Tilt-Rotor/Tilt-Wing": for tilt-rotor the torque control is effectuated by tilting one or more rotors. As for tilt-wing aircraft, the torque control is achieved by tilting the whole wing together with the rotors.
4. "Rotor $\leftrightarrow$ Wing": the rotors can function as wings and vice versa. For example, in Boeing X-50 prototype , the rotor could be stopped in flight and could act as a fixed wing. In the other example, Boeing DiscRotor could retract the blades at high speed to reduce the drag force.
5. "Different Lift/Propulsion": the aircraft use different devices for lift (e.g. main rotors) or propulsion (e.g. turbofan, turbo propellers)

In general, VTOL aerial vehicles come in various sizes and shapes, but most of them share the same components. Keeping in mind this fact, two common VTOL aerial vehicles, classical helicopter and quadrotor, are presented next.

a) Classical helicopter

Figure 1.7 shows the main components of a helicopter including the fuselage, the thrust-generated rotor system, and the anti-torque tail rotor. First of all, we focus on a very important component of a helicopter, the so-called swashplate/spider mechanism, as illustrated in figure 1.8. The blade pitch is applied via a bar projecting from the bearing housing known as pitch horn. The pitch horn is connected to its own individual track rod by a swivel bearing and vertical movement of the track rod will cause the change in blade angle of attack. The lower end of the track rod is connected to a spider (or rotating star) which is constrained to rotate with the rotor. The spider is kept in the same plane with a swashplate (which does not rotate with the rotor)

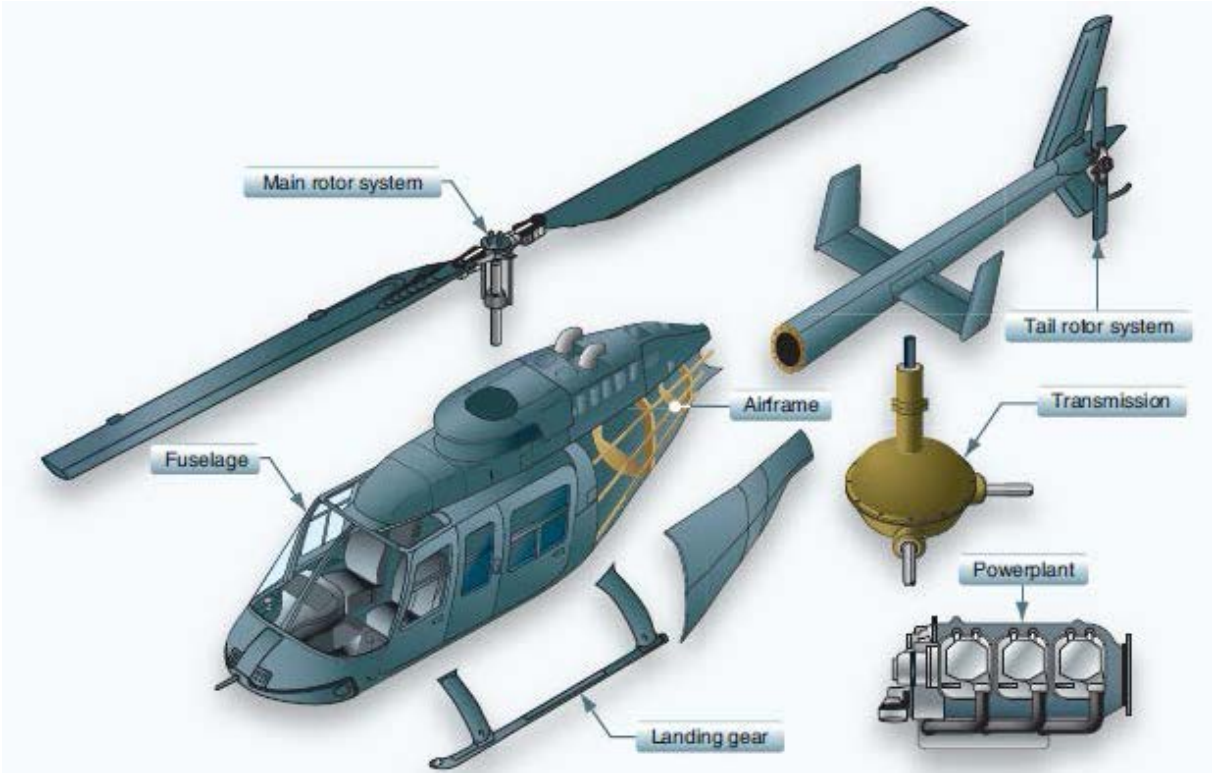

Figure 1.7: Main components of a helicopter [22]

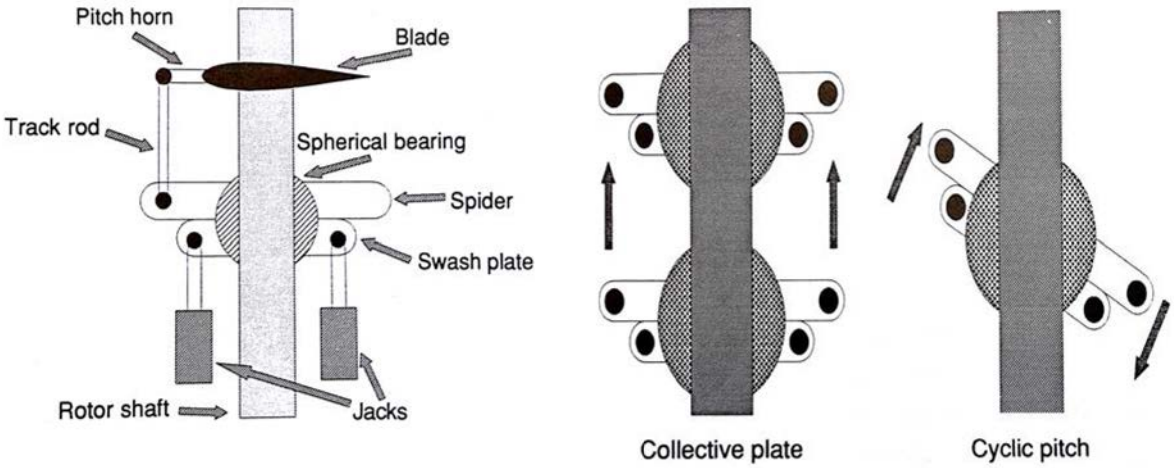

Figure 1.8: Schematic diagram of main rotor hub with collective and cyclic pitch control [23, Chap. 6]

via spherical bearing. The position and orientation of the swashplate are determined by three actuators, or jacks, connecting it to the top of the fuselage. If the actuators move in unison (figure 1.8 Collective plate), the spider and swashplate move up or down together, thereby all the blades have the same change in pitch angle. This action is called collective pitch control. If the actuator move unequally (figure 1.8 Cyclic pitch) then the rotation plane of the spider and swashplate combination is altered and cyclic pitch control is achieved [23].

Apart from collective and cyclic pitch controls, the other two major control components in a helicopter are antitorque control and throttle control. All these control modes are discussed in a global manner as follows:

- Collective pitch and throttle control: As shown above, the collective control changes the pitch angle of main rotor blades simultaneously. Modifying the pitch angle of the blades causes a change in drag force, which affects the rotor rotational speed. In order to maintain a constant rotor rotational speed, which is essential for helicopter operations, a proportional change in power is required. This is accomplished with the throttle control. For example, as the pilot raises the collective stick, blade pitch angle increases, drag increases, rotor rotational speed decreases, and engine power needs to be increased to maintain the same rotational speed. To relieve the pilot from the difficult task of controlling both collective and engine power at the same time, usually a mechanical connection is established between the collective level and engine throttle. When the collective level is raised, the engine throttle is automatically increased by internal mechanical linkages.

- Cyclic pitch control: The cyclic pitch control changes the rotor disk orientation as shown above. Since the total blade lift force is essentially perpendicular to the main rotor disk plane (more precisely, the tip-path plane), the direction of the total thrust force changes. By application of Newton's law, the equilibrium orientation of the whole helicopter is modified, thereby allowing the helicopter to fly in any desired direction: forward, rearward, left, or right.

- Anti-torque control: The rotation of the main rotor causes an opposing torque acting on the helicopter fuselage. There are many ways to counteract this torque: tail rotor, contra-rotating or counter-rotating rotors, NOTAR system, etc. By far, the most popular way is using a tail rotor - a small propeller mounted at helicopter tail generating thrust force to compensate for the torque as in figure 1.9.

b) Quadrotor

Quadrotor is a multirotor VTOL aerial vehicles propelled by four rotors. The history of quadrotor dates back to the early twentieth century with various attempts like the Breguet-Richet Gyroplane (1907), the Oehmichen No.2 (1920), and the Flying Octopus by De Bothezat (1922, see figure 1.10). These early prototypes had serious limitations in terms of control and especially endurance. The aforementioned Flying Octopus could remain airborne for only 2 minutes 45 seconds. Recently, quadrotor designs have become popular for many UAV applications, including inspection and surveillance. There are several advantages of quadrotors over similar-scaled helicopters. First, standard quadrotors are mechanically less complex than helicopters due to the absence of the sophisticated rotor hub. This greatly simplifies the design and maintenance of the quadrotor. Second, the use of four small-diameter rotors (usually) allows quadrotors to possess less kinetic energy during flight as compared to helicopters. Hence, they are safer to

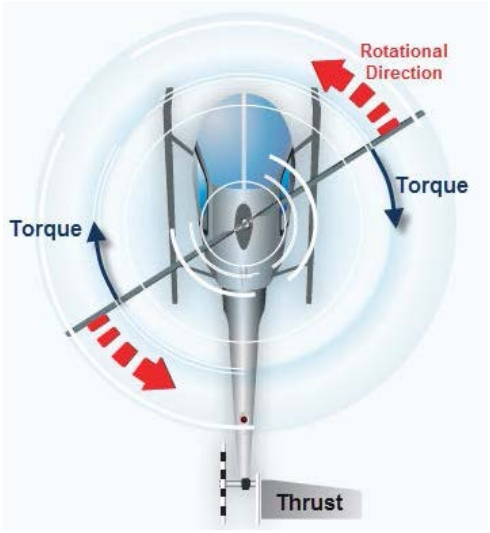

Figure 1.9: Tail rotor anti-torque to compensate for the torque (adapted image from [22, Chap. 3])

interact with. Finally, they are small, low cost, and can be built in large quantity. These advantages have motivated in recent years the development of swarms of quadrotors for cooperative works [24–26]. The principal disadvantage of quadrotors is their poor energy performance as compared to helicopters with similar sizes and weights (see section 1.2).

Some examples of mini-quadrotors are shown in figure 1.11 and their simple control principles are illustrated in figure 1.12. A standard quadrotor has two pairs of counter-rotating rotors. The first and the third rotors rotate clockwise whereas the second and the fourth rotors rotate anticlockwise. In practice, most quadrotors are symmetric around their center of mass (CoM), i.e. the distances between each rotor to the quadrotor CoM are all equal). The thrust is controlled by modifying the rotational velocity of the rotors. As a rotor spins around its axis, an opposing torque (due to propeller blades aerodynamic drag) is generated around the rotor axis. In hovering or in vertical climb/descent (figure 1.12(a)), all rotors spin at the same speed. Due to the counter-rotating nature of the two rotor pairs and the aforementioned symmetric property, the net torque on the quadrotor is zero, thereby no yaw motion is generated. Roll and pitch control can be achieved by increasing the speed of one rotor and decreasing that of the diagonally opposite rotor. For example, in figure 1.12(b), a forward pitch-down movement is generated by increasing the third rotor speed while decreasing the first rotor speed. The yaw control is achieved by the difference between the torques between a pair of opposite rotors and the remaining pair. For instance, in figure 1.12(c), a counterclockwise yaw movement is generated by increasing the first and the third rotor speeds while decreasing the second and the fourth rotor speeds.

As in the case of fixed-wing airplanes, VTOL aerial vehicles are usually *underactuated*. For example, the standard quadrotor has four independent control inputs (four propellers spinning velocity) versus six DoFs parameterizing the quadrotor position/orientation in space. Due to this limited mobility, some studies, e.g. [27, 28] add more DoFs to classical quadrotor by using tilting propellers. These configurations improve the versatility of quadrotor, i.e. it can track additional trajectories that are not possible with standard quadrotor, at the expense of more complexity in mechanical design.

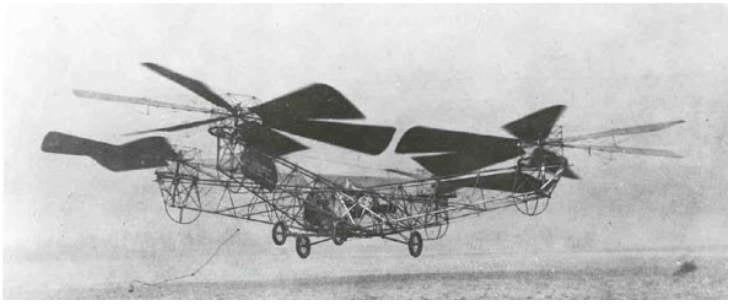

Figure 1.10: De Bothezat Quadrotor (source: Edison National Historic archive)

(a) (b)

Figure 1.11: Some examples of mini quadrotors: (a) Parrot AR.Drone 2.0 (parrot.com) and (b) Our ISIR Prototype

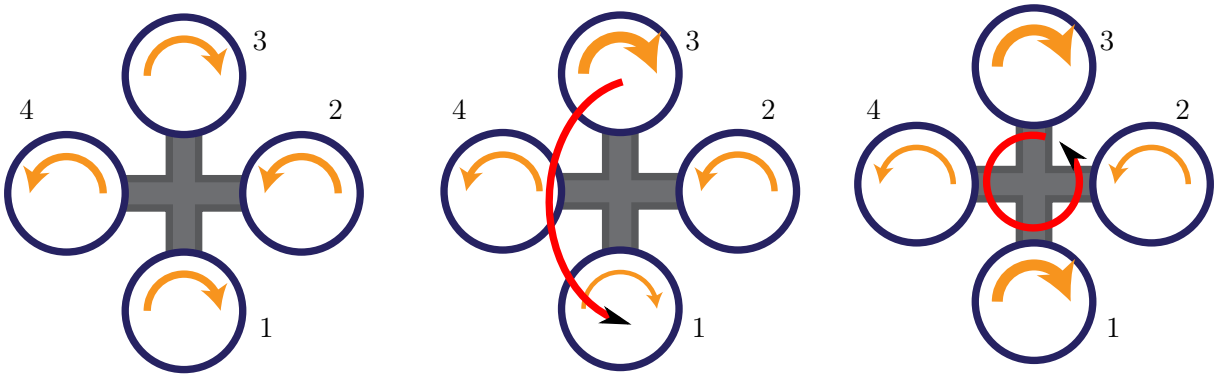

(a) (b) (c)

Figure 1.12: Quadrotor control for different cases: (a) hover or vertical climb/descent, (b) pitch down, and (c) counterclockwise yaw. The thickness of yellow arrow is proportional to rotor rotational velocity. The red arrow represents the movement direction of the quadrotor.

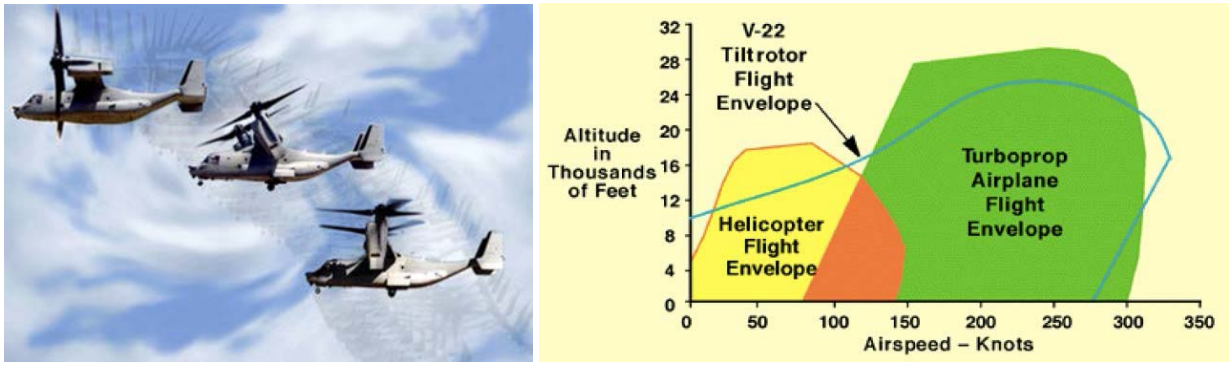

Figure 1.13: Bell Boeing V22 Osprey tilt-rotor in transition from hover to cruising flight and its flight envelope [31])

1.1.3 Convertible Aircraft

In this thesis, the term "convertible aircraft" refers to aircraft with wings that have the capacity of hover flight. There are many types of convertible aircraft as shown in figure 1.6: different lift/propulsion (compound helicopter), rotor-wing, tilt-rotor/tilt-wing, and tilt-body. The compound helicopters rely on dedicate lift or propulsion actuators. These aerial vehicles suffer from performance loss in cruising flight due to the drag on the large rotor(s). As for rotor-wing convertibles, they are difficult to control. The stoppable rotor Boeing X-50 is retired from development due to a flaw in design and testing crashes [29]. In this section, we will focus on tilt-rotor/tilt-wing and tilt-body aerial vehicles, which are increasingly popular in unmanned applications. The most common small convertible UAV configuration is a set of propellers and wing(s), where the relative orientation of the propellers with respect to wing(s) might change.

1.1.3.1 Tilt-Rotor/Tilt-Wing

The convertible aircraft of the type tilt-rotor like the one in figure 1.13 has two rotors, making vertical taking off and landing possible like helicopters. In addition, in cruising flight, the rotors can be rotated forward by nearly 90° to fly similar to the fixed-wing airplane. This convertible ability increases the tilt-rotor flight envelope to cover both helicopter and airplane regimes as illustrated in figure 1.13. However, the main disadvantage of tilt-rotors is the poor performance in hover caused by relatively small rotor diameters and large rotor mast. As an example for tilt-rotor mini-UAV, Wingcopter (figure 1.14) has four rotors and behaves like a quadrotor in hover mode. These rotors can be tilted simultaneously into cruising mode. A schematic model of tilt-rotor can be viewed in figure 1.15. The two rotors rotate in opposite directions, thereby canceling the reactive torques in order to keep the UAV stable. Altitude control is achieved by varying the rotational velocities of both rotors simultaneously. Modifying differently the speeds of the two rotors leads to roll control. Pitch control is performed by tilting the rotors simultaneously to the front, which also provides forward motion. For yaw control, the tilt angles of the right and left rotors are changed in opposite directions [30].

Concerning tilt-wing aircraft, Vertol VZ-2A in figure 1.16 was the first of this type to successfully perform the transition from vertical to horizontal flight. The aircraft can pivot entire wing upwards, along with its lifting propellers. As compared to tilt-rotor aircraft, this tilt-wing model has an advantage of only one mechanically tilting part. However, the latter have several drawbacks. First, high angle of attack of the wing may give rise to the stall phenomenon during

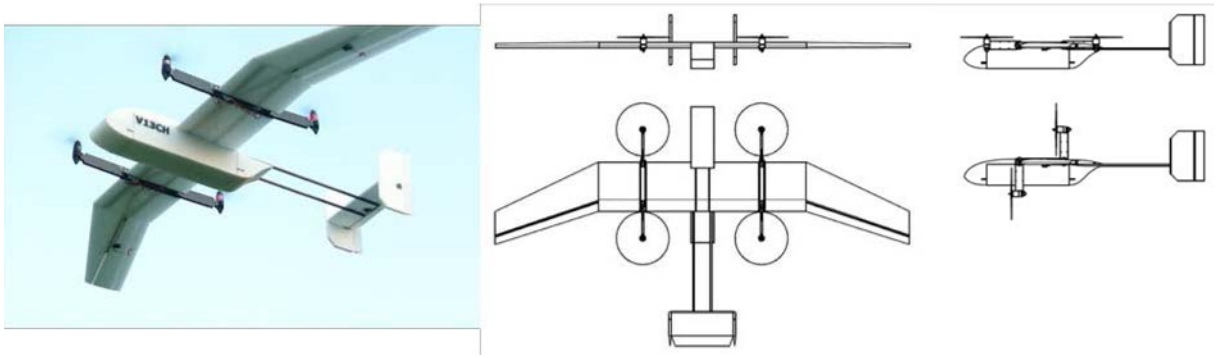

Figure 1.14: Wingcopter tilt-rotor mini-UAV (wingcopter.com)

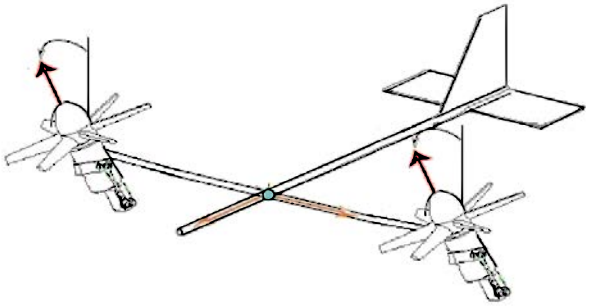

Figure 1.15: Tilt-rotor schematic model, adapted from [30]

Figure 1.16: Tilt-wing Vertol VZ-2 (1957, Smithsonian Air and Space Museum)

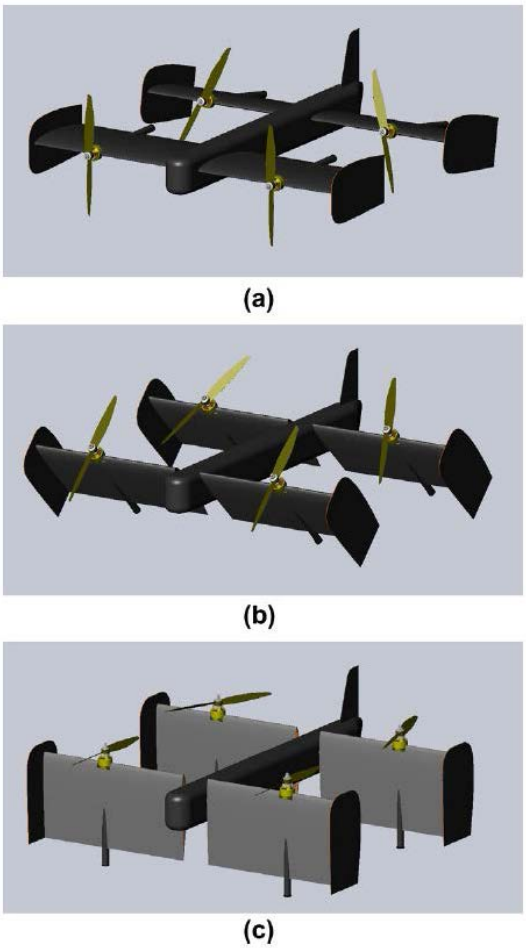

Figure 1.17: CAD model of a quad tilt-wing in three modes: (a) cruising flight (b) transition flight (c) vertical flight [33]

transition phase[3], leading to the loss of stability. Second, the aircraft is difficult to control when flying in gusty condition due to the large surface of the wing. Finally, this model requires additional control in helicopter mode, since there is no cyclic control but only auxiliary-thrust devices. Due to these disadvantages, the tilt-wing prototypes were discontinued (see the Smithsonian Air and Space Museum website).

In recent years, inspired by the rapid development of small UAVs, notably quadrotors, some hybrid prototypes (combining features of quadrotor and tilt-wing) have been developed, e.g. the quad tilt-wing SUAVI in figure 1.17 [33] or the QTW McArt2 by Japan Aerospace Exploration Agency [34].

[3] Although due to the downwash of the propellers on the wing, the angle of attack of the wing is reduced, i.e. stall is delayed at higher angle of attack [32].

Figure 1.18: Quadshot tilt-body mini-UAV (transition-robotics.com)

1.1.3.2 Tilt-Body

Tilt-body convertible requires the body aircraft to rotate during the transition fly. In addition, the rotor hubs are rigidly attached to the aircraft body. For example, the Quadshot UAV in figure 1.18 is the hybrid model with a slender wing and four rotors. In VTOL mode, this UAV works like a quadrotor. During transition flight, the thrust forces from two back rotors are larger than the thrust force from two front rotors, making the whole UAV tilting forward into cruising mode. The disadvantage of this model is that the four rotors are fixed on UAV body. Hence tilt-body has less flexibility to find optimal configuration to minimize the energy consumption or to control as compared to UAVs that can change the relative orientation of propellers w.r.t UAV main body like Wingcopter.

A special kind of tilt-body aircraft is the so-called tail-sitter due to the ability to take off and land on its tail. An early prototype was the Convair Pogo in 1954 as depicted in figure 1.19. The thrust generation was effectuated by a pair of three-bladed contra-rotating propellers. The main motivation for tail-sitter aircraft was their ability to perform VTOL from/to a limited surface, e.g. on a small warship. However, the inherent problem with this model was the difficulty for a pilot in the uncomfortable sitting position to land the aircraft. By contrast, unmanned systems do not suffer the above problem. An example of modern tail-sitter UAV is the HoverEye in figure 1.20. It is a ducted-fan UAV with two contra-rotating rotors to generate the thrust. Torque control is achieved by a set of governor surfaces that can change the tilting angles to deflect the propellers' downwash (see figure 1.20). Another example of small prototype is the tail-sitter SUPAERO VTOL MAV [35]. The propulsion system consists of two coaxial contra-rotating motors-propellers. Wind tunnel testing in that study has demonstrated a small loss of thrust in the contra-rotating system as compared to a single motor-propeller. However, the maximum residue torque for the contra-rotating system is about ten times lower than the torque measured on the single motor-propeller system.

1.2 Aerial Vehicle Performance

The aerial vehicle performance is largely determined by the power calculation over a range of flight conditions. This calculation may then be translated into quantities such as climb rate, ceiling, range, optimal speed, and maximum speed. These quantities define the operational capability of aerial vehicles. To quantify the performance of aerial vehicles, various indicators are used: disk loading and power loading in hover flight; glide ratio and specific energy consumption ratio in

Figure 1.19: Tail-sitter XFY Pogo (1954, source: Wikipedia)

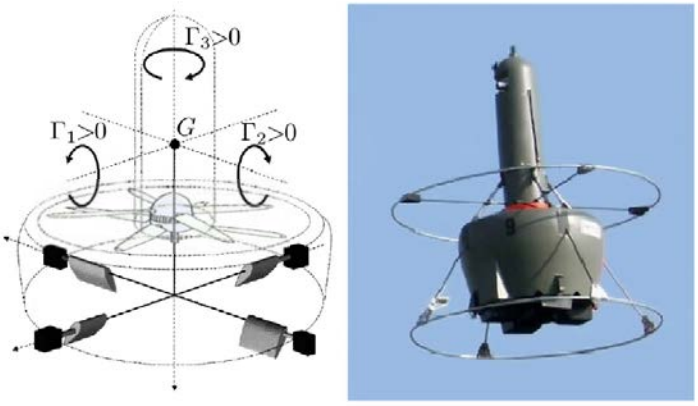

Figure 1.20: Hover Eye ducted-fan tail-sitter UAV [9]

cruising flight. In this section, we also present some simple energy performance comparisons of different fixed wing, VTOL, and convertible aerial vehicles.

1.2.1 Hover Performance

Aerial vehicles hover efficiency is usually characterized by the power loading, defined by amount of thrust generated per required unit power. In addition, a related parameter frequently used in helicopter analysis is the disk loading, defined as thrust on one square meter of rotor. It can be shown that the power loading is inversely proportional to the disk loading (see Eq. (2.17)). Vertical lift aircraft that have a low disk loading will require low power (i.e., they have high power loading) and will tend to be more efficient [36, Sec. 2.3]. Table 1.1 shows that helicopters are the most efficient aerial vehicles in hover.

Aerospace vehicle designation	Aerospace vehicle type	Equivalent disc loading (N/m^2)	Ideal induced velocity (m/s)	Ideal power loading (N/kW)
Robinson R44	Modern utility helicopter	140	7.6	132.3
Westland Lynx	Utility helicopter	364	12.2	82.0
Mil Mi-10k	Crane helicopter	388	12.6	79.4
Sikorsky S64A	Crane helicopter	496	14.2	70.3
Sikorsky CH-53E	Heavy helicopter	718	17.1	58.5
Bell V22 Osprey	Tilt rotor	1161	21.8	45.9
Hiller-Ryan XC-142	Tilt wing	2387	31.2	32.1
Ryan XV5A	Fan lift	16823	82.8	12.1
Harrier GR3	Jet lift	114403	216	4.6
Space shuttle	Rocket	465479	436	2.3
Saturn V F1	Rocket	2964912	1087	0.9

Table 1.1: Equivalent disk loading, ideal induced velocity, and ideal power loading comparison of different aerial vehicles and rockets [23]

To proceed with hover performance, comparison between helicopter and quadrotor efficiency

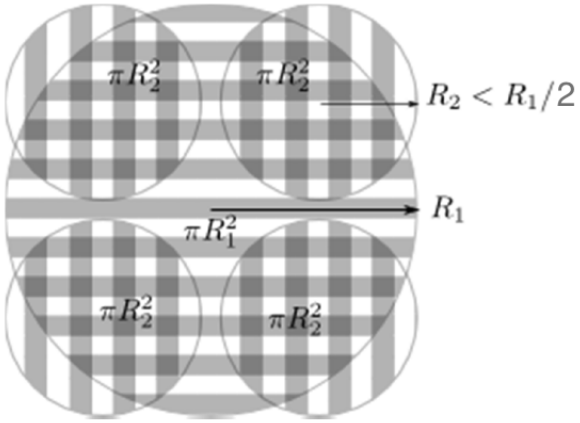

Figure 1.21: Comparison between helicopter and quadrotor disk areas for same footprint

will be discussed. Although the first manned quadrotors appeared in early twentieth century (see section 1.1.2), they were not popular as compared to helicopters. One of the main reasons is that quadrotors (usually) have lower endurance as compared to helicopters with similar weight and footprint. Indeed, from figure 1.21, the disk area of helicopter is:

$$A_{\text{heli}} = \pi R_1^2$$

For quadrotors, there is usually a gap between adjacent propellers to avoid aerodynamic interference. The quadrotor propeller radius is usually smaller than half of helicopter disk radius $A_2 < A_1/2$. The disk area of quadrotor is:

$$A_{\text{quad}} = 4\pi R_2^2 < 4\pi (R_1/2)^2 = \pi R_1^2 = A_{\text{heli}}$$

The above formula proves that the total disk area of the quadrotor is smaller than the helicopter. Hence, with the same total thrust, the disk loading of the quadrotor is higher than the helicopter. Consequently a standard quadrotor is usually less efficient than a helicopter with the same footprint and mass. [37] performs similar analysis and suggests that traditional helicopter (even with 15% loss due to tail rotor) is 25% more efficient than a standard quadrotor.

In practice, when evaluating the performance of aerial vehicles, one must take into account the effect of Reynolds number and the flow interaction between different components. These are even more important concerning small UAVs, since the effects of low Reynolds number degrade significantly the performance of the propellers [38].

In order to improve the performance of quadrotor, Driessens and Pounds [37] presents a prototype with a single fixed-pitch main rotor and three small rotors that provide both counter-torque and maneuvering control (figure 1.22). They report a hover performance improvement of 15% over a classic prototype with the same mass and footprint.

1.2.2 Cruising Performance

Cruising performance of aerial vehicles is often characterized by indicators like glide ratio or specific energy consumption. Glide ratio is the ratio of lift force over drag force on an aircraft:

$$\text{GR} = \frac{\text{Lift}}{\text{Drag}} \tag{1.1}$$

Figure 1.22: Y4 Triangular Quadrotor [37]

Figure 1.23: Robinson R44 helicopter (robinsonheli.com)

High value of GR is desirable. For example, a Boeing 747 has glide ratio of 17.7 in cruising flight. That means if all the engines of the airplane are turned off, it is able to glide forward 17.7 km when it descends 1 km. By contrast, the helicopter Robinson Raven II like the one in figure 1.23 has glide ratio of only 4.5, which is four times smaller than that of a Boeing 747. To characterize further the energy efficiency of an aircraft, the specific energy consumption is used:

$$E = \frac{P}{WV} \tag{1.2}$$

where P is the power, W is the weight of the aircraft and $V > 0$ is the speed. E registers energy consumption per meter traveled for each newton of gross weight. A small E is desirable. As an example, a Boeing 747 weighs $W = 3 \times 10^6$ N during mid-flight at cruising speed of $V = 250$ m/s. It is powered by 45 MW engines. Hence, the specific energy consumption ratio E is 0.06 [39]. Unlike the case of fixed-wing aircraft where the thrust compensates the drag force only, the thrust force on VTOL aircraft has to compensate both the vehicle's weight and the drag force. Therefore, the energy performance of VTOL aircraft in cruising fly is generally poor. For example, the Robinson Raven II helicopter weighs $W = 11$ kN at cruising speed $V = 55$ m/s and is powered by 183 kW engines (source: robinsonheli.com). Hence, the specific energy consumption ratio E is 0.29, which is five times more than that of a Boeing 747.

Figure 1.24 demonstrates the specific energy consumption of various aircraft, automobiles, trains, birds, etc. against the speed. The most striking feature of figure 1.24 is that helicopters have the highest E. Although modern helicopters like the aforementioned Robinson Raven II

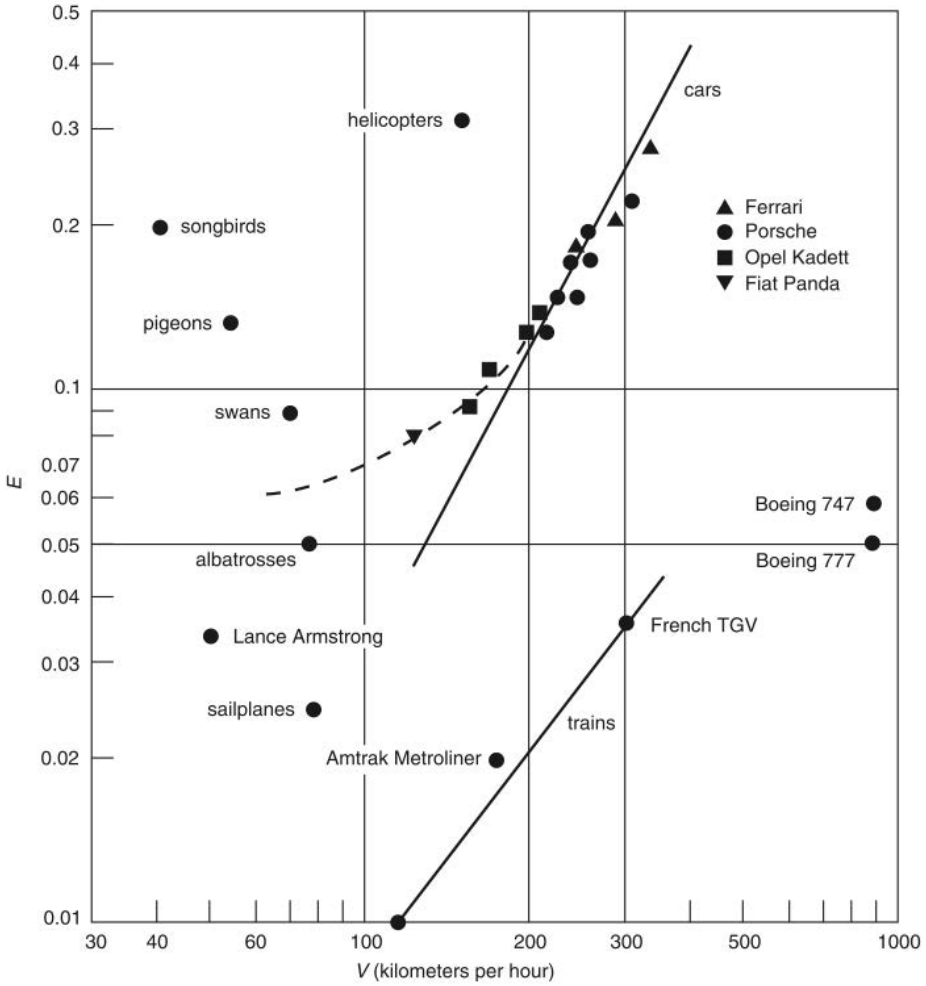

Figure 1.24: Specific energy consumption plotted against the speed [39]

should place more to the right for increasing cruising speed and slightly below for improving E, they still perform worse than even automobiles in energy scale. We can take another example of a small quadrotor like the one described in the article by Aleksandrov and Penkov [40]. It has dimensions 500 mm × 500 mm × 90 mm and the weight is 1.4 kg. Its battery capacity is 4900mAh at 11.1 V and the power of all four motors is 130 W. At $V = 5$ m/s, we can calculate $E = 1.8$. High specific energy consumption explains why this quadrotor can stay in the air for only 15 min. This limits the duration of a typical mission.

Focusing now on VTOL aerial vehicles, figure 1.25 compares required power for four different aerial vehicles with the same mass [20]. For fair comparison, the rotor solidity (the ratio of total blade area over rotor area, defined in Eq. (2.70)) in all configurations are kept the same (see [20]): the helicopter has one rotor with four blades; the coaxial has two rotors with two blades each; the tandem has identical rotors as the coaxial but separated; the tilt-rotor has two smaller rotors but with three blades. At low speed, the tandem spends the least power thanks to its two large separated rotors. The coaxial, also with two rotors, is less efficient than the tandem but still spend less energy than the traditional helicopter. The tilt-rotor spends the most power since it suffers from loss due to the smaller rotors producing downwash on wings. When the speed

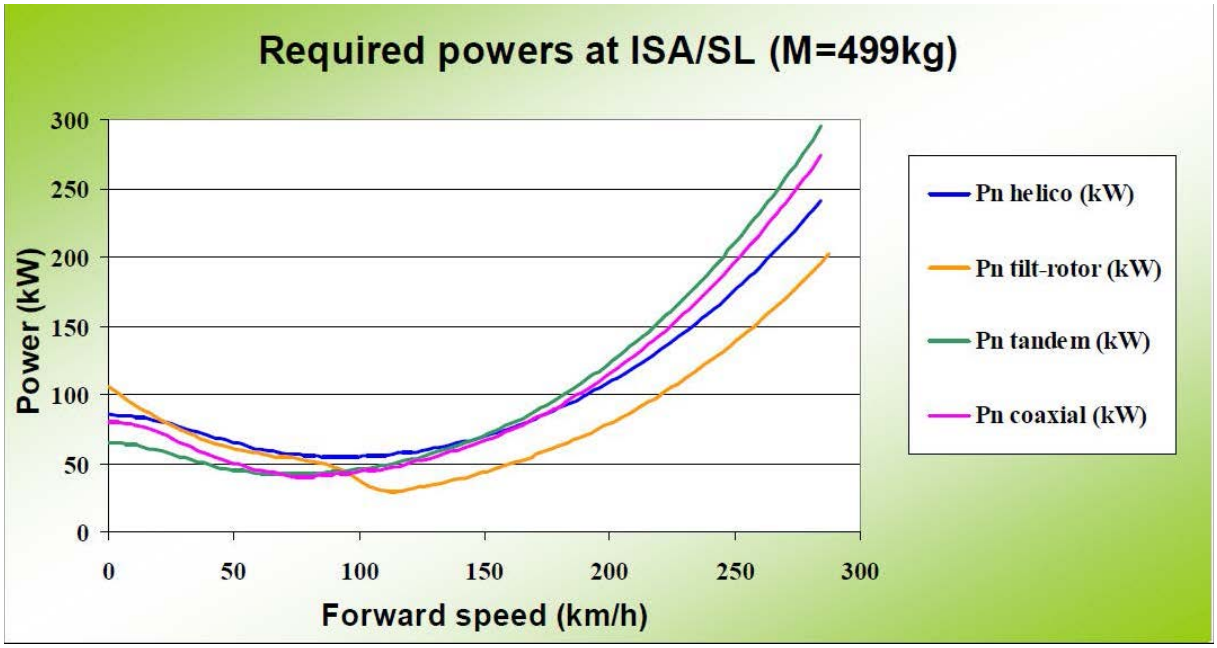

Figure 1.25: Comparison of the required powers for the equivalent helicopter, coaxial, tandem, and tilt-rotor at International Standard Atmosphere at sea level [20]

.

increases (especially from 60 to 120 km/h), the power curve of the tilt-rotor rapidly approaches the one of the tandem, since the interference of the two rotors becomes negligible. At high speed, the tilt-rotor in its airplane mode is the most efficient while the rest suffers high parasite drag, especially the tandem. The coaxial with the drag penalty due to big rotor mast is less efficient than the helicopter.

1.3 Chapter Summary

A short introduction to aerial vehicles was presented in this chapter. Although there are many different types of aerial vehicles, they can be classified into three main classes: fixed-wing, VTOL, and convertible. For each class, a brief overview of its components, including control components was presented. Any aerial vehicle has its advantages and disadvantages. Helicopters have the best hover efficiency thanks to their small disk loading, but their cruising performance is mediocre. Fixed-wing aircraft are efficient in cruising flight but they require long runway or catapult/net system for take-off and landing. Convertible aerial vehicles possess the advantages of both fixed-wing and VTOL aircraft, but they usually have additional mechanical complexity. Nonetheless, convertibles have a great potential. Starting from 1950s, countless different manned convertible experimental prototypes have been built. Although not all of these were successful, important lessons have been learned along the route. In the last few decades, the development of digital computers and the minimization of electronic components paved the way for small unmanned aerial systems. Some manned aerial prototypes that were not so successful in the past become popular in unmanned systems thanks to the simplicity of the latter. The quadrotor along with some small convertible UAVs are good examples of this trend. In addition, the flexibility of unmanned systems allows many new and innovative convertible configurations. However, there

are some challenges associated with small prototypes. Firstly, the effects at small Reynolds number can degrade significantly the performance of these systems. Secondly, according to square-cube law, small UAVs tend to be highly sensitive to turbulence [41]. The next chapter will focus on energy modeling of these small UAVs.

Chapter 2

Energy Modeling

The previous chapter shows that many convertible UAV configurations consist of a set of propellers and one or several wings where the relative orientation of the wing(s) w.r.t. the propellers' plane may change. Since the prototype that we have developed also belongs to these configurations, this thesis focuses on such systems, in particular in this chapter, their energy modeling. To our knowledge, there are few works on the energy modeling of convertible UAVs in the available literature, despite the fact that energy efficiency is the main incentive for using these systems in place of more classical structures. There is little doubt that convertible UAVs constructors have developed dedicated models, but those are not available in general publications. There exists of course a large literature on the modeling of helicopters [23, 42–44]. In these references, momentum and blade element theories are the main ingredients for propeller modeling and these tools can be used for the modeling of convertible UAVs as well. The case of small convertible UAVs needs to be specifically addressed, however, due to particular characteristics of these systems. First of all, lift forces acting on the wings of a convertible vehicle can be important and must be taken into account in the analysis since they modify substantially the thrust necessary to sustain the vehicle's weight and impact on the vehicle's orientation. By contrast, energy evaluation for helicopters typically assumes that the propellers must sustain the vehicle's weight. Secondly, we are interested here by fixed-pitch propellers so that modifications of the thrust are accomplished by changing the main rotor's rotational velocity. This contrasts with the case of helicopters. For example, Newman [23] presents the procedure to calculate the energy of helicopters while assuming that the propeller's velocity (blade tip velocity) is constant. Furthermore, the power decomposition in terms of induced power, profile power, and parasite power is always used for helicopters but its justification for convertible vehicles is not clear due to the aforementioned large variations of thrust and vehicle orientation. Finally, one must also account for a degradation in performance of propellers at low Reynolds number compared to larger propellers for full-scale aircraft, as mentioned by Brandt and Selig [38]. Having identified the special characteristics of small convertible UAVs, our approach to energy modeling of these systems is presented in the following sections 2.1-2.3. Based on this modeling, a comparison between different UAV configurations is proposed in section 2.4.

To conclude this short introduction, let us finally mention that more accurate models can be obtained by applying more elaborate (but also much more complex) methods than those used here. This thesis is not an aerodynamics thesis. The objectives of the modeling here developed are twofold: first, to easily allow one to evaluate the energy consumption in terms of the geometrical and mechanical characteristics of the structure so as to facilitate presizing [20], and next to provide useful information for the control design.

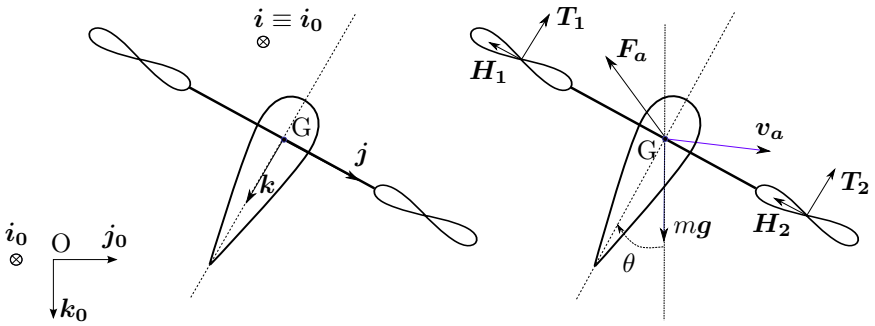

Figure 2.1: 2D Model of the UAV

2.1 Overview of the Modeling Approach

Before detailing the calculations to model the energy consumption, we provide in this section an overview of the modeling approach. In view of the diversity of existing structures, it is not possible to provide a modeling directly pertinent to any specific system. Our objective is to provide a modeling approach applicable to most of them. We start from two observations:

1. Most convertible UAVs, and especially the prototype we have built, are composed of a set of coplanar propellers and one (or several coplanar) wing(s). Of course, it is not difficult to find exceptions. For example, on many tilt-rotor systems, rotors can be inclined independently, so that the propellers are no longer coplanar. In most flight phases like hover flight or cruising flight along straight lines, however, the propellers are indeed coplanar.

2. In agreement with the existing literature, the main scenario of interest is the evaluation of the energy consumption on motion at constant linear velocity (possibly zero).

Based on these observations, we consider a VTOL-UAV composed of a set of N coplanar propellers of same size and characteristics and a main body including wing(s), as depicted in vertical projection on the left part of figure 2.1. The following notation is used:[1]

- $\mathcal{I} = \{\mathrm{O}, \boldsymbol{i_0}, \boldsymbol{j_0}, \boldsymbol{k_0}\}$ is an inertial frame with $\boldsymbol{k_0}$ pointing downward. This choice is consistent with the common use of NED (North-East-Down) frames in aeronautics.

- $\mathcal{B} = \{\mathrm{G}, \boldsymbol{i}, \boldsymbol{j}, \boldsymbol{k}\}$ denotes a body frame with G the vehicle's center of mass (CoM) and $\{\boldsymbol{i}, \boldsymbol{j}, \boldsymbol{k}\}$ coinciding with $\{\boldsymbol{i_0}, \boldsymbol{j_0}, \boldsymbol{k_0}\}$ when the vehicle is in hover. The plane $(\mathrm{G}, \boldsymbol{i}, \boldsymbol{j})$ also coincides with the propellers' plane.

- $\boldsymbol{v_a}$ denotes the linear air-velocity of the UAV and the vector of coordinates of $\boldsymbol{v_a}$ in $\mathcal{I}$ is denoted as v_a, i.e. $\boldsymbol{v_a} = v_{a,1}\boldsymbol{i_0} + v_{a,2}\boldsymbol{j_0} + v_{a,3}\boldsymbol{k_0}$.

Assumptions: We focus on a 2D motion[2] in the plane $(\mathrm{O}, \boldsymbol{j_0}, \boldsymbol{k_0}) = (\mathrm{G}, \boldsymbol{j}, \boldsymbol{k})$ spanned by the gravity vector and the UAV's linear velocity vector. It is assumed that the vehicle moves at zero angular velocity and constant linear velocity. It is also assumed that all aerodynamic forces acting on the UAV (i.e. forces acting either on the propellers or on the main body) are tangent to the motion plane $(\mathrm{O}, \boldsymbol{j_0}, \boldsymbol{k_0})$. This requires, in particular, the wind velocity to be parallel

[1] Throughout this thesis, bold letters are used for vectors in Euclidean space whereas ordinary letters are used for coordinates of these vectors in a basis.

[2] This work can be extended to the general 3D case, for example to take into account lateral forces induced by a non-zero side-slip angle, at the expense of a more complicated modeling.

to the plane $(\mathrm{O}, \boldsymbol{j_0}, \boldsymbol{k_0})$. Finally, it is assumed that the pitch moment due to asymmetric flow around the propellers in cruising flight is zero (see section 2.2.5).

From these assumptions, the vehicle's orientation is fully determined by the angle θ between $\boldsymbol{k_0}$ and $\boldsymbol{k}$.

The following forces, orthogonal to $\boldsymbol{i_0}$, act on the vehicle (see the right part of figure 2.1):

- The vehicle's weight $\boldsymbol{W} = mg\,\boldsymbol{k_0}$ with m the vehicle's mass and g the gravity constant;
- The aerodynamic force $\boldsymbol{F_a} = F_{a,2}\,\boldsymbol{j_0} + F_{a,3}\,\boldsymbol{k_0}$ acting on the vehicle's main body;
- The thrust forces $\boldsymbol{T_i} = -T_i\,\boldsymbol{k}$ $(i = 1, \cdots, N)$ acting on the propellers, with $T_i \geq 0$ the intensities of these forces;
- The in-plane forces $\boldsymbol{H_i} = H_i\,\boldsymbol{j}$ $(i = 1, \cdots, N)$ acting on the propellers, with H_i the coordinates along $\boldsymbol{j}$ of these forces.

Since the vehicle moves at constant linear velocity, Newton's law implies that the following two relations are satisfied:

$$\sum_{i=1}^{N} T_i = (mg + F_{a,3})\cos\theta - F_{a,2}\sin\theta \tag{2.1}$$

$$\sum_{i=1}^{N} H_i = -F_{a,2}\cos\theta - (mg + F_{a,3})\sin\theta \tag{2.2}$$

In order to satisfy the assumption of motion with zero angular velocity, the moment of external forces must also be zero. On a multi-rotor system this is typically achieved by a proper choice of T_i, consistent with Eq. (2.1). For simplicity we assume that this property is satisfied with $T_i = T, \forall i$, i.e. all propellers deliver the same thrust. This is usually satisfied with a good degree of accuracy for a well-built quadrotor. Then, Eq. (2.1) and Eq. (2.2) reduce to:

$$T = \frac{1}{N}\Big[(mg + F_{a,3})\cos\theta - F_{a,2}\sin\theta\Big] \tag{2.3}$$

$$H = \frac{1}{N}\Big[-F_{a,2}\cos\theta - (mg + F_{a,3})\sin\theta\Big] \tag{2.4}$$

with T and H the respective thrust and in-plane force intensities on each propeller.

The approach used to model the energy consumption proceeds as follows.

1. **Analytical modeling of aerodynamic forces:** Using momentum and blade element theories, analytical models of T, H, and the torque Q needed to drive each propeller are derived:

$$\begin{cases} T = f_T(\theta, v_a, \varpi, \nu_{\text{ind}}) \\ H = f_H(\theta, v_a, \varpi, \nu_{\text{ind}}) \\ Q = f_Q(\theta, v_a, \varpi, \nu_{\text{ind}}) \end{cases} \tag{2.5}$$

where ϖ is the propeller rotational speed and the so-called "induced velocity" ν_{ind} is the solution of an implicit analytic equation:

$$f_\nu(\theta, v_a, T, \nu_{\text{ind}}) = 0 \tag{2.6}$$

Aerodynamic forces acting on the vehicle's main body are defined as:

$$F_a = f_a(\theta, v_a) \tag{2.7}$$

where the function f_a will be specified further. Note that, by assuming F_a does not depend on ϖ and ν_{ind}, we implicitly neglect interactions between the flow induced by the propellers and the flow over the wing(s). This assumption needs to be justified (or relaxed) on a case by case basis, depending on the vehicle's structure.

2. **Determination of the orientation equilibrium and propellers' speed:** Using the fact that the function f_T is invertible with respect to $\varpi \geq 0$, ϖ can be expressed as a function of θ, v_a, T, and ν_{ind}:

$$\varpi = f_\varpi(\theta, v_a, T, \nu_{\text{ind}}) \tag{2.8}$$

where the function f_ϖ is obtained by inversion of f_T with respect to ϖ. From Eq. (2.5), (2.7), and (2.8), Eq. (2.3) and Eq. (2.4) can be written as:

$$T = \frac{1}{N}\Big[\big(mg + f_{a,3}(\theta, v_a)\big)\cos\theta - f_{a,2}(\theta, v_a)\sin\theta\Big] \tag{2.9}$$

$$f_H\Big(\theta, v_a, f_\varpi(\theta, v_a, T, \nu_{\text{ind}}), \nu_{\text{ind}}\Big) = \frac{1}{N}\Big[-f_{a,2}(\theta, v_a)\cos\theta - \big(mg + f_{a,3}(\theta, v_a)\big)\sin\theta\Big] \tag{2.10}$$

Replacing T in Eq. (2.6) and Eq. (2.10) by the right-hand side of Eq. (2.9), given the air velocity v_a one obtains two implicit equations in two unknowns θ and ν_{ind}. This system of equations is solved numerically to obtain the equilibrium orientation θ and the induced velocity ν_{ind}. The value of T is then given by Eq. (2.9) and the propeller speed ϖ by Eq. (2.8).

3. **Energy consumption:** The torque Q is obtained directly from Eq. (2.5). This allows one to compute the power $P = NQ\varpi$ and subsequently the energy consumption.

Before proceeding with the details, a few remarks are necessary.

i) The proposed approach can be simplified by neglecting the in-plane force $\boldsymbol{H}$ which are typically small w.r.t. the aerodynamic forces acting on the wing(s). This corresponds to setting $H = 0$ in Eq. (2.4) (i.e. $f_H = 0$ in Eq. (2.10)). Then, θ is first determined by numerically solving Eq. (2.10) and ν_{ind} is determined next from Eq. (2.6) using expression Eq. (2.9) for T. In this way solving a system of two equations in two unknowns is reduced to solving independently two systems of one equation in one unknown.

ii) Concerning Step 2, there may exist several solutions (θ, ν_{ind}) to Eq. (2.10). In particular, even when the in-plane force $\boldsymbol{H}$ is neglected, strong lift forces and the associated stall phenomenon can lead to several equilibrium orientations for a given airspeed v_a [45]. We will come back to this issue in a next chapter. In practice, being essentially interested in optimizing the energy consumption, only the equilibrium orientation associated with the minimum energy consumption is of interest.

2.2 Propeller Modeling

Propeller modeling for aerial vehicles is usually based on classical theories like momentum theory and blade element theory. These theories utilize fundamental equations of aerodynamics to construct analytical equations. In order to model more precisely the propeller and the flow interaction between components of the system, an advanced theory named vortex theory is employed to realistically take into account the vortex field generated by moving airfoils (an

example of a vortex field created by a VTOL aircraft is shown in figure 2.2). In vortex theory, each rotor blade is modeled by single vortices or vorticity surfaces. This opens possibilities for studying the time-average and instantaneous flow fields generated by the propeller [42]. However, the price of vortex theory is high computational complexity, which usually does not justify the small increase of accuracy in practical modeling. The detailed discussion of vortex theory is beyond the scope of this thesis. Interested readers can refer to numerous available references on the subject [42–44]. Coming back to momentum and blade element theories, application to propeller modeling is now recalled.

Figure 2.2: Vortex field generated by a Bell Boeing V22 Osprey tilt-rotor flying over the ocean (courtesy of Ted Carlson / Check Six on time.com)

2.2.1 Recalls on Momentum Theory

Momentum theory or actuator disk theory is a classical analysis to estimate the rotor performance based on overall flow velocites and the total thrust and power. Momentum theory applies the fundamental conservation law of fluid mechanics (conservation of mass, momentum, and energy). It was developed for marine propellers by W. J. M. Rankine in 1865 and R. E. Froude in 1885, and later extended in the twentieth century for airplane propellers [44]. This theory is based on several assumptions (see [23, Chap. 3]):

1. The propeller has an infinite number of blades.
2. The propeller is modeled by a constant pressure difference across its disk.
3. The air downwash velocity through the propeller area is constant across the disk.
4. The vertical velocity is continuous through the disk.
5. There is no swirl in the wake (see the discussion in section 2.2.5).
6. The airflow is divided into two non-interacting regions, namely that which passes through the propeller disk and that which is external to the disk.

These are simplifying assumptions, but it is recognized in the literature that they lead to a good approximation of many characteristic quantities associated with a propeller.

2.2.1.1 Hover Flight

Consider a propeller in hover. The actuator disk is depicted on figure 2.3. The symbols p_u and p_l denote respectively the atmospheric pressures above and below the propeller disk. The atmospheric static pressure is p_∞. Due to the rotation of the propeller blades, the air is accelerated through the rotor disk with velocity $\boldsymbol{\nu_{ind}} = \nu_{\text{ind}}\boldsymbol{k}$, $\nu_{\text{ind}} \geq 0$, called induced velocity.[3] The velocity in the wake, far downstream, is denoted as $\boldsymbol{\nu_D} = \nu_D\boldsymbol{k}$, $\nu_D \geq 0$. The propeller thrust is given by:

$$T = (p_l - p_u)A \tag{2.11}$$

where A is the area swept by the propeller blades.

Energy conservation equates the work done by the rotor to the rate of change of energy in the fluid. As an integration form of energy conservation law for the fluid, Bernoulli's equation can be applied above and below the propeller disk:

$$\begin{cases} p_\infty &= p_u + \frac{1}{2}\rho\nu_{\text{ind}}^2 \\ p_\infty + \frac{1}{2}\rho\nu_D^2 &= p_l + \frac{1}{2}\rho\nu_{\text{ind}}^2 \end{cases} \tag{2.12}$$

where ρ is the air density. Equation (2.11) and Eq. (2.12) yield:

$$T = \frac{1}{2}\rho A\nu_D^2 \tag{2.13}$$

By conservation of mass, the mass flux[4] is constant all along the wake and equal to the mass flow through the propeller disk per unit time:

$$M_{\text{FLOW}} = \rho A\nu_{\text{ind}} \tag{2.14}$$

In addition, conservation of momentum law dictates that the propeller thrust is equal to the rate of change of axial momentum of the air per unit time:

$$T = M_{\text{FLOW}}\nu_D = \rho A\nu_{\text{ind}}\nu_D \tag{2.15}$$

From Eq. (2.13) and Eq. (2.15), we have $\nu_D = 2\nu_{\text{ind}}$ i.e. the fluid velocity at the wake is double the induced velocity at the actuator disk. Substituting this into Eq. (2.13) and rearranging gives:

$$\nu_{\text{ind}} = \sqrt{\frac{T}{2\rho A}} \tag{2.16}$$

Having relating the induced velocity with the thrust and physical parameters A and ρ, we can now characterize the hover performance by the power loading - which is thrust generated per unit of power (in this case, induced power):

$$\frac{T}{P} = \frac{1}{\nu_{\text{ind}}} = \sqrt{\frac{2\rho}{T/A}} \tag{2.17}$$

In order to hover efficiently, the ideal power loading T/P needs to be large, and by consequence small disk loading T/A is required. In addition, the Figure of Merit (FM) compares the performance of an ideal rotor to the actual rotor:

$$\text{FM} = \frac{P_{\text{ideal}}}{P} = \frac{T\nu_{\text{ind}}}{P} \tag{2.18}$$

[3] We use without distinction the term "induced velocity" for the vector $\boldsymbol{\nu_{ind}}$ and its coordinate ν_{ind} along $\boldsymbol{k}$.

[4] The mass flux is defined here as the amount of fluid mass per unit time. Hence, its unit is kg/s.

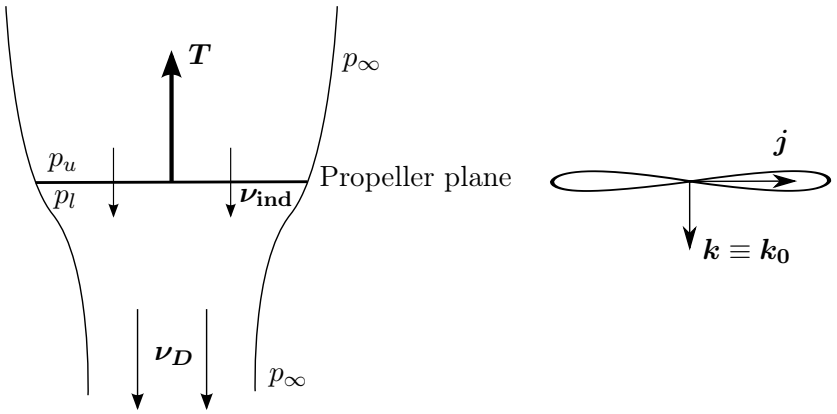

Figure 2.3: Actuator disk streamtube in hover flight (adapted from [23, p. 28 Fig. 3.1])

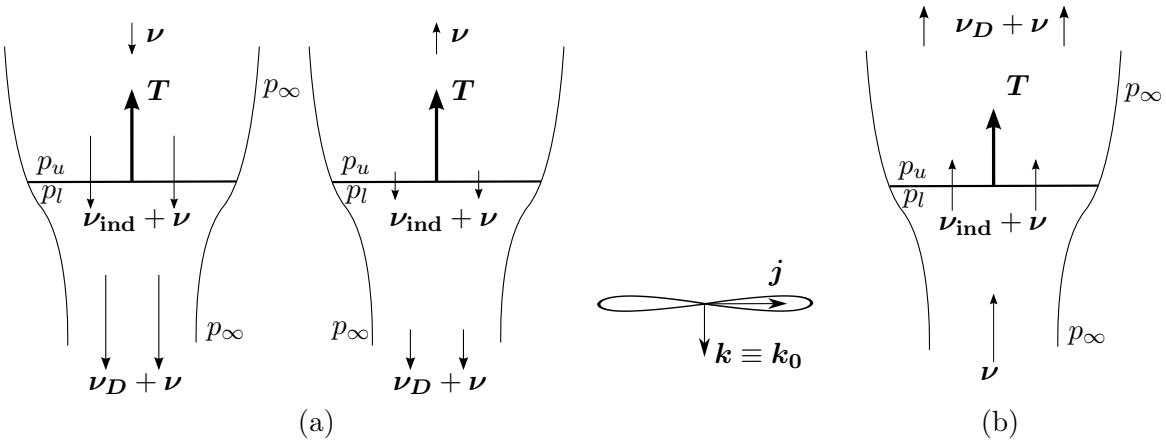

Figure 2.4: Actuator disk streamtube in axial flight, when the total flow through propeller disk is (a) downward and (b) upward (adapted from [23, Chap. 4])

The ideal Figure of Merit is FM = 1, when the entire mechanical power is converted to produce thrust. The Figure of Merit is lower for real rotor because of power loss for blade drag, parasite drag, friction, etc. For full-size helicopter rotors, the maximum Figure of Merit is typically FM = 0.75 to 0.80 [44, p. 36].

2.2.1.2 Axial Flight

Assume that the propeller is flying vertically so that its shaft direction is aligned with $\boldsymbol{k_0}$ (i.e. $\boldsymbol{k} \equiv \boldsymbol{k_0}$) with (air-)velocity $\boldsymbol{v_a}$. The flow velocity is $\boldsymbol{\nu} = -\boldsymbol{v_a}$ where $\boldsymbol{\nu} = \nu \boldsymbol{k}$. We classify axial flight in two cases depending on the direction of the total flow ($\boldsymbol{\nu_{ind}} + \boldsymbol{\nu}$) through the propeller disk: downward flow in the direction of $\boldsymbol{k}$ in figure 2.4(a) and upward flow opposite direction of $\boldsymbol{k}$ in figure 2.4(b). The first case corresponds to a propeller in climb $\nu > 0$ or in descend with slow rate $\nu < 0$ and $|\nu|$ is small (so that $|\nu| \leq \nu_{\text{ind}}$). The second case corresponds to a propeller in high speed descent with $\nu < 0$ and $|\nu| > \nu_{\text{ind}}$.

We consider in detail the axial flight equations when propeller disk flow is downward as in figure 2.4(a). Bernoulli equation is applied above and below the propeller disk as in the hover

case:

$$\begin{cases} p_\infty + \frac{1}{2}\rho\nu^2 &= p_u + \frac{1}{2}\rho(\nu_{\text{ind}} + \nu)^2 \\ p_\infty + \frac{1}{2}\rho(\nu_D + \nu)^2 &= p_l + \frac{1}{2}\rho(\nu_{\text{ind}} + \nu)^2 \end{cases} \tag{2.19}$$

The propeller thrust is obtained:

$$T = \frac{1}{2}\rho A(\nu_D + 2\nu)\nu_D \tag{2.20}$$

The mass flux is:

$$M_{\text{FLOW}} = \rho A(\nu_{\text{ind}} + \nu) \tag{2.21}$$

In addition, conservation of momentum law yields:

$$T = M_{\text{FLOW}}(\nu_D + \nu - \nu) = \rho A(\nu_{\text{ind}} + \nu)\nu_D \tag{2.22}$$

From Eq. (2.20) and Eq. (2.22), we deduce $\nu_D = 2\nu_{\text{ind}}$ as in the hover case. Substituting this into Eq. (2.22) and rearranging gives:

$$\nu_{\text{ind}}^2 + \nu\nu_{\text{ind}} - \frac{T}{2\rho A} = \nu_{\text{ind}}^2 + \nu\nu_{\text{ind}} - \nu_{\text{ind},0}^2 = 0 \tag{2.23}$$

where $\nu_{\text{ind},0} = \sqrt{\frac{T}{2\rho A}}$ is the induced velocity at hover, as in Eq. (2.16).

Consider the case when propeller flow is upward as figure 2.4(b). The analysis is similar to the downward case above, except that now the free stream velocity is directed upward, and therefore the wake is above the rotor disk. We can easily obtain:

$$\nu_{\text{ind}}^2 + \nu\nu_{\text{ind}} + \nu_{\text{ind},0}^2 = 0 \tag{2.24}$$

Equation (2.23) gives one positive induced velocity solution which is plotted as the curve ABC in figure 2.5. Equation (2.24) gives two positive solutions of induced velocity: one solution corresponds to the dashed curve DE, and one solution corresponds to the solid curve EF. The dashed portions of the curves are branches of the solution that do not correspond to the real physical behavior of the rotor wake. The line $\nu + \nu_{\text{ind}} = 0$ is where the total flow through the actuator disk changes sign, which separates the downward case from the upward case in our current classifications. The line $\nu + 2\nu_{\text{ind}} = 0$ is where the flow in the far wake changes sign. The lines $\nu = 0$, $\nu + \nu_{\text{ind}} = 0$, and $\nu + 2\nu_{\text{ind}} = 0$ divide the non-negative half-plane ($\nu_{\text{ind}} \geq 0$) into four regions: normal working state (climb and hover), vortex ring state, turbulent wake state, and windmill brake state. Momentum theory can only predict the normal working state and windmill brake state. For vortex ring state and turbulent wake state, vortex theory or experimental results need to be invoked to quantify the behavior of the propeller [23, 44]. As an example, figure 2.6(a) shows the flow in vortex ring state. As the propeller descends, there is no longer clearly defined slipstream. That is because the downwash by the propeller meets the upwash air by the descending movement of the propeller. The flow recirculation occurs with high turbulence. As the descending speed increases, the recirculation extends from the tip regions to envelop the whole of the rotor disk. The limit of vortex ring state and turbulent wake state occurs when the net flow through the rotor disk is zero ($\nu + \nu_{\text{ind}} = 0$). This is the basis of ideal autorotation when the induced power is zero. Therefore, this condition permits helicopters to

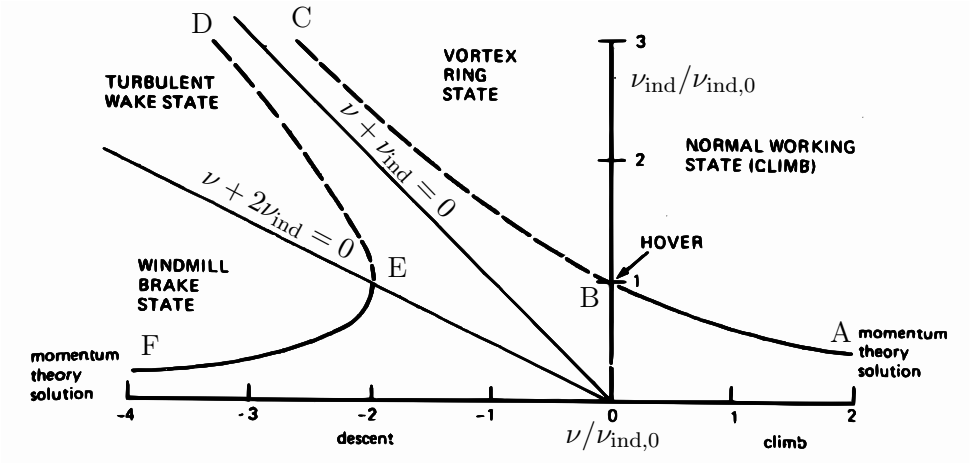

Figure 2.5: Momentum theory results in axial flight (adapted from [44, Fig. 3-2])

land even if the main engines have failed (see [23, Chap. 7] for more information). Figure 2.6(b) sketches the flow around the propeller in turbulent wake state, so-called because of the flow similar to the turbulent wake of a bluff body. The flow is rather turbulent but there is much less recirculation through the actuator disk since the flow velocity at the disk is upward.

Finally, it is worth noting that in most references on helicopters in the literature [23, 42–44], axial flights are often classified into two cases according to the direction of the propeller velocity: climb or descent. In climb case, the induced velocity equation (e.g. [23, Eq. (4.17)]) gives a solution that belongs to the descent case. Such classifications, albeit commonly used and seemingly simple at first glance, are confusing.

2.2.1.3 Forward Flight

Assume now that the propeller is flying forward at (air-)velocity $\boldsymbol{v_a}$. The diagram of the flow streamtube is illustrated in figure 2.7. The flow velocity is $\boldsymbol{\nu} = -\boldsymbol{v_a}$. The vector $\boldsymbol{\nu}$ is decomposed along the vectors $\boldsymbol{j}$ and $\boldsymbol{k}$ attached to the propeller: $\boldsymbol{\nu} = \nu_2\boldsymbol{j} + \nu_3\boldsymbol{k}$. The velocity intensity of the total flow across the disk is thus:

$$\nu' = \sqrt{\nu_2^2 + (\nu_3 + \nu_{\text{ind}})^2} \tag{2.25}$$

Based on momentum considerations (i.e. assuming that, as in hover flight, the wake velocity is $\nu_D = 2\nu_{\text{ind}}$), Glauert [43] proposed to express the thrust intensity as:

$$T = 2\rho A \nu' \nu_{\text{ind}} \tag{2.26}$$

Note that Eq. (2.26) reduces to the momentum Eq. (2.16) in hover flight. In forward flight with $\nu_{\text{ind}} << |\nu|$, it is the same as for the induced velocity of an elliptically loaded wing. Indeed, fixed-wing theory shows that the induced velocity on a circular wing moving with velocity ν is [46]:

$$\nu_{\text{ind}} = \frac{T}{2\rho A \nu} \tag{2.27}$$

Equation (2.27) is precisely Eq. (2.26) when $\nu' = \sqrt{\nu_2^2 + (\nu_3 + \nu_{\text{ind}})^2} \approx \nu$ at high speed flight. In addition, results from the method of Mangle and Squire's induced velocity calculation, wind

(a) (b)

Figure 2.6: Rotor flow in (a) vortex ring state and (b) turbulent wake state [44, Chap. 3]

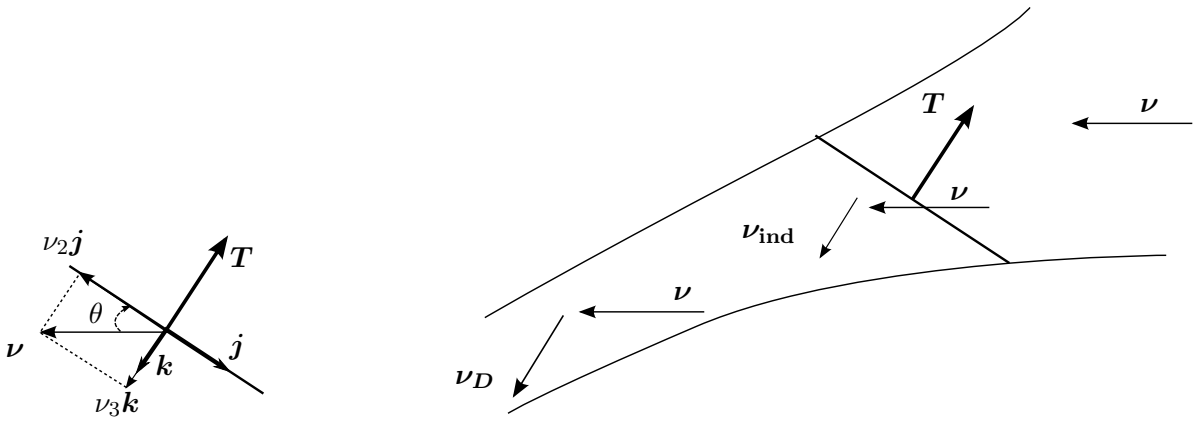

Figure 2.7: Actuator disk streamtube in forward flight(adapted from [23, p. 64 Fig. 5.1])

tunnel experiments, and flight tests (see [43, Chap. 3]) confirm the validity of Glauert's formula. From Eq. (2.25) and Eq. (2.26):

$$\nu_{\text{ind}} - \frac{T}{2\rho A}\frac{1}{\sqrt{\nu_2^2 + (\nu_3 + \nu_{\text{ind}})^2}} = 0 \tag{2.28}$$

or equivalently,

$$\nu_{\text{ind}}\sqrt{\nu_2^2 + (\nu_3 + \nu_{\text{ind}})^2} - \nu_{\text{ind},0}^2 = 0 \tag{2.29}$$

A special case of Eq. (2.29) is when $\nu = \nu_3$, i.e. the propeller is in axial flight:

$$\nu_{\text{ind}}|\nu + \nu_{\text{ind}}| - \nu_{\text{ind},0}^2 = 0 \tag{2.30}$$

If $\nu + \nu_{\text{ind}} \geq 0$, Eq. (2.30) is the same as Eq. (2.23): the propeller is in normal working state (climb or hover) or in vortex ring state. If $\nu + \nu_{\text{ind}} < 0$, Eq. (2.30) is the same as Eq. (2.24): the propeller is descending in turbulent wake state or windmill brake state. We can conclude that Eq. (2.29) is the general momentum theory equation to find the induced velocity at any air-velocity of the propeller (except in vortex ring state or turbulent wake state for which the momentum theory assumptions are not satisfied).

Expressing ν in terms of v_a and θ, i.e.

$$\nu_2 = -(v_{a,2}\cos\theta + v_{a,3}\sin\theta)\,, \quad \nu_3 = v_{a,2}\sin\theta - v_{a,3}\cos\theta$$

it follows from Eq. (2.28) that Eq. (2.6) is satisfied with:

$$f_\nu(\theta, v_a, T, \nu_{\text{ind}}) = \nu_{\text{ind}} - \frac{T}{2\rho A}\frac{1}{\sqrt{|v_a|^2 + \nu_{\text{ind}}^2 + 2\nu_{\text{ind}}(v_{a,2}\sin\theta - v_{a,3}\cos\theta)}} \tag{2.31}$$

2.2.2 Recalls on Blade Element Theory

Momentum theory provides the analysis of the propeller as an actuator disk with an infinite number of blades. Hence, it is insufficient to take into account the propeller blade geometry and aerodynamics. To fill these gaps, blade element theory is often applied to further the understanding of propeller forces and energy. As its name implies, this theory considers that a propeller blade is composed of a spanwise collection of elements. Each element is considered as a small airfoil of infinitesimal width (2D). The air flow around each element generates lift and drag forces on this element. The propeller forces acting on the propeller as a whole are obtained by the spanwise integration of the aerodynamic forces on the blade elements. Figure 2.8 shows the flow components in the propeller plane. Let $\mathcal{E} = \{\text{M}, \boldsymbol{i}_\Psi, \boldsymbol{j}_\Psi, \boldsymbol{k}_\Psi\}$ denote a frame attached to the blade element at M (at distance r from the rotor hub) and defined by the following relations:

$$\boldsymbol{i}_\Psi = \cos\Psi\boldsymbol{i} + \sin\Psi\boldsymbol{j}, \quad \boldsymbol{j}_\Psi = -\sin\Psi\boldsymbol{i} + \cos\Psi\boldsymbol{j}, \quad \boldsymbol{k}_\Psi = \boldsymbol{k}$$

The flow velocity $\nu_2\boldsymbol{j}$ parallel to the propeller plane can be decomposed in two terms: a chord-wise component and a span-wise component, i.e. $\nu_2\boldsymbol{j} = \nu_2\sin\Psi\boldsymbol{i}_\Psi + \nu_2\cos\Psi\boldsymbol{j}_\Psi$. These components will account for the in-plane drag forces. To non-dimensionalize the equations, the following notation is used with the rotor tip speed $\nu_T = \varpi R$:

$$\bar{\nu} = \frac{\nu}{\nu_T} \tag{2.32}$$

$$\bar{\nu}_2 = \frac{\nu_2}{\nu_T} \tag{2.33}$$

$$\bar{\nu}_3 = \frac{\nu_3}{\nu_T} \tag{2.34}$$

$$\bar{\nu}_{3,\text{ind}} = \frac{\nu_3 + \nu_{\text{ind}}}{\nu_T} \tag{2.35}$$

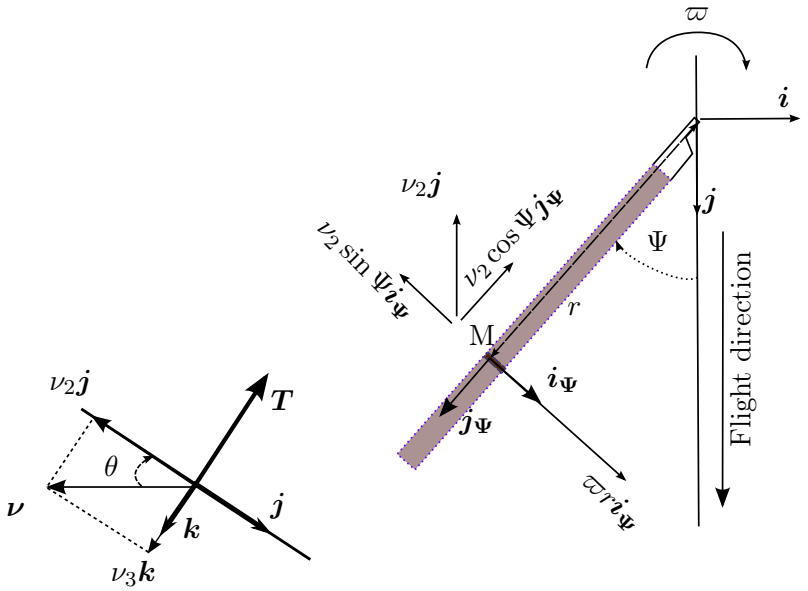

Figure 2.8: Velocity components in the propeller plane (adapted from [23, p. 68 Fig. 5.3])

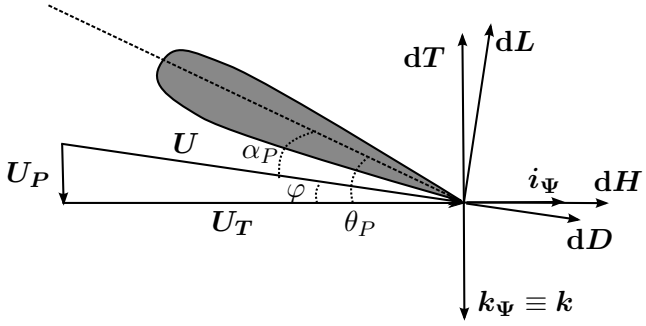

Figure 2.9: Force components on a blade element (adapted from [23, p. 68 Fig. 5.4])

Consider now the blade element depicted on figure 2.9. It is a proper small airfoil. The flow velocity $\boldsymbol{U}$ in the blade element's plane can be decomposed as $\boldsymbol{U} = \boldsymbol{U_T} + \boldsymbol{U_P}$ with $\boldsymbol{U_T} = U_T \boldsymbol{i}_\Psi$, $\boldsymbol{U_P} = U_P \boldsymbol{k}_\Psi$, and

$$\begin{cases} U_T &= \varpi r + \nu_2 \sin\Psi = \nu_T(\bar{r} + \bar{\nu}_2 \sin\Psi) \\ U_P &= \nu_T \bar{\nu}_{3,\text{ind}} \end{cases} \tag{2.36}$$

where $\bar{r} = r/R$ is the normalized radius station on the blade. The norm of the total flow velocity in the plane of the blade element is then given by

$$\begin{aligned} |U| &= \sqrt{U_T^2 + U_P^2} \\ &= \nu_T \sqrt{(\bar{r} + \bar{\nu}_2 \sin\Psi)^2 + \bar{\nu}_{3,\text{ind}}^2} \end{aligned} \tag{2.37}$$

The inflow angle, i.e. the angle between $\boldsymbol{U}$ and $\boldsymbol{U_T}$, is expressed by the following equation:

$$\varphi(\bar{r}) = \operatorname{atan2}\left(\bar{\nu}_{3,\text{ind}}, \bar{r} + \bar{\nu}_2 \sin\Psi\right) \tag{2.38}$$

The angle of incidence is the difference between the pitch angle $\theta_P(\bar{r})$ and the inflow angle:

$$\alpha_P(\bar{r}) = \theta_P(\bar{r}) - \varphi(\bar{r}) \tag{2.39}$$

The elementary lift force on the blade element is:

$$\mathbf{d}\boldsymbol{L} = \frac{1}{2}\rho c_P(\bar{r})\mathrm{d}r C_{LP}(\alpha_P, \bar{r})|U|\boldsymbol{U}^{\perp} \tag{2.40}$$

with $c_P(\bar{r})$ the blade's chord at radius r, $\mathrm{d}r$ the infinitesimal blade element's width, $C_{LP}(\alpha_P, \bar{r})$ the lift coefficient of the blade element, and $\boldsymbol{U}^{\perp}$ the vector obtained by rotating anticlockwise the vector $\boldsymbol{U}$ by 90° in the plane $(M, \boldsymbol{i_\Psi}, \boldsymbol{k_\Psi})$, i.e.

$$\boldsymbol{U}^{\perp} = U_P\boldsymbol{i_\Psi} - U_T\boldsymbol{k_\Psi}$$

The elementary drag force on the blade element is:

$$\mathbf{d}\boldsymbol{D} = \frac{1}{2}\rho c_P(\bar{r})\mathrm{d}r C_{DP}(\alpha_P, \bar{r})|U|\boldsymbol{U} \tag{2.41}$$

where $C_{DP}(\alpha_P, \bar{r})$ is the drag coefficient of the blade element. In general case, there is a elementary moment on the blade element. This moment is ignored in our modeling. Discussion of the moment effects is given in section 2.2.5.

The sum of the lift force $\mathbf{d}\boldsymbol{L}$ and drag force $\mathbf{d}\boldsymbol{D}$ can be decomposed along the thrust direction and the in-plane direction normal to the blade span, i.e.

$$\mathbf{d}\boldsymbol{L} + \mathbf{d}\boldsymbol{D} = \mathbf{d}\boldsymbol{T} + \mathbf{d}\boldsymbol{H}$$

where, by identification,

$$\begin{cases} \mathbf{d}\boldsymbol{T} = -\mathrm{d}T\boldsymbol{k_\Psi} \\ \mathbf{d}\boldsymbol{H} = \quad \mathrm{d}H\boldsymbol{i_\Psi} \end{cases} \text{with} \begin{cases} \mathrm{d}T = \mathrm{d}L\cos\varphi - \mathrm{d}D\sin\varphi \\ \mathrm{d}H = \mathrm{d}L\sin\varphi + \mathrm{d}D\cos\varphi \end{cases} \text{and} \begin{cases} \mathrm{d}L = \dfrac{1}{2}\rho c_P(\bar{r})\mathrm{d}r C_{LP}(\alpha_P, \bar{r})|U|^2 \\ \mathrm{d}D = \dfrac{1}{2}\rho c_P(\bar{r})\mathrm{d}r C_{DP}(\alpha_P, \bar{r})|U|^2 \end{cases} \tag{2.42}$$

The torque acting around the rotor axis is the cross product of the distance vector $\boldsymbol{r} = r\boldsymbol{j_\Psi}$ and the in-plane force $\mathbf{d}\boldsymbol{H}$:

$$\mathbf{d}\boldsymbol{Q} = \boldsymbol{r} \times \mathbf{d}\boldsymbol{H} = -r\mathrm{d}H\boldsymbol{k_\Psi} = -r\mathrm{d}H\boldsymbol{k} = -\mathrm{d}Q\boldsymbol{k} \tag{2.43}$$

The mean values for the forces and torque are found by integration around the total azimuthal angle and along the blade length, i.e.

$$T = \frac{N_P}{2\pi}\int_0^R\int_0^{2\pi} \mathrm{d}T\,, \quad H = \frac{N_P}{2\pi}\int_0^R\int_0^{2\pi} \mathrm{d}H\,, \quad Q = \frac{N_P}{2\pi}\int_0^R\int_0^{2\pi} \mathrm{d}Q \tag{2.44}$$

with N_P the number of blades in a propeller. Gathering all the equations above, one finally obtains the following: (see appendix A for details)

$$T = \frac{N_P}{4\pi}\rho R \int_0^1\int_0^{2\pi} |U|^2 c_P(\bar{r})\Big[C_{LP}(\alpha_P, \bar{r})\cos\varphi - C_{DP}(\alpha_P, \bar{r})\sin\varphi\Big]\,\mathrm{d}\Psi\mathrm{d}\bar{r} \tag{2.45}$$

$$H = \frac{N_P}{4\pi}\rho R \int_0^1\int_0^{2\pi} |U|^2 c_P(\bar{r})\Big[C_{LP}(\alpha_P, \bar{r})\sin\varphi + C_{DP}(\alpha_P, \bar{r})\cos\varphi\Big]\sin\Psi\,\mathrm{d}\Psi\mathrm{d}\bar{r} \tag{2.46}$$

$$Q = \frac{N_P}{4\pi}\rho R^2 \int_0^1\int_0^{2\pi} |U|^2 c_P(\bar{r})\Big[C_{LP}(\alpha_P, \bar{r})\sin\varphi + C_{DP}(\alpha_P, \bar{r})\cos\varphi\Big]\bar{r}\,\mathrm{d}\Psi\mathrm{d}\bar{r} \tag{2.47}$$

The propeller power is the product of the torque driving the rotor by the rotational velocity:

$$P = Q\varpi = \frac{N_P}{4\pi}\rho R\nu_T \int_0^1\int_0^{2\pi} |U|^2 c_P(\bar{r})\Big[C_{LP}(\alpha_P, \bar{r})\sin\varphi + C_{DP}(\alpha_P, \bar{r})\cos\varphi\Big]\bar{r}\,\mathrm{d}\Psi\mathrm{d}\bar{r} \tag{2.48}$$

2.2.3 Analytical Model for the Propellers

The propeller modeling equations are complex, with the double integration and the variations of aerodynamic coefficients, chord length, and pitch angle along the blade. In order to obtain simple closed-form expressions, modeling assumptions are made and an eight-parameter-analytical model is proposed. These assumptions are as follows:

1. The chord length $c_P(\bar{r})$ and the pitch angle $\theta_P(\bar{r})$ of the propeller blades vary along the blade. To simplify the modeling, we assume that the average values of these quantities can be considered. This amounts to assuming that the propeller blade has a rectangular shape with width c_P and fixed pitch θ_P. It is shown in [44, Chap. 2] and [23, Chap. 3] that for many propeller blades, one can take the chord length c_P and the pitch angle θ_P at 75% radius ($\bar{r} = r/R = 0.75$) to have good average values.

2. It is assumed that the rotational speed of the rotor is high w.r.t. the air-velocity. This is usually true for small quadrotors (i.e. weigh a few kilograms), for which typical values of ϖ in normal operating conditions are $\varpi \in [3000, 6000]$ RPM. This allows us to neglect the reverse flow region and assume that the angle of attack α_P of the blade is always small.

From the second assumption, the tangential velocity component U_T is much larger than the perpendicular U_P (this is of course not true when $\bar{r}$ is small but the blade element at small $\bar{r}$ does not generate significant lift and consequently power). Hence, from Eq. (2.37) we can approximate the total flow velocity U:

$$U \approx \nu_T(\bar{r} + \bar{\nu}_2 \sin\Psi) \tag{2.49}$$

This also means that the inflow angle is small:

$$\varphi(\bar{r}) = \operatorname{atan2}(\bar{\nu}_{3,\text{ind}}, \bar{r} + \bar{\nu}_2 \sin\Psi) \approx \frac{\bar{\nu}_{3,\text{ind}}}{\bar{r} + \bar{\nu}_2 \sin\Psi} \tag{2.50}$$

Using the assumption of fixed pitch angle, the angle of attack is:

$$\alpha_P(\bar{r}) = \theta_P - \frac{\bar{\nu}_{3,\text{ind}}}{\bar{r} + \bar{\nu}_2 \sin\Psi} \tag{2.51}$$

The lift force on the blade section is:

$$\mathrm{d}L = \frac{1}{2}\rho|U|^2 c_P \mathrm{d}r C_{LP}(\alpha_P) \tag{2.52}$$

where c_P is the chord length of the blade at 75% radius and $C_{LP}(\alpha_P)$ is the blade lift coefficient, modeled as a linear function of α_P:

$$C_{LP}(\alpha_P) = C_{L0} + a\alpha_P \tag{2.53}$$

where C_{L0} is the lift coefficient at zero angle attack, a is the lift curve slope. Here, it is assumed that the angle of incidence α is small. For simplicity reason, the effect of stall is neglected in the current modeling. [5] The drag force on the blade section is:

$$\mathrm{d}D = \frac{1}{2}\rho|U|^2 c_P \mathrm{d}r C_{DP}(\alpha_P) \tag{2.54}$$

[5] If the blade aerodynamic airfoil data are available for full range of angle of attack, the effect of stall can be taken into account similar to the wing model in section 2.3. In practice, the propeller blade data are usually not available, as discussed in section 2.2.6.

where $C_{DP}(\alpha_P)$ is the blade drag coefficient, modeled as a quadratic function of α_P:

$$C_{DP}(\alpha_P) = b_0 + b_1\alpha_P + b_2\alpha_P^2 \tag{2.55}$$

which b_i with $i \in \{0, 1, 2\}$ are constant values. The force in the propeller thrust direction is:

$$\mathrm{d}T = \mathrm{d}L\cos\varphi - \mathrm{d}D\sin\varphi \approx \mathrm{d}L \tag{2.56}$$

The thrust expression in Eq. (2.45) then reduces to (detailed calculation steps are provided in appendix A):

$$T = \frac{\rho N_P c_P R}{4}\left[C_{Lt}\left(\frac{2}{3} + \bar{\nu}_2^2\right) - a\bar{\nu}_{3,\mathrm{ind}}\right]\nu_T^2 \tag{2.57}$$

where

$$C_{Lt} = C_{L0} + a\theta_P \tag{2.58}$$

is the value of the blade lift coefficient at the fixed pitch angle. We can simplify Eq. (2.57) further by noting that $\bar{\nu}_2 = \nu_2/\nu_T$ is small in normal conditions since it is assumed that $|\nu_2| \in [0, 20]$ m/s, whereas ν_T is typically in the range $[60, 115]$ m/s and increases when $|\nu_2|$ increases. Typically $\bar{\nu}_2 \leq 0.2$ so that one can neglect the $\bar{\nu}_2^2$ term:

$$T = \frac{\rho N_P c_P R}{4}\left(\frac{2}{3}C_{Lt} - a\bar{\nu}_{3,\mathrm{ind}}\right)\nu_T^2 \tag{2.59}$$

The in-plane force $\mathrm{d}H$ normal to the blade span is:

$$\mathrm{d}H = \mathrm{d}L\sin\varphi + \mathrm{d}D\cos\varphi \approx \varphi\,\mathrm{d}L + \mathrm{d}D \tag{2.60}$$

Let us define constants β_i with $i \in \{0, 1, 2\}$ as follows:

$$\begin{aligned}\beta_0 &= b_2 - a\\ \beta_1 &= C_{Lt} - 2\theta_P b_2 - b_1\\ \beta_2 &= b_2\theta_P^2 + b_1\theta_P + b_0\end{aligned} \tag{2.61}$$

Then, the in-plane drag force expression in Eq. (2.46) reduces to (detailed calculation steps are provided in appendix A):

$$H = \frac{\rho N_P c_P R}{4}\bar{\nu}_2(\beta_1\bar{\nu}_{3,\mathrm{ind}} + \beta_2)\nu_T^2 \tag{2.62}$$

Finally, the torque expression in Eq. (2.47) reduces to (detailed calculation steps are provided in appendix A):

$$\begin{aligned}Q &= \frac{\rho N_P c_P R^2}{4}\left[\bar{\nu}_{3,\mathrm{ind}}\left(\frac{2}{3}\beta_1 + \beta_0\bar{\nu}_{3,\mathrm{ind}}\right) + \frac{\beta_2}{2}(1 + \bar{\nu}_2^2)\right]\nu_T^2\\ &\approx \frac{\rho N_P c_P R^2}{4}\left[\bar{\nu}_{3,\mathrm{ind}}\left(\frac{2}{3}\beta_1 + \beta_0\bar{\nu}_{3,\mathrm{ind}}\right) + \frac{\beta_2}{2}\right]\nu_T^2\end{aligned} \tag{2.63}$$

From Eq. (2.59), (2.62), (2.63), we can express T, H, Q as functions of θ, v_a, ϖ, ν_{ind}. Therefore, Eq. (2.5) is satisfied with:

$$\left\{\begin{aligned}
f_T(\theta, v_a, \varpi, \nu_{\mathrm{ind}}) &= \frac{\rho N_P c_P R^2}{4}\left[\frac{2}{3}C_{Lt}R\varpi^2 - a(v_{a,2}\sin\theta - v_{a,3}\cos\theta + \nu_{\mathrm{ind}})\varpi\right]\\
f_H(\theta, v_a, \varpi, \nu_{\mathrm{ind}}) &= -\frac{\rho N_P c_P R}{4}(v_{a,2}\cos\theta + v_{a,3}\sin\theta)\left[\beta_1(v_{a,2}\sin\theta - v_{a,3}\cos\theta + \nu_{\mathrm{ind}}) + \beta_2 R\varpi\right]\\
f_Q(\theta, v_a, \varpi, \nu_{\mathrm{ind}}) &= \frac{\rho N_P c_P R^2}{4}\Bigg\{(v_{a,2}\sin\theta - v_{a,3}\cos\theta + \nu_{\mathrm{ind}})\\
&\qquad \left[\frac{2}{3}\beta_1 R\varpi + \beta_0(v_{a,2}\sin\theta - v_{a,3}\cos\theta + \nu_{\mathrm{ind}})\right] + \frac{\beta_2}{2}R^2\varpi^2\Bigg\}
\end{aligned}\right. \tag{2.64}$$

2.2.4 Comparison With Literature

In this section, we provide a short discussion of the proposed modeling approach with respect to what is traditionally done in the helicopter literature, on two aspects: the power calculation and the aerodynamic model.

Helicopter modeling usually divides the required power into three components [23, 42, 43](see figure 2.10): induced power, profile power, and parasite power. Johnson [44] even considers the changing of gravitational potential energy as a fourth component, named climb power. This division, or "superposition" principle, is an attempt to identify the different sources of energy consumption. For example, induced power is usually associated with the aerodynamic lift whereas profile power and parasite power are primarily associated with the aerodynamic drag. While this principle might work well with axial flight case, in forward flight the division of power components is no longer clear. Indeed, during forward flight, the induced power includes the inflow ratio, part of which is due to the inclination of the propeller disk. The thrust force compensates not only for the gravity force but also for the aerodynamic drag. In convertible UAVs, this power division is even less clear due to the presence of large aerodynamic forces. In other words, justification of this decomposition principle is not that straightforward, and this is the reason why we have preferred not to rely on it. Our approach simply starts from the force balance (i.e. Newton's law) and computes directly the total power, without relying on this decomposition. The power is purely calculated as the product of the torque driving the rotor by the rotational velocity (Eq. (2.48)).

Concerning the blade element theory, in nearly all helicopter modeling references, for example [23, 43], the blade aerodynamic model is over-simplified: the lift coefficient versus angle of attack is a linear lift curve through the origin whereas the drag coefficient is a constant. Our calculation uses more accurate blade aerodynamic models. Indeed, the blade lift function is a linear equation taking into account the lift coefficient at zero angle attack as in Eq. (2.53) since modern propeller blade cross-sections are usually not symmetric.[6] In addition, the blade drag function is a quadratic equation taking into account the non-symmetric variation of blade drag as in Eq. (2.55). Our calculations and simulations have shown improvements in modeling thrust and power coefficients (see the modeling and identification in section 2.2.6) over the aforementioned classical helicopter modeling.

A modeling of aerodynamic effects on propellers is proposed in [47]. That modeling is more complete than the one here presented since it considers the 3D case includes angular velocity dependence, and also provides a modeling of aerodynamic moments. On the other hand, the above expressions in this thesis specify the explicit dependence of force coefficients on geometric/aerodynamic parameters of the propellers and include the vertical flight velocity dependence.

2.2.5 Classical Propeller Modeling Limitation

This section briefly discusses the effects that have been ignored in our modeling. Some of them could be easily incorporated in our model; others required more profound modifications.

1. Moments on propellers: in general, in addition to the blade aerodynamic forces, each blade element (equivalent to an airfoil) is subjected to an elementary moment. The total moments on the blades can be found by integration of all elementary moments. Consider a

[6] The advantages of a non-symmetric or cambered airfoil are positive lift at zero angle of attack, increased lift-drag ratios, and more desirable stall characteristics. The disadvantages are more complicated design and greater center of pressure variation compared to symmetric airfoil.

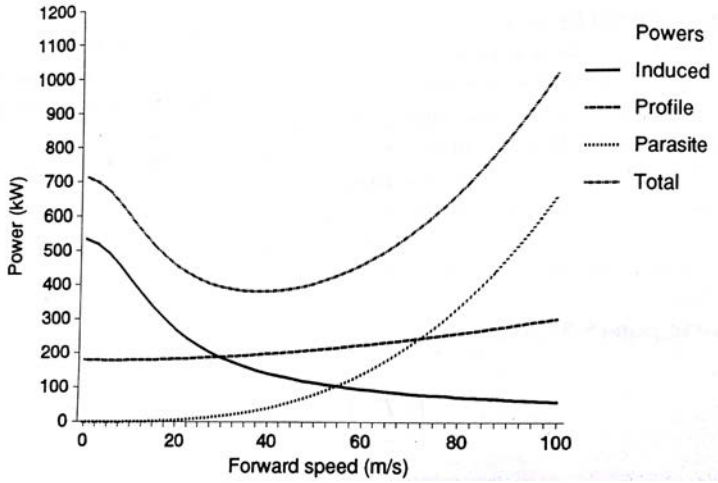

Figure 2.10: Power variation in forward flight [23]

two-blade propeller in forward flight, the air-velocity of the advancing blade is greater than the air-velocity of the retreating blade. The total moment of advancing blade is larger than that of retreating blade. Therefore, there is a total pitch moment on the propeller. Define a reference linear line though propeller hub and perpendicular to propeller axis that goes from one blade tip to the other blade tip. If the propeller blade airfoil is symmetric, the quarter-chord point is the center of pressure [48, Sec. 4.7]. If this point is on the reference line, the pitch moment is equal to zero. Otherwise, there is an offset between the center of pressure and the reference line. In such cases, the pitch moment is no longer zero.

If the blade airfoil is cambered, the center of pressure varies [48, Sec. 4.8] and the pitch moment can be significant. Finding this moment is difficult, especially without the knowledge of blade airfoil profile. This moment is ignored in the current modeling.

2. Tip effect: this effect means that the blade loading falls to zero at the tip and the effective thrust is reduced. A pressure difference must be produced by the rotor blade to generate the lift force. However, at a blade tip, the air can flow around the blade edge, thereby does not generate any lift. In helicopter literature, the lift loss is evaluated to be about 3-5% of the total lift [23, 43].

3. Non-uniform induced velocity distribution and swirl effect: recall the assumption made in the beginning of section 2.2.1 that the induced velocity is uniformly distributed, which gives the minimum induced power loss for a given thrust (this is proved by calculus of variations, e.g. in [44, Sec. 2-1]). In reality, the induced velocity is far from uniform since the flow field is not continuous with a wake of discrete vorticity corresponding to discrete loading. Stepniewski [42] presents examples of non-uniform disk loading in the form of triangular, polynomial, square root, etc. However, these non-uniform induced velocity distributions seem to apply to specific cases, and they are only rough approximations of real induced flow.

   Apart from non-uniformity, the rotational nature of the flow generates spiral vortex lines that cause the swirl effect [43]. Figure 2.11 shows the distribution of inflow and swirl velocities of a hovering propeller. This effect can be easily incorporated in the modeling

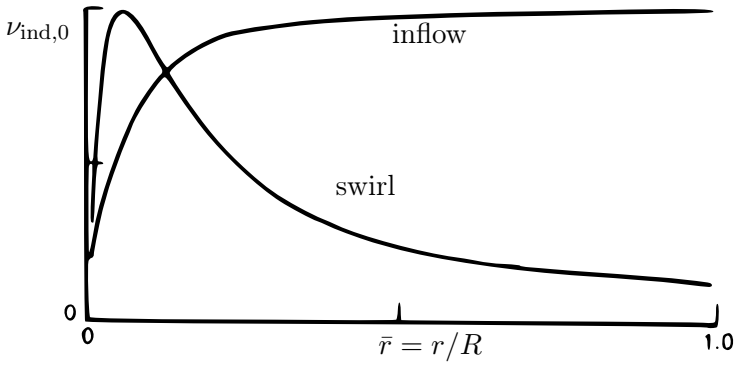

Figure 2.11: Radial distribution of the inflow and the swirl velocities of the hovering propeller [44, Fig. 2-5]

following [44, Sections 2-3.2 and 2-3.3]. The swirl velocity is small when $\bar{r} > 0.25$ and generally can be ignored in the analysis.

4. Ground effect: it is well-known that a propeller operating near ground benefits from a small added lift. Since this is usually a very particular and short flight phase, this effect is not considered in this thesis.

5. Reverse flow: when the propeller is in retreating phase as depicted in figure 2.8, there is a reverse region where the tangential velocity U_T is negative. Examining Eq. (2.36) shows that this region is a circle with diameter $\bar{\nu}_2$ and center defined by polar coordinate $(r = \bar{\nu}_2/2, \Psi = \pi/2)$. This effect causes performance loss with higher advance ratio $\bar{\nu}$ for full-scaled helicopter. For small UAVs at low Reynolds number, the reverse flow is negligible since the speed ratio $\bar{\nu}_2$ is small.

6. Span-wise velocity component: the flow velocity $\nu_2 \cos\Psi \boldsymbol{j}_{\boldsymbol{\Psi}}$ (see figure 2.8) gives rise to another drag force, called Y-force [44]. This Y-force contribution to the profile power is about half of the H-force contribution according to [42, Chap. 3], [23, p. 73-74], and [44, p. 219]. The current modeling does not take into account the Y-force.

2.2.6 Eight-parameter Model and Identification

The model defined by Eq. (2.64) depends on eight parameters associated with the propellers' blades:

- three geometric parameters: N_P, c_P, and R,
- five coefficients related to aerodynamic parameters: C_{Lt}, a, β_0, β_1, and β_2.

From Eq. (2.58) and Eq. (2.61), this model can also be parameterized by the following (more physical) nine parameters:

- four geometric parameters: N_P, c_P, R, and θ_P,
- two lift coefficients: C_{L0} and a,
- three drag coefficients: b_0, b_1 and b_2.

In both cases the geometric parameters can be easily obtained from direct measurements on the blade[7](or from data available by manufacturers), and one is left with the determination of five parameters characterizing the blade aerodynamic coefficients (lift and drag). These parameters are usually not available by the propeller manufacturers. It is possible to measure manually each blade profile at different radius stations on the blade, and then use a vortex panel program like XFoil [49] (see [50] for more information on the procedure). This is complicated and time consuming, however, and the result may be significantly affected by measurement errors. A better solution, when possible, is to use direct thrust and torque (or power) measurements. We will illustrate this possibility below. Before that, let us recall the definitions of non-dimensional coefficients used for the characterization of propellers (see, e.g. [23]):

$$C_T \triangleq \frac{T}{\frac{1}{2}\rho A \nu_T^2} \tag{2.65}$$

$$C_H \triangleq \frac{H}{\frac{1}{2}\rho A \nu_T^2} \tag{2.66}$$

$$C_Q \triangleq \frac{Q}{\frac{1}{2}\rho A R \nu_T^2} \tag{2.67}$$

$$C_P \triangleq \frac{P}{\frac{1}{2}\rho A \nu_T^3} \tag{2.68}$$

Since $P = Q\varpi = Q\nu_T/R$, we deduce that $C_P = C_Q$. From Eq. (2.59) and Eq. (2.65),

$$C_T = \frac{s}{2}\left(\frac{2}{3}C_{Lt} - a\bar{\nu}_{3,\text{ind}}\right) \tag{2.69}$$

where s is the solidity of the propeller, which is the ratio of the area of the blades over the area of the propeller disk:

$$s = \frac{N_P c_P R}{A} = \frac{N_P c_P}{\pi R} \tag{2.70}$$

From Eq. (2.62) and Eq. (2.66) the drag coefficient for H force is:

$$C_H = \frac{s\bar{\nu}_2}{2}(\beta_1 \bar{\nu}_{3,\text{ind}} + \beta_2) \tag{2.71}$$

From Eq. (2.63) and Eq. (2.67), the power (torque) coefficient is:

$$C_P = C_Q = \frac{s}{2}\bar{\nu}_{3,\text{ind}}\left(\frac{2}{3}\beta_1 + \beta_0 \bar{\nu}_{3,\text{ind}}\right) + \frac{s}{4}\beta_2 \tag{2.72}$$

The propeller power can be calculated from the power coefficient and the tip velocity:

$$P = \frac{\frac{1}{2}\rho A C_P \nu_T^3}{\eta_M} \tag{2.73}$$

where the factor η_M is introduced in this expression as motor efficiency. In order to compare the thrust and power coefficients with those in some articles (for example in [38] or [51]), these

[7]The geometrical pitch angle at 75% propeller radius can be considered the mean blade pitch for a linear-twist propeller blade [23, Chap. 3]. The mean blade pitch angle can be calculated from propeller diameter and pitch length: $\theta_P = \text{atan}(\text{PitchLength}/(0.75 \times \pi \times 2R))$. For example, the propeller APC 11× 4.7, with 11-inch diameter and 4.7-inch pitch length (approximately linear blade twist), has mean pitch angle $\theta_P = \text{atan}(4.7/(0.75 \times \pi \times 11)) = 0.179$ rad.

coefficients have to be scaled by certain constant factors to be consistent with another common convention[8]:

$$C_T^{'} = \frac{\pi^3}{8} C_T \,, \quad C_P^{'} = \frac{\pi^4}{8} C_P \tag{2.74}$$

In addition, we define the axial advance ratio as the ratio of the propeller air speed along the thrust (axial) direction over the tip velocity:

$$J_a = \frac{|\nu_3|}{\nu_T} \tag{2.75}$$

Again, the factor π is the scaling factor to match with the usual convention. The efficiency of a propeller is defined as:

$$\eta_P = J_a \frac{C_T^{'}}{C_P^{'}} \tag{2.76}$$

Coming back to the problem of estimating the five aerodynamic coefficients, we propose to make use of a few measurements of the thrust coefficient $C_T^{'}$ and the power/torque coefficient $C_P^{'}$ in axial flight. We illustrate this on the APC 11x4.7 propeller.[9] One essentially needs five measurements. Firstly, two of them can be easily obtained from thrust and torque measurements on a static test bench (corresponding to stationary flight). We carried out such experiments (see the setup in appendix B), and the result is displayed in figure 2.12 (blue line with circle markers). The data from UIUC [52] (black line with asterisk markers) and from propeller manufacturer APC [53] (magenta line with square markers) are also plotted for comparison. As shown in figure 2.12, our experimental data have very similar trend with those from UIUC. Secondly, the three remaining measurements can be done in axial flight. For simplicity and consistence, we make use of UIUC wind tunnel measurements to identify all five aerodynamic coefficients. UIUC measurements of thrust coefficient $C_T^{'}$ and power/torque coefficient $C_P^{'}$ are shown on figure 2.13. It is worth noting that increasing the Reynolds number improves propeller performance, as mentioned in many studies, including [38]. We do not try to model this effect here because propellers typically operate relatively close to a given angular speed. On figure 2.13(a), at each angular speed ϖ, two points are selected on the curve of $C_T^{'}$: a point at minimum J_a and another point at maximum J_a. Then from Eq. (2.69), we can easily solve two equations for two unknowns C_{L0} and a. For each rotor angular speed ϖ, we obtain a pair of C_{L0} and a. For example, $C_{L0} = [0.418; 0.457; 0.499; 0.540]$ at corresponding $\varpi = [3000; 4000; 5000; 6000]$. We can take the average value $C_{L0} = 0.478$ for the mean value of lift coefficient at zero angle of attack at angular speed $\varpi \in [3000 - 6000]$. Similarly, using Eq. (2.72), taking three points (two points at the extremes and one point in the middle) on each curve of $C_P^{'}$ versus J_a in figure 2.13(b), we can obtain the blade drag coefficients b_0, b_1, and b_2.

In order to validate our eight-parameter-analytical model, we compare our result at rotor angular speed 6000 RPM with the manufacturer data, experimental data from literature, and a propeller calculation software called PropCalc [54]. Figure 2.14 shows the thrust coefficient, the power coefficient, and the axial efficiency of the propeller versus the axial advance ratio. PropCalc results manifest similar trends but different values of the coefficients and efficiency, as

[8] In some references, e.g. [38, 51], the coefficients are based on the revolutions per second n and the propeller's diameter d: $C_T^{'} = \frac{T}{\rho n^2 d^4}$ and $C_P^{'} = \frac{P}{\rho n^3 d^5}$.

[9] We have chosen the propeller APC SlowFlyer 11×4.7 because among more than 140 small propellers (most with diameters ranging from 9 inches to 11 inches) from the UIUC database [52], it has high efficiency (max $\eta_P \approx 0.6$ for angular speed of 6000 RPM) and its efficient operating region falls in a suitable range of advance ratio $J_a \in [0.2, 0.5]$.

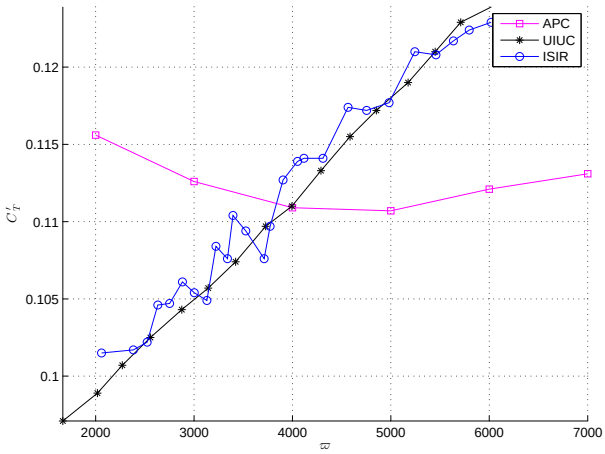

Figure 2.12: Comparison of scaled static thrust coefficients of APC SlowFlyer 11×4.7 propeller versus angular speed, between APC [53], UIUC [52], and our ISIR data

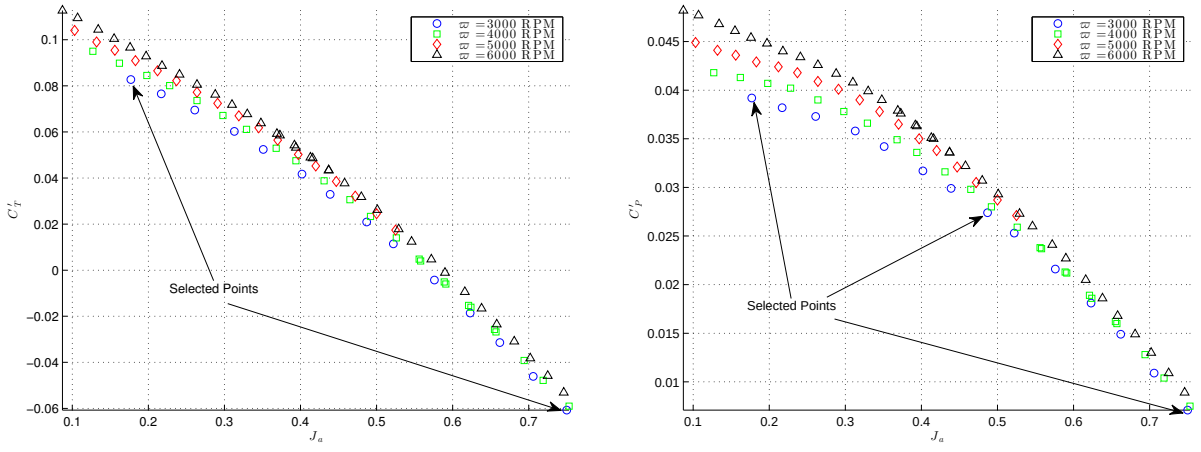

(a) (b)

Figure 2.13: APC SlowFlyer 11×4.7 UIUC data of scaled (a) thrust and (b) power coefficient versus axial advance ratio at different angular speeds. [52] This example shows the selection of points at $\varpi = 3000$ RPM.

compared to UIUC data. APC data give different trends for small advance ratio and significantly dissimilar amplitudes too. Compared to UIUC, this yields a different efficiency curve, shifted to the right. Finally, our model provides values close to UIUC. This is of course not a surprise since we made use of UIUC data to identify our model parameters. The value of this comparison is to show that with very few measurements, we can obtain a model that fits well to measurements in a large range of advance ratio and angular speeds (recall that the identification was not made from the 6000 RPM rotor angular speed here considered).

Based on thrust and power measurements in axial flight at different angular speeds, one can slightly refine the proposed model by taking into account variations of the aerodynamic coefficients with the speeds. A simple generalization consists in considering each of these coefficients as a function of ϖ instead of a constant. The only additional difficulty is that the function f_{ϖ} in Eq. (2.8), i.e. the inverse w.r.t. ϖ of f_T, is slightly more complex. Indeed, when all aerodynamic coefficients are constant scalars, it follows from Eq. (2.59) that T is a quadratic function of ϖ, so that inversion of f_T is straightforward. When the aerodynamic coefficients are linear functions of ϖ, T becomes a third order polynomial in ϖ.

2.3 Main Body Modeling

The material of this section is essentially based on [55] and [18, Chap. 6]. The objective is to provide a model for the aerodynamic force $\boldsymbol{F}_a$ acting on the UAV's main body valid in a large operating domain. When the airspeed v_a belongs to the subsonic range, the aerodynamic forces F_a can be modeled as a function that depends only on the constant air density ρ, the Reynolds number Re, the effective aerodynamic area, the airspeed v_a and the angle of attack α. This latter variable is the angle between the zero-lift line (along which the airspeed does not produce lift forces) and the airspeed vector $\boldsymbol{v_a}$, as shown in figure 2.15. We define μ as the angle between the propeller thrust direction $\boldsymbol{k}$ and the zero-lift line. By denoting the angle of the airspeed vector and the fixed vertical direction $\boldsymbol{k_0}$ as $\xi(v_a)$, one has:

$$\xi(v_a) = \text{atan2}(v_{a,2}, v_{a,3}) \tag{2.77}$$

The angle of attack of the wing is calculated as:

$$\alpha(v_a, \theta, \mu) = \pi - \theta - \xi(v_a) - \mu \tag{2.78}$$

The aerodynamic force $\boldsymbol{F_a}$ is decomposed into three parts: a lift force $\boldsymbol{F_L}$ and a drag force $\boldsymbol{F_D}$ acting on the wing, and a parasite drag $\boldsymbol{D}$ (assuming no parasite lift) acting on the vehicle's main body, i.e.

$$\boldsymbol{F_a} = \boldsymbol{F_L} + \boldsymbol{F_D} + \boldsymbol{D}$$

According to [55], the lift and draft forces are written as:

$$\begin{cases} \boldsymbol{F_L} &= k_a |\boldsymbol{v_a}| c_L(\alpha, \text{Re}) \boldsymbol{v_a^{\perp}} \\ \boldsymbol{F_D} &= -k_a |\boldsymbol{v_a}| c_D(\alpha, \text{Re}) \boldsymbol{v_a} \end{cases} \tag{2.79}$$

with $\boldsymbol{v_a^{\perp}}$ obtained by rotating counter-clockwise vector $\boldsymbol{v_a}$ by 90° in the plane $(O, \boldsymbol{j_0}, \boldsymbol{k_0})$, i.e. $\boldsymbol{v_a^{\perp}} = v_{a,3}\boldsymbol{j_0} - v_{a,2}\boldsymbol{k_0}$. One has $k_a = \frac{1}{2}\rho\Sigma$ with Σ the area of the wing. The Reynolds number is $\text{Re} = \frac{\rho |\boldsymbol{v_a}| c}{\mu_{\text{vis}}}$ where c is wing chord length and μ_{vis} is air viscosity. The term $c_L(\alpha, \text{Re})$ and

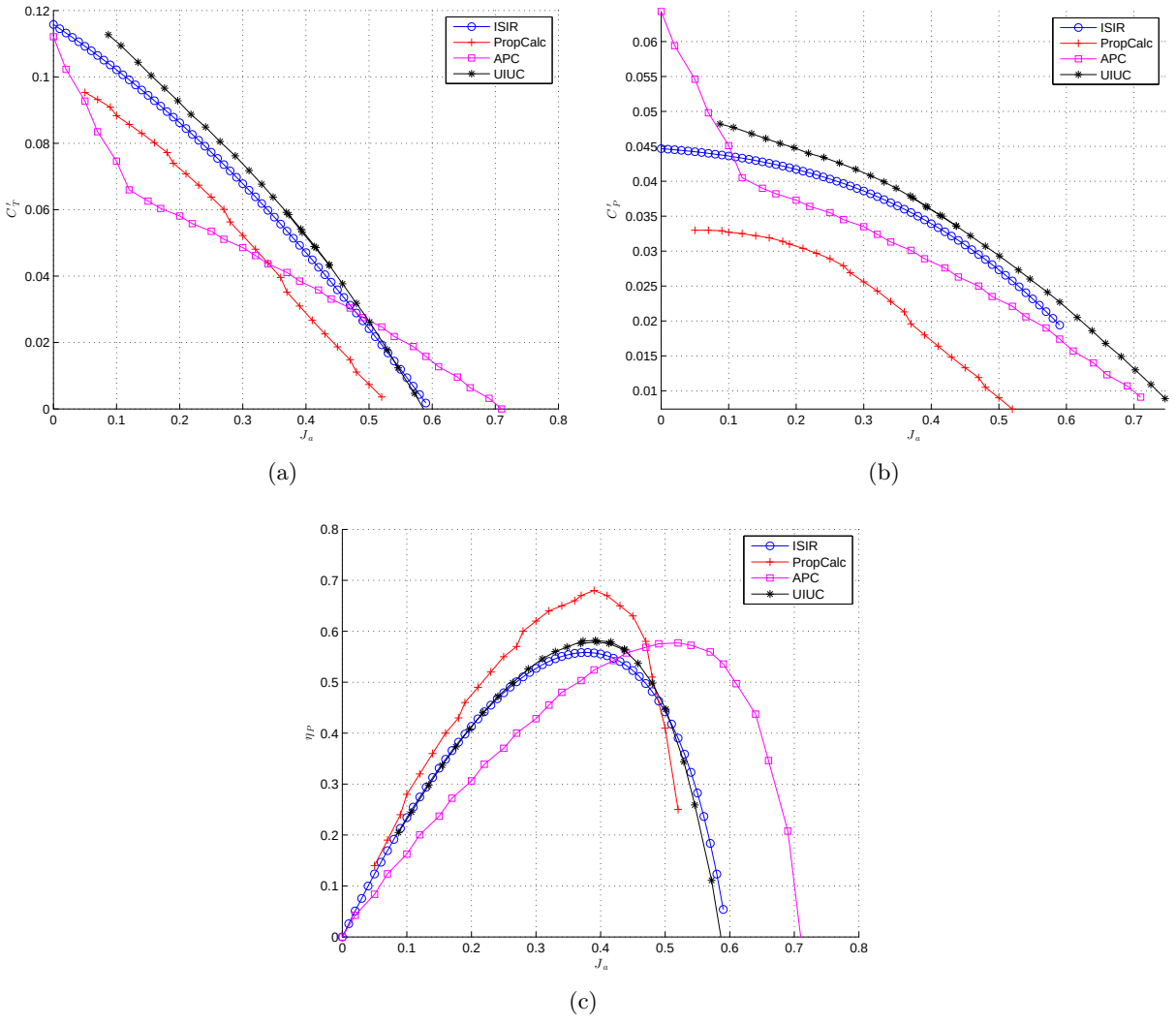

Figure 2.14: Comparison of (a) scaled thrust coefficients, (b) scaled power coefficients, and (c) efficiency of the propeller APC SlowFlyer 11 × 4.7 versus the axial advance ratio - axial flight case with rotor angular speed of 6000 RPM

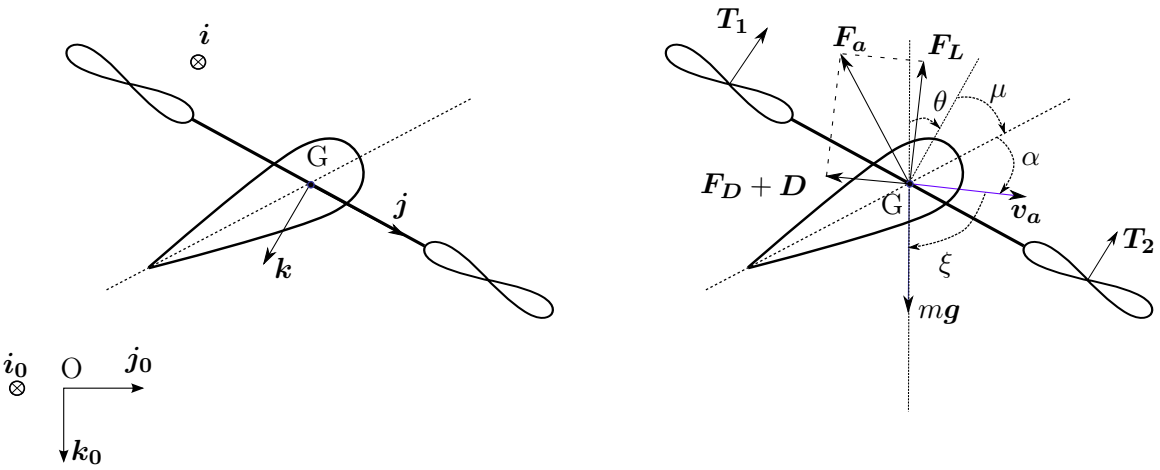

Figure 2.15: 2D Model of the convertible UAV with inclined wing

$c_D(\alpha, \mathrm{Re}) > 0$ denote respectively the lift and drag aerodynamic coefficients of the wing. The parasite drag acting on the UAV's main body (i.e. UAV's body except wing(s) and propellers):

$$\boldsymbol{D} = -k_{\mathrm{para}} c_{\mathrm{para}} |\boldsymbol{v_a}| \boldsymbol{v_a} \tag{2.80}$$

where $k_{\mathrm{para}} = \frac{1}{2}\rho \Sigma_{\mathrm{para}}$ with Σ_{para} the effective parasite area and c_{para} a parasite constant. The total aerodynamic forces $\boldsymbol{F_a}$ is then:

$$\boldsymbol{F_a}(\alpha, \boldsymbol{v_a}) = k_a |\boldsymbol{v_a}| \Big[c_L(\alpha, \mathrm{Re}) \boldsymbol{v_a^\perp} - c_D(\alpha, \mathrm{Re}) \boldsymbol{v_a} \Big] - k_{\mathrm{para}} c_{\mathrm{para}} |\boldsymbol{v_a}| \boldsymbol{v_a} \tag{2.81}$$

For any fixed value of μ, Eq. (2.7) is satisfied by substituting Eq. (2.78) into Eq. (2.81):

$$\begin{aligned} \boldsymbol{f_a}(\theta, \boldsymbol{v_a}) = k_a |\boldsymbol{v_a}| \Big[c_L\big(\pi - \theta - \xi(v_a) - \mu, |\boldsymbol{v_a}|\big) \boldsymbol{v_a^\perp} - c_D\big(\pi - \theta - \xi(v_a) - \mu, |\boldsymbol{v_a}|\big) \boldsymbol{v_a} \Big] \\ - k_{\mathrm{para}} c_{\mathrm{para}} |\boldsymbol{v_a}| \boldsymbol{v_a} \end{aligned} \tag{2.82}$$

In this project, for simplicity, the NACA symmetric airfoils are chosen for the wing. The NACA airfoils are popular and well-documented in literature. The symmetric airfoils have the code NACA00xx where the last two digits denote the percentage thickness of the airfoil with respect to the chord length. The aerodynamic characteristic of an airfoil strongly depends on its Reynolds number. We are interested in the forward operating speed in the range of 6 to 20 m/s, which translates to the Reynolds number of 0.62×10^5 to 2.05×10^5 based on the reference wing chord of $c = 0.15$ m. NACA0018 wing is selected for our model because of its moderate stall zone and rather high lift-over-drag ratio. Figure 2.16 shows the lift and drag coefficients of the airfoil NACA0018 at dissimilar Reynolds numbers. One can observe that the lift coefficients vary significantly at small α for different Reynolds numbers whereas the drag coefficients remain essentially the same over the whole range of α. In order to model the aerodynamic coefficients in a wide flight envelope, it is proposed in [18] to interpolate the lift coefficients from two models: one for small angles of attack and the other one for large angles of attack. More precisely, consider the two following lift models:

$$\begin{cases} c_{L1}(\alpha, \mathrm{Re}) = c_{2T} \sin(2\alpha), & \text{for } \Big(0 \le \alpha \bmod 180^\circ \le \alpha_0(\mathrm{Re})\Big) \\ & \text{or } \Big(180^\circ - \alpha_0(\mathrm{Re}) \le \alpha \bmod 180^\circ \le 180^\circ\Big) \\ c_{L2}(\alpha, \mathrm{Re}) = c_2 \sin(2\alpha), & \text{for other values of } \alpha \end{cases}$$

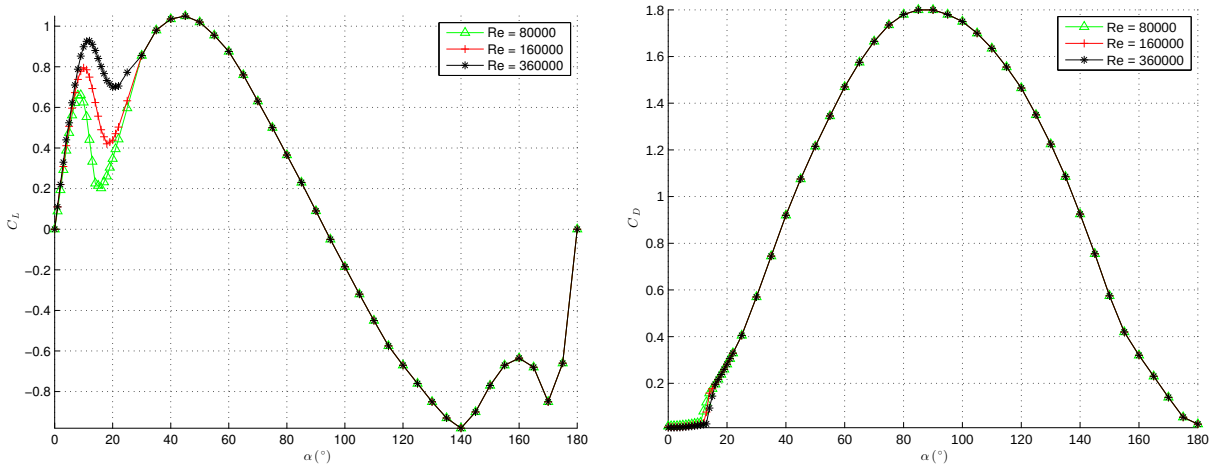

(a) (b)

Figure 2.16: The (a) lift and (b) drag coefficients versus the angle of attack of the airfoil NACA0018 at different Reynolds numbers [56]

where c_{2T} is the lift constant for small angles of attack, c_2 is an "average" lift constant, $\alpha_0(\mathrm{Re})$ is the angle where the stall zone starts. To combine $c_{L1}(\alpha, \mathrm{Re})$ and $c_{L2}(\alpha, \mathrm{Re})$ into a continuous and differentiable curve, a function $\sigma\Big(\alpha, \alpha_0(\mathrm{Re})\Big)$ combining two sigmoid curves is used:

$$\sigma\Big(\alpha, \alpha_0(\mathrm{Re})\Big) = \frac{1}{1 + e^{\alpha - \alpha_0(\mathrm{Re})}} + \frac{1}{1 + e^{180^\circ - \alpha - \alpha_0(\mathrm{Re})}} \tag{2.83}$$

In this thesis, we propose to scale the angle $\alpha_0(\mathrm{Re})$ for the change of Reynolds number (which is not presented in the works of [55] and [18]):

$$\alpha_0(\mathrm{Re}) = \alpha_{0\mathrm{ref}} \left(\frac{\mathrm{Re}}{\mathrm{Re}_{\mathrm{ref}}}\right)^{\mathrm{Re}_{\mathrm{exp}}} \tag{2.84}$$

where $\mathrm{Re}_{\mathrm{ref}}$ is the reference Reynolds number, $\alpha_{0\mathrm{ref}}$ is the angle where the stall zone starts for the airfoil at reference Reynolds number, and $\mathrm{Re}_{\mathrm{exp}}$ is the exponential scaling constant. The numerical values of these constants are given in appendix C. A sample function $\sigma(\alpha, 12^\circ)$ is shown is figure 2.17. Now the lift coefficient can be formulated as:

$$c_L(\alpha, \mathrm{Re}) = c_{L1}(\alpha, \mathrm{Re})\sigma\Big(\alpha, \alpha_0(\mathrm{Re})\Big) + c_{L2}(\alpha, \mathrm{Re})\Big(1 - \sigma\Big(\alpha, \alpha_0(\mathrm{Re})\Big)\Big) \tag{2.85}$$

From figure 2.16(b), it can be observed that the drag coefficient is almost independent of the Reynolds number. Hence, it is modeled as:

$$c_D(\alpha, \mathrm{Re}) \approx c_D(\alpha) = c_1 + 2c_2 \sin^2(\alpha) \tag{2.86}$$

The coefficients c_1 and c_2 are estimated following the method described in [55] for minimizing the cost function between the measured and estimated aerodynamic coefficients. c_{2T} is estimated by interpolation of the origin and another point on the lift curve of figure 2.16(a) at low angles of attack. (The lift curve is approximately linear at small α.) Figure 2.18 shows the comparison result between the modeled aerodynamic coefficients and those obtained from experiments. The

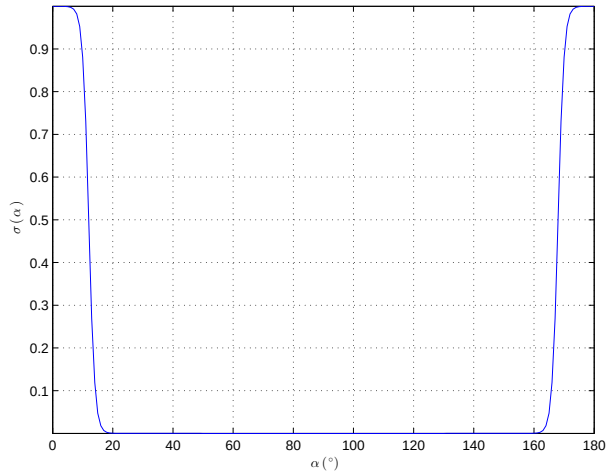

Figure 2.17: The sigmoid function at $\alpha_0 = \alpha_{0\text{ref}} = 12^\circ$ and $\text{Re} = 160000$

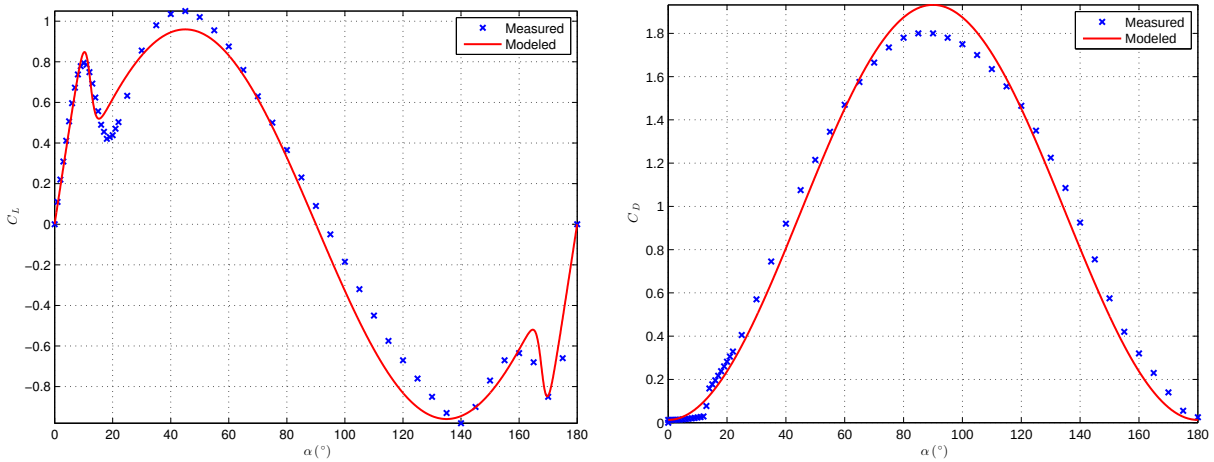

(a) (b)

Figure 2.18: The measured (wind tunnel measurement and computer synthesis [56]) and modeled (a) lift and (b) drag coefficients versus the angle of attack at $\text{Re} = 160000$ for NACA0018 airfoil

modeled values are fairly close to the measured data. At the end of the stall region or at some high angles of attack, the lift data are slightly different. In some region of very high angle of attack (α near 80°), the drag coefficients are overestimated. Figure 2.19 demonstrates the comparison of the lift coefficients at a different Reynolds numbers. It can be observed that the coefficients are well-modeled, especially at small angles of attack till the middle of the stall region.

2.4 Comparison Between Different UAV Configurations

Based on the previous modeling, in this section different UAV configurations are considered and evaluated in terms of their energy consumption at constant velocity in horizontal cruising flight. We are primarily interested in evaluating the importance of the inclination angle μ between the propellers' plane and the wing (see figure 2.15). As a second objective of this section, we also want to assess the impact of some parameters (wing(s) area, UAV's mass, choice of propellers)

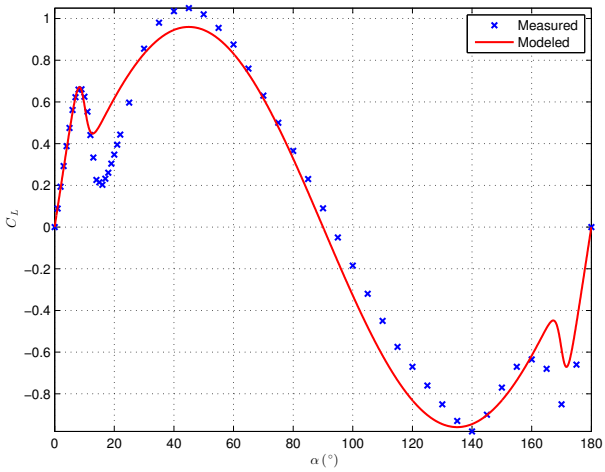

Figure 2.19: The measured (wind tunnel measurement and computer synthesis [56]) and modeled lift coefficients versus the angle of attack at Re = 80000 for NACA0018 airfoil

on the energy consumption. All physical dimensions of the simulated UAVs are elaborated in appendix C. Before proceeding to the detailed simulation, some assumptions are necessary:

- As suggested in section 2.1, the energy consumption calculation in this section is simplified by neglecting the small in-plane force H. We have tested the simulation including the H force, and compared with the simulation without H. The power calculation results are nearly identical.
- The propellers-wing(s) interaction, might be important depending on the geometry of the UAV, is not considered in this simulation in favor of simplicity of the model.
- The small power to actuate the wing(s) joints is neglected in the power calculation.

2.4.1 Power Evaluation of Different UAV Configurations

Following the notation of figure 2.15, five UAV configurations are considered:

- Case 1: μ is chosen so as to minimize the thrust force,
- Case 2: μ is chosen so as to minimize the propellers' power,
- Case 3: μ is chosen so as to maximize the ratio lift/drag on wing(s),
- Case 4: $\mu = 0$,
- Case 5: no wing on the UAV (standard quadrotor case).

The weight of the convertible UAV for the first four cases are equal. With the absence of the wing(s), the quadrotor in Case 5 is lighter than the convertible. Figure 2.20 and figure 2.21 illustrate the UAV configuration in these five distinct cases at flying speed $|\boldsymbol{v_a}| = 10$ m/s and $|\boldsymbol{v_a}| = 18$ m/s. The orientations of propellers and wing(s) are different for various cases. Figure 2.22 shows the evolution of total mechanical power in these different cases. The power curve trending is similar to the total power curve in figure 2.10 for a helicopter model, as expected. Case 1 (thrust minimization) power consumption is higher than Case 5 for speeds smaller than

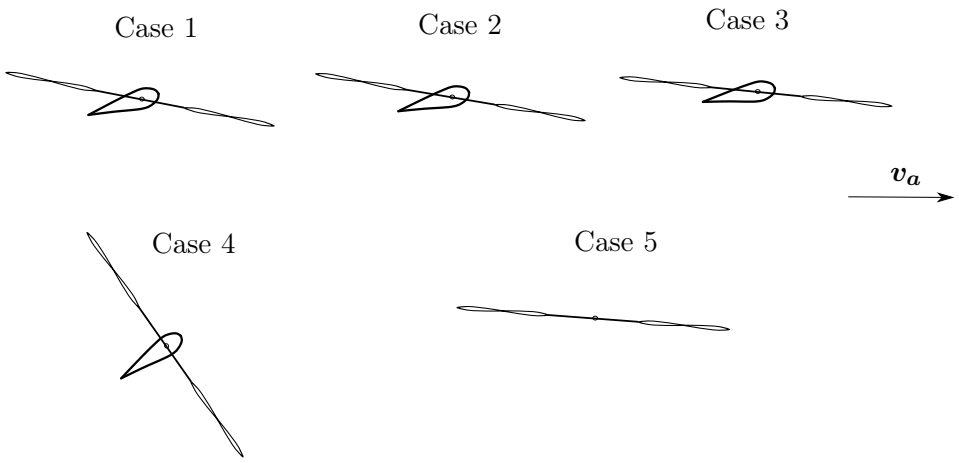

Figure 2.20: The configuration in five cases for $|\boldsymbol{v_a}| = 10$ m/s

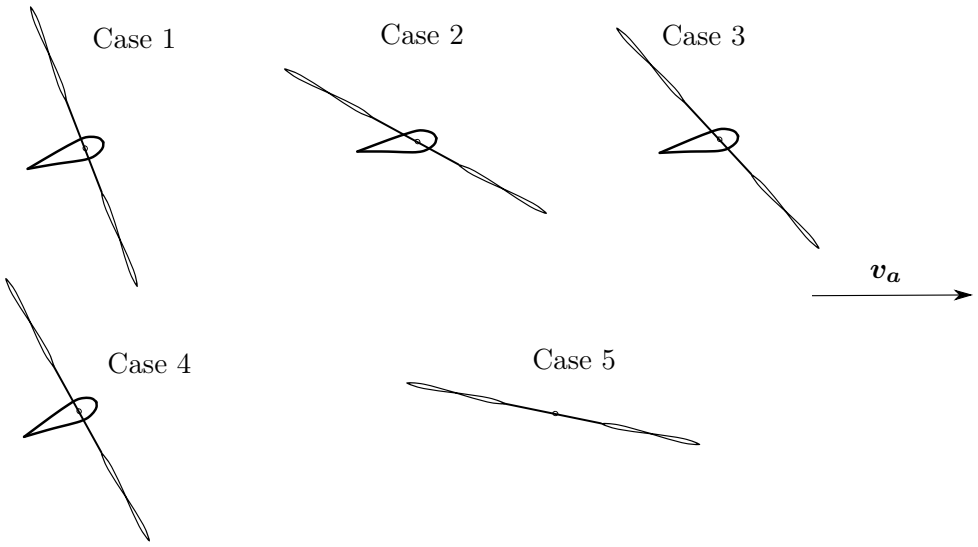

Figure 2.21: The configuration in five cases for $|\boldsymbol{v_a}| = 18$ m/s

6.5 m/s. In fact, at low speed, Case 5 spends the least power because the UAV is evidently lighter without the wing(s). At speeds $|\boldsymbol{v_a}| = |v_{a,2}| \in [10, 14]$ m/s, Case 1 and Case 2 are very similar. Beyond these speeds, Case 1 decreases rapidly in efficiency to approach the inefficient Case 4 ($\mu = 0$). At high speeds indeed, the intensity of the upward vertical aerodynamic (lift) force in Case 1 is among the highest (see figure 2.24(b)) which translates into the lowest thrust force in figure 2.25. With high parasite drag, the intensity of the horizontal aerodynamic (drag) force is also large as shown in figure 2.24(a). With strong aerodynamic forces, the propellers incline at a very large angle θ from the horizontal line as shown in figure 2.27. For example, at speed $|\boldsymbol{v_a} = 18$ m/s, $\theta \approx 1.5$ rad in Case 1, so that the propellers' plane is nearly vertical as illustrated in figure 2.21. At high speed, the propellers act like large disks that block the high speed airflow. The propellers are then required to spin very fast to generate even small thrust force (recall that we are considering low-pitch propellers APC 11×4.7). One can verify this point by examining figure 2.30. Generally when the magnitude of θ increases towards $\pi/2$, the rotor angular speed ϖ rises fast. The propeller power is a function of the cube of the rotor angular speed, hence the variation of ϖ dictates the variation of P, as proven by the similarity of the

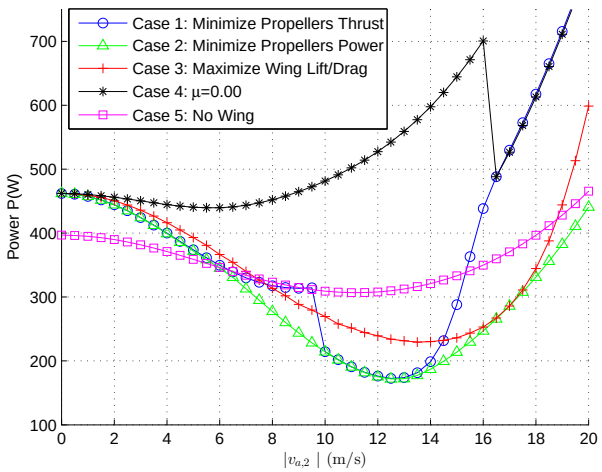

Figure 2.22: The power comparison versus the speed

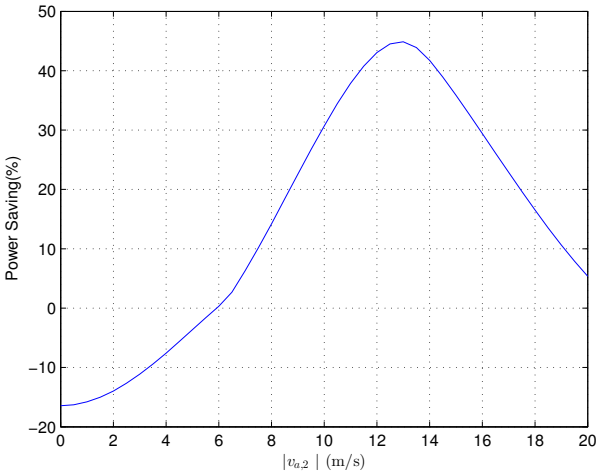

Figure 2.23: The percentage of power saving versus the speed

trends of figure 2.22 and figure 2.31. Since ϖ in Case 1 is larger than in Case 2, the propeller power of the former case is also greater. By contrast, for the optimal Case 2, the thrust is larger but the drag is kept at low value. One could of course argue that the use of propellers better suited to high-speed flight could lead to improved results at high speed for Case 1. The choice of fixed-pitch propellers, however, is constrained by the requirement of good efficiency in stationary flight.

Concerning the optimal Case 2, figure 2.23 shows the percentage of power saving w.r.t. Case 5 at different horizontal speeds. Adding the wing(s) significantly saves energy at "medium" speed. The configuration in Case 2 will save energy for a forward-flying UAV at speeds between 6 and 20 m/s. The power saving is 45% at the climax. One can note that the power saving varies with the forward speed in a "bell-curve" fashion: the gain of power is negative at very low speeds, small at very high speeds, but significant in between.

Case 3 is an example of a configuration that maximizes the wing(s) lift/drag ratio. That also means keeping the angle of attack constant and small, as shown in figure 2.29. Case 3 achieves relatively satisfactory results. Although not as efficient as Case 2, it compares favorably with Case 5 in a significant range of velocities.

Finally, Case 4 is quite inefficient. The lift force acting on the wing is high, as shown in figure 2.24(b). The drag force is the highest, however, as depicted in figure 2.24(a).

Figure 2.26 shows the in-plane drag force H acting on the propellers. This drag is small even at high speeds. Figure 2.28 highlights notably the different evolution of the angle μ for the convertible UAV. The optimal inclination angle (Case 2) varies significantly with the speeds, especially from 6 to 14 m/s.

Figure 2.29 depicts the plots of the wing angle of attack versus the speed. Note that when $|\boldsymbol{v_a}| = 0$, α is not defined and the values on the plots are simply results of numerical evaluation. An imminent feather of these plots is the presence of the stall phenomenon when the angles of attack change suddenly. It is because the UAV passes from a configuration with low speed and high angle of attack to a configuration with high speed and low angle of attack. We are mostly interested in choosing the optimal angle of attack for minimum power consumption (Case 2) starting from medium speed ($|v_{a,2}| > 6$ m/s). Here, the plot of the angle of attack can be

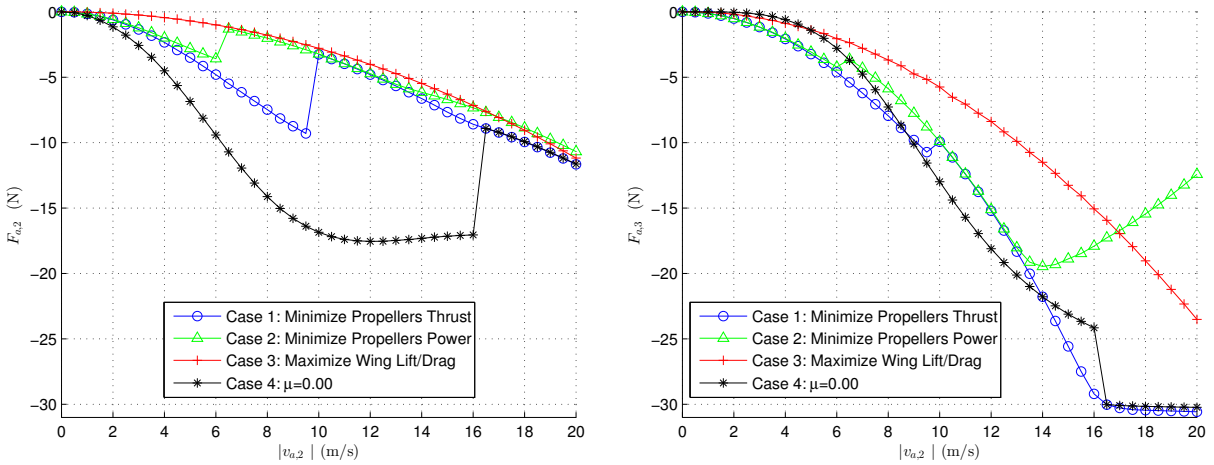

(a) (b)

Figure 2.24: The (a) horizontal and (b) vertical aerodynamic forces versus the speed

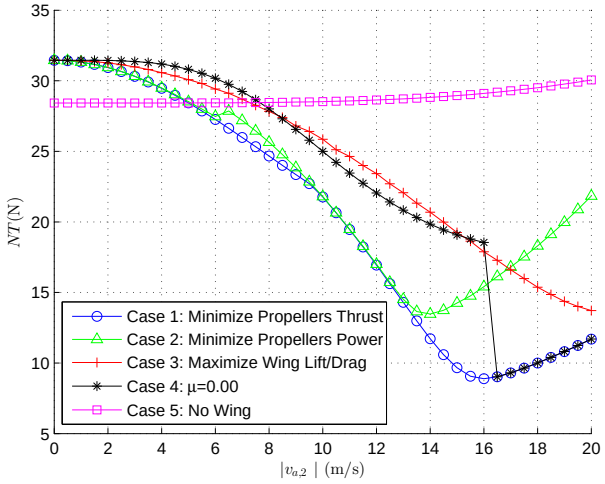

Figure 2.25: The total thrust force on all propellers versus the speed

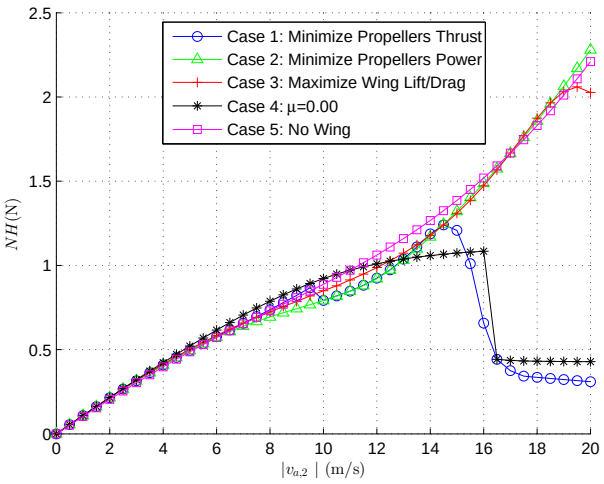

Figure 2.26: The total in-plane drag H force on all propellers versus the speed

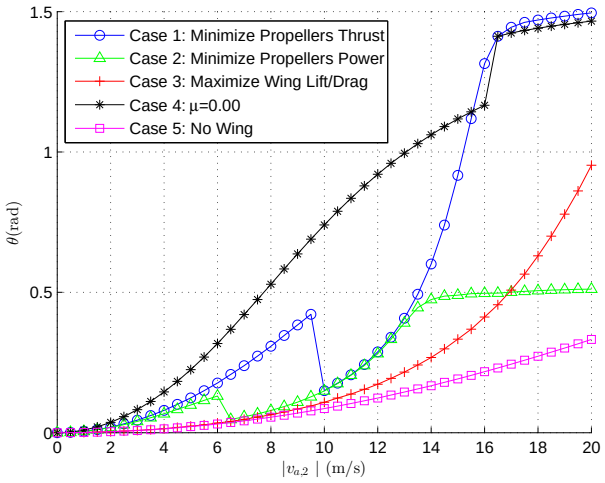

Figure 2.27: The UAV's orientation angle θ versus the speed

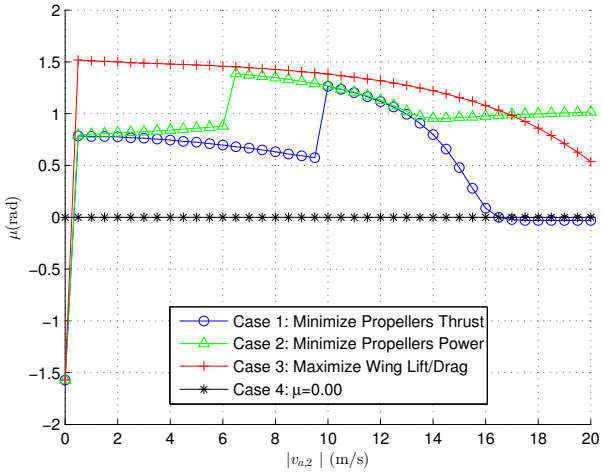

Figure 2.28: The wing(s) inclination angle μ versus the speed

considered as two quasi-linear segments. For the first segment with speeds $|v_{a,2}| \in [6.5, 13]$ m/s, α increases with higher speed. This can be expected since higher aerodynamic lift reduces the required propellers thrust. At the same time, the UAV's pitch is still relatively small ($\theta \leq 0.4$ rad) so that the propellers are in their efficient configurations. Beyond 13 m/s, the UAV's pitch angle θ is high. When $\theta > 0.4$ rad, small increment in θ causes a sharp rise in the propellers' rotational speeds, and consequently the power consumption. Therefore, the optimal α decreases at higher speed to limit the aerodynamic forces and UAV's pitch angle.

We can observe discontinuities of the power in figure 2.22. For example, in Case 1 there is a discontinuity when speed increases from 9.5 m/s to 10 m/s. The angle of attack (figure 2.29) jumps from $\alpha = 0.57$ rad to $\alpha = 0.15$ rad. The vehicle goes from an equilibrium point after the stall zone to an equilibrium point just before the stall. This can be explained by looking at figure 2.18(a), if we limit α to the range of $[0, 180°]$, for each C_L, there are several solutions for α. By contrast, one does not notice a power discontinuity in Case 2 for example. One can remark on figure 2.29, however, that the angle of attack of the wing also jumps from $\alpha = 0.56$ rad to $\alpha = 0.14$ rad when speed increases from 6 m/s to 6.5 m/s. The discontinuity in power is not noticeable in figure 2.22 because there is one local minimum very close to the global minimum on the power curve (see figure 2.32). As speed increases from 6 m/s to 6.5 m/s, the optimal angle α jumps to a very different value but the minimum power does not vary much. We do not know at this time whether this is just a matter of chance or there is an explanation for this property.

2.4.2 Impact of Some Parameters on the Energy Consumption

Figure 2.33 plots the percentage of power saving in Case 2 as compared to Case 5 for different propellers. Other simulated parameters are kept the same. We can observe greater power saving for the configurations with small propellers, since the impact of wing(s) is even more prominent. In addition, the power gain is more significant at medium and high speeds for propellers which have higher average pitch. This comparison concerns only three APC SlowFlyer propellers. Future developments will include the performance evaluation of more propellers (possibly from different manufacturers) and selection of propellers optimized for hover or cruising flight.

Figure 2.34 illustrates the influence of the wing(s) area on the energy consumption. The

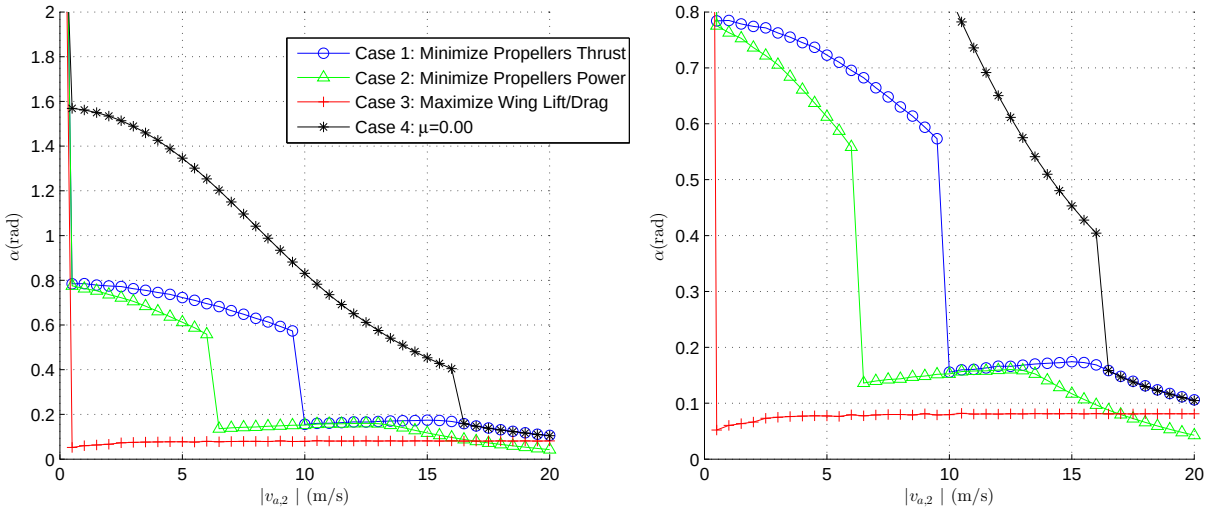

Figure 2.29: The angle of attack α versus the speed (when $|\boldsymbol{v_a}| = 0$, α is not defined)

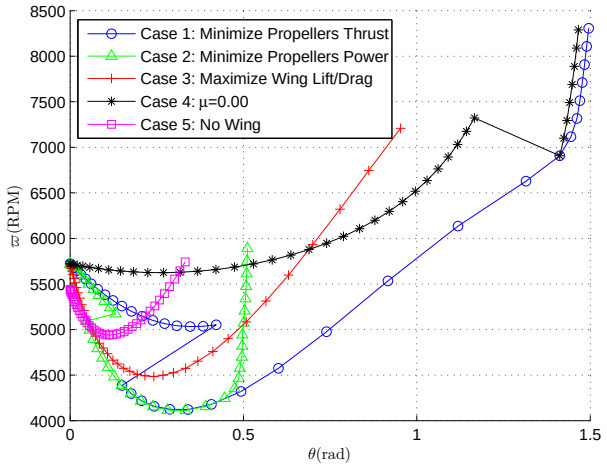

Figure 2.30: The rotor angular velocity versus the UAV's orientation angle θ

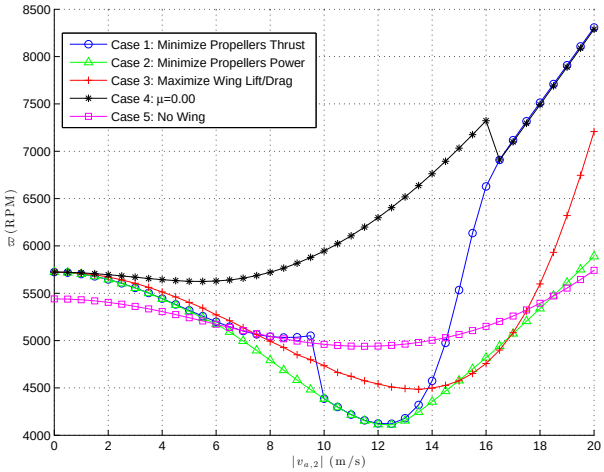

Figure 2.31: The rotor angular velocity versus the speed

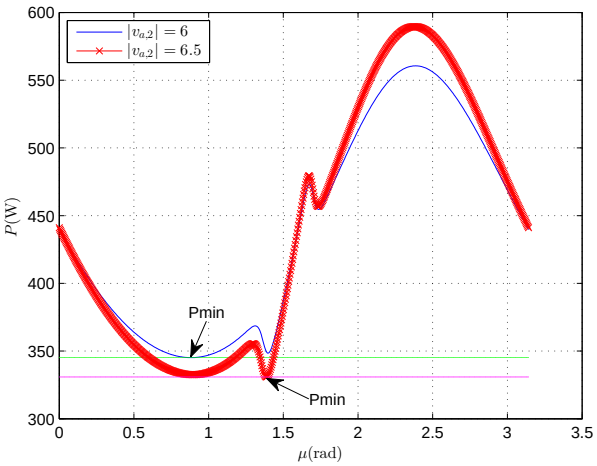

Figure 2.32: Case 2: power versus angle μ at two different speeds

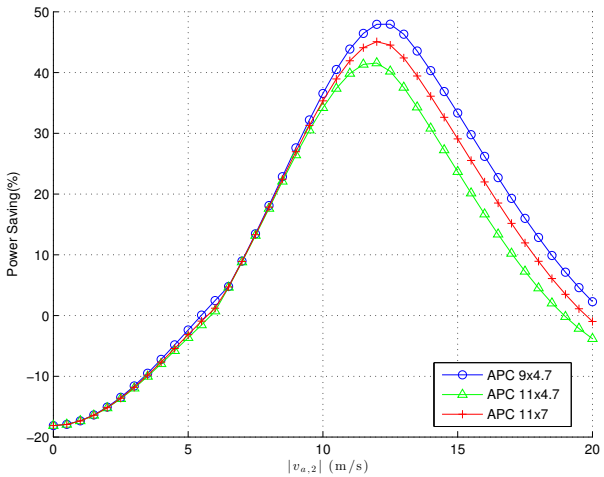

Figure 2.33: Percentage of power saving w.r.t. Case 5 for different propellers

propellers used are APC SlowFlyer 11×4.7. The mass of the UAV except the wing(s) is kept at 2.9 kg, whereas the mass of the wing(s) are proportional to the wing(s) area. Unsurprisingly, the larger the wing(s) the higher the power gain at medium speed. At low speeds, configurations with larger wing(s) obviously spend more power.

Figure 2.35 compares the percentage of power saving for different total masses of the UAV with a given wing(s) area (total wing area 0.22 m^2). The propellers used are still APC SlowFlyer 11×4.7. If the total weight of the UAV increases, the maximum gain of power will occur at higher speeds. In addition, the overall power gain is greater for heavier UAVs with the same wing(s). The reason is that with heavier UAV, the lift force holds an even more important role to compensate for the increased weight.

2.5 Chapter Summary

We have proposed a method to evaluate the energy consumption of VTOL UAVs composed of coplanar propellers and a main body that may include wing(s). This method makes use of two analytical models of aerodynamic coefficients: a model of the propellers derived by combining momentum and blade element theories, and a model of the wing(s) recently proposed in the literature. From these models, energy evaluation is reduced to solving numerically a simple optimization problem. Energy consumption for five UAV configurations is then compared and analyzed in detail, allowing to determine the most efficient configuration in terms of the inclination angle between the propellers' plane and the wing(s). It is shown that the optimal value of this angle depends on the airspeed and that adding wing(s) may be detrimental for energy consumption if this angle is poorly chosen. Indeed, adding wing(s) reduces the thrust force but increases the drag force, thereby yielding a larger inclination angle of the propellers' plane - which is not efficient from the energy point of view. Thus, the optimal configuration is the one that provides the best trade-off between small thrust force and low total drag force on the UAV. At the end of this chapter, the important impacts of propeller size, wing area, and UAV mass are evaluated. This chapter paves the way to the possibilities to evaluate the global performance of the UAV in terms of fuel consumption and mission performance (maximum endurance,

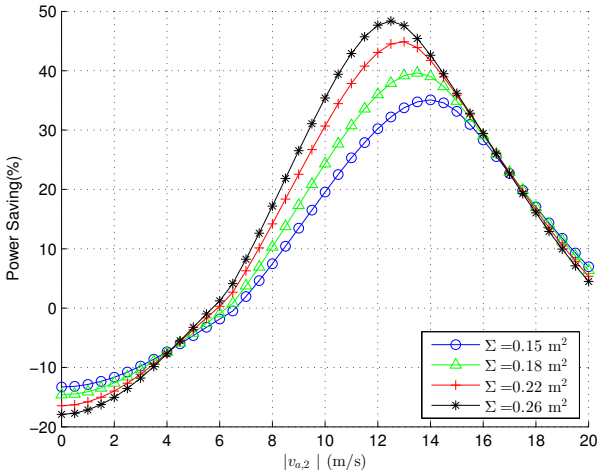

Figure 2.34: Percentage of power saving w.r.t. Case 5 for different wing(s) area Σ

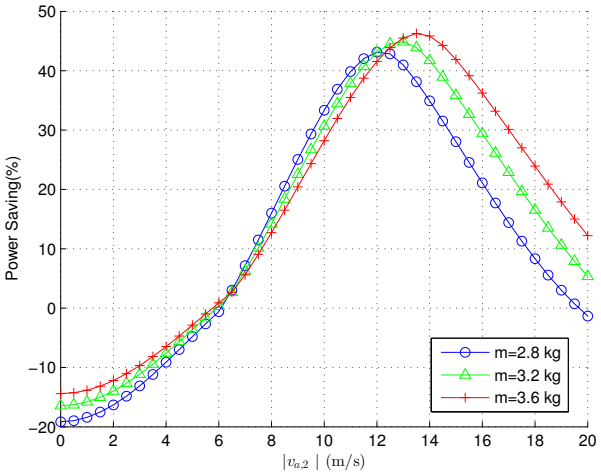

Figure 2.35: Percentage of power saving w.r.t. Case 5 for different UAV's mass

maximum range, ceiling, etc.). Besides, the interaction between wing(s) and propellers is the area that needs further exploration. The model in this chapter will be complemented with the estimation and control laws in the next chapter to build the complete control system.

Chapter 3

Control Design

As seen from the previous chapter, good understanding of aerodynamic effects and fine modeling of these effects are crucial to design an aerial vehicle's geometry in order to optimize the energy efficiency. For control design, however, precise modeling is not as important because the feedback control is expected to grant robustness in the sense of performance insensitivity w.r.t. model inaccuracies. Thanks to this robustness property, a simplified aerodynamic model of propellers and wings can be used for the control design, as shown later in this chapter.

Control of convertible aerial vehicles appeals to the control of both fixed-wing and VTOL vehicles. In the first section of this chapter, existing control techniques for these aerial vehicles are recalled. Then, we develop control design approaches for our convertible vehicle.

- The first strategy applies for cases when no velocity (neither UAV velocity nor wind velocity) measurement is available. The control design utilizes the measurement data from IMU (gyrometer, accelerometer) and barometer. One of the most common scenarios is the teleoperation case, where the UAV is controlled in attitude and altitude. The essential idea for attitude control is to stabilize the gravitational vector's direction in the body frame around its reference value. As for altitude control, the magnitude of the thrust force can be used as a direct control variable for vertical speed and position, provided that the vertical aerodynamic force is either known or can be estimated. This control strategy is made possible with the estimation of state variables via sensor system including IMU and barometer (or another altitude sensor).

- In the second strategy, the same IMU/barometer measurement data are used. We present a control strategy involving a spring-damper type controller to control the wings' angle of attack near their optimal values in the presence of unknown winds.

- The third strategy is suitable for cases when the UAV velocity measurement is available (e.g. obtained from GPS signal), the UAV is controlled to follow a reference trajectory or velocity. The aerodynamic forces and torques are estimated based on the velocity measurement. The wings' pitch angles are adjusted so that the angles of attack remain constant. The propellers/wings interaction is also taken into account by a simple model.

3.1 Recalls on Aerial Vehicles Control

Following [57], we consider a class of thrust-propelled aerial vehicles that encompasses many systems found in practice, including conventional aircraft, helicopter, multicopter, tail-sitter UAV, etc. Such vehicles are controlled via a thrust force $\boldsymbol{T} = -T\boldsymbol{k}$ with thrust intensity $T \in$

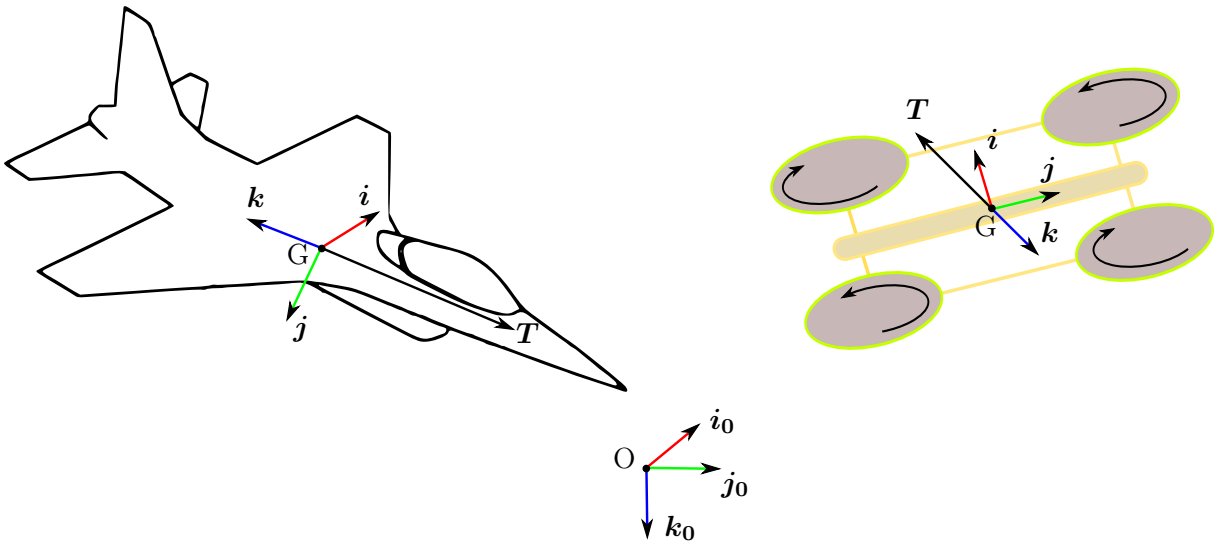

Figure 3.1: Diagram of fixed-wing and VTOL aerial vehicles

$\mathbb{R}$, $T \geq 0$ along body direction $-\boldsymbol{k}$ (figure 3.1) and a torque vector $\Gamma \in \mathbb{R}^3$ to control the attitude. In practice, this torque is produced in various ways, typically with propellers (VTOL vehicles), elevators, rudders, and ailerons (airplanes), control moment gyros (spacecrafts), etc.

In order to simplify the exposition, the following assumptions are made for the control model:

- The thrust force $\boldsymbol{T}$ applies at a point that lies on, or close to, the axis $\{\mathrm{G}; \boldsymbol{k}\}$, so that it does not create an important torque at G.
- The gyroscopic torque associated with rotorcraft is either negligible or known so that it can be directly compensated by the control torque action.
- The thrust and torque couplings are neglected.
- The aerodynamic forces and torques depend only on the vehicle's velocity, orientation, and wind disturbance. Added mass effects and forces that depend on the vehicle angular velocity/acceleration are neglected.

Applying the Newton-Euler formalism, the simplified equations for an aerial vehicle can be obtained:

$$\left\{ \begin{array}{lcl} \dot{x} & = & v \\ m\dot{v} & = & -T\mathcal{R}e_3 + mge_3 + F_a \\ \dot{\mathcal{R}} & = & \mathcal{R}\mathcal{S}(\omega) \\ J\dot{\omega} & = & -\omega \times J\omega + \Gamma + \Gamma_a \end{array} \right. \tag{3.1}$$

where the following notation is used:

- $\mathcal{I} = \{\mathrm{O}, \boldsymbol{i_0}, \boldsymbol{j_0}, \boldsymbol{k_0}\}$ is a NED (North-East-Down) inertial frame.
- $\mathcal{B} = \{\mathrm{G}, \boldsymbol{i}, \boldsymbol{j}, \boldsymbol{k}\}$ is the body-frame with G the vehicle's center of mass (CoM).
- m is the vehicle's mass and $J \in \mathbb{R}^{3\times3}$ is its inertia matrix.
- $x = (x_1, x_2, x_3)^\top \in \mathbb{R}^3$ is the vector of coordinates of the vehicle's CoM position expressed in the inertial frame $\mathcal{I}$.

- $v = (v_1, v_2, v_3)^\top \in \mathbb{R}^3$ is the vector of coordinates of the linear velocity of the body-fixed frame $\mathcal{B}$ relative to the inertial frame $\mathcal{I}$ and expressed in $\mathcal{I}$.
- $\mathcal{R} \in \mathrm{SO}(3)$ is the rotation matrix representing the orientation of the body-fixed frame $\mathcal{B}$ with respect to the inertial frame $\mathcal{I}$. The column vectors of $\mathcal{R}$ correspond to the vectors of coordinates of $\boldsymbol{i}$, $\boldsymbol{j}$, $\boldsymbol{k}$ expressed in the basis of $\mathcal{I}$.
- $\omega = (\omega_1, \omega_2, \omega_3)^\top \in \mathbb{R}^3$ is the angular velocity vector of the body-fixed frame $\mathcal{B}$ relative to the inertial frame $\mathcal{I}$ and expressed in $\mathcal{B}$.
- F_a and Γ_a denote the aerodynamic forces and torques acting on the vehicle, respectively.
- $\mathcal{S}(\,\cdot\,)$ is the skew-symmetric matrix associated with the cross product (i.e., $\mathcal{S}(u)v = u \times v, \forall u, v \in \mathbb{R}^3$).
- $e_3 = (0, 0, 1)^\top$ is the third vector of the canonical basis of $\mathbb{R}^3$ and also the vector of coordinates in $\mathcal{B}$ of $\boldsymbol{k}$.

3.1.1 Recalls on Fixed-wing Aircraft Control

There exists a large literature on fixed-wing aircraft control, thus a thorough review is clearly beyond the scope of this thesis. Nonetheless, this section attempts to provide a brief recall on classical and modern control techniques for this type of aerial vehicles.

Fixed-wing aircraft usually operates at small angles of attack where accurate aerodynamic coefficient data can be obtained via wind-tunnel measurements. Consequently, aerodynamic forces can be explicitly taken into account. With known aerodynamic forces, the control design then usually relies on a linearized model for the aircraft motion. More precisely, the following state and control vectors are defined [58]:

- a 9D state vector comprising airspeed, sideslip angle, angle of attack, 3D attitude vector (roll, pitch, and yaw angles), and 3D angular velocity;
- a 4D control vector composed of thrust intensity and three deflection angles of elevator, aileron, and rudder.

The aircraft dynamics is then linearized around equilibrium points e.g. constant velocity cruising flight, steady turning flight, etc. In constant velocity cruising mode, the linearized system can be decoupled into two dynamics [58]:

- The longitudinal dynamics with a 4D state vector (airspeed, angle of attack, pitch rate, and pitch angle) and a 2D control vector (thrust intensity and elevator deflection angle).
- The lateral/directional dynamics with a 4D state vector (sideslip angle, roll angle, roll and yaw rates) and 2D control vector (aileron and rudder deflection angles).

This dynamics provides practical insights on the aircraft characteristics closed to standard operating flight. However, over the entire flight envelope, especially with highly maneuverable aircraft, there may be large changes in aircraft dynamics, e.g. a dynamic mode that is stable and adequately damped in one flight condition may become unstable or inadequately damped in another flight condition. In addition, in some fast oscillation modes of the aircraft, the oscillatory frequencies tend to be sufficiently high that a pilot would find it difficult or impossible to control the aircraft. Therefore, it is necessary to provide an automatic feedback control system to aid the pilot. Such control systems are known as stability augmentation systems (SAS). If the

augmentation system is tailored for specific goals, it is known as a control augmentation system (CAS). Beyond SAS and CAS, autopilot control systems are developed to improve the response and to achieve minimal steady-state errors and rapid disturbance rejections [58].

Despite their simplicity, control methods based on linear approximation have several disadvantages:

- The principal disadvantage of linear control techniques is the local nature of the controllers. Due to aerodynamic perturbations, the real dynamics may be far from the desired trajectory. Therefore, the linearized system is no longer representative of the real system.
- When the reference trajectory is time-varying or there exists strong disturbance, the system stability is difficult to establish. In such a case, one may apply gain-scheduling techniques [59, 60]:
  - designing a set of local controllers,
  - scheduling these controllers depending on the actual state of the system's evolution.

  However, this technique is merely a heuristic approach. The robustness and stability properties of the global gain-scheduling controller are not guaranteed.
- Linearizing an aircraft's dynamics often requires a minimal parametrization of the rotation matrix (e.g. Euler angles), they induce singularities that artificially limit the stability domain of the controlled system (e.g. the well-known Gimbal lock).

To alleviate some drawbacks of classical control approaches, modern control design often appeals to different techniques:

- Pole-placement/Eigenvector assignment: usually multiple poles are assigned simultaneously in multi-input/multi-output (MIMO) systems and closed-loop eigenvectors are selected based on flying qualities specifications (degree of manual intervention by pilots, frequency response, time response, etc.) or performance criteria (energy efficiency, max range, max speed, ceiling, etc.) [58].
- Dynamic inversion [61,62]: this technique is fundamentally based on feedback linearization. Dynamic inversion design includes an inner full state variable feedback loop and a linear outer tracking loop. Since the system nonlinearities are taken into account in the inner loop, the controller is suitable for a wide range of operating conditions, including high angle of attack conditions or aggressive maneuvers. The drawback of dynamic inversion is that it requires precise knowledge of nonlinear functions in the aircraft equations. Otherwise, the control system may include undesirable zero dynamics [58, 63].

Guaranteeing stability in a large flight envelope is clearly a desirable property for aerial vehicles. For fixed-wing aircraft, however, there are severe obstructions to this property, essentially due to stall. Typical airfoil lift curves similar to the ones in figure 2.16 consist of a region associated with sudden decrease of lift coefficients, i.e. the so-called stall phenomenon. It can be observed that there may be several angles of attack associated with the same lift coefficient. Consequently, given a continuous reference velocity profile, the associated equilibrium orientation may be discontinuous [18]. If such discontinuities are encountered, the stabilization problem is no longer well-posed. For example, consider an aerial vehicle with wing aerodynamic coefficients similar to the ones in figure 2.16 tracking a continuous reference velocity $v_r(t) = [0, c_v t, 0]^\top$ with c_v a small positive number. Figure 3.2 shows the evolution of the equilibrium angle of attack α_e

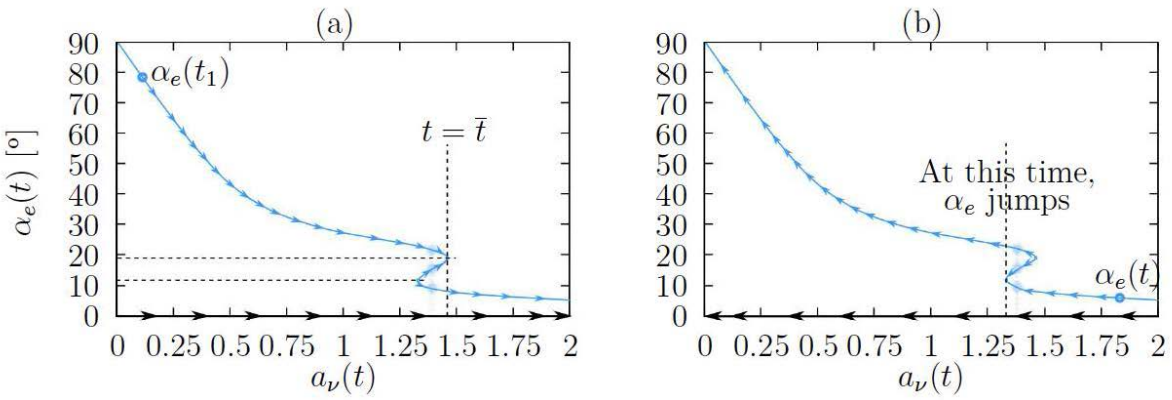

Figure 3.2: Equilibria pattern for (a) $v_r(t) = [0, c_v t, 0]^\top$ and (b) $v_r(t) = [0, v_h - c_v t, 0]^\top$ with $v_h \gg 1$, $0 < c_v \ll 1$ [18]

over a number $a_\nu \triangleq k_a v^2/(mg)$ that characterizes the ratio of aerodynamic force over the gravity force (therefore dictates the equilibrium points). As time goes by, the intensity of the reference velocity increases, and this implies smaller values of angle of attack at equilibrium condition. At $t = \bar{t}$, the equilibrium angle of attack $\alpha_e(t)$ instantaneously goes from 19° to 12°, thus making the vehicle equilibrium trajectory discontinuous. Consequently, this reference velocity cannot be smoothly tracked by any fixed-wing aircraft that has similar aerodynamic characteristics to the current example [18].

3.1.2 Recalls on VTOL Aircraft Control

This section is essentially based on the review article on feedback control of underactuated VTOL UAV [64]. As in the case of fixed-wing aircraft, classical linear control techniques can also apply to VTOL UAV. A summary of linear control techniques is presented next, with their advantages and drawbacks.

3.1.2.1 Linear Control Techniques

Linear control techniques usually rely on linear approximations of the system dynamics about some points or some reference trajectories. To simplify the current presentation, the focus is on VTOL UAV at hovering flight in the absence of wind. Similar conclusions can be drawn for other trajectories and flight conditions, such as constant velocity with constant wind, provided that the aerodynamic forces are either measured or estimated online (so that the equilibrium position can be found). In view of these simplified assumptions, the approximated orientation matrix is: $\mathcal{R} \approx I_3 + \mathcal{S}(\Theta)$ with $\Theta \in \mathbb{R}^3$ any minimal parametrization of $SO(3)$ around the identity matrix (e.g., the vector of Euler angles θ_1: roll, θ_2: pitch, θ_3: yaw). We then have the following linear approximation of system (3.1) at the equilibrium $(x = 0, v = 0, \Theta = 0, \omega = 0, T = mg, \Gamma = 0)$:

$$\left\{ \begin{array}{lcl} \dot{x} & = & v \\ m\dot{v} & = & -mg\mathcal{S}(\Theta)e_3 - \tilde{T}e_3 \\ \dot{\Theta} & = & \omega \\ J\dot{\omega} & = & \Gamma \end{array} \right. \tag{3.2}$$

where $\tilde{T} = T - mg$. Without loss of generality, we assume that the UAV's inertia matrix is diagonal, i.e. $J = \text{diag}(J_{11}, J_{22}, J_{33})$. It is possible to decompose the system into four independent Single-Input-Single-Output (SISO) linear subsystems:
The first subsystem describes the horizontal dynamics along $\boldsymbol{i_0}$:

$$\begin{cases} \dot{x}_1 &= v_1 \\ \dot{v}_1 &= -g\theta_2 \\ \dot{\theta}_2 &= \omega_2 \\ J_{22}\dot{\omega}_2 &= \Gamma_2 \end{cases} \tag{3.3}$$

The second subsystem describes the horizontal dynamics along $\boldsymbol{j_0}$:

$$\begin{cases} \dot{x}_2 &= v_2 \\ \dot{v}_2 &= g\theta_1 \\ \dot{\theta}_1 &= \omega_1 \\ J_{11}\dot{\omega}_1 &= \Gamma_1 \end{cases} \tag{3.4}$$

The third subsystem describes the vertical dynamics along $\boldsymbol{k_0}$:

$$\begin{cases} \dot{x}_3 &= v_3 \\ m\dot{v}_3 &= -\tilde{T} \end{cases} \tag{3.5}$$

The fourth subsystem describes the yaw dynamics:

$$\begin{cases} \dot{\theta}_3 &= \omega_3 \\ J_{33}\dot{\omega}_3 &= \Gamma_3 \end{cases} \tag{3.6}$$

Note that the vertical dynamics subsystem (3.5) does not depend on the orientation, i.e. it is independent of θ and ω. By contrast, the yaw dynamic (3.6) does not depend on position nor linear velocity. We now detail the control of subsystems (3.3) and (3.4) (Subsystems (3.5) and (3.6) are second-order and they are straightforward to control.). With appropriate changes of coordinates, each of subsystems (3.3) and (3.4) can be rewritten as a fourth-order linear system with u the control variable:

$$\begin{cases} \dot{y}_1 &= y_2 \\ \dot{y}_2 &= y_3 \\ \dot{y}_3 &= y_4 \\ \dot{y}_4 &= u \end{cases} \tag{3.7}$$

The most common strategy to control system (3.7) is hierarchical control. This technique considers y_3 as the control input for the outer system, and the desired value y_3, denote as $y_{d,3}$ is used as a reference value for outer system:

$$\begin{cases} \dot{y}_1 = y_2 \\ \dot{y}_2 = y_{d,3} + \tilde{y}_3 \\ \dot{\tilde{y}}_3 = \tilde{y}_4 \\ \dot{\tilde{y}}_4 = -\ddot{y}_{d,3} + u \end{cases} \tag{3.8}$$

with $\tilde{y}_3 = y_3 - y_{d,3}$ and $\tilde{y}_4 = y_4 - \dot{y}_{d,3}$. The outer subsystem (the first two equations in system (3.8)) has slow dynamics whereas the inner subsystem (the last two equations in system (3.8)) has fast dynamics. For the outer loop, often called Guidance loop, we can take a PD controller

represented by $y_{d,3} = -k_1 y_1 - k_2 y_2$ with $k_{1,2} > 0$. Taking the derivative yields $\dot{y}_{d,3} = -k_1 y_2 - k_2 y_3$ and $\ddot{y}_{d,3} = -k_1 y_3 - k_2 y_4$. Finally for the inner loop, often called Control loop, the control law for u is:

$$u = \ddot{y}_{d,3} - k_3 \tilde{y}_3 - k_4 \tilde{y}_4 \text{ with } k_{3,4} > 0.$$

Since the characteristic polynomial of the closed-loop system is $(p^2 + k_2 p + k_1)(p^2 + k_4 p + k_3)$, the positivity of all gains k_i $(i = 1, \ldots, 4)$ ensures, by a straightforward application of the Routh-Hurwitz criterion, the exponential stability of the origin of the initial fourth-order system. A variation of hierarchical control strategy consists in using y_4 as a virtual control input.

$$\begin{cases} \dot{y}_1 &= y_2 \\ \dot{y}_2 &= y_3 \\ \dot{y}_3 &= y_{d,4} + \tilde{y}_4 \\ \dot{\tilde{y}}_4 &= -\dot{y}_{d,4} + u \end{cases}$$

with $\tilde{y}_4 = y_4 - y_{d,4}$. The control law is:

$$\begin{cases} y_{d,4} &= -k_1 y_1 - k_2 y_2 - k_3 y_3 \\ u &= \dot{y}_{d,4} - k_4 \tilde{y}_4 \end{cases} \tag{3.9}$$

with $k_i > 0 (i = 1, \ldots, 4)$. This strategy groups the translational and orientation variables together in the slow outer Guidance loop. Indeed, it is consistent with the fact that the angular velocity measurement is accurate with IMU whereas the UAV's orientation estimation is much more difficult [64].

Modern linear control theory consists in searching control gains to optimize some objectives, e.g. energy efficiency and robustness w.r.t model uncertainties or external disturbances (like wind gusts). Examples of studies with optimization policy are: Linear-Quadratic-Regulator (LQR) controller for the control of the rotational dynamics of a quadrotor [65]; Linear-Quadratic-Gaussian (LQG) controller incorporating a quadratic criterion for weighting the model sensibility with respect to parametric variations for a quadrotor [66] ; robust H_2 and H_∞ control techniques for helicopter models [67–69].

As mentioned in section 3.1.1, there are some limitations associated with classical or even modern linear control techniques. First, the stability analysis is local so that the stability domain is difficult to specify, then in the case of reference trajectories with time-varying velocities or in the case of wind gusts, the equilibrium orientation varies with time. This is especially true for VTOL systems, since their orientation variation w.r.t airflow can be much more significant than the one of fixed-wing aircraft. Therefore, the linearized system is also time-varying, and the stability of the system is difficult to analyze. To overcome these shortcomings, nonlinear control techniques are presented as the extensions to linear methods.

3.1.2.2 Nonlinear Control Techniques

Nonlinear controllers provide enlarged domain of stability and enhanced robustness as compared to linear controllers. The nonlinear controllers may be seen as natural extensions of locally approximating linear control schemes. Indeed, linear control gain optimization techniques are useful for the tuning of a certain number of parameters of nonlinear controllers.

Providing a survey of existing nonlinear control techniques for VTOL vehicles is beyond the scope of this section. Instead, we focus on one of the most popular technique, namely hierarchical control. This approach is easy to understand and it appears as a natural extension of the linear hierarchical control presented above for the stabilization of system (3.7).

As discussed in the previous linear control section, fast and accurate gyroscope measurement allows us to control ω to a reference value easily. We can then use ω as the control input instead of Γ. We assume that the aerodynamic force does not depend on the orientation of the vehicle and they apply close to the vehicle's CoM. This assumption corresponds ideally to the case of a spherical vehicle, for which there is no lift force and the resultant of drag forces applies at the CoM.

System (3.1) is then simplified to:

$$\begin{cases} m\dot{v} &= -T\mathcal{R}e_3 + mge_3 + F_a(v,t) \\ \dot{\mathcal{R}} &= \mathcal{R}\mathcal{S}(\omega) \end{cases} \tag{3.10}$$

with T and ω as control inputs.

Hierarchical control applies similarly to many similar objectives like velocity (or position) control without or with integral correction. For details on integral correction and position control, interested readers are invited to consult the references [21] and [64]. The following describes a short summary of velocity control.

Let v_r denote a reference translational velocity expressed in inertial frame $\mathcal{I}$ and let $\tilde{v} = v - v_r$ denote the error in velocity expressed in $\mathcal{I}$. We then obtain the error model:

$$\begin{cases} m\dot{\tilde{v}} &= -k_v(v,t) - T\mathcal{R}e_3 + F(v,t) \\ \dot{\mathcal{R}} &= \mathcal{R}\mathcal{S}(\omega) \end{cases} \tag{3.11}$$

with $F(v,t) = k_v(v,t) + F_a(v,t) + mge_3 - m\dot{v}_r(t)$, where $k_v(v,t)$ is a feedback term designed so as to ensure the stability of $v = v_r$ for the system $m\dot{v} = -k_v(v,t)$. A simple choice is $k_v(v,t) = k(v - v_r)$ with k a positive gain but one may use a more sophisticated control expression, e.g. incorporating integral correction terms, etc. From here, the objective is to ensure the convergence of $-TRe_3 + F(v,t)$ to zero. Indeed, this implies that asymptotically the control system behaves like the stable system $m\dot{v} = -k_v(v,t)$. For $\tilde{v} = 0$ to be an equilibrium of system (3.11), the acceleration error must vanish at this point, i.e. $\dot{\tilde{v}} = 0$ and we obtain the following equation:

$$T\eta = F(v_r,t) \tag{3.12}$$

with $\eta = \mathcal{R}e_3$ denoting the thrust direction unit vector in the initial frame. If $F(v_r,t)$ is different from zero, there exist only two solutions to this equation, which define possible reference thrust intensity T_r and thrust direction η_r:

$$(T_r, \eta_r) = \left(\pm|F(v_r,t)|, \pm\frac{F(v_r,t)}{|F(v_r,t)|} \right). \tag{3.13}$$

The above relation calls for some important remarks:

- In practice, the chosen solution among those in (3.13) is the one that ensures the positivity of the thrust intensity, i.e. $T_r = |F(v_r,t)|$, $\eta_r = \dfrac{F(v_r,t)}{|F(v_r,t)|}$.
- If $F(v_r,t) = 0$, we have a singular case where any unit vector η satisfies Eq. (3.12) when $T = 0$. This situation is uncommon since the gravity term in $F(v_r,t)$ usually prevents the latter from vanishing. However high wind gusts or aggressive reference trajectories may provoke this situation. In such case, the stabilization of the system involves very specific nonlinear control technique (e.g. [70]). This situation is not addressed in this thesis.

- When $F(v_r, t) \neq 0$, well-posedness of the solutions (3.13) to Eq. (3.12) is related to the independence of F upon the vehicle's orientation. More precisely, if the external force F_a depends on the orientation, i.e. $F_a = F_a(v, \mathcal{R}, t)$, then $F(v, t)$ in system (3.11) depends on $\mathcal{R}$ also:
$$F(v, \mathcal{R}, t) = mg + F_a(v, \mathcal{R}, t) - m\dot{v}_r(t). \tag{3.14}$$
Since $\eta = \mathcal{R}e_3$, Eq. (3.12) then becomes implicit in η and the existence and uniqueness of solution (given sign of T_r) are no longer systematic.

Once the reference thrust direction η_r has been defined, the next control step is using ω to ensure the convergence of η to η_r. We can generalize the control solution by considering the problem of stabilizing a given desired direction characterized by a unit vector η_d, independently of other possible control objectives. This desired direction may equally be specified by the orientation of a user's joystick, or be the (locally) unique solution η_r previously evoked for velocity control purposes. For instance, in the case of hovering, one can take $\eta_d = e_3$ and nonlinear solutions to the control problem can be compared to the linear ones presented in the previous section. Defining $\omega_{1,2} := (\omega_1, \omega_2)^\top$, a possible nonlinear control solution, among many other possibilities, is [57]

$$\omega_{1,2} = \left\{ \mathcal{R}^\top \left[k_0 \frac{\eta \times \eta_d}{(1+\eta^\top \eta_d)^2} - \mathcal{S}(\eta)^2 (\eta_d \times \dot{\eta}_d) \right] \right\}_{1,2} \tag{3.15}$$

with $k_0 > 0$. This control ensures the exponential stability of the equilibrium point $\eta = \eta_d$ provided that the initial conditions $\eta(0)$ and $\eta_d(0)$ are not opposite to each other.

Note that the expression of aerodynamic forces along arbitrary reference trajectories is seldom known. Then, neither $F(v_r, t)$ nor η_r is known. In practice, one possibility is to obtain an online estimation of $F(v, t)$ via accelerometer measurements or high-gain observers ([21, Chap. 2] and [71]). We will come back to this issue later.

3.1.3 Recalls on Convertible Aircraft Control

Control of convertible aerial vehicles is concerned not only with VTOL mode or cruising mode separately but also with the transition maneuvers between the two modes. From the time of early prototypes (e.g. Bell Helicopter XV-3, XV-15, etc.) to the present days of modern aircraft (e.g. Bell Boeing V-22 Osprey and AgustaWestland AW609), tilt-rotors always represent significant control challenges. Indeed, the pilot is required to control not only helicopter mode (collective pitch, cyclic pitch, rotor RPM) but also airplane mode (rudders, elevators, flaps) and pylons tilt angle. There are usually several options for a control purpose. For instance, the roll control can be accomplished by the differential collective pitch on the two rotors in helicopter mode or by ailerons in airplane mode. During the transition between helicopter and airplane modes, one method of control is washed out as another control washes in. A transition function using tilting angle is often invoked to blend in the two modes. Simple linear interpolation is easiest, but the sinusoidal function is often used for a smoother transition [72]. As for small convertible UAVs, various control techniques have been introduced in recent years:

- [73,74] calculate numerically the reference maneuvers based on minimum time and minimum-energy transition for a mini tilt-rotor UAV. Then a robust control is implemented to switch between the control values in the transition period.

- [75] implements on a model-scale tilt-body UAV a linear controller for hover and cruising flight, and a nonlinear locally input-to-state stable controller in transition flight. When an

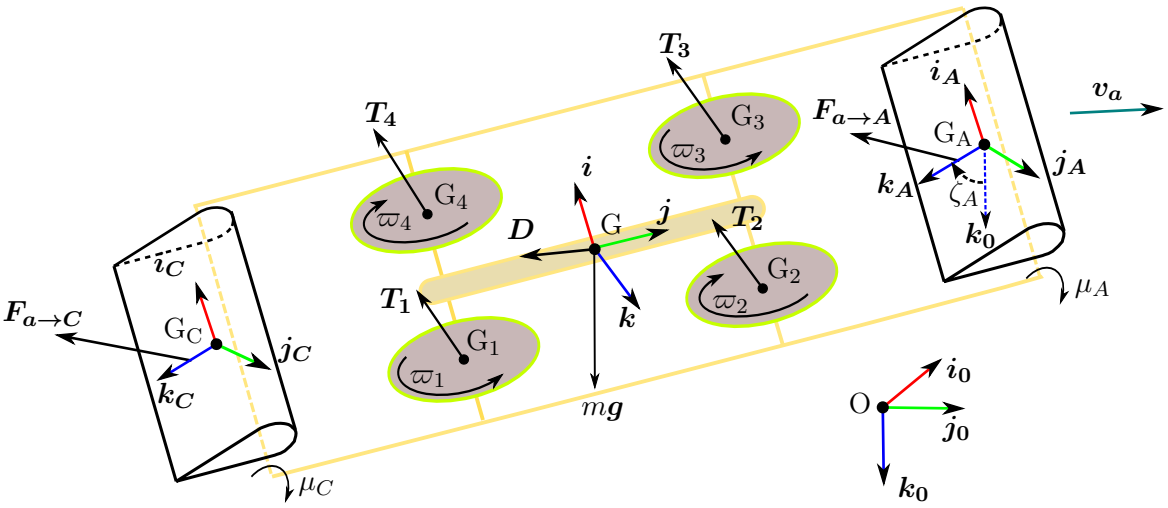

Figure 3.3: 3D convertible UAV model

unexpected state is detected, the recovery controller is triggered towards hover flight, and transition maneuver is re-tried.

The common denominator of these techniques is the "switching" policy between hover and cruise control. However, this policy is local and only suitable to some specific desired trajectories. Recently, [76] performs wind tunnel testing to find the equilibrium states of a tilt-body UAV during the transition flight. Taking advantage of these equilibrium data, a linear fractional representation model is implemented to improve the longitudinal control of the UAV .

Comparing to fixed-wing aircraft and convertible aerial vehicle with rotors and wings fixed rigidly together (e.g. tilt-body or tilt-wing aircraft), convertible vehicle with changeable orientation of rotors w.r.t wings (e.g. tilt-rotor aircraft or our convertible UAV) has the advantage of control flexibility. This point will be elaborated in the control design of our convertible UAV in the next section.

Finally, it is worth pointing out one challenge of controlling convertible UAV: the rotor downwash can have negative impacts on the wings. This problem is even more difficult when the direction of the downwash varies in the transition period for convertible UAVs such as tilt-rotor. We examine this behavior in simulation and propose a simple control design to deal with such challenge in section 3.2.3.

After a brief review of the aerial vehicle control techniques in the literature, the control design of our convertible UAV is presented next.

3.2 Control of Our Convertible UAV

Figure 3.3 shows the diagram of the convertible UAV. Before proceeding into details, some notation is introduced (note that the following notation is consistent with that of chapter 2, see figure 2.1):

- Let $W \in \{A, C\}$, where A stands for the front wing, and C for the back wing. All variables relative to the front and back wing are denoted with A and C respectively, i.e. angles of attack α_A, α_C, angles ζ_A, ζ_C, etc.

- $\mathcal{W} = \{\mathrm{G}_W, \boldsymbol{i_W}, \boldsymbol{j_W}, \boldsymbol{k_W}\}$ denotes the wing frame, with $\boldsymbol{i_W} \equiv \boldsymbol{i}$ and $\boldsymbol{k_W}$ chosen so that the line with direction $\boldsymbol{k_W}$ passing through the wing's CoM $\mathrm{G_W}$ corresponds to the wing's zero-lift line.

  It is assumed that the wing is symmetric (i.e., its shape is symmetric w.r.t. the zero-lift line).

- θ_1, θ_2, θ_3 denote three parametrization Euler angles of $SO(3)$ around axes $\boldsymbol{i_0}, \boldsymbol{j_0}, \boldsymbol{k_0}$ to pass from frame $\mathcal{I}$ to $\mathcal{B}$.

- μ_W denotes the angle from $\boldsymbol{k}$ to $\boldsymbol{k_W}$.

- ζ_W denotes the angle from $\boldsymbol{k_0}$ to $\boldsymbol{k_W}$. Note that $\boldsymbol{k_0}$, $\boldsymbol{k}$, and $\boldsymbol{k_W}$ do not necessarily belong to the same plane. When these three vectors are on the same plane, we have the relation $\zeta_W = \theta_1 + \mu_W$.

- ϖ_i $(i = 1, ..., 4)$ denote the rotational speed of the rotors.

- l denotes the distance between G and any propeller center, i.e. $l = \mathrm{GG_1} = \mathrm{GG_2} = \mathrm{GG_3} = \mathrm{GG_4}$.

- L denotes the distance between either wing pivot axis and G.

- $\boldsymbol{T_i} = -T_i\boldsymbol{k}$ $(i = 1, ..., 4)$ are the thrust forces acting on the propellers. The total thrust force intensity is $T = \sum_{i=1}^{4} T_i$. For simplicity of control analysis, small in-plane drag H-forces considered in chapter 2 are ignored.

- $\boldsymbol{F_{a\to A}}$ and $\boldsymbol{F_{a\to C}}$ denote aerodynamic forces acting on wing A and wing C, respectively. It is assumed that the aerodynamic forces acting on the vehicle's body (i.e. excluding wings and propellers) can be modeled as a parasite drag $\boldsymbol{D}$ acting at G. The total aerodynamic force is then $\boldsymbol{F_a} = \boldsymbol{F_{a\to A}} + \boldsymbol{F_{a\to C}} + \boldsymbol{D}$.

- $\boldsymbol{\Gamma_a}$ denotes the total aerodynamic torque acting on the UAV (except the propellers).

As mentioned in the introduction of this manuscript, the additional DoFs of our convertible UAV permit the decoupling between the wings and body, thus facilitates the control. In light of this advantage, the first objective of the control design is achieving desired angles of attack that may depend on the reference cruising velocity as suggested in chapter 2, in order to minimize the UAV energy consumption. After achieving the first objective, the convertible UAV is considered like a rigid body of quadrotor and two wings. The second objective then is to control this UAV by nonlinear control techniques as described in section 3.1.2, with additional steps to estimate state variables and aerodynamic forces/torques. Before proceeding with the detailed design, it is important to discuss the preliminary assumptions for the control model:

- The principal modes of operation of the UAV are axial flight (including hover) and cruising flight. In these types of movement, the UAV trajectories are essential planar, which implies that the reference velocity vector $\boldsymbol{v_r}$ is also restricted to a plane. Given a general 3D reference velocity and small cross wind disturbance along $\boldsymbol{i}$, the sideslip angle can be controlled to reduce to zero by changing the UAV's yaw angle. The wings will be then facing directly the UAV's directional movement, and the problem is essentially to control a convertible planar UAV. Most of this section is devoted to such 2D case, unless otherwise stated, since this is sufficient to capture the main flight dynamics effects and present the basic control principles.

- We are aware that for VTOL aerial vehicles and especially convertibles, there exist many aerodynamic interference problems, including but not limited to self-induced interference (rotor self-influence, wing self-influence, bluff-body self-influence), downwash influence of propellers on fuselage and wings, and modification of the flow around wings that affect propellers [72]. A detailed treatment of these phenomena, e.g. using the Navier-Stokes equations, would be unrealistic for real-time simulation and control design. We consider in our control design, the seemingly most important interference for our convertible UAV: the propeller downwash influence on wings[1]. For more practical insights on aerodynamic interference on helicopter and tilt-rotor, interested readers can refer to [72].

- We assume that the actuation of the wings' orientation with respect to the UAV's main body can be modeled as a first-order system: $\dot{\mu}_W = u_W$ with $W \in \{A, C\}$.

Taking into account the above objectives and assumptions, the dynamic equations of the system are then given by

$$\left\{\begin{array}{lcl} \dot{x} & = & v \\ m\dot{v} & = & -T\mathcal{R}e_3 + mge_3 + F_a \\ J\dot{\omega} & = & -\omega \times J\omega + \Gamma + \Gamma_a \\ \dot{\mathcal{R}} & = & \mathcal{R}\mathcal{S}(\omega) \\ \dot{\mu}_A & = & u_A \\ \dot{\mu}_C & = & u_C \end{array}\right. \tag{3.16}$$

3.2.1 Control Without Velocity Measurement

Consider the case where we do not have the UAV velocity measurement. Assuming for now that the wings have fixed angles of attack. Detailed description of wing control is presented in section 3.2.1.5. First, we define $\gamma = \mathcal{R}^\top e_3 \in \mathbb{R}^3$ as the gravitational vector's direction in the body frame $\mathcal{B}$.[2] We illustrate the control by the following typical teleoperation case study. Via a joystick, the UAV is given the following references: two components of the attitude reference $\gamma_{r,1}$ and $\gamma_{r,2}$, the vertical reference position $x_{r,3}$, and yaw angular velocity $\omega_{r,3}$. The objective is to design a controller for the UAV to track these references.

3.2.1.1 Equilibrium Existence

Before proceeding to the control design, we consider here the existence of equilibrium of system (3.16). More precisely, with a given UAV orientation (characterized by gravitational vector's direction γ or Euler angle θ) and a given orientation of the wing (characterized by angle α or ζ), can we find a desired UAV velocity v that is an equilibrium solution to system (3.16)? To simplify the exposition, we consider a typical horizontal cruising case with no wind, i.e. $|\boldsymbol{v_a}| = v = v_2$, as shown in figure 3.4. The angle of attack α is kept constant.

[1] Firstly, for quadrotors and our convertible UAV, the fuselage is not directly under the rotor as in the case of helicopter, thus the downwash influence of propellers on the fuselage is negligible. Secondly, in most situations, the speed of airflow generated by the propellers is greater than the air-velocity along the propeller axis generated by the UAV movement. Adding the fact that the sizes of the wings are not too large, the influence of wings on propellers is relatively small. Finally, self-influence interference is very difficult to model. We simply consider them as unknown disturbances with the objective of making the control robust enough to achieve performance insensitivity w.r.t model inaccuracies.

[2] Note the difference between γ the gravitational vector's direction in the body frame and η the thrust vector's direction in the inertial frame defined in section 3.1.2.2.

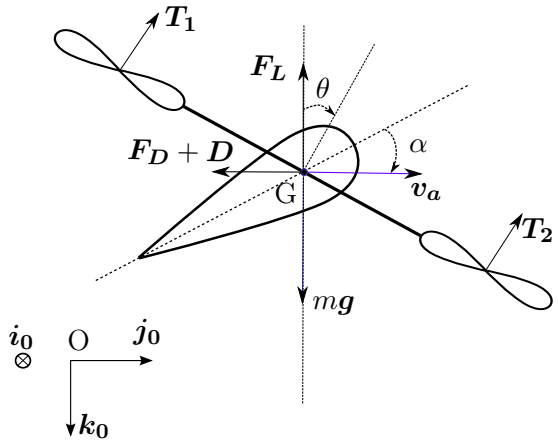

Figure 3.4: Simplified convertible UAV model in cruising flight

With these assumptions, the second equation in system (3.16) becomes

$$m\dot{v} = -T\mathcal{R}(\theta)e_3 + mge_3 - F_L e_3 - (F_D + D)e_2 \tag{3.17}$$

where $e_2 = (0, 1, 0)^\top$ is the second vector of the canonical basis of $\mathbb{R}^3$. From Eq. (2.81) in view of horizontal velocity ($|\boldsymbol{v_a}| = v = v_2$) and constant angle of attack α, the intensities of aerodynamic forces are simplified to:

$$\begin{cases} F_L &= k_a c_L v^2 \\ F_D &= k_a c_D v^2 \\ D &= k_{\text{para}} c_{\text{para}} v^2 \end{cases} \tag{3.18}$$

where c_L and c_D are now constant. Substituting Eq. (3.18) into Eq. (3.17), we obtain the following expressions on horizontal and vertical dynamics:

$$\begin{cases} m\dot{v} &= T\sin\theta - (k_a c_D + k_{\text{para}} c_{\text{para}})v^2 \\ 0 &= mg - T\cos\theta - k_a c_L v^2 \end{cases} \tag{3.19}$$

Substituting T in the second expression into the first one, the horizontal speed differential equation is obtained:

$$\dot{v} = C_0 + C_1 v^2 \tag{3.20}$$

where $C_0 = g\,\tan\theta$ and $C_1 = \dfrac{k_a}{m}(c_L \tan\theta + c_D) + \dfrac{k_{\text{para}} c_{\text{para}}}{m}$.

A solution of the above equation can be found :

$$v = \sqrt{\frac{C_0}{C_1}}\tanh(\sqrt{C_0 C_1}(t - t_0) + C_2)$$

where C_2 is a constant which depends on the initial condition. This solution converges towards an equilibrium $v = \sqrt{\dfrac{C_0}{C_1}}$. We conclude that there exists a velocity v that is an equilibrium solution to system (3.16) given the UAV orientation and wing orientation. With this existence of equilibrium, we can now proceed to detail the hierarchical control, starting with attitude control.

3.2.1.2 Attitude Control

As explained above, the UAV is given reference values $\gamma_{r,1}, \gamma_{r,2}$ for for roll/pitch control. We detail in this section the control law used to stabilize γ to the direction induced by $\gamma_{r,1}, \gamma_{r,2}$. Taking the derivative

$$\dot{\gamma}_{1,2} = \gamma_3 \mathcal{S}_2 \omega_{1,2} - \omega_3 \mathcal{S}_2 \gamma_{1,2} \text{ with } \mathcal{S}_2 = \begin{bmatrix} 0 & -1 \\ 1 & 0 \end{bmatrix}$$

Selecting a controller in the form

$$\omega_{1,2} = \omega_{r,1,2} := k_\gamma S_2(\gamma_{1,2} - \gamma_{r,1,2}) + \frac{\omega_3}{\gamma_3}\gamma_{r,12} \tag{3.21}$$

where k_γ is a gain to be specified, the nonlinear feedback control loop becomes:

$$\dot{\gamma}_{1,2} = -k_\gamma \gamma_3 (\gamma_{1,2} - \gamma_{r,1,2}) - \omega_3 \mathcal{S}_2 (\gamma_{1,2} - \gamma_{r,1,2}).$$

For all the values $\gamma_{r,1,2}$ constant, $\|\gamma_{1,2} - \gamma_{r,1,2}\|^2$ decreases if $k_\gamma \gamma_3 > 0$. From here, it is easy to deduce that the above control expression makes $\gamma = \gamma_r := \left(\gamma_{r,1}, \gamma_{r,2}, \sqrt{1 - \gamma_{r,1}^2 - \gamma_{r,2}^2}\right)$ locally exponentially stable whatever the value of ω_3. When $\omega_3 = 0$, one can even deduce that for any $\gamma_{r,1,2}$ constant with $\|\gamma_{r,1,2}\| < 1$ and any initial condition $\gamma(0)$ with $\gamma_3(0) > 0$, $\gamma(t)$ converges exponentially to $\gamma_r(t)$. Indeed, in this case, trajectories $(\gamma_1(t), \gamma_2(t))$ consist in straight lines between $(\gamma_1(0), \gamma_2(0))$ and $(\gamma_{r,1}(0), \gamma_{r,2}(0))$. Therefore $\|(\gamma_1(t), \gamma_2(t))\| < 1$ for all t and $\gamma_3(t)$ remains strictly positive. This is typically enough in practice to address "normal" flight modes (i.e. UAV's thrust vector and reference thrust direction pointing upward). When ω_3 is not identically zero, the domain of stability is more difficult to characterize.

The advantage of this solution is its large stability domain and the fact that it only relies on accelerometers and gyrometers (i.e., magnetometers measurements, which are not always reliable, are not used here). The control input ω_3 can then be used for yaw control (either with yaw velocity reference values $\omega_{r,3}$ sent by the pilot, or with yaw reference values).

In case a very large stability domain is required (e.g., UAV's thrust vector and reference thrust direction may point downward), one could use the control law

$$\omega = -k_\gamma \left(\gamma \times \gamma_r\right)$$

which ensures convergence of γ to γ_r if at $t = 0$ these two vectors are not opposite (This can be checked by considering the candidate Lyapunov Function $\mathcal{L} = 1 - \gamma^\top \gamma_r$.).

To avoid the division by zero in the control expression (3.21), an alternative solution is

$$\omega_{r,1,2} = k_\gamma \mathcal{S}_2(\gamma_{1,2} - \gamma_{r,1,2}) + \frac{\omega_3 \gamma_3}{\epsilon + \gamma_3^2}\gamma_{r,1,2} \tag{3.22}$$

with $0 < \epsilon \ll 1$.

As for the outer loop of system (3.16), the angular velocity is controlled by the torque Γ. There are many possible solutions, e.g.

$$\Gamma = \omega \times J\omega - \Gamma_a - JK(\omega - \omega_r) \tag{3.23}$$

where K is a constant 3×3 diagonal matrix.

3.2.1.3 Altitude Control

The vertical dynamics is given by:

$$\begin{cases} \dot{x}_3 &= v_3 \\ \dot{v}_3 &= -\frac{T}{m} e_3^\top \mathcal{R} e_3 + g + \frac{F_{a,3}}{m} \\ &= -\frac{T}{m}\gamma_3 + g + \frac{F_{a,3}}{m} \end{cases} \tag{3.24}$$

The above system suggests the following simple control:

$$T = \frac{m}{\gamma_3}\left[g + \frac{F_{a,3}}{m} + k_{v,3}v_3 + k_{p,3}(x_3 - x_{r,3})\right] \tag{3.25}$$

One then obtains the closed loop system:

$$\begin{cases} \dot{x}_3 &= v_3 \\ \dot{v}_3 &= -k_{v,3}v_3 - k_{p,3}(x_3 - x_{r,3}) \end{cases} \tag{3.26}$$

whose stability is ensured given $k_{v,3} > 0$ and $k_{p,3} > 0$. Again, in order to avoid division by zero in (3.25), an alternative solution is:

$$T = \frac{m\gamma_3}{\epsilon + \gamma_3^2}\left[g + \frac{F_{a,3}}{m} + k_{v,3}v_3 + k_{p,3}(x_3 - x_{r,3})\right] \tag{3.27}$$

with $0 < \epsilon \ll 1$.

3.2.1.4 Control allocation

In this section, we recall the procedure [77] to compute the reference propeller rotational speeds $\varpi_{r,1}, \varpi_{r,2}, \varpi_{r,3}$, and $\varpi_{r,4}$ as a function of control vector $[T, \Gamma]^\top$ where T and Γ are given by Eq. (3.27) and Eq. (3.23), respectively.

Modeling for multirotors often relates each propeller thrust force T_i and torque Q_i with its rotational speed ϖ_i by two simple constants κ_T and κ_Q:

$$\begin{cases} T_i &= \kappa_T \varpi_i^2 \\ Q_i &= \kappa_Q \varpi_i^2. \end{cases} \tag{3.28}$$

The constants κ_T and κ_Q are simpler representations of the thrust coefficient C_T defined in Eq. (2.65) and the torque coefficient C_Q introduced in Eq. (2.67), respectively. Refer to the end of appendix A for more detailed relations of these coefficients.

The relation between the wrench vector and the propeller rotational speeds can be easily obtained from examining the forces and torques acting on the quadrotor main body in figure 3.3:

$$\begin{bmatrix} T \\ \Gamma \end{bmatrix} = \begin{bmatrix} \kappa_T & \kappa_T & \kappa_T & \kappa_T \\ \kappa_T l/\sqrt{2} & \kappa_T l/\sqrt{2} & -\kappa_T l/\sqrt{2} & -\kappa_T l/\sqrt{2} \\ \kappa_T l/\sqrt{2} & -\kappa_T l/\sqrt{2} & -\kappa_T l/\sqrt{2} & \kappa_T l/\sqrt{2} \\ -\kappa_Q & \kappa_Q & -\kappa_Q & \kappa_Q \end{bmatrix} \begin{bmatrix} \varpi_1^2 \\ \varpi_2^2 \\ \varpi_3^2 \\ \varpi_4^2 \end{bmatrix} \tag{3.29}$$

Finally, it is possible to inverse the above relation to determine the reference $\varpi_{r,1}, \varpi_{r,2}, \varpi_{r,3}$, and $\varpi_{r,4}$ from $[T, \Gamma]^\top$

$$\begin{bmatrix} \varpi_{r,1}^2 \\ \varpi_{r,2}^2 \\ \varpi_{r,3}^2 \\ \varpi_{r,4}^2 \end{bmatrix} = \frac{1}{4\kappa_T} \begin{bmatrix} 1 & \sqrt{2}/l & \sqrt{2}/l & -\kappa_T/\kappa_Q \\ 1 & \sqrt{2}/l & -\sqrt{2}/l & \kappa_T/\kappa_Q \\ 1 & -\sqrt{2}/l & -\sqrt{2}/l & -\kappa_T/\kappa_Q \\ 1 & -\sqrt{2}/l & \sqrt{2}/l & \kappa_T/\kappa_Q \end{bmatrix} \begin{bmatrix} T \\ \Gamma \end{bmatrix} \tag{3.30}$$

3.2.1.5 Control design for the wings

Up to now, the controls u_A and u_C for the wings' pitch angle have not been specified. A simple solution would consist in maintaining the wings fixed with respect to the UAV's main body, i.e. μ_A and μ_C constant. There are two reasons why this solution does not seem very appropriate. First, we have seen in chapter 2 that from an energy point of view, the optimal pitch angle of the wing(s) much varies with the velocity. Thus, keeping μ_A and μ_C constant would be inefficient in most situations. Then, from a control point of view, keeping μ_A and μ_C constant would mean that the aerodynamic force F_a varies with the UAV's main body attitude $\mathcal{R}$. For example, in forward flight, increasing the UAV's main body pitch angle would increase by the same amount the wing pitch angle, and thus reduce angle of attack and lift force. In other words, since F_a now varies with $\mathcal{R}$, the second equality in (3.58) becomes an implicit equation with no guarantee of existence/unicity of the solution. This problem has already been evoked in section 3.1.2 and is studied in more details in [18].

To fully benefit from the additional degrees of freedom given by the wings' actuation, we simply propose to control the wings' pitch angles ζ_A, ζ_C to desired values $\zeta_{r,A}$, $\zeta_{r,C}$. To simplify this current presentation, the three vectors $\boldsymbol{k_0}$, $\boldsymbol{k}$, and $\boldsymbol{k_W}$ are assumed to be on the same plane. One has for $W \in \{A, C\}$:

$$\zeta_W = \theta_1 + \mu_W$$

Thus $\tilde{\zeta}_W := \zeta_W - \zeta_{r,W}$ satisfies:

$$\dot{\tilde{\zeta}}_W = \dot{\zeta}_W = \omega_1 + \dot{\mu}_W = \omega_1 + u_W$$

Setting the control

$$u_W = -\omega_1 - k_W \tilde{\zeta}_W$$

implies that

$$\dot{\tilde{\zeta}}_W = -k_W \, \tilde{\zeta}_W$$

Choosing $k_W > 0$ thus ensures the exponential convergence of ζ_W to the desired value $\zeta_{r,W}$. In this way the wings' pitch angles are controlled to their desired values and aerodynamic forces on the wings do not depend on the UAV's main body attitude since the wings' pitch angle are controlled independently. We also note that this control expression only requires the measurement of ω_1 and ζ_W. In practice, the first one is given by gyrometers of an IMU while ζ_W is given by the sum of the UAV's pitch angle and the angle μ_W.

3.2.1.6 Estimation

The above control implementation requires the knowledge of the UAV state variables, aerodynamic forces and torque. Before proceeding to describe the estimation process, we present the sensors that are available on the IMU unit (The detailed descriptions of these sensors are available in section 4.1.1.):

- a barometer to measure the altitude and the vertical speed (by derivation/filtering) in the inertial frame $\mathcal{I}$,
- a three-axis accelerometer to measure the specific acceleration $a_s = \mathcal{R}^\top(\dot{v} - ge_3)$ in the body frame $\mathcal{B}$,
- a three-axis gyroscope to measure the rotational velocity ω in the body frame $\mathcal{B}$,

- a three-axis magnetometer to measure UAV orientation w.r.t the Earth's magnetic field (These magnetometer measurements might be utilized by sensor fusion to improve the attitude measurements, but they are usually not required for close-range teleoperation.),

After low-level data treatment, the angular speed estimation $\hat{\omega}$, the specific acceleration estimation $\hat{a}_s$, the altitude estimation $\hat{x}_3$, and the vertical speed estimation $\hat{v}_3$ are obtained.

a) Estimation of orientation vector

The standard approach to estimate a VTOL UAV attitude consists in fusing gyrometers and accelerometers/magnetometers data, where accelerometers are used as inclinometers under the hypothesis that the linear acceleration is zero. In this case indeed, we have:

$$\hat{a}_s = a_s = -g\mathcal{R}^\top e_3 = -g\gamma. \tag{3.31}$$

Then, the orientation vector γ can be estimated by the following:

$$\begin{cases} \dot{\hat{\gamma}} = \mathcal{S}(\hat{\gamma})(\hat{\omega} - k_{\text{est},\gamma}(\hat{a}_s \times \hat{\gamma})) \\ \hat{\gamma}(0) = -\hat{a}_s(0)/g \end{cases} \tag{3.32}$$

where gain $k_{\text{est},\gamma} > 0$. Substituting Eq. (3.31) into Eq. (3.32) yields:

$$\dot{\hat{\gamma}} = \mathcal{S}(\hat{\gamma})(\hat{\omega} - k_{\text{est},\gamma} g(\hat{\gamma} \times \gamma))$$

Assuming that $\omega = \hat{\omega}$, stability of the above observer can be obtained by considering the Lyapunov function $\mathcal{L} = 1 - \gamma^\top \hat{\gamma}$ whose derivative satisfies:

$$\dot{\mathcal{L}} = -k_{\text{est},\gamma} g \|\hat{\gamma} \times \gamma\|^2$$

where we deduce the convergence of $\hat{\gamma}$ to γ if initially these two vectors are not opposite. In practice, this observer is discretized and we must guarantee that the norm of $\hat{\gamma}$ is always 1. Besides, the gain $k_{\text{est},\gamma}$ is chosen to be small (to trust the gyroscope measurements more than the accelerometer ones). When needed, the information on γ is combined with the magnetometer information to derive an estimation of $\mathcal{R}$. This is achieved through a filtering procedure with gyros, such as the complementary filter [78,79]. Since we are here only interested in the estimation of γ, the (not always reliable) magnetometer information will not be used.

Using accelerometers as inclinometers is a common practice with UAVs. However, it relies on the assumption that the vehicle's linear acceleration is negligeable, which is not always the case. In a recent work [47], the aerodynamics of a quadrotor are used to specify what is really measured by accelerometers. Recalling that the accelerometer measures $a_s = \mathcal{R}^\top(\dot{v} - ge_3)$. From the second equation of system (3.16), a_s can be rewritten as:

$$a_s = -\frac{Te_3}{m} + \mathcal{R}^\top \frac{F_a}{m}. \tag{3.33}$$

The first two components of a_s are then:

$$\begin{cases} a_{s,1} = e_1^\top \mathcal{R}^\top \dfrac{F_a}{m} \\ a_{s,2} = e_2^\top \mathcal{R}^\top \dfrac{F_a}{m} \end{cases} \tag{3.34}$$

We can clearly observe from here that the accelerometer gives the measurements of aerodynamic forces. Looking closer at the aerodynamics of propellers, it can be shown that at low velocities, accelerometers provide a measurement of the horizontal linear velocity expressed in the body frame (see also Eq. (2.64) and the remark thereafter in chapter 2 of this thesis). This is used in [47] to propose a new velocity/attitude observer with improved performance. That solution has not been tested on our platform. Indeed, preliminary analysis of accelerometer measurements on the low-cost IMU used on our platform has shown high noise level, which seems to make it difficult to recover significant velocity information.

b) Estimation of vertical position, velocity, and aerodynamic force

The vertical dynamics in (3.24) suggests the following observer:

$$\left\{\begin{array}{lcl} \dot{\hat{x}}_3 &=& \hat{v}_3 - k_{\mathrm{est,x}}(\hat{x}_3 - x_3) \\ \dot{\hat{v}}_3 &=& -\dfrac{T}{m}\gamma_3 + g + \dfrac{\hat{F}_{a,3}}{m} - k_{\mathrm{est,v}}(\hat{x}_3 - x_3) \\ \dot{\hat{F}}_{a,3} &=& -mk_{\mathrm{est,F}}(\hat{x}_3 - x_3) \end{array}\right. \tag{3.35}$$

where $k_{\mathrm{est},*}$ denote positive gains. Denoting $\tilde{x} = \hat{x} - x$, $\tilde{v} = \hat{v} - v$, and $\tilde{F}_{a,3} = \hat{F}_{a,3} - F_{a,3}$ the estimation errors, one deduces from (3.24) and (3.35) that:

$$\left\{\begin{array}{lcl} \dot{\tilde{x}}_3 &=& \tilde{v}_3 - k_{\mathrm{est,x}}\tilde{x}_3 \\ \dot{\tilde{v}}_3 &=& \dfrac{\tilde{F}_{a,3}}{m} - k_{\mathrm{est,v}}\tilde{x}_3 \\ \dot{\tilde{F}}_{a,3} &=& -mk_{\mathrm{est,F}}\tilde{x}_3 - \dot{F}_{a,3} \end{array}\right. \tag{3.36}$$

This is the dynamics of a Hurwitz-stable linear system perturbed by the additive term $\dot{\tilde{F}}_{a,3}$. The estimator provides reliable estimate of $F_{a,3}$ provided that this term does not vary too fast. We consider now the rotation dynamics:

$$J\dot{\omega} = -\omega \times J\omega + \Gamma + \Gamma_a \tag{3.37}$$

The above system suggests the following classic observer:

$$\left\{\begin{array}{lcl} J\dot{\hat{\omega}} &=& -\omega \times J\omega + \Gamma + \hat{\Gamma}_a - Jk_{\mathrm{est},\omega}(\hat{\omega} - \omega) \\ \dot{\hat{\Gamma}}_a &=& -Jk_{\mathrm{est},\Gamma}(\hat{\omega} - \omega) \end{array}\right. \tag{3.38}$$

Denoting $\tilde{\omega} = \hat{\omega} - \omega$ and $\tilde{\Gamma}_a = \hat{\Gamma}_a - \Gamma_a$ the estimation errors, (3.37) and (3.38) yield:

$$\left\{\begin{array}{lcl} J\dot{\tilde{\omega}} &=& \tilde{\Gamma}_a - Jk_{\mathrm{est},\omega}\tilde{\omega} \\ \dot{\tilde{\Gamma}}_a &=& -Jk_{\mathrm{est},\Gamma}\tilde{\omega} - \dot{\Gamma}_a \end{array}\right. \tag{3.39}$$

The estimator provides reliable estimate of Γ_a provided that the aerodynamic torque does not vary too quickly.

3.2.1.7 Simulation

The parameters for simulated model are detailed in appendix C. Simulation is performed with a reference altitude of 5 m, a reference pitch angle of 10° around axis $\boldsymbol{i}$, and the wings are given

constant reference angles 10° w.r.t the ground (i.e. $\zeta_{r,A} = \zeta_{r,C} = 80°$). The reference yaw angular velocity $\omega_{r,3}$ is set to zero. No wind is blowing.

The control parameters are: $k_\gamma = 2$, $K = \begin{bmatrix} 6 & 0 & 0 \\ 0 & 6 & 0 \\ 0 & 0 & 6 \end{bmatrix}$, $k_{p,3} = 0.36$, $k_{v,3} = 3.6$, and $\epsilon = 0.001$. The control gains for the wings are: $k_A = k_C = 10.2$. The estimation gains are: $k_{\text{est},\gamma} = 0.002$, $k_{\text{est,x}} = 4$, $k_{\text{est,v}} = 3.2$, $k_{\text{est,F}} = 4$, $k_{\text{est},\omega} = 9$, and $k_{\text{est},\Gamma} = 4.8$.

The results of the simulation are shown in figure 3.5. The UAV is able to track well the reference altitude, with small overshoot, fast response time, and very small steady-state error, as proven in figure 3.5(b). The outer loop control for the attitude response is even faster as expected, with just a few seconds for the UAV to achieve its desired pitch angle of (figure 3.5(c)). This control strategy is successful thanks to quite accurate estimation of the vertical aerodynamic force, as depicted in figure 3.5(d).[3]

Next, we perform the simulation in the presence of wind. The UAV is given the same references as in the previous case. However, from $t = 40$ s, the UAV is perturbed by wind with constant components $v_{\text{wind}} = [0, 3, 1.5]^\top$ as in figure 3.6. The wind varies strongly in both magnitude and direction. Figure 3.7 illustrates the attitude response. In general, the UAV is able to resist the wind disturbance. In particular, the horizontal component of the wind (e.g. from $t = 70$ s to $t = 120$ s) does not affect the system so much, since the angles of attack only vary slightly. By contrast, the vertical component of the wind causes large errors in altitude, up to more than 4 m. In addition, the UAV's pitch angle oscillates slightly, as proven by figure 3.8. The biggest problem is that the wind reduces the angles of attack of the wings to below zero (figure 3.9), effectively decreases the lift force, and increases the power consumption (figure 3.10).

3.2.2 Control Without Velocity Measurement Based on a Modified Mechanical Design

From the previous section, we have seen that unknown aerodynamic disturbances can have negative impacts on system performance. In particular, there might be strong and rapid variations of the aerodynamic forces and torques acting on the vehicle. These forces and torques must be finely controlled in order to avoid flight instability and inefficient configurations. The main issue here is the control of the aerodynamic forces acting on the wings, which typically relies on the control of the wing's angle of attack in terms of the air-velocity magnitude, and therefore on air-velocity measurements. For conventional airplanes flying at high speed, the air-velocity vector can be accurately measured via different devices such as classical Pitot tubes or vanes (See, e.g. [80]), or more recent flush air-data sensing (FADS) systems [81, 82]. Small VTOL UAVs typically operate at low speed (less than 20 m/s), however, and due to their sensitivity to wind they can be subjected to fast and large variations of the angle of attack. Obtaining precise and high-frequency measurements of the air-velocity vector in such conditions is difficult. In this section, we propose a strategy to efficiently control the wing's angle of attack. The main point is that air-velocity measurements are not needed to implement this feedback control strategy. In fact, like in the case of the previous control design, the control can be implemented with IMU/barometer measurements only. The proposed solution relies on a modified mechanical design and the torque induced by aerodynamic forces. The spring-damper like controller with variable stiffness ensures the convergence of the angle of attack to a desired value. This value may depend on the (non-measured) air-velocity magnitude. A stability analysis of the proposed

[3] In the simulation, the values of $F_{a,3}$ are from system dynamics whereas the values of $\hat{F}_{a,3}$ are estimated from vertical position as in (3.35).

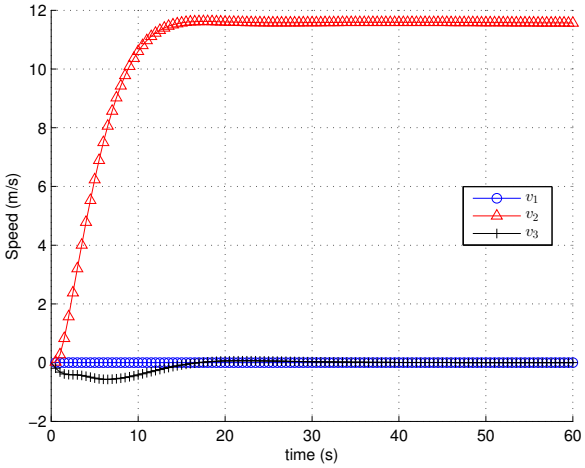

(a) UAV velocity components

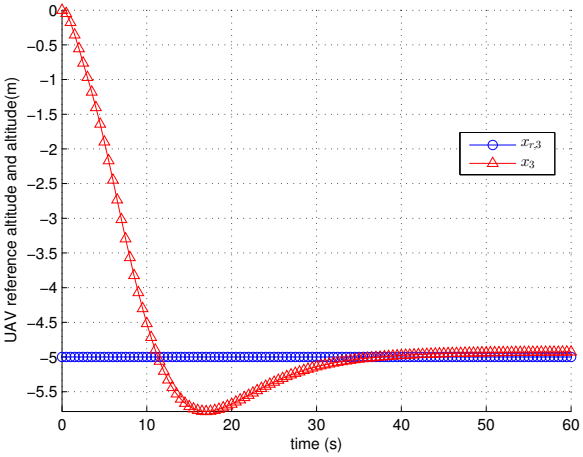

(b) Reference altitude versus UAV altitude

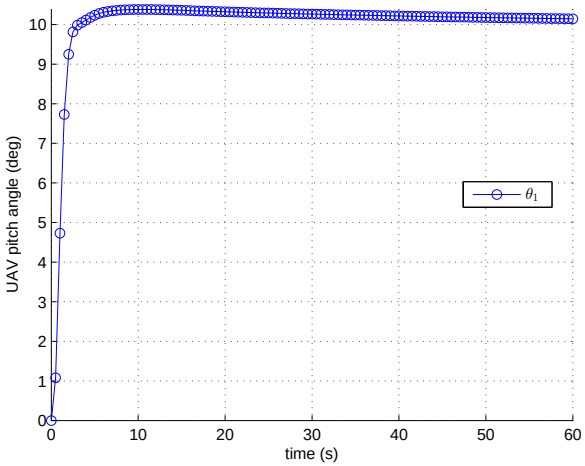

(c) UAV's pitch angle

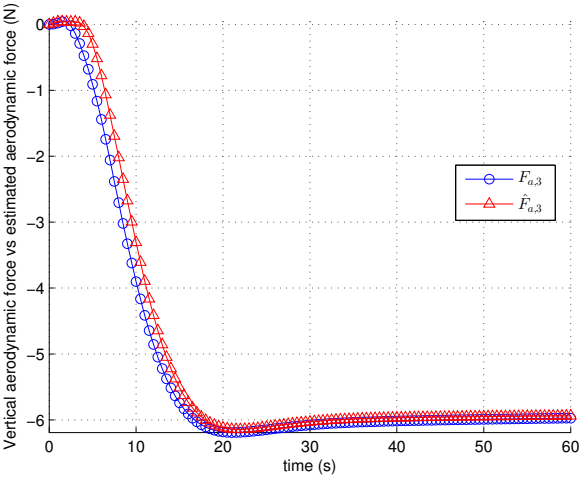

(d) Total vertical aerodynamic force on wings versus its estimated value

Figure 3.5: Teleoperation simulation with attitude and altitude control

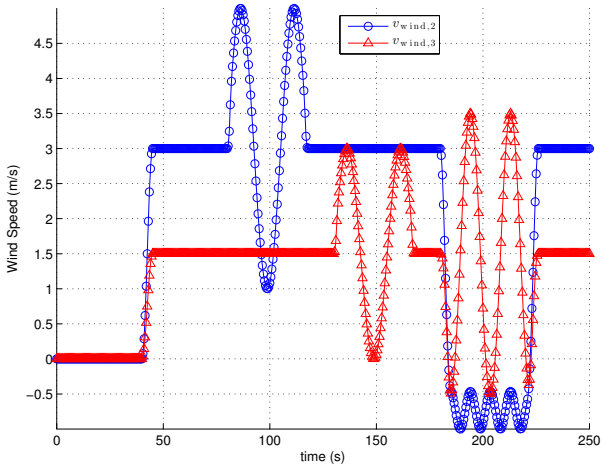

Figure 3.6: Wind speed

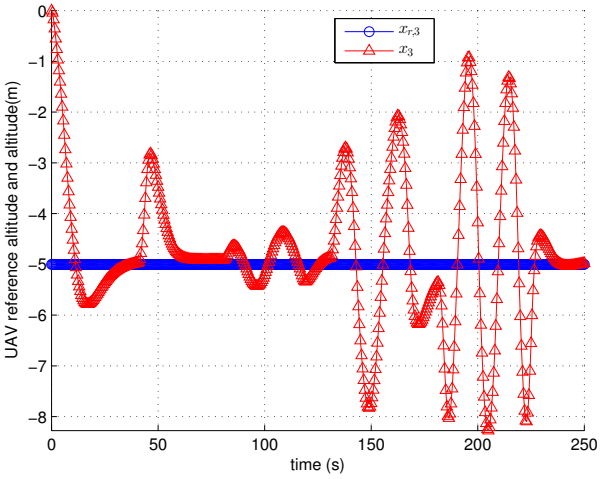

Figure 3.7: Reference altitude versus UAV altitude (teleoperation with wind simulation)

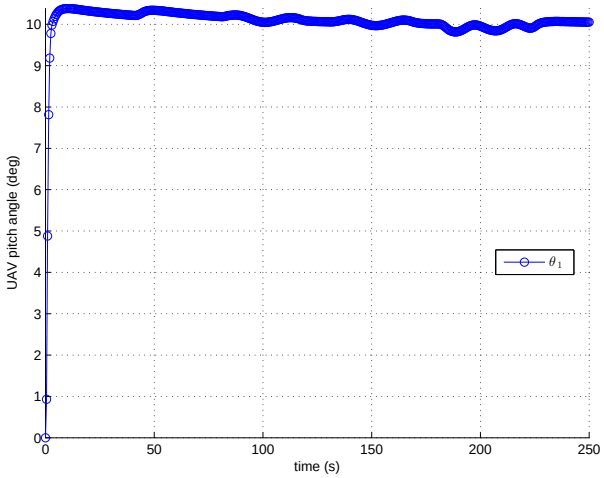

Figure 3.8: UAV's pitch angle (teleoperation with wind simulation)

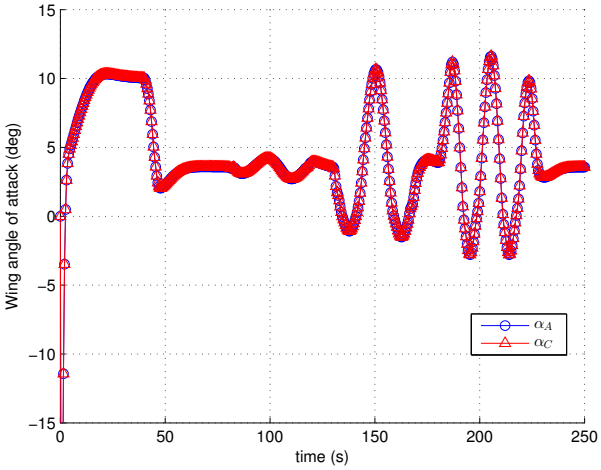

Figure 3.9: Angles of attack of the wings (teleoperation with wind simulation)

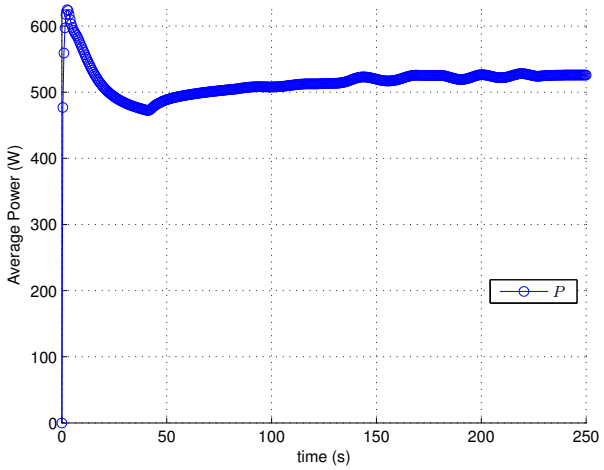

Figure 3.10: The average power consumption since $t = 0$ (teleoperation with wind simulation)

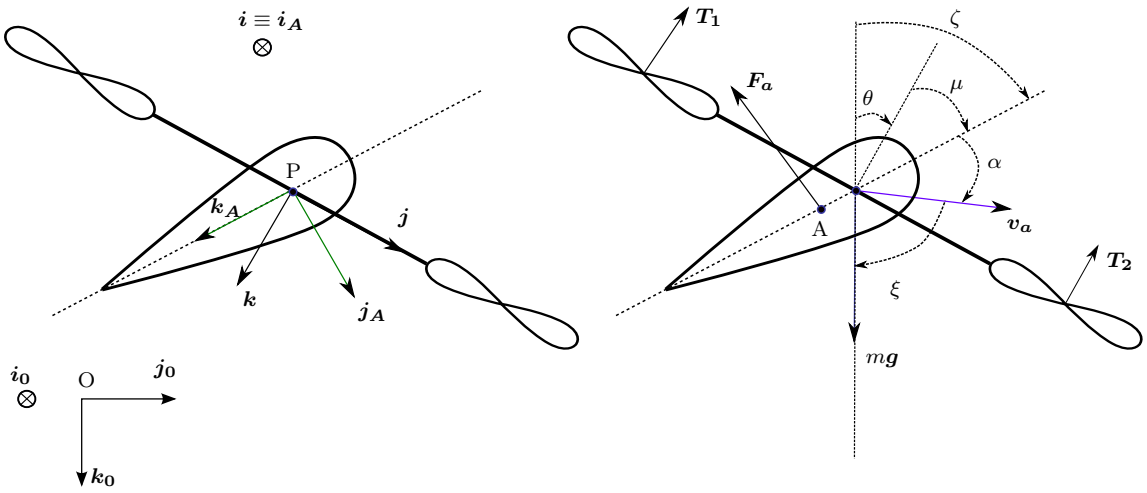

Figure 3.11: 2D simplified model

feedback controller is provided, showing a large convergence domain of the angle of attack to the desired value.

To keep the current exposition simple without impairing its generality too much, the control approach will be discussed on the basis of the simplified model with only one wing and two propellers (figure 3.11). We assume that P $\equiv$ G_B, i.e. the pivot point is also the CoM of the vehicle's main body, and that the wing's CoM G_A is close enough to P so that the effect of a possible offset on the linear motion dynamics can be neglected. The 2D model here considered is more realistic than the model in figure 3.4. Indeed, the pivot point P can be different from the CoM G_A of the wing. In addition, the aerodynamic force acting on the wing at a point A which typically does not coincide with neither P nor G_A (figure 3.12).

Let $\xi = \xi(\boldsymbol{v_a})$ denotes the angle from $\boldsymbol{v_a}$ to $\boldsymbol{k_0}$. Recall the linear motion equation:

$$m\dot{v} = -T\mathcal{R}(\theta)e_3 + mge_3 + F_a \tag{3.40}$$

Although $v \in \mathbb{R}^3$, since we consider here only the planar case, we are only interested in the components v_2 and v_3 of v. In other words, the dynamics of v_1 is unimportant. The torque

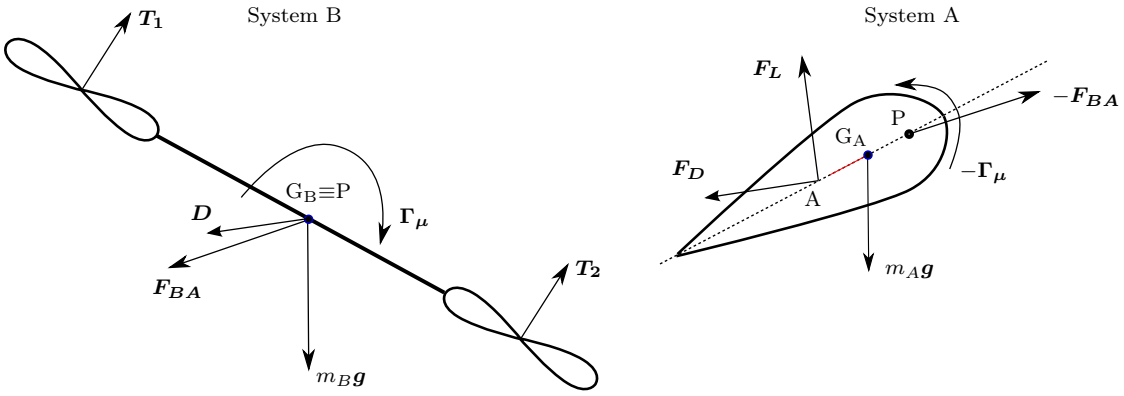

Figure 3.12: The model decoupled into the main body and the wing

around P acting on the main body consists of the torque induced by the propellers and the torque $\boldsymbol{\Gamma_\mu} = \Gamma_\mu \boldsymbol{i}$ induced by the wing. By applying the Euler theorem of momentum, with the assumption that aerodynamic forces acting on the vehicle's main body do not generate torque, the following equation of angular motion is obtained:

$$J_B \ddot{\theta} = \Gamma + \Gamma_\mu \tag{3.41}$$

with J_B the main body's inertia and $\Gamma = (T_1 - T_2)l$ where l is the distance between UAV's CoM and either propeller's center. The torque around P acting on the wing consists of the torque induced by gravity, the torque $-\boldsymbol{\Gamma_\mu}$ induced by the main body, and the aerodynamic torque $\boldsymbol{\Gamma_a}$ induced by the aerodynamic force $\boldsymbol{F_a}$. This yields the following equation:

$$J_A \ddot{\zeta} = -\Gamma_\mu - m_A g d_A \sin\zeta + \Gamma_a \tag{3.42}$$

with J_A the wing's inertia, m_A the wing's mass, and d_A the distance between P and G_A. Gathering Eq. (3.40), (3.41), (3.42) yields the following control model:

$$\begin{cases} m\dot{v} &= -T\mathcal{R}(\theta)e_3 + mge_3 + F_a \\ J_B\ddot{\theta} &= \Gamma + \Gamma_\mu \\ J_A\ddot{\zeta} &= -\Gamma_\mu - m_A g d_A \sin\zeta + \Gamma_a \end{cases} \tag{3.43}$$

with the control inputs T, Γ, and Γ_μ. The control Γ_μ results from the actuation of the joint between the main body and the wing.

3.2.2.1 Aerodynamic forces and torque

The aerodynamic force $\boldsymbol{F_a}$ is composed of three parts: lift force $\boldsymbol{F_L}$ and drag force $\boldsymbol{F_D}$ acting on the wing, and a parasite drag $\boldsymbol{D}$ (assuming no parasite lift) acting on the vehicle's main body, i.e.

$$\boldsymbol{F_a} = \boldsymbol{F_L} + \boldsymbol{F_D} + \boldsymbol{D}$$

Recall from section 2.3 that the lift and drag forces are written as

$$\begin{cases} \boldsymbol{F_L} &= k_a |\boldsymbol{v_a}| c_L(\alpha, \mathrm{Re}) \boldsymbol{v_a^\perp} \\ \boldsymbol{F_D} &= -k_a |\boldsymbol{v_a}| c_D(\alpha, \mathrm{Re}) \boldsymbol{v_a} \end{cases} \tag{3.44}$$

and

$$\boldsymbol{D} = -k_{\mathrm{para}} c_{\mathrm{para}} |\boldsymbol{v_a}| \boldsymbol{v_a}$$

with the angle of attack α from Eq. (2.78) rewritten as

$$\alpha = \pi - \theta - \mu - \xi(\boldsymbol{v_a}) = \pi - \zeta - \xi(\boldsymbol{v_a}) \tag{3.45}$$

To lighten the notation, the Reynolds number dependence will often be omitted, i.e., we often simply write $c_L(\alpha)$ and $c_D(\alpha)$.

To specify the aerodynamic torque $\boldsymbol{\Gamma_a}$ induced by the aerodynamic force $\boldsymbol{F}_a$, first recall the assumption that the parasite drag is acting at P, and thus it does not generate any torque around P. The aerodynamic forces $\boldsymbol{F_L}$ and $\boldsymbol{F_D}$ act at the center of pressure, here denoted as A. For a symmetric airfoil, the center of pressure is located on the zero-lift line and its distance w.r.t. the leading edge is constant over a wide range of α and Reynolds number [48, Sec. 4.7]. Although the present approach can be extended to the case when the center of pressure location is not constant, we will thus assume for simplicity that $\mathbf{PA} = d\boldsymbol{k_A}$ with d a constant scalar. The aerodynamic torque around P is thus

$$\boldsymbol{\Gamma_a} = d\boldsymbol{k_A} \times (\boldsymbol{F_L} + \boldsymbol{F_D}) = \Gamma_a \boldsymbol{i}_0$$

and we deduce from Eq. (3.44) that

$$\Gamma_a(v_a, \alpha) = dk_a |v_a|^2 (c_D \sin\alpha + c_L \cos\alpha) \tag{3.46}$$

We rewrite the previous equation as

$$\Gamma_a(v_a, \alpha) = |v_a|^2 h(\alpha)\, \sin\alpha \tag{3.47}$$

where

$$h(\alpha) = dk_a\, (c_D(\alpha) + c_L(\alpha)\cot(\alpha)) \tag{3.48}$$

For a symmetric airfoil the term $c_L(\alpha)\cot(\alpha)$ is typically well defined everywhere (it is defined by continuity at $\alpha = k\pi$ provided $(\partial c_L)/(\partial\alpha)(k\pi) \neq 0$) and strictly positive. Since the aerodynamic drag coefficient c_D also shares these properties, we conclude that h is well defined and strictly positive everywhere. Note that considering a distance d which varies with α does not change the fact that h is strictly positive if $d(\alpha)$ itself remains strictly positive, i.e. if the center of pressure is "below" the pivot point P.

We proceed with the detailed control strategy. The aerodynamic force and torque depend on the air-velocity vector $\boldsymbol{v_a}$ and the angle of attack α. From (3.45), α is a function of $\boldsymbol{v_a}$ and ζ. Therefore, the control system (3.43) can be written as

$$\left\{ \begin{array}{rcl} \dot{v} &=& ge_3 - u_1 \mathcal{R}(\theta) e_3 + \bar{F}_a(v_a, \zeta) \\ \ddot{\theta} &=& u_2 \\ \ddot{\zeta} &=& u_3 + \bar{\Gamma}_a(v_a, \zeta) \end{array} \right. \tag{3.49}$$

with

$$u_1 = \frac{T}{m},\ u_2 = \frac{\Gamma + \Gamma_\mu}{J_B},\ u_3 = -\frac{\Gamma_\mu + m_A g d_A \sin\zeta}{J_A}$$

and

$$\begin{array}{rcl} \bar{F}_a(v_a, \zeta) &=& \dfrac{F_a(v_a, \alpha)}{m} = \dfrac{F_a(v_a, \pi - \zeta - \xi(v_a))}{m} \\ \bar{\Gamma}_a(v_a, \zeta) &=& \dfrac{\Gamma_a(v_a, \alpha)}{J_A} = \dfrac{\Gamma_a(v_a, \pi - \zeta - \xi(v_a))}{J_A} \end{array} \tag{3.50}$$

The mapping $(T, \Gamma, \Gamma_\mu) \longmapsto (u_1, u_2, u_3)$ is bijective for any ζ. Therefore, one can view u_1, u_2, u_3 as the control inputs.

System (3.49) suggests the following control strategy. Firstly, u_3 is used to control ζ so as to achieve a satisfactory angle of attack, e.g., a wing configuration that ensures a low energy consumption of the UAV. Secondly, the (normalized) thrust input u_1 and angular velocity control u_2 can be used to monitor the UAV's attitude θ and altitude x_3, similar to section 3.2.1, with $\bar{F}_a(v_a, \zeta)$ viewed as an external force that needs to be compensated via the propeller thrust.

3.2.2.2 Control of the wing's pitch angle

When the air-velocity vector $\boldsymbol{v_a}$ is known, it is straightforward to control ζ so as to achieve a desired angle of attack. However, obtaining a precise measure of $\boldsymbol{v_a}$ in real-time and at high frequency is very difficult, especially for small UAVs. The objective of this section is to propose a control solution that does not rely on such measures. While this approach cannot compete with the case when high-quality measure/estimates of v_a were available, we will show that it can still provide interesting results. Throughout this section it is assumed that ζ is measured or estimated. Since $\zeta = \theta + \mu$, it can be computed from an estimate of θ (typically obtained via an IMU), and a measure of μ.

It follows from (3.47), (3.49), and (3.50) that

$$\ddot{\zeta} = u_3 + \frac{|v_a|^2 h(\alpha) \sin \alpha}{J_A} \tag{3.51}$$

Assume that a model of a "desired" angle of attack as a function of the air-velocity is available, i.e.

$$\alpha^*(v_a) = f_0(v_a)$$

For example, such a desired angle of attack could be the one that minimizes the energy consumption of the UAV for a given air-velocity (see chapter 2). The vector v_a is fully determined by its amplitude and direction, so that we can rewrite the previous equation as

$$\alpha^*(v_a) = f(|v_a|, \xi(v_a))$$

Since the UAV has a symmetric geometry (i.e., when $\theta = \mu = 0$, the vehicle's shape is symmetric w.r.t. $\boldsymbol{k}$-axis), a natural requirement is that

$$f(\tau, -\xi) = -f(\tau, \xi) \tag{3.52}$$

For example, in the absence of wind, if at a certain speed the desired angle of attack when flying in the direction of $\boldsymbol{j_0}$ is $\alpha = \alpha^*$, the desired angle of attack when flying in the direction of $-\boldsymbol{j_0}$ at the same speed should be $\alpha = -\alpha^*$. We further specify the class of functions f via the following assumption.

Assumption 1 *The function f is of the form*

$$\alpha^*(v_a) = f(|v_a|, \xi(v_a)) = \operatorname{acot}\left(\frac{g_1(|v_a|^2)}{g_2(\xi(v_a))}\right) \tag{3.53}$$

where the functions g_1, g_2 satisfy the following properties:

1. *$g_1 : \mathbb{R} \longrightarrow \mathbb{R}$ is continuous, strictly increasing, odd (i.e., $g_1(-\tau) = -g_1(\tau)$), and*

$$\lim_{\tau \to +\infty} \frac{g_1(\tau)}{\tau} = b > 0 \tag{3.54}$$

2. g_2 is odd and $g_2(\xi) > 0 \; \forall \xi \in (0, \pi)$.

Let us comment this assumption. First, $g_1(\tau)$ tends to $+\infty$ as τ tends to $+\infty$. Therefore, α^* tends to zero as $|v_a|$ tends to infinity. This is a desired property in practice because when the air-velocity amplitude gets large, the only way to keep aerodynamic forces bounded is to impose a small angle of attack. Then, the function g_2 is introduced to model possible dependence of α^* on the air-velocity direction. From the positivity of $g_1(|v_a|^2)$ and Condition 2, note that (3.52) is satisfied since acot is an odd function. Note also that if g_2 is continuous at $\xi = 0, \pi$, then it vanishes at these points. The function f is still defined by continuity, however, provided that $v_a \neq 0$. When $v_a = 0$, the definition of the angle of attack does not make sense anyway.

We can now state the main result of this section.

Proposition 1 *Define two functions k_p, k_v as follows:*

$$\begin{array}{rcl} k_p(\zeta, \xi) & = & g_1^{-1}\left(g_2(\xi)\cot(\pi - \zeta - \xi)\right) h(\pi - \zeta - \xi)\sin(\pi - \zeta - \xi) \\ k_v(\zeta, \xi) & = & 2\eta_0\sqrt{|k_p(\zeta, \xi)|} \end{array} \tag{3.55}$$

with $\eta_0 > 0$. Suppose that Assumption 1 is satisfied and that v_a is constant with $v_{a,2} \neq 0$. Then, the control law

$$u_3 = -\frac{k_p(\zeta, \xi(v_a)) + k_v(\zeta, \xi(v_a))\dot{\zeta}}{J_A} \tag{3.56}$$

ensures the asymptotic stability of $\alpha = \alpha^*$ with convergence domain $(\alpha^* - \pi, \alpha^* + \pi)$.

The proof of this proposition is given in appendix E.

This proposition calls for remarks.

First, u_3 can be viewed as a nonlinear spring-damper type feedback control. The main idea is that the spring-like feedback term k_p is designed so as to compensate the aerodynamic torque at the desired value α^*. This strategy thus strongly relies on the fact that the center of pressure is below the pivot point P.

Then, from an application point of view, the main benefit of this result is to show how to stabilize the "desired" angle of attack α^* without a measure of $|v_a|$. Note that the direction $\xi(v_a)$ of the air-velocity vector is needed to compute the control law. While this is not as demanding as knowing the air-velocity vector itself, this may still seem a strong requirement in practice. As a matter of fact, in many situations knowledge of this angle is not really needed. First, horizontal flight with horizontal wind (i.e. v_a being horizontal) constitutes the most standard flight condition. In this case, the direction of the air-velocity is typically known ($\xi(v_a) = \pm\pi/2$) without the need of a sensor. Then, since the controller ensures the asymptotic stability of $\alpha = \alpha^*(v_a)$ when $\xi(v_a)$ is known, it will also ensure the convergence of α to a neighborhood of $\alpha^*(v_a)$ when the functions k_p, k_v are computed with $\xi(v_a)$ replaced by a "reasonable" estimate $\hat{\xi}$. For example, if v is measured one may take $\hat{\xi} = \xi(v)$, or even simply $\hat{\xi} = \xi(v_r)$ when the objective is to follow a reference trajectory v_r. Simulation results reported later will support these simple strategies.

Finally, let us also remark that the function k_p is defined by continuity when $\pi - \zeta - \xi = 0, \pi$ (see the proof in appendix E). Therefore, the control expression is well-defined everywhere.

3.2.2.3 Simulation results

We report in this section simulation results obtained from the modeling equations (3.43). The simulated parameters are given in appendix C. Some additional specific parameters for the current simulations are:

- $d(\alpha) = d = 0.03$ m. We take $d(\alpha)$ constant because, for symmetric airfoils, the distance between the center of pressure and the leading edge is constant over a wide range of α and Reynolds number [48, Sec. 4.7],
- $d_A = 0.01$ m.

Based on the previous model of aerodynamic lift coefficient of NACA0018 airfoil in Eq. (2.85) and Eq. (2.86), one verifies from (3.48) that the function h in (3.47) is given by

$$h(\alpha) = dk_a(c_1 + 2c_2 + 2(c_{2T} - c_2)\sigma(\alpha)\cos^2\alpha)$$

It is straightforward to verify that h is strictly positive since $d, k_a, \sigma, c_1 > 0$ and $c_{2T} > c_2 > 0$.

Model of desired angle of attack

The functions g_1, g_2 that define the desired angle of attack in (3.53) are chosen as follows:

$$g_1(\tau) = b\tau, \quad g_2(\xi) = \frac{\sin\xi}{(1 + a\cos\xi)} \tag{3.57}$$

with $|a| < 1$. This yields

$$\alpha^* = \operatorname{acot}\left(\frac{b|v_a|^2(1 + a\cos\xi)}{\sin\xi}\right)$$

with $b = 0.05$ and $a = -0.99$. Figure 3.13 shows a comparison of the so-obtained "desired angle of attack" α^* with the angle of attack α_{opt} that minimizes the energy consumption, for three flight configuration: horizontal flight ($\xi(v_a) = 90°$), descending flight ($\xi(v_a) = 75°$), and ascending flight ($\xi(v_a) = 105°$). The solid-line curves are associated with α_{opt} whereas the dashed curves are associated with α^*. Although the trends are similar, α^* only provides a very rough approximation of α_{opt}. A better approximation could be obtained by using a more complex function g_1. The very simple function g_1 here chosen will illustrate that even a rough estimate of the optimal angle of attack can yield satisfactory results in terms of energy efficiency. Figure 3.14 provides the energy consumption as functions of $|v_a|$ for the same horizontal, descending, and ascending flights. For comparison, the energy consumption for a classical quadrotor (i.e. without wings) is also shown in red with triangular markers. Energy consumption with $\alpha = \alpha^*$ is close to the optimal case $\alpha = \alpha_{\text{opt}}$, except in the velocity range $[7, 10]$ m/s. Note that for low velocities the classical quadrotor provides better energy consumption since it is lighter than the convertible UAV.

Teleoperation with wind simulation

We report in this section the results obtained with the proposed control approach for the teleoperation case with wind.

The control u_3 for the wing's pitch angle is defined by (3.56) with the parameter η_0 in (3.55) given by $\eta_0 = 1$ and $\xi(v_a)$ replaced by the approximation $\hat{\xi} = \xi(v_r)$. In other words, we do not use any velocity measurement for the control of the wing's pitch angle.

The attitude and altitude are controlled in the same fashion as in section 3.2.1. Simulation results presented next support the use of this simplified control expression.

The system is perturbed by the wind as in figure 3.6. The errors in altitude are less than the previous case (compare figure 3.15 with figure 3.7). The UAV's pitch angle is kept almost

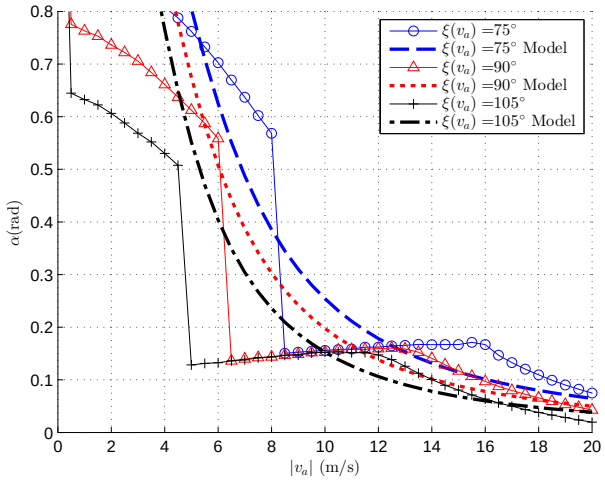

Figure 3.13: Comparison of desired angle of attack α^* (dashed curves) and optimal angle of attack α_{opt} (solid curves) versus the airspeed at different directions

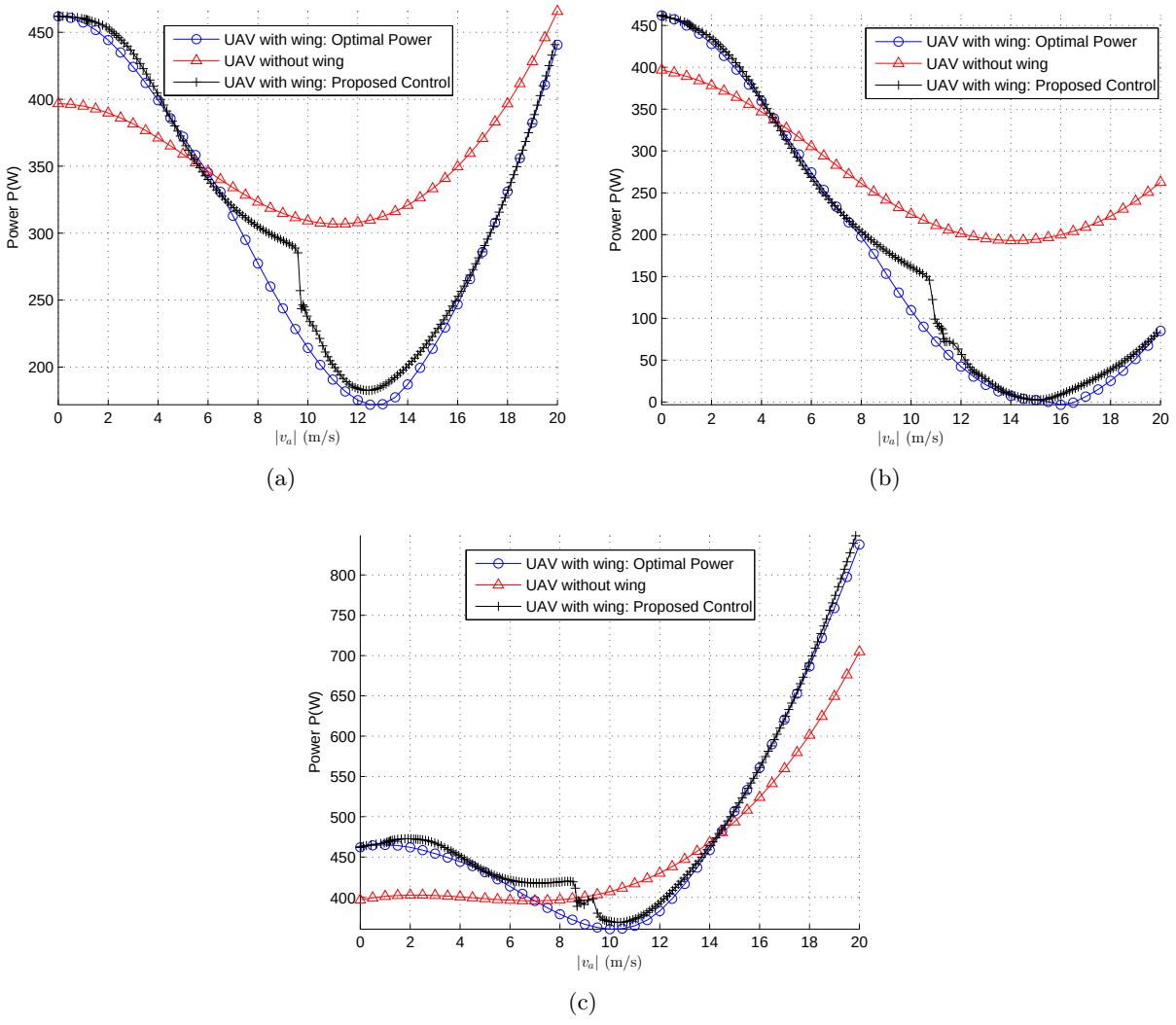

Figure 3.14: Power comparison in (a) horizontal, (b) descending, and (c) ascending forward flight

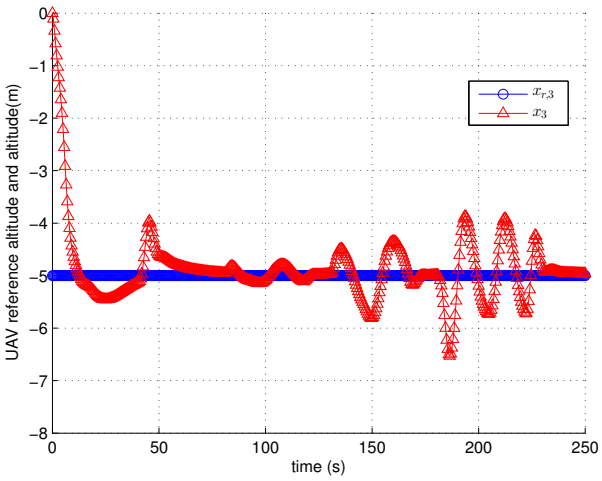

Figure 3.15: Reference altitude versus UAV altitude (second control design)

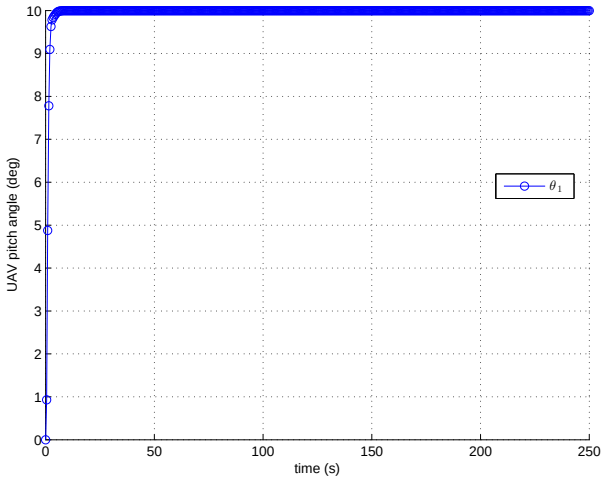

Figure 3.16: UAV's pitch angle (second control design)

perfectly at reference value, as proven in figure 3.16. This point is important since the UAV main body is kept from the influence of disturbances and vibrations. The wing's pitch angle is controlled so as to counteract the influences of the wind, and consequently the wing's angle of attack varies, as depicted in figure 3.17. Note that in the simulation, it is assumed that there is no delay in the wing servos' response.

Figure 3.18 plots the average power consumption since $t = 0$ s. The power consumption is lower than the previous case (compared with figure 3.10). This energy improvement is achieved since the wing's angle of attack is controlled with the goal of minimizing the power.

Finally we present the results for the teleoperation case with wind modeled according to the common reference U.S. Military Handbook MIL-HDBK-1797 [83]. Specifically, the wind speeds are the superposition of wind shear model, Dryden wind turbulence model (the angular velocity effects of turbulence are ignored), and discrete wind gust. The total wind velocity components are illustrated in figure 3.19, showing highly turbulence and wind gusts. Similar to the previous simulation, the altitude and attitude tracking is accurate, as shown in figure 3.20 and figure 3.21. The average power consumption is low, as depicted in figure 3.22.

3.2.3 Control With Velocity Measurement

With velocity measurement typically obtained by GPS, the control objective is essentially to stabilize a constant velocity reference trajectory v_r.

3.2.3.1 Control design for the propellers

The control design is based on [57] and has already been summarized in section 3.1.2. Let us first assume that F_a and Γ_a are known. The second equation in (3.16) can be written as

$$m\dot{v} = -k_v(v,t) - T\mathcal{R}e_3 + mge_3 + k_v(v,t) + F_a$$

where $k_v(v,t)$ is a feedback term designed so as to ensure the stability of $v = v_r$ for the system $m\dot{v} = -k_v(v,t)$. A simple choice is $k_v(v,t) = k_{v_1}(v - v_r)$ with k_{v_1} a positive gain but one may use

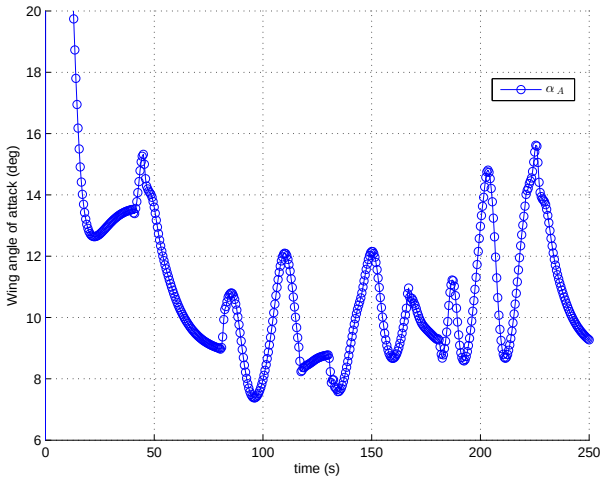

Figure 3.17: Angle of attack of the wing (second control design)

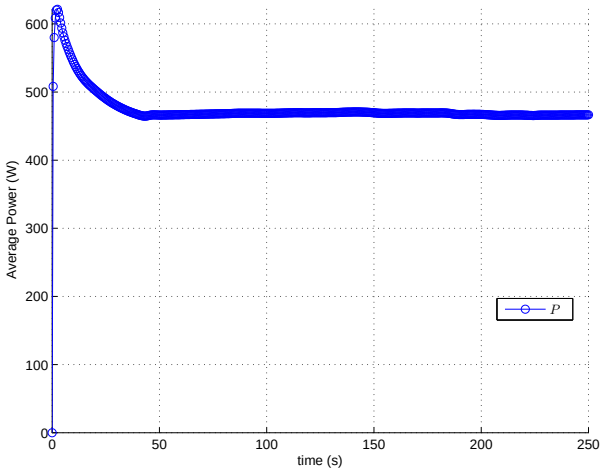

Figure 3.18: The average power consumption since $t = 0$ (second control design)

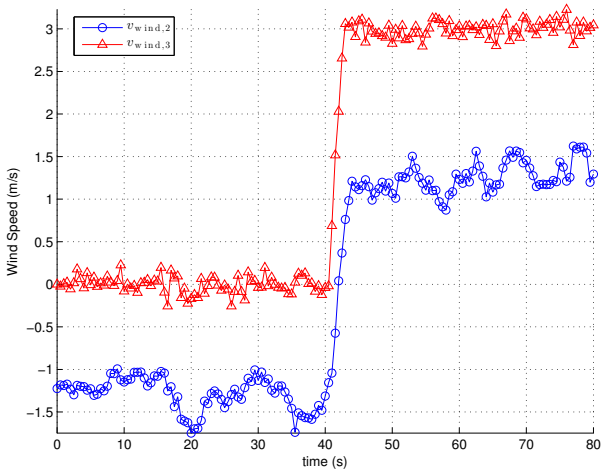

Figure 3.19: Wind speed components, which are superposition of wind shear model, Dryden wind turbulence model, and discrete wind gust.

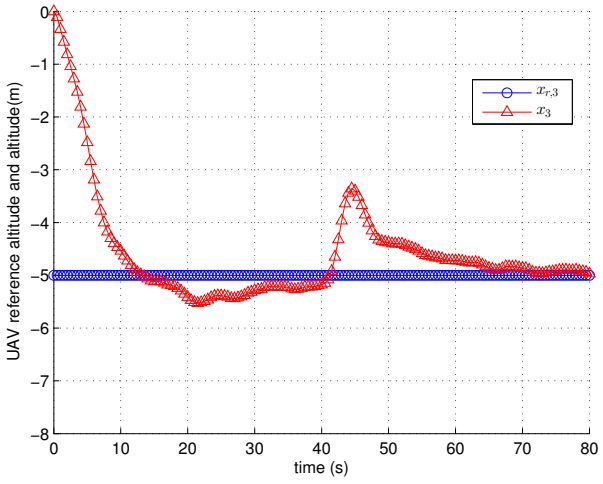

Figure 3.20: Reference altitude versus UAV altitude (simulation with a different wind model)

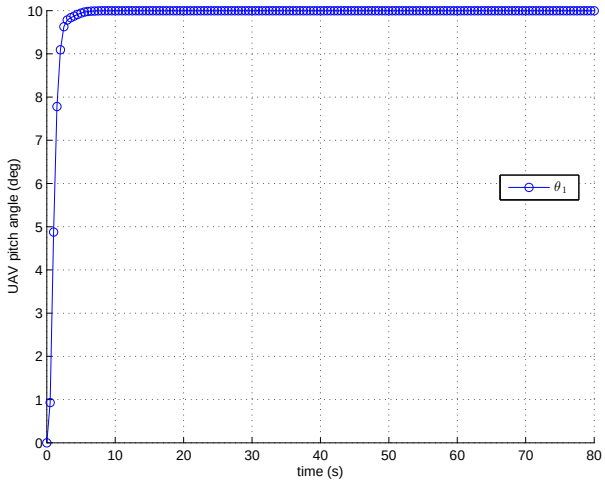

Figure 3.21: UAV's pitch angle (simulation with a different wind model)

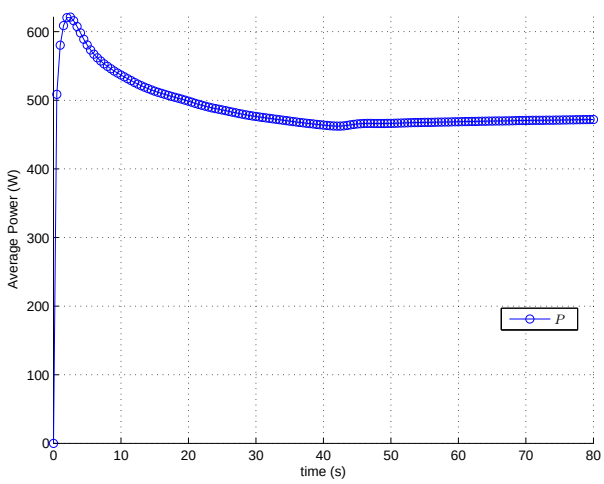

Figure 3.22: The average power consumption since $t = 0$ (simulation with a different wind model)

a more sophisticated control expression, e.g. incorporating integral correction terms, etc. From here, the objective is to ensure the convergence of $-T\mathcal{R}e_3 + mge_3 + k_v(v,t) + F_a$ to zero. Indeed, this implies that asymptotically the control system behaves like the stable system $m\dot{v} = -k_v(v,t)$. Provided that $mge_3 + k_v(v,t) + F_a \neq 0$, the relation $-T\mathcal{R}e_3 + mge_3 + k_v(v,t) + F_a = 0$ is equivalent to

$$T = \pm\|mge_3 + k_v + F_a\|\,, \quad \mathcal{R}e_3 = \pm\frac{mge_3 + k_v + F_a}{\|mge_3 + k_v + F_a\|}$$

From these two solutions, the constraint of positive thrust T allows one to specify a unique physically admissible solution:

$$T = \|mge_3 + k_v + F_a\|\,, \quad \mathcal{R}e_3 = \frac{mge_3 + k_v + F_a}{\|mge_3 + k_v + F_a\|} \tag{3.58}$$

This equation specifies the thrust control input and a "reference thrust direction":

$$\eta_r = \frac{mge_3 + k_v + F_a}{\|mge_3 + k_v + F_a\|}$$

The torque control input is then designed so as to ensure the convergence of $\eta = \mathcal{R}e_3$ to η_r. This is a classical problem in the attitude control of rigid bodies and in theory, it is a problem easy to solve since the system is fully actuated in torque. A possible solution [57] is given by:

$$\Gamma = \omega \times J\omega - \Gamma_a - k_\omega(\omega - \omega_r)$$

where ω_r, which denotes a vector of "reference (or desired) angular velocity", can be defined as in Eq. (3.15) in section 3.1.2:

$$\omega_{r,1,2} = \left\{\mathcal{R}^\top\left[k_\theta\frac{\eta \times \eta_r}{(1+\eta^\top\eta_r)^2} - \mathcal{S}(\eta)^2(\eta_r \times \dot{\eta}_r)\right]\right\}_{1,2} \tag{3.59}$$

with $\omega_{r,1,2} := (\omega_{r,1}, \omega_{r,2})^\top$. In the above equations, k_ω and k_θ denote positive gains. The derivation term $\dot{\eta}_r$ is difficult to obtain. In practice, this term is simply set to zero. Simulation suggests

that doing so will not degrade too much the performance of the above nonlinear controller. At this point, note that $\omega_{r,3}$ is not specified yet. Indeed, convergence of η to η_r puts no requirement on the yaw angle. In the case of our convertible UAV, a natural requirement is to align the wings towards the apparent wing (zero sideslip angle). In the absence of wind, a simple solution is

$$\omega_{r,3} = -k_{\theta_3}\left[\theta_3 + \text{asin}\left(\frac{v_{r,1}}{\|(v_{r,1}, v_{r,2})\|}\right)\right] \tag{3.60}$$

with k_{θ_3} a positive control gain, and θ_3 any parametrization of the UAV's yaw, like the Euler angle $\theta_3 = \text{asin}(e_2^T \mathcal{R} e_1)$. More sophisticated attitude control solutions can be found in [21].

Before going any further, let us make a few remarks. The reference thrust direction given by the second equality in (3.58) is well defined if and only if $mge_3 + k_v + F_a \neq 0$. For high-speed flight, the amplitude of the aerodynamic force F_a can be large and close to the gravity force amplitude mg. Thus, in theory one cannot rule out the possibility that $mge_3 + k_v + F_a$ vanishes, although this is relatively unlikely. In the same line, to limit the risk that this term vanishes it seems preferable to use a bounded feedback term k_v. In particular, the maximum amplitude of the vertical component $e_3^T k_v$ should be significantly smaller than mg.

3.2.3.2 Control design for the wings

This short section can be seen as an extension of the wing control in section 3.2.1.5. Specifically, we propose to control the wings' pitch angle so as to obtain desired angles of attack $\alpha_{r,A}$ and $\alpha_{r,C}$. These angles should be chosen so as to ensure a good energy efficiency. We assume that the desired values are defined in function of the desired velocity: $\alpha_{r,A} = \alpha_{r,A}(v_r)$, $\alpha_{r,C} = \alpha_{r,C}(v_r)$. At this point we also assume that the UAV's yaw angle has been controlled so that the sideslip angle is zero. In this case, the motion is essentially planar and we can assume without loss of generality that v_r is of the form $v_r = (0, v_{r,2}, v_{r,3})$. Along the desired velocity profile (i.e. for $v = v_r$), one has for $W \in \{A, C\}$:

$$\alpha_W = \frac{\pi}{2} + \text{atan2}(v_{r,3}, v_{r,2}) - \zeta_W$$

Thus $\tilde{\alpha}_W := \alpha_W - \alpha_{r,W}$ satisfies:

$$\dot{\tilde{\alpha}}_W = \dot{\alpha}_W = -\dot{\zeta}_W = -\omega_1 - \dot{\mu}_W = -\omega_1 - u_W$$

Setting

$$u_W = -\omega_1 - k_W\left[\zeta_W - \left(\frac{\pi}{2} + \text{atan2}(v_{r,3}, v_{r,2})\right) + \alpha_{r,W}\right]$$

implies that

$$\dot{\tilde{\alpha}}_W = -k_W\,\tilde{\alpha}_W$$

Choosing $k_W > 0$ thus ensures the exponential convergence of α_W to the desired value $\alpha_{r,W}$. If one assumes that the system is perfectly symmetric, it is natural to choose the reference values $\alpha_{r,A}, \alpha_{r,C}$ equal: $\alpha_{r,A} = \alpha_{r,C} = \alpha_r$, and also the control gains equal: $k_A = k_C = k$. Then, in the case of a horizontal reference velocity, the control u_A, u_C reduce to

$$\begin{cases} u_A = -\omega_1 - k\left(\zeta_A - \dfrac{\pi}{2} + \alpha_r\right) \\ u_C = -\omega_1 - k\left(\zeta_C - \dfrac{\pi}{2} + \alpha_r\right) \end{cases} \tag{3.61}$$

3.2.3.3 Estimation of aerodynamic force and torque

Implementation of the above control solution requires, among other things, the knowledge of the aerodynamic force and torque F_a and Γ_a. One could obtain an estimation of these forces from the analytical model of lift and drag forces and the velocity measurements. Due to the difficulty to obtain very precise models of these forces and to account for wind perturbation, it seems more reliable in practice to estimate F_a and Γ_a online. To this purpose, a classical estimator can be defined as

$$\left\{\begin{array}{lcl} m\dot{\hat{v}} &=& -T\mathcal{R}e_3 + \hat{F}_a - mk_{\text{est,v}}(\hat{v}-v) \\ J\dot{\hat{\omega}} &=& -\omega\times J\omega + \Gamma + \hat{\Gamma}_a - Jk_{\text{est},\omega}(\hat{\omega}-\omega) \\ \dot{\hat{F}}_a &=& -mk_{\text{est,F}}(\hat{v}-v) \\ \dot{\hat{\Gamma}}_a &=& -Jk_{\text{est},\Gamma}(\hat{\omega}-\omega) \end{array}\right. \tag{3.62}$$

where $k_{\text{est},*}$ denote positive gains and, for any variable x, $\hat{x}$ denotes its estimate. Denoting $\tilde{x} = \hat{x} - x$ the estimation error, one deduces from (3.16) and (3.62) that:

$$\left\{\begin{array}{lcl} m\dot{\tilde{v}} &=& \tilde{F}_a - mk_{\text{est,v}}\tilde{v} \\ J\dot{\tilde{\omega}} &=& \tilde{\Gamma}_a - Jk_{\text{est},\omega}\tilde{\omega} \\ \dot{\tilde{F}}_a &=& -mk_{\text{est,F}}\tilde{v} - \dot{F}_a \\ \dot{\tilde{\Gamma}}_a &=& -Jk_{\text{est},\Gamma}\tilde{\omega} - \dot{\Gamma}_a \end{array}\right. \tag{3.63}$$

These are the dynamics of a Hurwitz-stable linear system perturbed by the additive terms $\dot{F}_a, \dot{\Gamma}_a$. Provided that F_a and Γ_a do not vary too fast, such an observer will be able to provide reliable estimates of these quantities. The convertible structure, with angles of attack independent of the UAV's main body attitude, is also a positive aspect in order to avoid fast variations of F_a and Γ_a.

3.2.3.4 Simulation results

We first evaluate this control strategy under the following conditions:

1. No wind;
2. Air-velocity on both front and back wing is given by $v_{a,A} = v_{a,C} = v$; i.e. the propellers have no impact on the air-velocity on the wings.

The following control parameters are used:

$$k_v(\tilde{v}) = \begin{bmatrix} \text{sat}_\delta(k_{1,p}\tilde{v}_1 + k_{1,I}\int\tilde{v}_1) \\ \text{sat}_\delta(k_{2,p}\tilde{v}_2 + k_{2,I}\int\tilde{v}_2) \\ \text{sat}_\delta(k_{3,p}\tilde{v}_3 + k_{3,I}\int\tilde{v}_3) \end{bmatrix}$$

with $\text{sat}_\delta(\tau) = \tau\min(1, \delta/|\tau|)$ the classical saturation function. The gains are: $k_{1,p} = 1$, $k_{1,I} = 2$, $k_{2,p} = 1$, $k_{2,I} = 2$, $k_{3,p} = 0.2$, $k_{3,I} = 1.2$ with $\delta = 10$. The attitude gains are $k_\omega = 14$, $k_\theta = 10$, and $k_{\theta_3} = 0.25$. The wings control gains are $k_A = k_C = k = 9$. The estimation gains are: $k_{\text{est,v}} = 4.8$, $k_{\text{est},\omega} = 9$, $k_{\text{est,F}} = 13.5$, and $k_{\text{est},\Gamma} = 4.8$.

The reference altitude is $x_{r,3} = -5$ m. The reference motion consists in a horizontal flight with $v_{r,1} = v_{r,3} = 0$ and $v_{r,2}$ ramps from 0 to 8 m/s in 15 s. From $t = 15$ s to $t = 35$ s, $v_{r,2}$ ramps to 14 m/s. As for the reference angle of attack of the wings, $\alpha_{r,A} = \alpha_{r,C} = \alpha_r$ ramp from 90° to

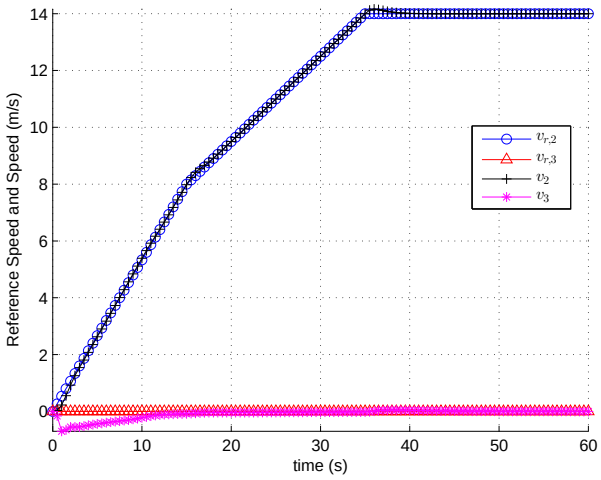

Figure 3.23: Reference speed and UAV speed (velocity tracking simulation)

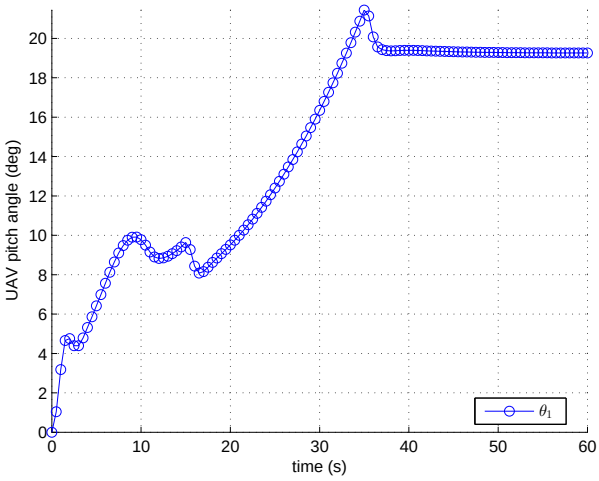

Figure 3.24: UAV's pitch angle (velocity tracking simulation)

12° in 10 s and then these angles are kept constant. The initial ramp of the reference angles of attack simulates the transition between hover/axial flight to horizontal forward flight.

Figure 3.23 compares the reference speed and the UAV speed. The velocity tracking is almost perfect. Until $t = 12$ s, the vertical velocity is negative, which reflects the climbing movement of the UAV to achieve the desired altitude. At $t = 0$ s, the wings are at neutral vertical positions ($\boldsymbol{k_A} \equiv \boldsymbol{k_C} \equiv \boldsymbol{k}$). Since the air-velocity is zero, the wings' angles of attack are not defined. The values on figure 3.25 are just a matter of numerical evaluation, in this case, $\alpha_A = \alpha_C = 0$. As the UAV gathers horizontal speed, the angles of attack increase rapidly to 60°. From $t = 15$ s, the angles of attack track closely their reference values. Figure 3.24 shows the evolution of UAV's pitch angle. The UAV orientation does not vary too fast although there are significant changes of aerodynamic forces acting on the wings (which depend on the air-velocity and wings angle of attack). Note that in the current simulation, the wings' pitch angle are kept constant. Consequently, the UAV's orientation is modified depending on the UAV speed. More stable UAV's pitch can be achieved when incorporating the wings control as in section 3.2.2.

In this current simulation, we assume that the airflow to the front and back wings are the same. Adding the fact that the angles of attack of the wings are equal, this implies the aerodynamic forces acting on front and back wings are identical. Since the wings are located at equal distances from the UAV's CoM, total aerodynamic torque on the UAV is nearly zero, as shown in figure 3.26 (note the scale of the vertical axis). For later reference, figure 3.27 plots the average power consumption since the beginning of the simulation.

We now evaluate this control strategy under the following conditions:

1. The UAV is perturbed by strong and varying wind, as shown in figure 3.28.

2. As in the previous simulation, air-velocity on both front and back wing is given by $v_{a,A} = v_{a,C} = |\boldsymbol{v}|$; i.e. the propellers have no impact on the air-velocity on the wings.

Figure 3.29 shows that the UAV is capable of tracking the reference velocity with very small errors.

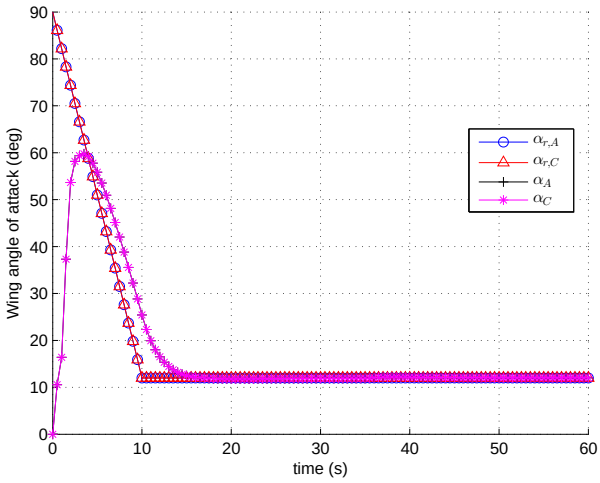

Figure 3.25: Comparison of wing reference angle of attack and angle of attack (velocity tracking simulation)

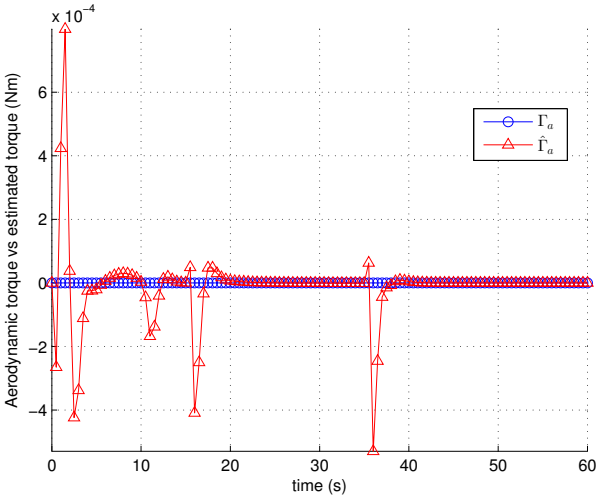

Figure 3.26: Aerodynamic torque and estimated torque (velocity tracking simulation)

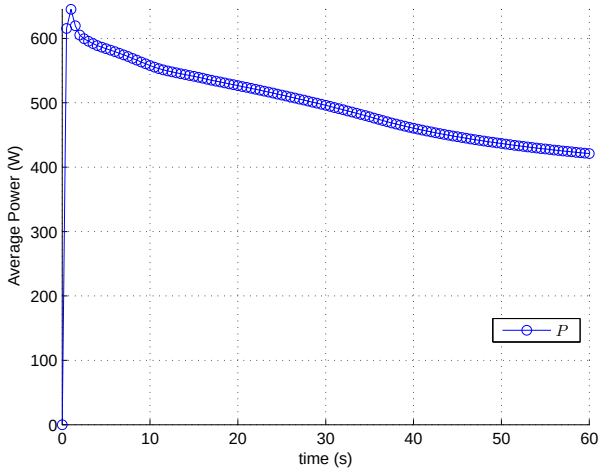

Figure 3.27: The average power consumption since $t = 0$ (velocity tracking simulation)

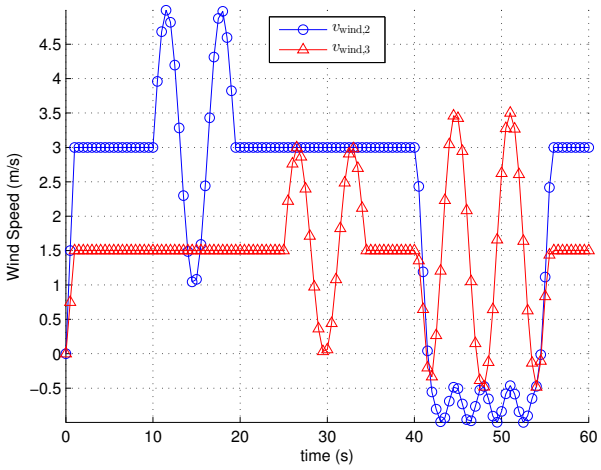

Figure 3.28: Wind speed (velocity tracking simulation)

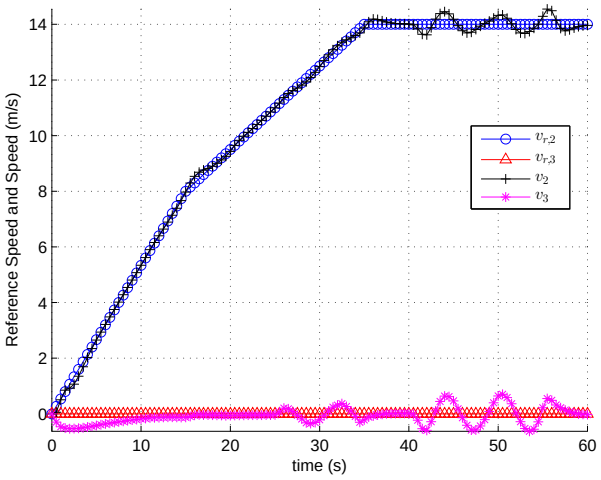

Figure 3.29: Reference speed and UAV speed (velocity tracking simulation with wind)

Finally, to evaluate the possible impact of propellers downwash on the wings, we evaluate this control strategy under the following conditions:

1. No wind;
2. Air-velocity on front wing is given by $\boldsymbol{v_{a,A}} = \boldsymbol{v}$ and air-velocity on back wing is given by $\boldsymbol{v_{a,C}} = \boldsymbol{v} - \varepsilon|\boldsymbol{v}|\boldsymbol{k}$; ε is small with respect to $|\boldsymbol{v}|$. In this simulation, the downwash flow speed is kept constant at $\varepsilon|\boldsymbol{v}| = 2$ m/s, which already represents significant airflow interference.

The reason for considering this expression of the air-velocity on the back wing is the following. When the UAV is flying forward, the downwash flow induced by the propellers, especially the first and fourth propellers as represented in figure 3.3, creates additional flow in the direction of propeller axis (i.e. $\boldsymbol{k}$ direction, see figure 3.30) to the back wing. By contrast, the air-velocity on the front wing is not perturbed by the propellers. It is assumed that front wing does not induce interference on the propellers and the back wing. We are aware that it is probably a very simplified model of interaction effects that take place. We hope, however, that it captures some of these phenomena.

We proceed next to analyze the result of this simulation with interference on the back wing. Figure 3.31 shows the result of velocity tracking, which is as good as the result in the first simulation without flow interference (figure 3.23). However, in the present simulation case, the propellers' downwash to the back wing effectively reduces the angle of attack of the latter. In fact, at some time instances, the angle of attack of the back wing is reduced to zero or negative as shown in figure 3.33. Consequently, the aerodynamic force on the back wing is reduced significantly. Due to the imbalance of the forces on front and back wings, the strong aerodynamic torque (figure 3.34) acting on the UAV has the tendency to pitch the aerial vehicle "nose-up". Consequently, the UAV's pitch angle is smaller compared to the previous case (see figure 3.32 versus figure 3.24). To counter the above aerodynamic torque, the controller commands the first and fourth propellers to spin faster and the second and third propellers to spin slower, as depicted in figure 3.35. This propeller control compensation is made possible thanks to accurate estimation of the aerodynamic torque as shown in figure 3.34.

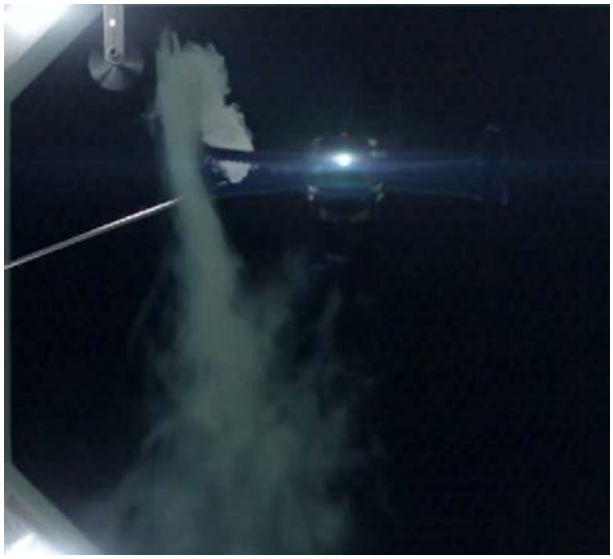

Figure 3.30: Propeller downwash along its axis direction, image capture of IRIS+ drone in wind tunnel (cnet.com)

The current simulation results call for some remarks. First, the reduced angle of attack of the back wing significantly decreases the aerodynamic force on it, thereby degrading the energy performance of the UAV (compare figure 3.36 with figure 3.27). This performance is even worse when $\alpha_C < 0$, which implies that the aerodynamic lift on the back wing is negative. Second, the imbalance of the propeller rotational speeds may pose significant control problem since saturation may occur possibly causing instability.

3.2.3.5 Control With Propellers Influence on Wings

We have seen that different air-velocity on the back and front wings can have a negative impact on the system's stability and performance. Concerning the latter issue, this leads to very asymmetric thrust distribution on the different propellers. The objective of this section is to modify the above-proposed control design so as to take into account such asymmetry on back and front wings aerodynamic forces. The main difficulty is that the value ε that characterizes this asymmetry is unknown. The idea, relatively simple, consists in using the estimation of the torque Γ_a that results from this asymmetry to modify the angles of attack on the wings, with the objective of reducing Γ_a. In order to analyze this strategy, we first need to relate Γ_a to ε. We perform this analysis under the following assumptions.

Assumptions: The following assumptions are made:

1. The velocity is $\boldsymbol{v} = v_2 \boldsymbol{j_0}$;
2. The sideslip angle is zero;
3. Wind is neglectable;
4. Air-velocity on the wings are given by $\boldsymbol{v_{a,A}} = \boldsymbol{v}$ and $\boldsymbol{v_{a,C}} = \boldsymbol{v} - \varepsilon|\boldsymbol{v}|\boldsymbol{k}$;
5. Angles of attack on both wings are "small" so that first-order approximations of lift and drag aerodynamic coefficients are valid; small angles of attack typically means amplitude less than 0.2 rad.

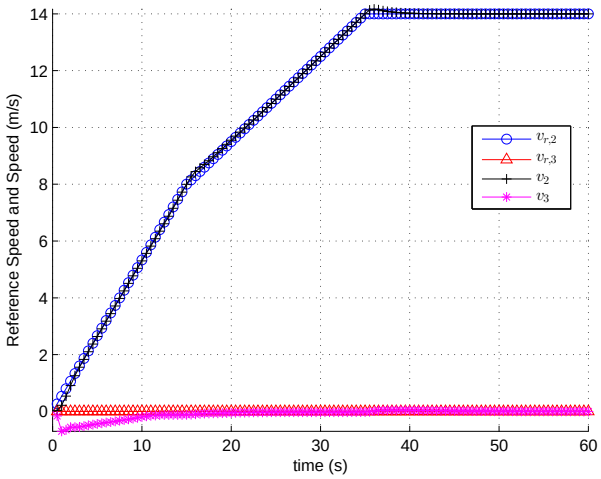

Figure 3.31: Reference speed and UAV speed (velocity tracking simulation with propellers' downwash on wing)

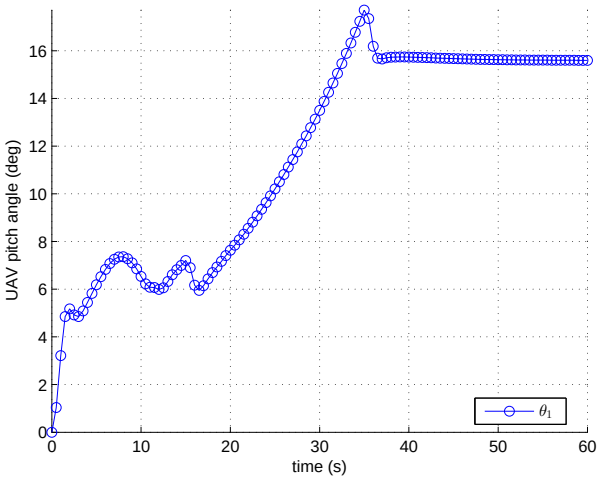

Figure 3.32: UAV's pitch angle (velocity tracking simulation with propellers' downwash on wing)

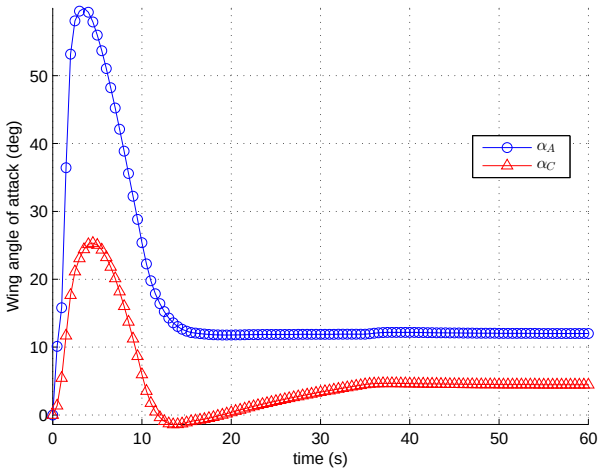

Figure 3.33: Wing angle of attack (velocity tracking simulation with propellers' downwash on wing)

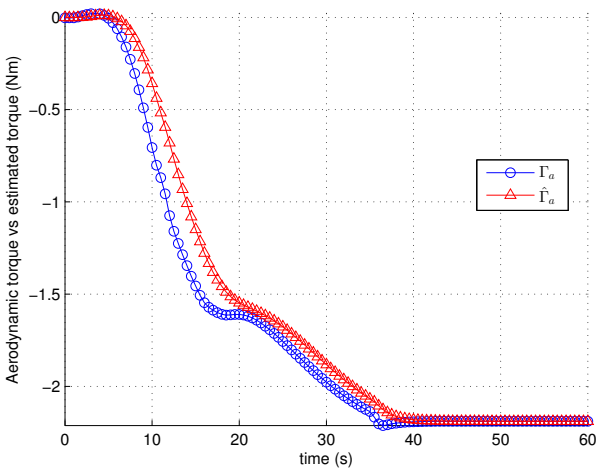

Figure 3.34: Aerodynamic torque and estimated torque (velocity tracking simulation with propellers' downwash on wing)

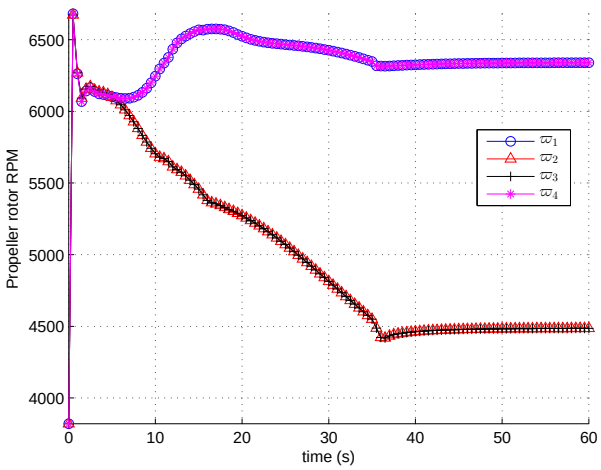

Figure 3.35: Propeller rotational speed (velocity tracking simulation with propellers' downwash on wing)

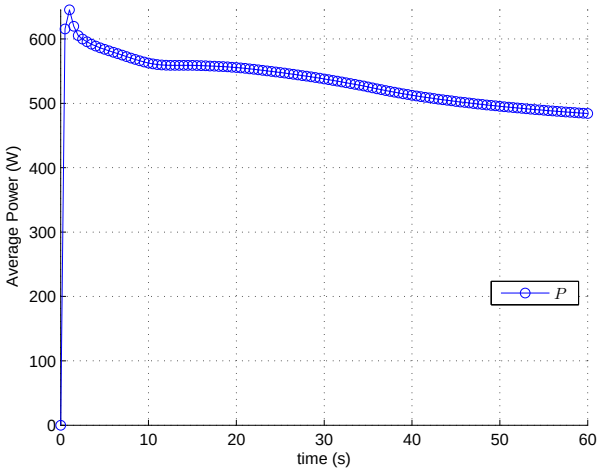

Figure 3.36: The average power consumption since $t = 0$ (velocity tracking simulation with propellers' downwash on wing)

Proposition 2 *Under the above assumptions, one has*

$$\begin{aligned}\Gamma_a \;\approx\; & Lk_a|v|^2\Big\{\sin\theta\Big[\frac{\partial c_D}{\partial\alpha}(\alpha_C,\mathrm{Re}_C)(\alpha_A-\alpha_C)+\varepsilon\big(c_L(\alpha_C,\mathrm{Re}_C)\cos\theta-c_D(\alpha_C,\mathrm{Re}_C)\sin\theta\big)\Big]\\ & -\cos\theta\frac{\partial c_L}{\partial\alpha}(\alpha_C,\mathrm{Re}_C)(\alpha_A-\alpha_C)+\varepsilon c_D(\alpha_C,\mathrm{Re}_C)\Big\}\end{aligned} \tag{3.64}$$

where the approximation holds up to second-order terms in $(\alpha_A-\alpha_C)$ *and* ε.

The proof of this proposition is given in appendix F.

Eq. (3.64) provides an approximation of Γ_a under the assumption that both $\alpha_A-\alpha_C$ and ε are small. If we further assume that α_C is small, the above expression can be further simplified as:

$$\begin{aligned}\Gamma_a \;&\approx\; -Lk_a|v|^2\Big(\cos\theta\frac{\partial c_L}{\partial\alpha}(\alpha_C,\mathrm{Re}_C)-\sin\theta\frac{\partial c_D}{\partial\alpha}(\alpha_C,\mathrm{Re}_C)\Big)(\alpha_A-\alpha_C)\\ &\approx\; -Lk_a|v|^2 g(\theta,\alpha_C,\mathrm{Re}_C)(\alpha_A-\alpha_C)\end{aligned} \tag{3.65}$$

with

$$g(\theta,\alpha_C,\mathrm{Re}_C)=\cos\theta\frac{\partial c_L}{\partial\alpha}(\alpha_C,\mathrm{Re}_C)-\sin\theta\frac{\partial c_D}{\partial\alpha}(\alpha_C,\mathrm{Re}_C) \tag{3.66}$$

The above expression is important as it relates the expression of Γ_a with the UAV's pitch angle θ and the difference of wings angle of attack $\alpha_A-\alpha_C$. In particular, it shows that an estimate of $\alpha_A-\alpha_C$ can be obtained from an estimate of Γ_a. In this respect, particular attention must be given to the term $g(\theta,\alpha_C,\mathrm{Re}_C)$ and more precisely to its sign. In "normal conditions", this term is positive, i.e. α_C is small so that $\frac{\partial c_L}{\partial\alpha}(\alpha_C,\mathrm{Re}_C)$ is much larger than $\frac{\partial c_D}{\partial\alpha}(\alpha_C,\mathrm{Re}_C)$, and the UAV's pitch angle θ is significantly less than $\pi/2$. A numerical evaluation with our simulation model, for $\alpha_C=0.2$ rad, yields that

$$g(\theta,\alpha_C,\mathrm{Re}_C)>0 \quad \text{for} \quad \theta<1.4 \text{ rad}$$

Let us now develop the expression of $\alpha_A - \alpha_C$. Since $\boldsymbol{v_{a,A}} = \boldsymbol{v} = v_2 \boldsymbol{j_0}$,

$$\alpha_A = \frac{\pi}{2} - \zeta_A$$

and from the expression of $\boldsymbol{v_{a,C}}$,

$$\begin{aligned}
\alpha_C &= \frac{\pi}{2} + \operatorname{atan2}\big((\boldsymbol{j_0} - \varepsilon \boldsymbol{k}).\boldsymbol{k_0}, (\boldsymbol{j_0} - \varepsilon \boldsymbol{k}).\boldsymbol{j_0}\big) - \zeta_C \\
&= \frac{\pi}{2} + \operatorname{atan2}(-\varepsilon \boldsymbol{k}.\boldsymbol{k_0}, 1 - \varepsilon \boldsymbol{k}.\boldsymbol{j_0}) - \zeta_C \\
&= \frac{\pi}{2} + \operatorname{atan2}(-\varepsilon \cos\theta, 1 + \varepsilon \sin\theta) - \zeta_C \\
&= \frac{\pi}{2} - \varepsilon \cos\theta - \zeta_C + O^2(\varepsilon)
\end{aligned}$$

Therefore,

$$\begin{aligned}
\alpha_A - \alpha_C &= \zeta_C - \zeta_A + \operatorname{atan2}(\varepsilon \cos\theta, 1 + \varepsilon \sin\theta) \\
&= \mu_C - \mu_A + \varepsilon \cos\theta + O^2(\varepsilon)
\end{aligned} \tag{3.67}$$

We can now proceed with the definition of the wings control variables u_A, u_C. We propose the following expression (compare with (3.61)):

$$\begin{cases}
u_A = -\omega_1 - k\left(\zeta_A - \dfrac{\pi}{2} + \alpha_r + k_{\Gamma,A}\dfrac{\hat{\Gamma}_a}{1 + |\hat{\Gamma}_a|}\right) \\
u_C = -\omega_1 - k\left(\zeta_C - \dfrac{\pi}{2} + \alpha_r - k_{\Gamma,C}\dfrac{\hat{\Gamma}_a}{1 + |\hat{\Gamma}_a|}\right)
\end{cases} \tag{3.68}$$

The idea is simply to modify the reference angle of attack in function of the estimated torque $\hat{\Gamma}_a$. From (3.67),

$$\begin{aligned}
\frac{\mathrm{d}}{\mathrm{d}t}(\alpha_A - \alpha_C) &\approx \dot{\mu}_C - \dot{\mu}_A - \varepsilon\omega_1 \sin\theta \\
&\approx u_C - u_A - \varepsilon\omega_1 \sin\theta \\
&\approx -k\left(\alpha_A - \alpha_C - (k_{\Gamma,A} + k_{\Gamma,C})\frac{\hat{\Gamma}_a}{1 + |\hat{\Gamma}_a|} - \varepsilon\cos\theta\right) - \varepsilon\omega_1 \sin\theta
\end{aligned}$$

Assuming that the estimate $\hat{\Gamma}_a$ of Γ_a is perfect, it follows from (3.65) that

$$\begin{aligned}
\frac{\mathrm{d}}{\mathrm{d}t}(\alpha_A - \alpha_C) &\approx -k\left\{\left[1 + (k_{\Gamma,A} + k_{\Gamma,C})Lk_a|v|^2\frac{g(\theta, \alpha_C, \mathrm{Re}_C)}{1 + |\Gamma_a|}\right](\alpha_A - \alpha_C) - \varepsilon\cos\theta\right\} - \varepsilon\omega_1 \sin\theta \\
&\approx -k\Big[\big(1 + \bar{k}(\theta, v, \alpha_C, \mathrm{Re}_C)\big)(\alpha_A - \alpha_C) - \varepsilon\cos\theta\Big] - \varepsilon\omega_1 \sin\theta
\end{aligned} \tag{3.69}$$

with

$$\bar{k}(\theta, v, \alpha_C, \mathrm{Re}_C) = (k_{\Gamma,A} + k_{\Gamma,C})Lk_a|v|^2\frac{g(\theta, \alpha_C, \mathrm{Re}_C)}{1 + |\Gamma_a|}$$

We see from the above expression that $\bar{k}$ acts as a nonlinear gain. In particular, if $\omega_1 = 0$, the equilibrium of (3.69) is

$$\alpha_A - \alpha_C = \frac{\varepsilon\cos\theta}{1 + \bar{k}(\theta, v, \alpha_C, \mathrm{Re}_C)}$$

Thus the higher $\bar{k}$, the smaller $\alpha_A - \alpha_C$. In view of the expression of $\bar{k}$, this suggests to choose $k_{\Gamma,A}$ and $k_{\Gamma,C}$ large. Limitations associated with the use of high gains and the risk of crossing the stall zone, however, prevent one from choosing too large values. Also, one can observe the importance of the positivity of $1 + \bar{k}$ (and thus of g), to ensure that (3.69) defines a stable system.

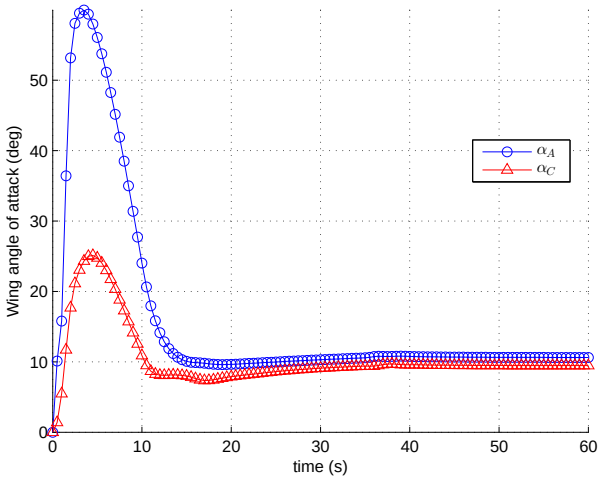

Figure 3.37: Wing angle of attack (velocity tracking simulation with aerodynamic torque compensation)

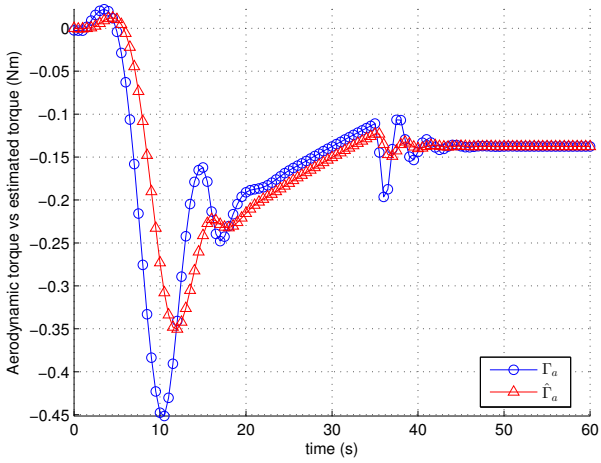

Figure 3.38: Aerodynamic torque and estimated torque (velocity tracking simulation with aerodynamic torque compensation)

3.2.3.6 Simulation Results for Control With Propellers Downwash Influence on the Wing

The simulation condition is identical to the one at the end of section 3.2.3.4 with $\varepsilon|v| = 2$ m/s. The additional control parameters are: $k_{\Gamma,A} = 0.2$ and $k_{\Gamma,C} = 0.7$. The reference angles of attack are adjusted as in (3.68) to take into account the aerodynamic torque. Hence, the angles of attack of the front and back wings are similar as shown in figure 3.37 (compared with figure 3.33). Consequently the aerodynamic torque on the UAV is much smaller (compare figure 3.38 to figure 3.34). The rotational speeds of the propellers are very close to each other, as shown in figure 3.39. This ensures more uniform thrust distribution than the case without reference angle of attack adjustment (see figure 3.35). The average power consumption in figure 3.40 is less than the previous case without torque compensation in figure 3.36 but slightly greater than the case without propeller downwash interaction in figure 3.27.

3.3 Chapter Summary

In this chapter, we have proposed three control law designs for our convertible UAV. The first one only makes use of IMU/barometer measurements and concern attitude/altitude teleoperation control mode. The basic (and classical) idea is a hierarchical controller for attitude, altitude, and motor control. The control model state variables are estimated based on measurements from sensors. The vertical aerodynamic force is estimated based on barometer measurement. The second control design also addresses the same teleoperation control mode. By using a slightly modified mechanical design, we show that it is possible to improve tracking precision and energy efficiency in the presence of wind. Finally, the last control design concerns velocity control with velocity measurements. The main objective is to take into account possible downwash of the propellers on the back wing. By using an estimate of the aerodynamic torque induced by asymmetric aerodynamic forces on the wings, we have shown that a simple control on the wings' reference pitch angle allows one to compensate the negative effects of the downwash. Simulation results have

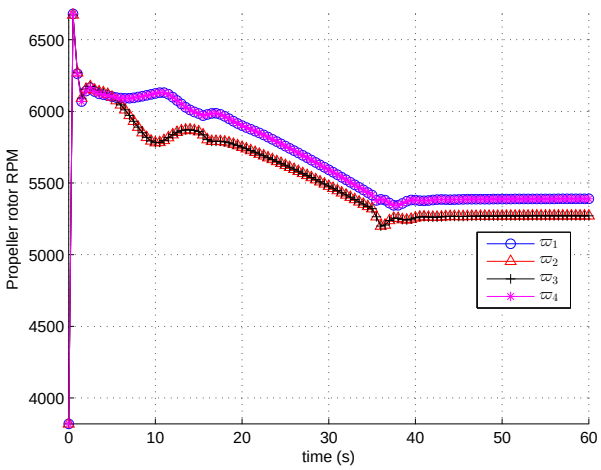

Figure 3.39: Propeller rotational speed (velocity tracking simulation with aerodynamic torque compensation)

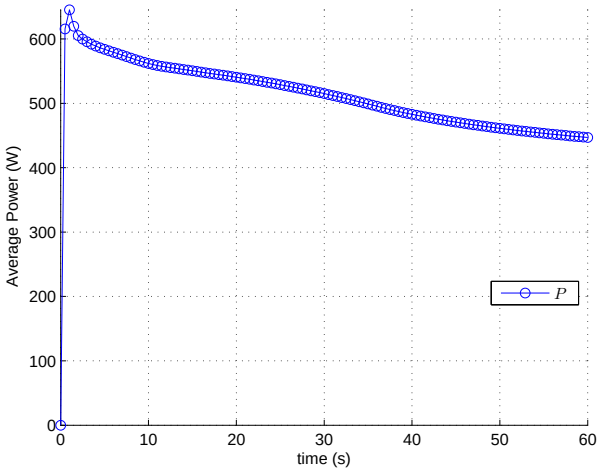

Figure 3.40: The average power consumption since $t = 0$ (velocity tracking simulation with aerodynamic torque compensation)

validated the control approaches. The next chapter introduces the physical convertible UAV prototype and presents the preliminary flight test results.

Chapter 4

Conception and Preliminary Experiments

This chapter focuses on the physical and experimental aspects of this thesis. In the beginning, the mechanical prototype of the convertible UAV and the software/hardware architecture are presented. Each major component of the UAV is described in detail. The preliminary experimental results are reported at the end of this chapter.

4.1 Mechanical Prototype

The prototype of the convertible UAV along with its major components is shown in figure 4.1. The main body structure of the UAV has several layers to improve the rigidity of the structure and to separate different components. The wing assembly consists in a set of foams, a set of guide pieces, a reinforced axis, and a rotating axis actuated by the one (or two) servo(s). The foams are made by expanded polystyrene foam, which are cut into roughly equal rectangular pieces. The guide pieces are made of plastic and are precisely fabricated by 3D printing to have the shape of NACA0018 airfoils. The foams and guide pieces are alternately attached together using strong glue. The rotating and reinforcing axes are made of glass fiber. They align the foams with the guide pieces. Using abrasive materials, the foams are repeatedly scraped until the surface of the wing is smooth. An illustration of the wings after fabrication is presented in figure 4.2. Finally, duct tapes are used to cover the surface of the wings.

The system architecture comprises a low level control layer connected with a high level control layer via the serial communication interface RS-232 as shown in figure 4.3. The main component of low level control is the Quanton flight controller with build-in Inertial Measurement Unit (IMU). The Quanton flight controller receives the control signals from a joystick via a Radio Control (RC) Receiver using Pulse Position Modulation (PPM). As for the actuation, the flight controller sends the signals to four Electronic Speed Controllers (ESC) which in turn control the rotational speeds of the four main rotors. The flight controller also transmits the Pulse Width Modulation (PWM) signals to control the servos mounted on the wings. The main component of high level control is the ODroid onboard computer. This mini computer runs on Linux with integrated Robot Operating System (ROS) framework. Various Universal Serial Bus (USB) ports on the computer board enable the connection to a GPS module, cameras (in the future), etc. Communication between the ODroid and a computer workstation is assured by Wifi data link.

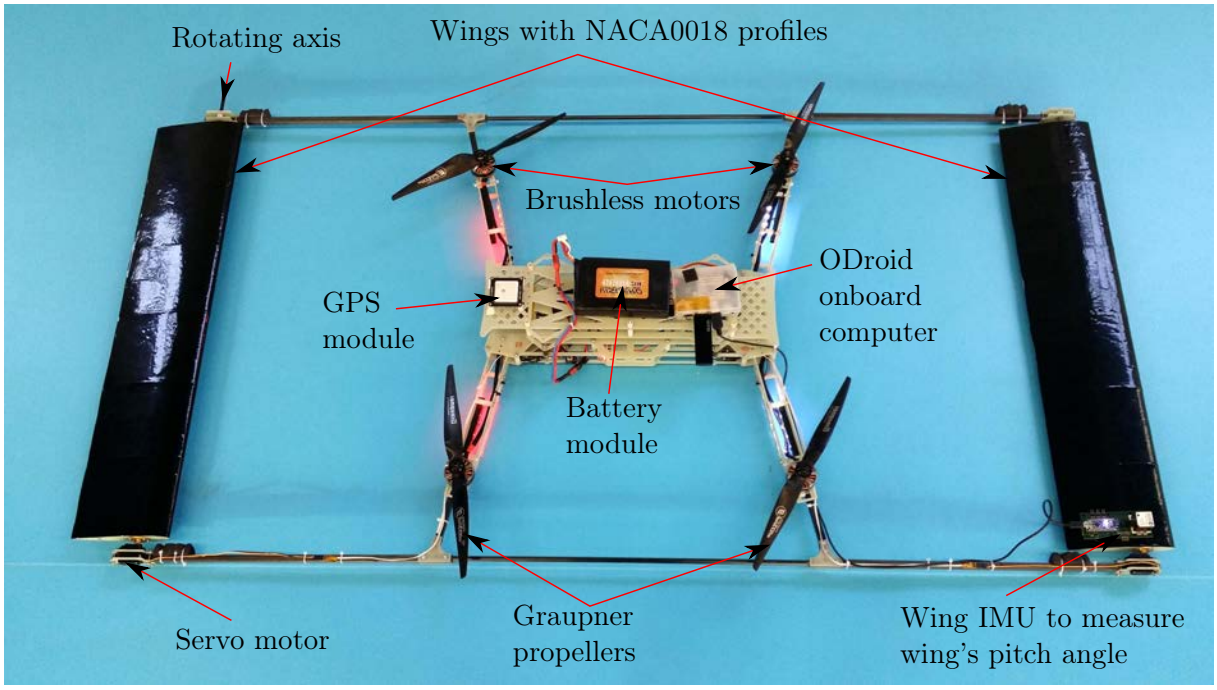

Figure 4.1: Convertible UAV prototype

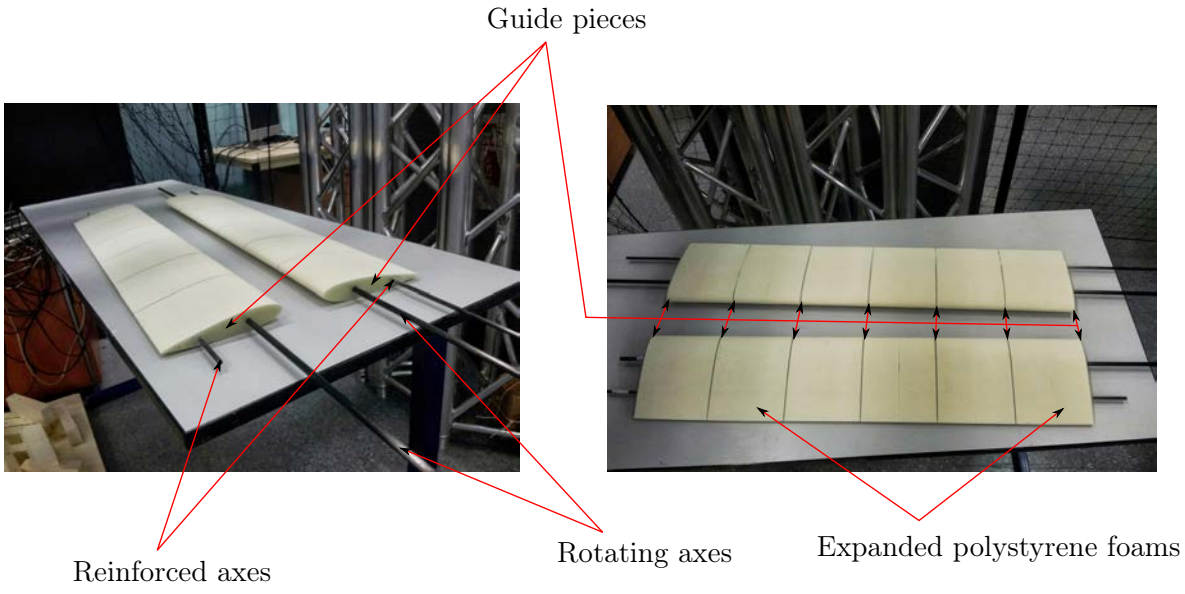

Figure 4.2: The wings after fabrication

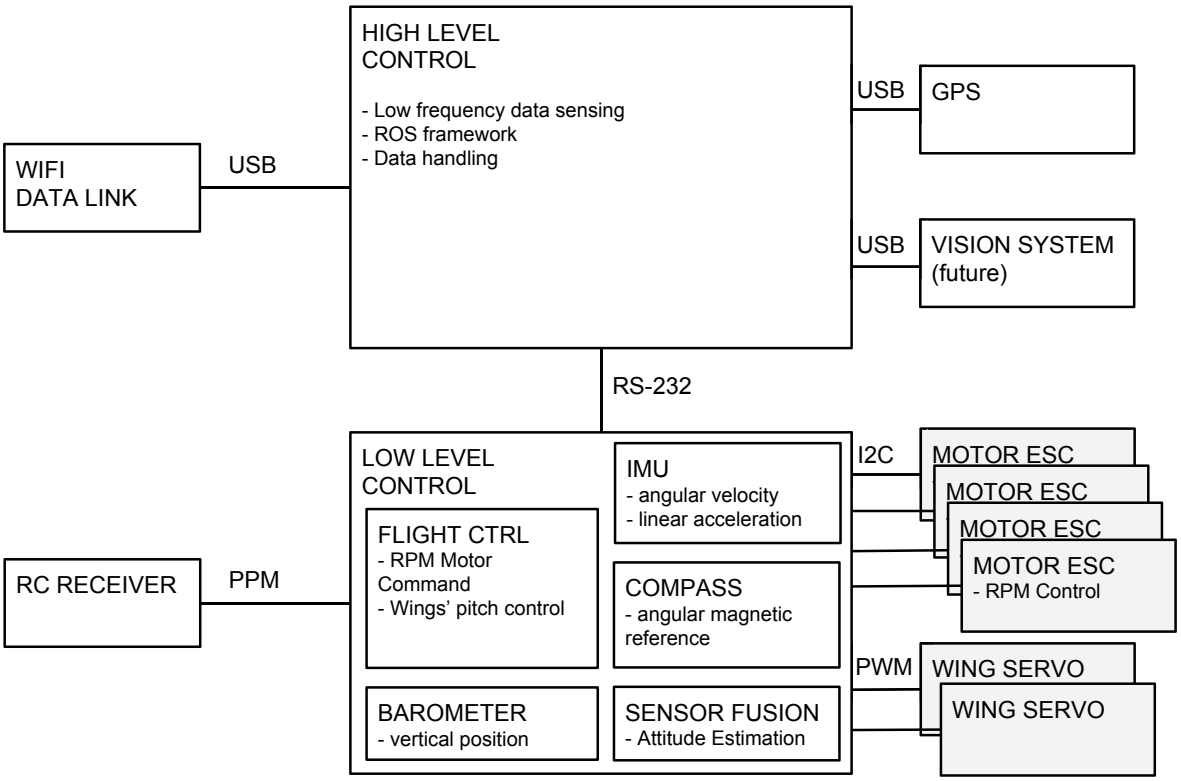

Figure 4.3: System architecture overview

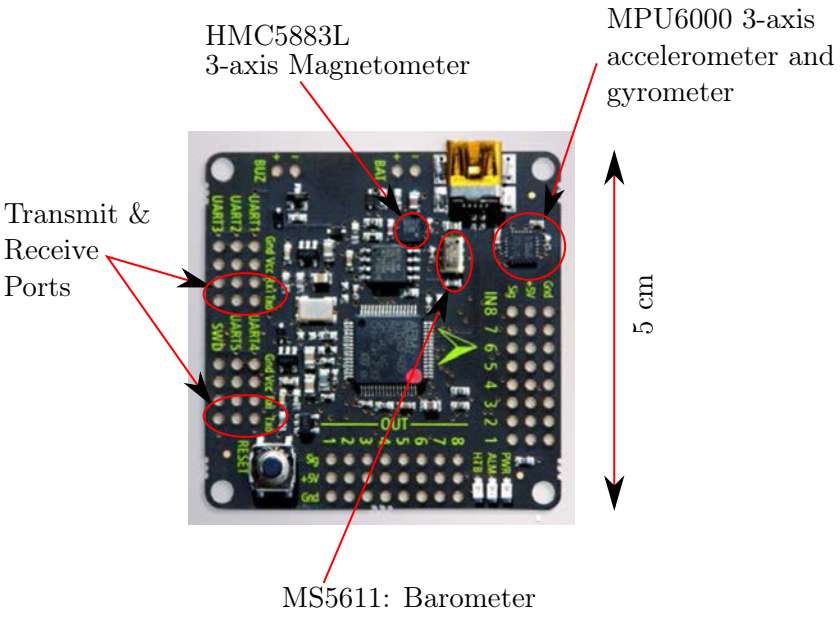

Figure 4.4: Quanton flight controller board

4.1.1 Low Level Control

The low level control is responsible for several tasks. First, it receives the control signals from the pilot's joystick via RC receiver. Second, it receives the data from built-in sensors for estimation of the UAV states such as altitude, angular velocity, linear acceleration, and (consequently via sensor fusion) attitude. Then, the embedded control algorithm is executed in the Quanton flight controller. Finally, the control output is sent to the motor ESCs and wing servos.

4.1.1.1 Quanton flight controller

The principle component of the low level control is a small-size (5 cm $\times$ 5 cm board as shown in figure 4.4) flight controller. It includes a microcontroller (STM32F405 32bit ARM Cortex-M4 CPU with FPU, 168MHz, 192kb RAM and 1024kb flash) and a set of embedded sensors (accelerometer, gyro, magnetometer, and barometer). Input and output ports are also presented in the microcontroller circuit in order to connect to additional peripherals (e.g. other sensors, radio receptors, motor controllers, etc.).

Accelerometer and gyro sensors

The IMU contains a three-axis accelerometer and a three-axis gyro on the same integrated circuit with the model MPU6000 with the following characteristics:

- The sensors communicate with the microcontroller using the SPI (Serial Peripheral Interface) bus.
- For accelerometer, we can configure the range to be $\pm 2g, \pm 4g, \pm 8g,$ or $\pm 16g$. At the smallest range $\pm 2g$, the resolution is highest at $6 \times 10^{-5} g$.
- For gyrometer, we can configure the range to be $\pm 250^\circ/\text{s}, \pm 500^\circ/\text{s}, \pm 1000^\circ/\text{s},$ or $\pm 2000^\circ/\text{s}$. At the range $\pm 250^\circ/\text{s}$ the resolution is $0.0075^\circ/\text{s}$.

Figure 4.5: Motor mounting on the UAV frame

Motor Dimensions (Diameter × Length)	44.3 mm × 25 mm
Weight	0.108 kg
Idle current at 10 V	0.5 A
Max continuous current	27 A
Max continuous power	450 W
Internal resistance	0.132 Ω

Table 4.1: Main characteristics of motor T-4008 KV600

- The data frequency can be programmable up to 200 Hz, which is largely sufficient for our UAV data acquisition.

Magnetometer (compass) and barometer

These two sensors are connected on the same bus I2C as slaves for the microcontroller. Therefore, it is not possible to obtain the data from these two sensors at the same time instance. We have to alternate the data demand.

The magnetometer (HMC5883L) enables 1° to 2° heading accuracy. The maximum output rate of this sensor is 160 Hz. The full-scale range is ±8 gauss whereas the field resolution is 2 mili-gauss.

The resolution of the barometer (MS5611) permits detecting the pressure variation of 0.01 mbar, which corresponds to altitude variation of approximately 8 cm. In practice, because of the important noise level, the altitude precision is about ±50 cm. Since the pressure data acquisition takes rather long (20 ms), we can obtain up to 50 data values per second.

4.1.1.2 Main Motor

The motors chosen in this project are T-4008. They are powerful motors capable of delivering high continuous power (maximum 450 W) and handling high current (maximum 27 A). When connecting with a 13-inch propeller, the maximum speed and maximum thrust of the motor are approximately 6500 RPM and 12 N respectively, which are largely sufficient for our project. The image and the main characteristics of these motors are shown in figure 4.5 and table 4.1.

Property	Mikrokopter 1.2	Mikrokopter 2.0	ESC32
Processing Power	ATMEGA8	ATMEGA168	STM32F103
Open Source (Software)	Yes	No	Yes
Open Source (Hardware)	Yes	Yes	No
Interface	I2C	I2C	I2C / CAN / CLI
FET	20A	35A	35A
Closed loop function	No	No	Yes

Table 4.2: Comparison between three ESCs

4.1.1.3 Electronic Speed Control (ESC)

The UAV developed in this project will be expected to operate mostly outdoor with partially unknown environment and obstacles. Therefore, precise control and fast response are required so that the UAV is able to avoid detected obstacles and to track the required trajectory accurately. Test flights with our early quadrotor prototypes highlighted a few issues:

- response of the quadrotor is different when battery is full and battery is almost emptied,
- badly damped transient is observed when trying to push the control gains for attitude control.

Moreover, for the convertible UAV, information about actual speed and current consumption of each motor is required in order to calculate the power consumption. Therefore, a fast and highly accurate ESC is required. Since ESCs have been traditionally designed for fixed-wing airplane or helicopter applications, they are programmed to vary the throttle command to the motor in a gentle way to prevent sudden stress on the propellers and the airframe. However, for multirotor applications, the rotational speeds of the motors usually change very fast. This rapid variation can be controlled by modern and dedicated ESCs for multirotors. Three ESCs are compared in this project: Mikrokopter 2.0, Mikrokopter 1.2, and Autoquad ESC32. These three ESCs are chosen because Mikrokopter was the initial based platform for quadrotor in our laboratory, and Autoquad ESC32 is a new controller with promising capabilities. Based on the comparison between different criteria as briefly shown in table 4.2, the Autoquad ESC32 (figure 4.6) is chosen because:

- it has more processing power, RAM, and flash memory than the Mikrokopter one;
- its CPU is Arm Cortex M3, therefore, Keil IDE (Integrated Development Environment) which is currently used to develop flight controller source code can be used;
- its source code is available;
- it supports both I2C and CAN (Controller Area Network) interface;

Figure 4.6: Autoquad ESC32 (autoquad.org)

	CAN	I2C
Bandwidth	1000 kbit	400 kbit
Maximum frame length	8 byte	No limit
Approach	Message based / Asychronous	Address based / Synchronous
Available tools	N/A	USB-ISS
Flight Controller code	N/A	Available
Transmission method	differential	signal and ground
Used before in other UAV	No (will be used in autoquad soon)	Yes (Mikrokopter)

Table 4.3: ESC communication comparison

- it has Command Line Interface (CLI) which eases the process of debugging and configuration;
- the current rating of the field-effect transistors (FETs) used in ESC32 is similar to those of Mikrokopter 2.1 which has high current rating (35A continuous and 40A peak);
- the closed loop speed control is already implemented in the official firmware.

However, a disadvantage of ESC32 is that the electronics schematic is not provided. Nevertheless, this is considered to be a minor disadvantage for this project. Furthermore Mikrokopter 2.0 is closed source (i.e. no source code available) and Mikrokopter 1.2 uses FETs with low current rating and weak CPU. Due to the shortcomings of Mikrokopter 1.2 and Mikrokopter 2.0, ESC32 easily stands out as the best candidate.

There are two options available regarding the communication between the AutoQuad and the flight controller Quanton: CAN and I2C. The advantages and disadvantages of each interface are highlighted in table 4.3. CAN interface has higher bit-rate, can communicate in asynchronous

Figure 4.7: Graupner E-prop 13 × 8

mode, and can tolerate noise slightly better. However, in this project I2C is selected and the reasons are shown below.

- I2C speed (400 kbit) is enough for this project.
- Development tools[1] for I2C are already available in our laboratory. This minimizes time and effort to acquire additional tools.
- Previous flight controller uses I2C interface. Therefore, I2C source code in the flight controller can be reused.
- It has been used for UAV community for some time (more than two years). Therefore, we can assume that the I2C interface can be safely used in UAV operating environment.

4.1.1.4 Propeller

Initially, we selected the APC propeller family for our convertible prototypes since they are well-documented [52, 53] and have high efficiency. In light of this reason, APC SlowFlyer 11 × 4.7 was selected for the simulations in chapter 2 and chapter 3 of this thesis.

Unfortunately, the weight of our prototype (current weight $m = 3.2$ kg) was under-estimated at that time so that APC SlowFlyer 11 × 4.7 propellers do not provide enough thrust to fly efficiently. For this reason we use Graupner E-prop 13 × 8 as depicted in figure 4.7.

The principal disadvantage of Graupner propeller is that their documentation is scarce in the literature. Indeed, the aerodynamic data are not available from the manufacturer. There are only a few references limited to small-diameter (maximum 11-inch diameter) Graupner propeller data from wind tunnel tests [52, 84]. Nonetheless, we have chosen Graupner E-prop 13 × 8 propellers for our platform purely based on mechanical requirements and control reasons. Since these propellers possess thin and rigid blades, they provide fast control responses with less vibrations than APC and a few other propellers. The energy performance of different propellers remains a subject for future experiments.

4.1.2 High Level Control

The high level control is principally responsible for receiving and logging the data from the low level controller and the UAV's position/speed information from the GPS module, Other high level tasks, such as visual servoing, image processing, trajectory planning, localization, etc. are envisaged for this convertible UAV in the future. In the following, we describe the main components of high level control.

4.1.2.1 ODroid onboard computer

The ODroid (Open Android) onboard computer is an open-source development platform. It includes a Samsung Exynos5 Octa : Cortex^{TM}-A15 and a Cortex^{TM}-A7 processors with 2GB DDR3 RAM together with various input/output ports such as USB, HDMI, etc. Robot Operating

[1] e.g. USB-ISS interface between PC and I2C, SPI, Serial port, see robot-electronics.co.uk

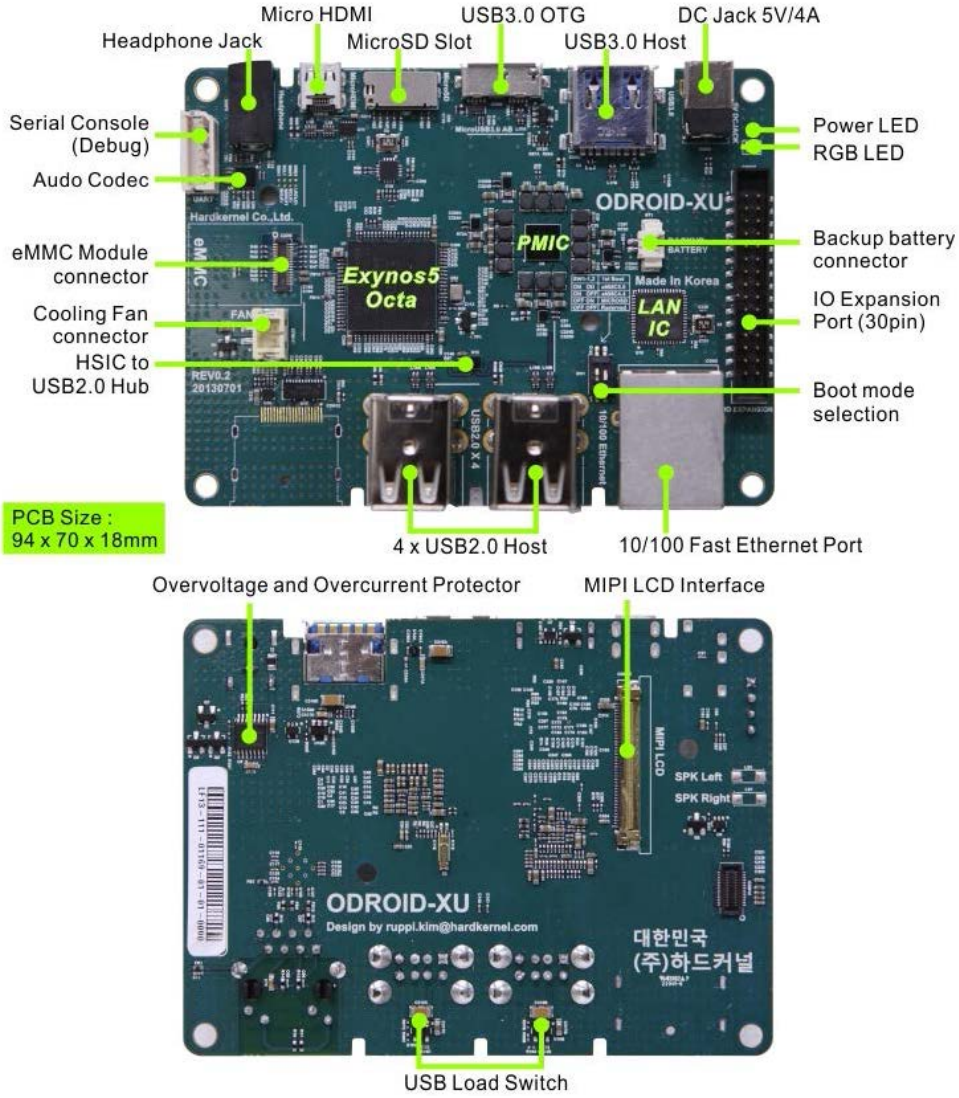

Figure 4.8: ODroid-XU onboard computer (hardkernel.com)

System (ROS) is installed on the ODroid. ROS is an open-source operating system for robots. It provides the services including hardware abstraction, low-level device control, implementation of commonly-used functionality, message-passing between processes, and package management. It also provides tools and libraries for obtaining, building, writing, and running code across multiple computers (see ros.org). The data can be displayed in real-time as well as saved as text files for analysis and plotting.

4.1.2.2 GPS Module

The GPS module is Ublox NEO-6M as illustrated in figure 4.9. It has fast satellite fix (1–27 s) and fast navigation update rate (10 Hz). The horizontal position accuracy is standard (2.5 m) but the velocity and heading accuracy are high (0.1 m/s and 0.5° respectively). This GPS module communicates with the ODroid via USB.

Figure 4.9: GPS module Ublox NEO-6M

4.2 Model Parameters

The main parameters of the convertible UAV are listed below:

- total mass of the UAV $m = 3.2$ kg with 0.5 kg battery (5.1 Ah, 4S1P) or $m = 3.0$ kg with 0.3 kg battery (2.6 Ah, 4S1P),
- NACA0018 wing chord length $c = 0.15$ m,
- total wing area $\Sigma = 0.22$ m^2.

The propellers Graupner E-prop 13×8 have the following parameters:

- propeller radius $R = 0.165$ m,
- propeller thrust coefficient $\kappa_T = 2.7 \times 10^{-5}$,
- propeller torque coefficient $\kappa_Q = 1.3 \times 10^{-6}$.

These propeller coefficients are obtained with our static test bench as described in appendix B. The mass distribution of the convertible UAV is illustrated in figure 4.10. The geometric parameters are:

$$2\ell_1 = 0.5,\ 2\ell_2 = 0.55,\ 2\ell_3 = 0.15,\ 2\ell_4 = 0.15,\ 2\ell_5 = 0.08,\ 2\ell_6 = 1.44,\ 2\ell_7 = 0.74$$

where we consider the battery (0.5 kg) dimension.

The moment of inertia (unit: kg m^2) around the axes $\boldsymbol{i}$, $\boldsymbol{j}$, $\boldsymbol{k}$ are (refer to appendix D for detailed calculations):

$$J_{11} = 0.273,\ J_{22} = 0.093,\ J_{33} = 0.366 \tag{4.1}$$

In the case without the wings, one has:

$$J_{11} = 0.083,\ J_{22} = 0.052,\ J_{33} = 0.135$$

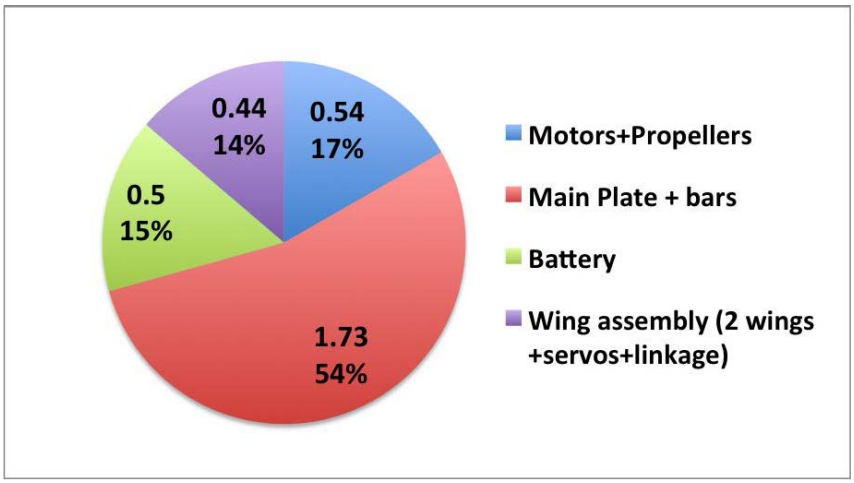

Figure 4.10: Mass distribution of our convertible UAV (unit: kg)

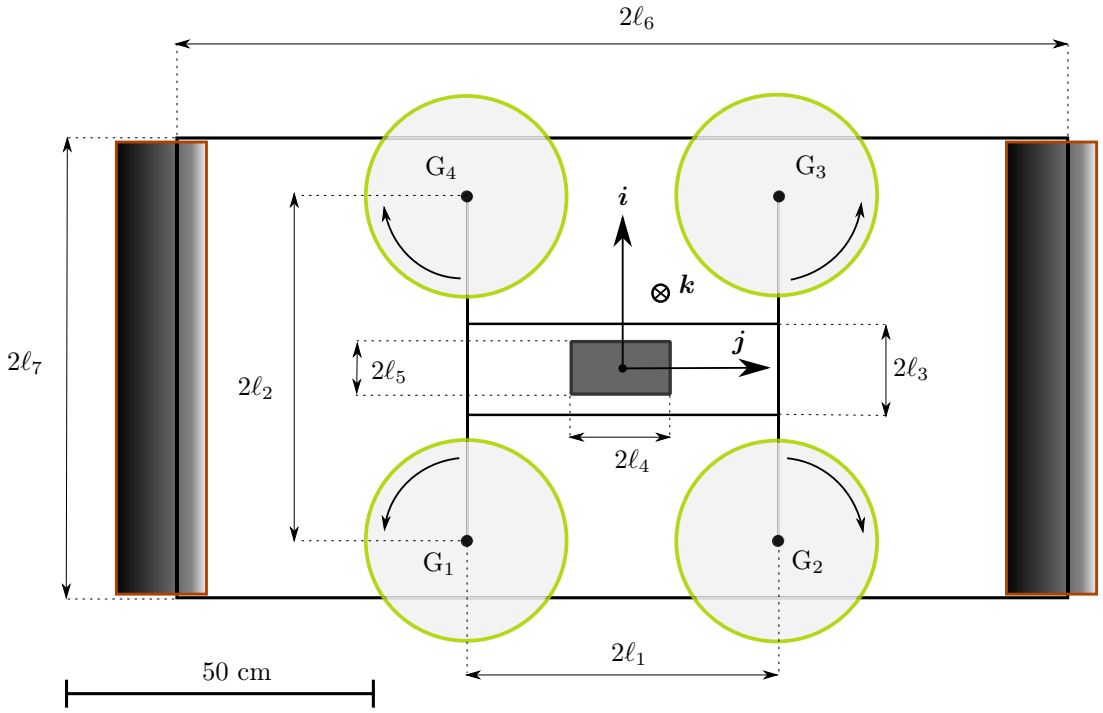

Figure 4.11: Top-view schematic of our convertible UAV

Figure 4.12: View of wing servo and IMU during the test

We can observe that impact of the wings in terms of inertia around $\boldsymbol{i}$ and $\boldsymbol{k}$ is particularly important. In addition, we can see how the distance $2\ell_6$ impacts on J_{11}:

$$2\ell_6 = 1.2 \Longrightarrow J_{11} = 0.215$$
$$2\ell_6 = 1 \Longrightarrow J_{11} = 0.175$$

The distance ℓ_6 can be reduced. For initial flight tests, we have chosen a relatively large value of ℓ_6 to diminish the risk of significant aerodynamic interaction between wings and propellers. In terms of flight maneuverability, small values of ℓ_6 leading to reduced moments of inertia are clearly desirable.

4.3 Wing Servo Control Tests

Currently the wings pitch angles w.r.t. the UAV's main body are controlled by servo motors. The servo model is Hitec HS-5087MH, which is very lightweight (22 g) and has maximum torque of 0.42 Nm. The purpose of these tests is to evaluate the response of the wing servos w.r.t the UAV desired orientation. An IMU is mounted on the wing in order to measure the wing pitch angle and angular velocity (i.e. accelerometer is used as inclinometer), as shown in figure 4.12. The wing's IMU model is ADIS16407. This is a spare unit that we used when testing various quadrotor prototypes.

In the first test, the UAV is inclined manually around its pitch axis (see the angular velocity in figure 4.13) and the servos are controlled so as to ensure that the wing's pitch angle (inclination angle w.r.t the ground, which is equal to $90^\circ - \zeta$ in this test) remains near zero. Indeed, figure 4.14 shows that this angle is quite close to zero, although in the transient zone, e.g. from $t = 14.7$ s to $t = 16$ s, there are oscillation in the measurements. The maximum non-transient deviation is small, around $\pm 3^\circ$. Nonetheless, these errors are not negligible since the wings' angle of attack have strong impact on the aerodynamic forces especially at high speed.

In the second test, the wing is given desired pitch angle with increment of about 10°. Figure 4.15 shows the response of the wing's pitch angle, as measured by the wing accelerometer. The pitch angle converges fast to desired attitude, but in some cases, there are offset errors of 2° to 3°. In the transient period the measurement deviation error is quite high due to sudden changes of attitude.

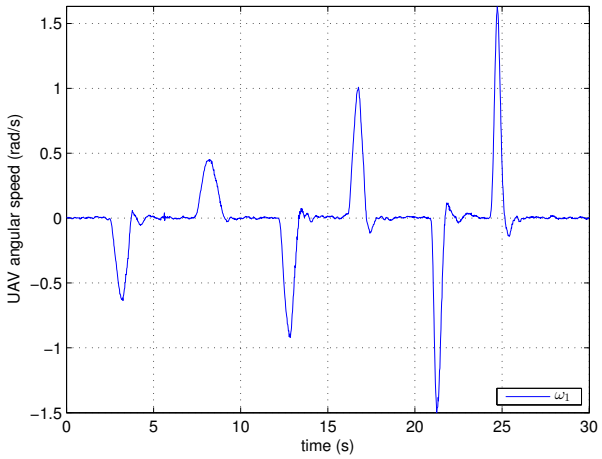

Figure 4.13: First component of angular velocity measured by UAV gyro

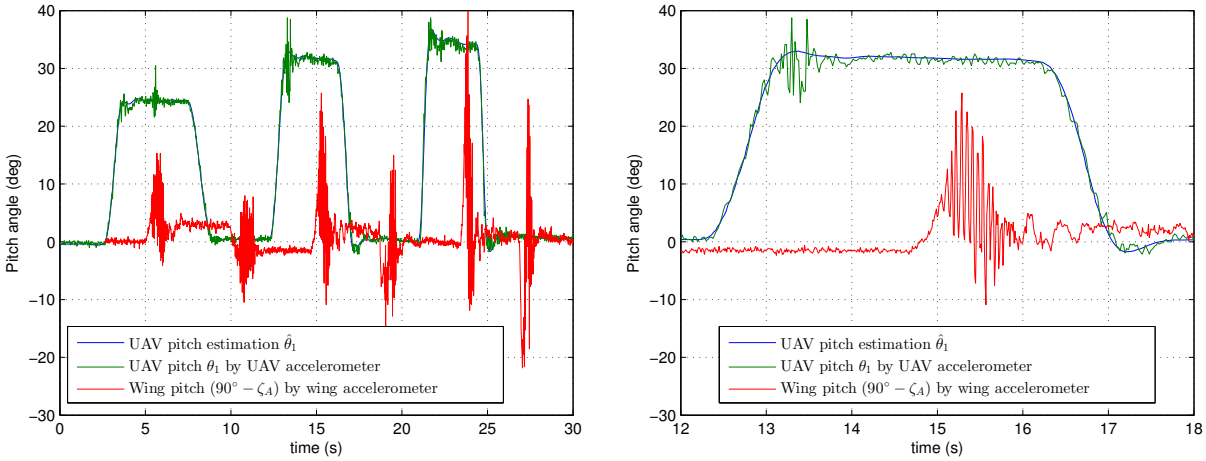

Figure 4.14: Comparison between UAV's pitch angle estimation, UAV's pitch angle measurement by accelerometer, and wing pitch measurement by wing accelerometer

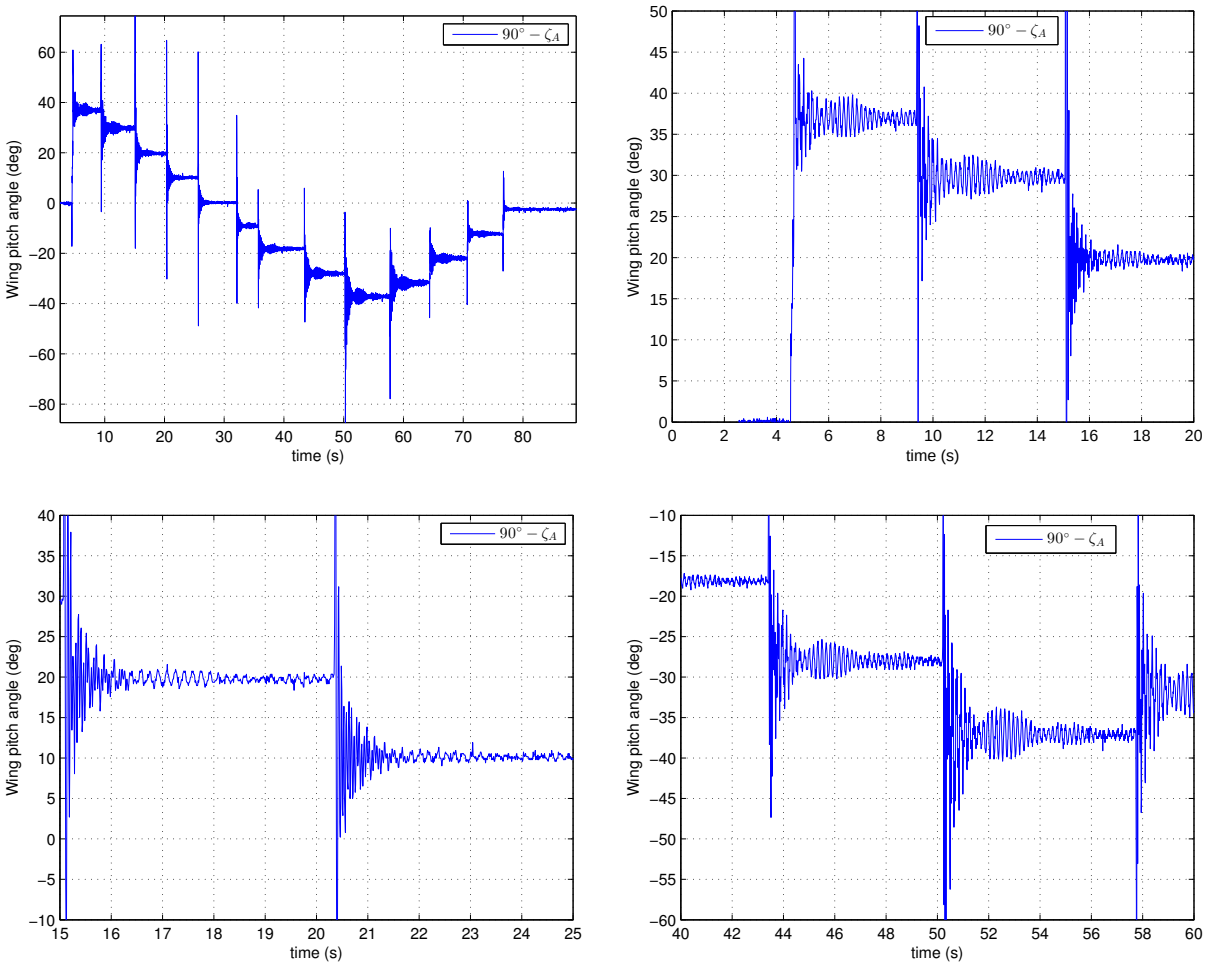

Figure 4.15: Wing pitch angle (inclination angle w.r.t the ground) estimated by wing accelerometer measurements

From these two small experiments, we can conclude that the response of the wing servos is quite fast but offset errors of up to 3° might be present. This accuracy is not enough to ensure a precise control of the wings angle of attack. Although our preliminary flight tests (including the first test reported below) have been made with the servos here presented, we are currently looking for a better solution to obtain a more precise wing control.

4.4 Preliminary Flight Tests

In this section, we present the results of the first few test flights. The objectives of these flight experiments are to verify the function of the hardware/software system and to test the attitude control in teleoperation. Due to the time needed to develop the platform, flight tests have only started this fall (in September). As could be anticipated, the first flights have revealed weaknesses of the initial design:

- Servo motors for wings control: We have already mentioned above that the servos were not accurate enough to ensure a very precise pitch angle of the wings w.r.t. the propellers' plane. In addition, these servos turned out to be not robust enough to sustain flight with significant speeds. They broke after a few outdoor flights. In these flights the UAV reached a velocity of 6–7 m/s (measured by the GPS), with a facing wind of a few m/s.
- Main motors control: Initially, I2C interface was used to control the motors. During first flight tests, it was discovered that the motors were saturated, although their rotational speeds were well below the maximum speed. In addition, motors disarmed in several occasions. It seems that data congestion (the magnetometer and barometer also communicate through I2C) and/or electrical interference (proximity of power cables with signal cables) had occurred. At present, I2C bus are only used to send logging data from motors to the flight control board. The motors are now controlled by PWM signals.

Nonetheless, during these first flights, other software and hardware components functioned well. We have also verified that the GPS model provides accurate longitudinal and latitude coordinates (less than 2 m error). The altitude information from GPS, however, was not reliable.

We now present experimental data of a few preliminary indoor flights. These flights have been made in the university's gymnasium. The obvious advantage of indoor flight is the absence of wind disturbance. However, the disadvantages are constraint space (the length of the gymnasium is about 30 m) and unavailability of velocity measurements.

4.4.1 First indoor teleoperation experiment

The control mode used in this experiment is teleoperation control without velocity measurement (see section 3.2.1). However, in this experiment, the desired thrust is given by the pilot via the joystick. In other words, the altitude measurements by barometer are not used and these experiments can only validate the control of the UAV's attitude. Both the main motors and the servos HS-5087MH are controlled by PWM. In this test, the lighter battery (0.3 kg) is used so that the UAV mass is about 3.0 kg. The wings are given zero reference pitch angles (the objective is that they remain parallel to the ground), i.e. $\zeta_{r,A} = \zeta_{r,C} = 90°$.

The gains for attitude control are: $k_{\gamma,1} = 3.2$, $k_{\gamma,2} = 3$, $K = \begin{bmatrix} 13 & 0 & 0 \\ 0 & 11.9 & 0 \\ 0 & 0 & 2.25 \end{bmatrix}$.

The attitude estimation is accomplished by fusing gyrometers and accelerometers data, as in Eq. (3.32) with $k_{\text{est},\gamma} = 0.01$. The flight can be divided into five different time zones (see e.g.

figure 4.16). In Zone 1, the UAV takes off and achieves a few meter altitude quasi-stationary flight at $t = 10$ s. Then in Zone 2, it inclines "nose-down" and flies forwards for a few seconds. At $t = 13$ s, the UAV is commanded to incline "nose-up" to reduce the speed and to fly rearward. In Zone 3, the UAV reduces the altitude and lands on the ground at $t = 27$ s. At $t = 30$ s, the UAV takes off again. In Zone 4, when it achieves sufficient altitude, the UAV performs forward, rearward, and again forward maneuvers. Finally it lands on the ground at $t = 59$ s. During the periods when the UAV is near or on the ground, i.e. in Zones 1, 3, and 5, the vehicle is in ground effect for a few seconds. Therefore, the data obtained in those periods are often perturbed by strong unknown disturbances.

Note that in this section, some data in the plots (essentially the angular velocity measurements given by the gyrometers) are filtered by simple moving-average filters to partly remove noise. Figure 4.16 compares the reference attitude (given by joystick) with the estimated attitude data from IMU measurements. The pitch angle response is fast and accurate except when the UAV is near the ground. By contrast, there is a deviation in the roll angles as compared to the reference values, as illustrated in figure 4.16(b). In an attempt to understand this deviation, we plot the reference angular velocity and the angular velocity components measured by the gyrometers in figure 4.17. Indeed, around the roll axis $\boldsymbol{j}$, there is a significant static offset of about 0.3 rad/s in Zone 2 and 4, as depicted in figure 4.17(b). As for the yaw control, although the rough trending of the angular speed is consistent with the reference values, the UAV seems unable to reach the reference angular speed (figure 4.17(c)). Figure 4.18 compares the reference thrust/torque with the values reconstructed from the angular speed of the rotors (the torque values are only available in Zone 1 and 2 due to unexpected I2C communication loss). The thrust and torque data show very good track with reference values. Then one might wonder why the angular velocity tracking is not very good. Figure 4.18 only proves that the response of the main rotors is fast and accurate. However, the real values of the thrust/torque may not match the values reconstructed from the angular speed of the rotors due to model imperfection. Indeed, UAV is slight heavier on the left side (i.e. the side which does not has the servo motors in figure 4.1). This creates an additive perturbation torque. Since the roll angular velocity offset is 0.3 rad/s, we can estimate the roll torque offset of about $0.3 \times J_{33} = 0.028$ Nm. In addition, we can estimate the attitude offset that is inversely proportional to the attitude gain (see Eq. (3.22)): $0.3/k_{\gamma,2} = 0.1$. Suppose that we have compensated for these offset, we can then plot the corrected roll angles and angular velocity as in figure 4.19. These static perturbation torque can be compensated via the observer proposed in section 3.2.1. This will be tested in the near future.

As for the yaw velocity offset, currently we have little yaw control authority because of very large moment of inertia around $\boldsymbol{k}$ and small reaction control torque of the propellers. We may increase the yaw control gain and re-perform the experiment.

Recall that we choose small gain for attitude estimation since the gyroscope measurements have faster update and more reliable than accelerometer ones. Indeed, when the UAV has just landed in Zone 5, the estimated attitude angles converge very slowly to zero, as shown in figure 4.16.

Figure 4.20(a) depicts the total current intensity of the main motors. As expected the trending is similar to the thrust trending in figure 4.18(a). From the current values, we can have an idea of the motor power consumption as illustrated in figure 4.20(b) assuming that the battery supply voltage is constant (14.8V with 4S1P battery). In reality, the battery supply voltage varies depending on the remaining charge. Since the flight period is short, the constant voltage assumption is valid.

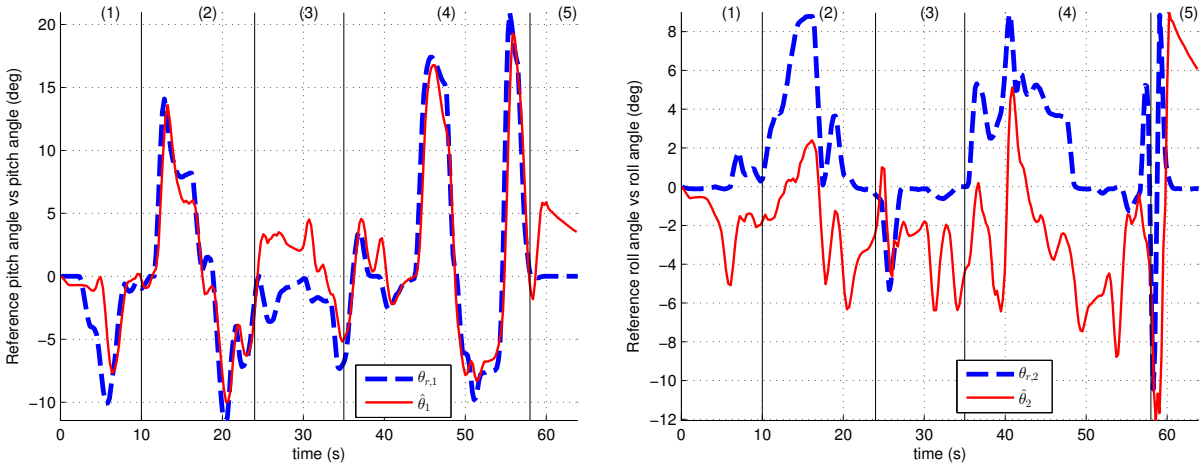

(a) (b)

Figure 4.16: Reference attitude (from joystick) versus UAV attitude estimated from IMU (first experiment)

4.4.2 Second indoor teleoperation experiment

We are finding better solution for wing control. The first solution that was replacing the broken Hitec servos by GMB5010 brushless motors (figure 4.21). This type of motors is designed to drive gimbal for cameras up to a weight of 0.5 kg. They are more robust than the servos but they are also heavier (98 g each). The two wing motors are now mounted diagonally as shown in figure 4.22.

The control and estimation gains are identical to the ones in the previous experiment. The results obtained for this second flight were not quantitatively different from the first one but the experiment consisted of stationary and quasi-stationary flight, which provide complementary information w.r.t. the previous flight.

In Zone 1, the UAV takes off to achieve an altitude of about 1 m in 13 s. Then it is given zero pitch and nearly 2° roll reference angles in Zone 2. Finally, in Zone 3, the UAV is controlled to track some small reference attitude angles. The attitude response is acceptable (see figure 4.23), although there are some oscillations, notably in the roll axis. With the wing motors mounting diagonally, the offsets in roll angle (figure 4.23(b)) and angular velocity (figure 4.24(b)) are less than the previous experiment. However, examining figure 4.24(b) reveals a small negative offset in yaw angular velocity. This can be explained by the mechanical imbalance of the UAV. Indeed, the wing motors are heavier than the previous servos, so that the structure slightly bends downward at the wing motors locations. Looking at figure 4.22, the front wing bends down to its left side, and the back wing bends down to its right side. When the UAV moves laterally towards its right side (The roll angle is positive in Zone 1, Zone 2, and partly Zone 3 as shown in figure 4.23(b).), the lateral airflow tends to generate greater aerodynamic forces on the front wing than the back wing. Consequently, the UAV has tendency to rotate counter-clockwise around its yaw axis. To alleviate this effect, we are currently considering changing the location of the wing motors.

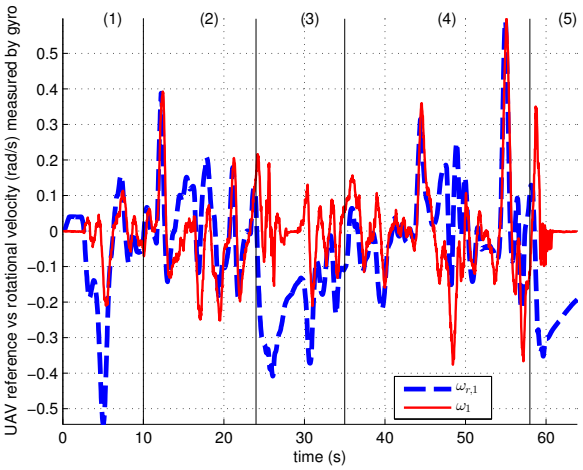

(a) Around pitch axis

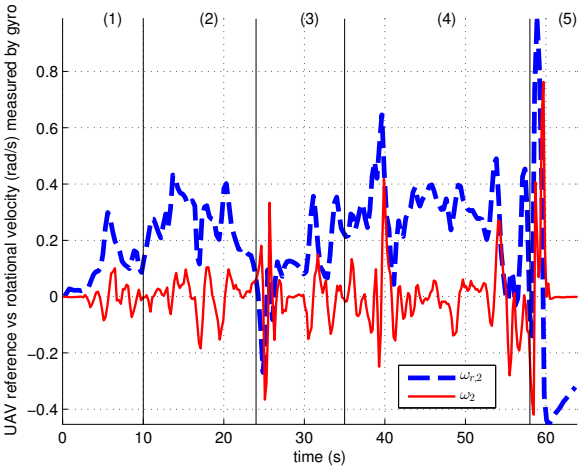

(b) Around roll axis

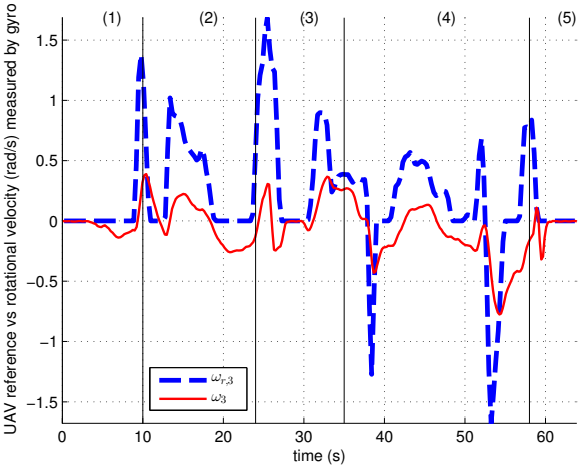

(c) Around yaw axis

Figure 4.17: Reference angular velocity versus UAV angular velocity estimated from IMU (first experiment)

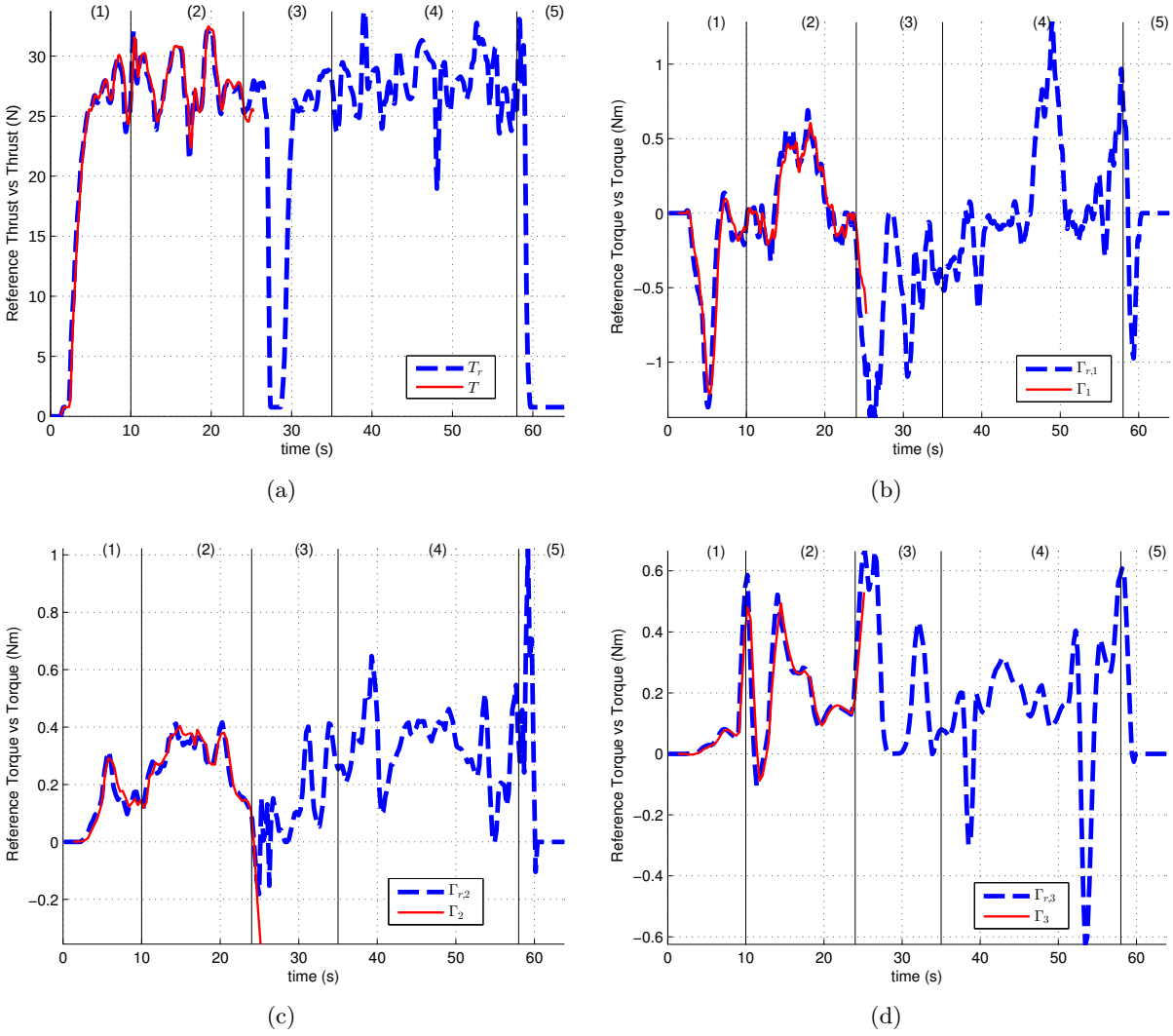

Figure 4.18: Reference control thrust/torque versus UAV thrust/torque reconstructed from angular speed of rotors (first experiment)

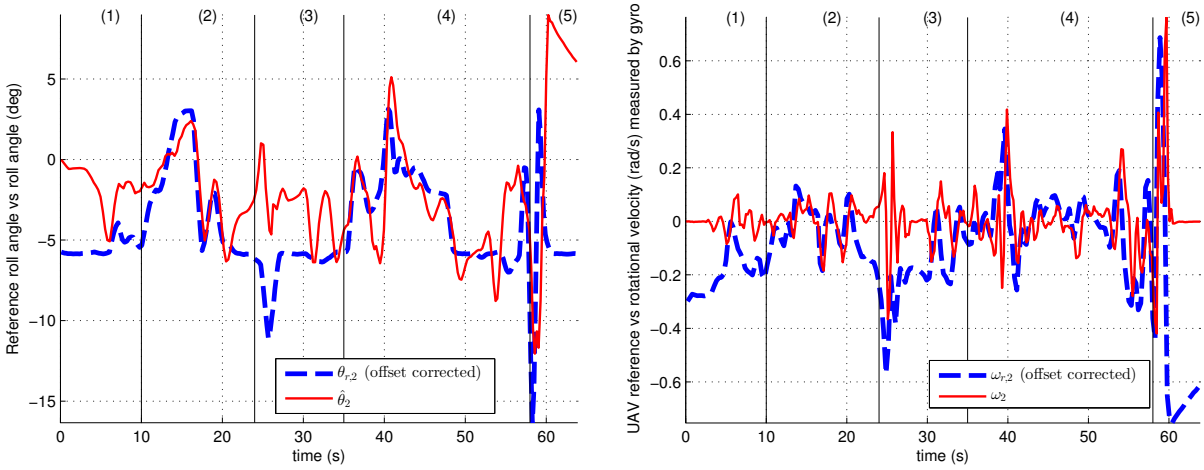

(a) (b)

Figure 4.19: Roll angle and angular velocity after offset correction (first experiment)

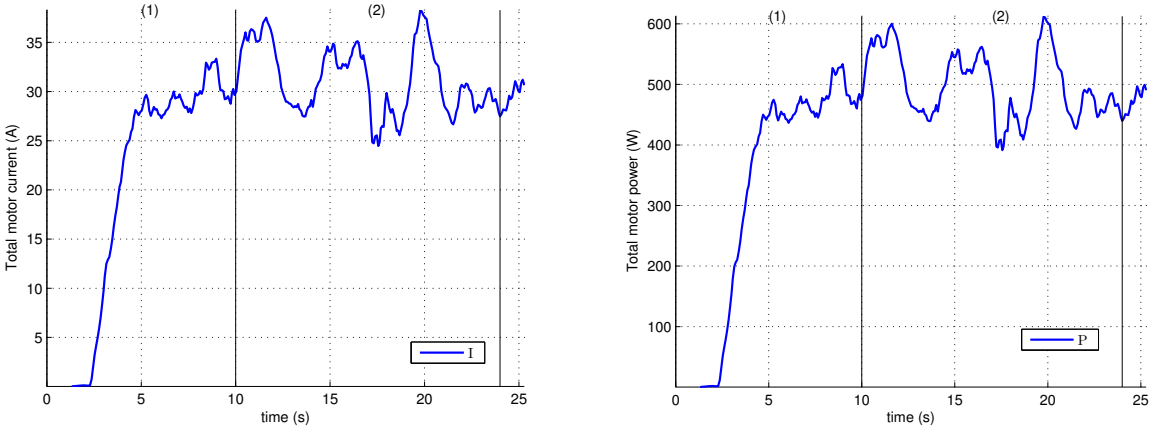

(a) (b)

Figure 4.20: (a) Total current intensity and (b) total power of the motors (first experiment)

Figure 4.21: GMB5010 wing motor (mikrokopter.altigator.com)

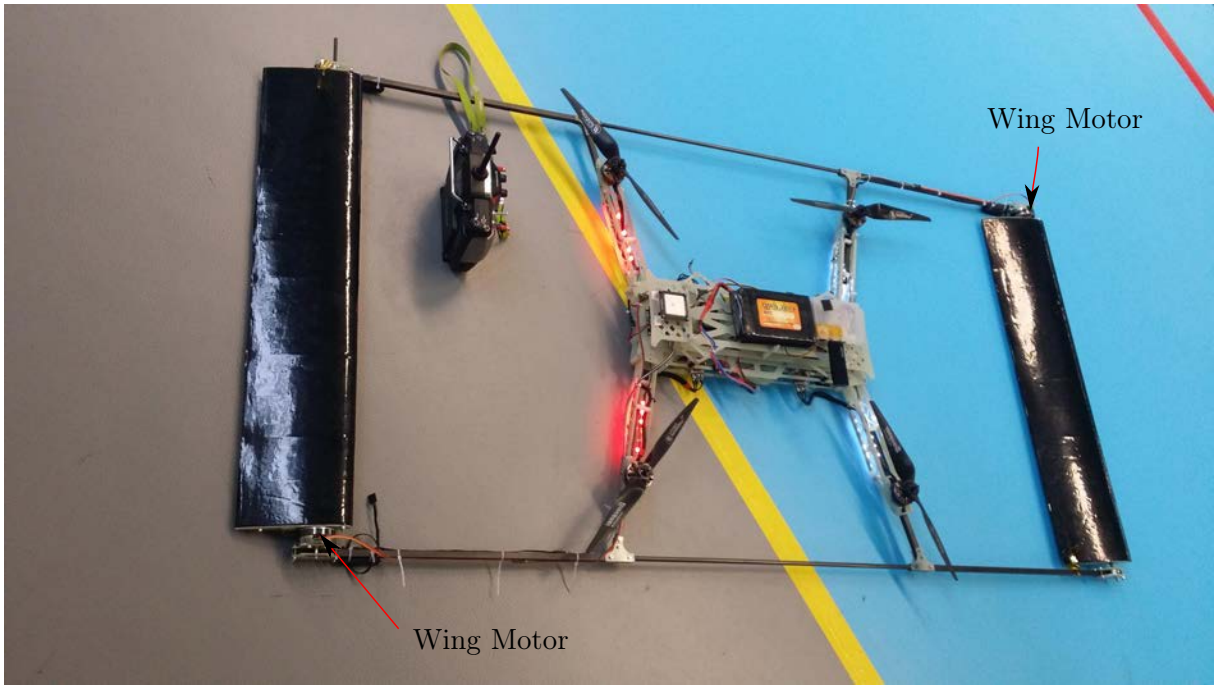

Figure 4.22: New wing motors installed on our convertible UAV

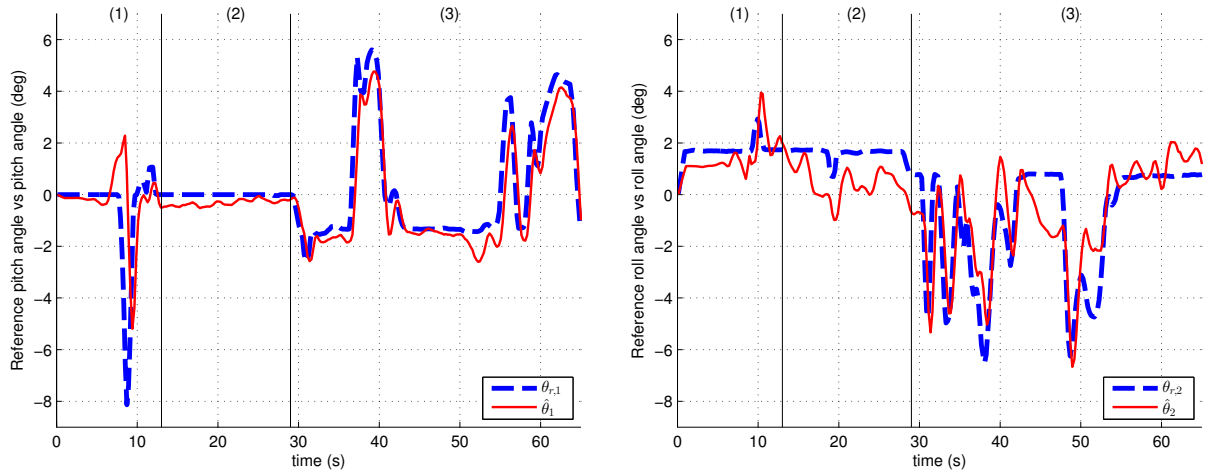

(a) (b)

Figure 4.23: Reference attitude (from joystick) versus UAV attitude estimated from IMU (second experiment)

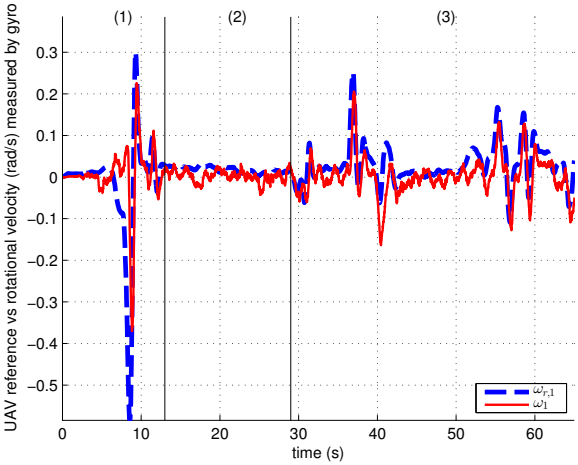

(a) Around pitch axis

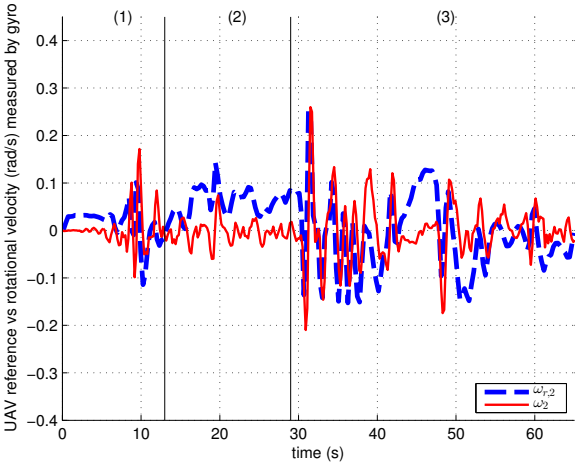

(b) Around roll axis

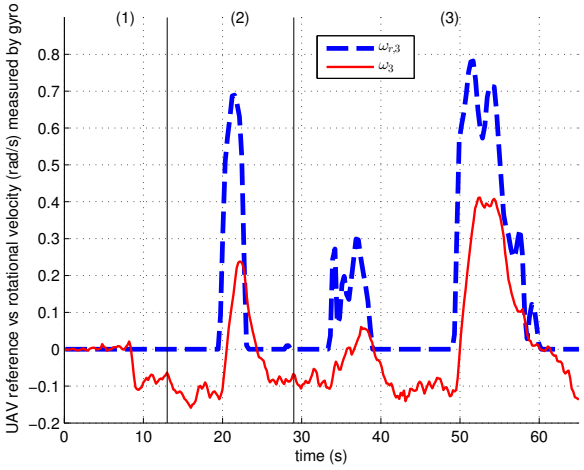

(c) Around yaw axis

Figure 4.24: Reference angular velocity versus UAV angular velocity estimated from IMU (second experiment)

4.5 Chapter Summary

In this chapter, we have presented the mechanical prototype and hardware/software architecture of our convertible UAV. A brief description of the fabrication of the UAV including the wings has been introduced. In addition, important components of the low level and high level architecture with their salient characteristics are described. In particular, some issues associated with the ESC (control at low battery level and badly transient response) during early experiments are briefly discussed. To address these issues, we have selected fast and reliable Autoquad ESC32. We have also described the inertia calculation of the convertible UAV, showing significant change in terms of inertia values when adding the wings. Before the flying experiments, the wing servos are tested and their responses are fast enough but the accuracy is not very good. Preliminary flight experiments revealed some shortcomings of servo motor robustness and propellers' motors control. Whereas issues concerning propellers' motors were resolved, the control of wings pitch angle is not completely satisfactory.

Finally, we have presented the results of two preliminary experiments and discussed the results. Clearly, we are only at the very beginning of the validations of our control algorithm and energy modeling models. The attitude control of the platform is now satisfactory. Estimation of torque and perturbations will be tested shortly and should provide more accuracy on the attitude control. Altitude control will come next and should allow us to start evaluating wings impact on the energy efficiency.

Conclusion and Perspectives

This thesis is devoted to the conception, modeling, and control of a new convertible UAV. The first chapter of this manuscript provides a short introduction to aerial vehicles: fixed-wing, VTOL, and convertible aircraft. Thanks to their flexibility, convertible aircraft, and especially convertible UAVs, have become increasingly popular. Inspired from a classical quadrotor, our convertible UAV has the potential of efficient cruising flight while retaining the simplicity of a quadrotor.

The main incentive for convertible UAVs is their energy performance in cruising flight but the literature on this subject for small convertible UAVs is relatively scarce. One of the main contributions of this work is the energy modeling and evaluation of those aerial vehicles. Specifically, in the second chapter of this thesis, we focus on a class of convertible UAV made up of coplanar propellers and a main body that may include wing(s). The propeller modeling is essentially based on classical momentum and blade element theories. An eight-parameter-analytical model is proposed, allows one to characterize easily propeller aerodynamic properties when the thrust and torque coefficient data are available. As for the wings, a symmetric NACA0018 airfoil for the wings is selected and a recent study in the literature is used to model the aerodynamic forces over the whole range of angle of attack while taking into account the influence of the Reynolds number.

It is quite natural to expect energy efficiency improvement in cruising flight when adding the wings to a multirotor structure. However, finding the configurations that provide best energy performance is not straightforward. Intuitively, one might consider that reducing propellers thrust will improve the energy efficiency. This is generally true for low and medium speed flights (less than 14 m/s in our simulation). However, at high speed, the propellers' plane inclines at a large angle, so that the drag force on the propellers increase. The propellers then spin very fast but generate little thrust. Consequently, the energy performance degenerates. It is clear that not only the intensity of the thrust but also its direction can have great impact on the UAV's power. Maximizing wing lift/drag generally seems to be a good strategy to minimize the energy consumption. This strategy, however, is not optimal since the power greatly depends on propeller thrust vector. With convertible UAVs, in order to achieve high energy efficiency, one has to find the right balance between high lift force on the wings and low total drag force (drag force on the wings, drag force on the propellers, and parasite drag acting on the main body). The energy modeling, especially the evolution of the optimal angles of attack to minimize the energy consumption, provides guidelines for the control design. Finally, the model allows one to conduct simulations with different parameters (different propeller size and pitch angle, various wings area, different mass of the UAV). This can be beneficial for UAV presizing.

The third chapter of this manuscript focuses on the control aspect. The additional DoFs of the wings offer a great flexibility for the control. Indeed, they permit the decoupling between propellers and wings control, in order to obtain a larger flight envelope and to avoid the dependency of aerodynamic forces on UAV orientation. In particular, transition between hover and

cruising flight can be achieved with the wings' angles of attack remaining small. Furthermore, the control design can strongly rely on existing methods for quadrotors, which have been already well-studied and validated. Three control law designs for our convertible UAV are proposed. The first two strategies make use of only IMU/barometer measurements. The first strategy involves classical hierarchical attitude/altitude control. The second strategy considers a more general model and takes advantage of a slightly modified mechanical design to improve the velocity tracking and energy efficiency. Simulations suggest the soundness of this strategy even in the presence of strong and varying wind. The third control strategy involves velocity tracking with velocity measurements. The effect of propellers' downwash on the wings is modeled as a small airflow vector onto the back wing. This airflow causes an imbalance between aerodynamic forces on the two wings and creates an adverse torque, potentially hampers the stability and the energy performance of the UAV. This adverse torque can be estimated and this estimation can be used in the controller to modify the reference angles of attack of the wings, in order to compensate for the undesirable asymmetry.

The last chapter of this thesis describes in detail the mechanical structure and hardware/ software architecture of our convertible UAV. Preliminary testing of the UAV highlighted some limitations of our initial design, including the lack of robustness of servo motors for the wings and communication/control problem with the main motors. While the latter problem has been resolved, we are still trying different solutions in order to ensure a fast and precise control of the wings' pitch angle. First flight tests here reported have demonstrated relatively good stability and precision in attitude, with some improvements still possible concerning roll response and static offsets due to small mechanical imbalance. These offsets should be addressed shortly by adding in the controller external torques estimation and compensation. Encouraged by the additional understanding of the system after the initial tests, the next experiments will focus on improving the wing control and the implementation of aerodynamic force/torque estimation.

As already mentioned, we are only at the beginning of the experimental validations of the models/control methods proposed in this thesis. We are aware that a lot of experimental work is still necessary at this level. Along the way, possible future developments for this convertible UAV, which would help us to better understand the potentials and limitations of this structure, are numerous and include, e.g.,

- Extending the energy model to 3D case.
- Design the yaw control to take into account the lateral wind.
- Experimental validation of propeller model in forward flight.
- Testing the UAV in wind tunnel: this would certainly be useful for a precise power evaluation in function of air-velocity.
- Comparison of flight performance and energy efficiency with different propellers and/or different wings.
- Evaluation of the effects of propellers/wings interaction and finding the optimal distance between the wing axis and propellers.

Bibliography

[1] Donald, D., *The Complete Encyclopedia of World Aircraft*, Barnes Noble Books, New York, NY, 1st ed., 1997.

[2] Pounds, P., *Design, construction and control of a large quadrotor micro air vehicle*, Ph.D. thesis, Australian National University, 2007.

[3] Beard, R. W., Kingston, D., Quigley, M., Snyder, D., Christiansen, R., Johnson, W., McLain, T., and Goodrich, M., "Autonomous Vehicle Technologies for Small Fixed-Wing UAVs," *Journal of Aerospace Computing, Information, and Communication*, Vol. 2, No. 1, Jan. 2005, pp. 92–108.

[4] Cai, G., Peng, K., Chen, B., and Lee, T., "Design and assembling of a UAV helicopter system," *International Conference on Control and Automation*, Vol. 2, June 2005, pp. 697–702 Vol. 2.

[5] Wang, F., Wang, T., Chen, B., and Lee, T., "An indoor unmanned coaxial rotorcraft system with vision positioning," *8th IEEE International Conference on Control and Automation*, June 2010, pp. 291–296.

[6] Hamel, T., Mahony, R., Lozano, R., and Ostrowski, J., "Dynamic modelling and configuration stabilization for an X4-flyer," *15th Triennial World Congress, International Federation of Automatic Control*, 2002.

[7] Bouabdallah, S., *Design and control of quadrotors with application to autonomous flying*, Ph.D. thesis, Lausanne Polytechnic University, 2007.

[8] Hoffmann, G. M., Huang, H., Waslander, S. L., and Tomlin, C. J., "Quadrotor helicopter flight dynamics and control: Theory and experiment," *Proceedings of the AIAA guidance, navigation, and control conference*, Vol. 4, 2007, p. 44.

[9] Pflimlin, J. M., *Commande d'un minidrone à hélice carénée : De la stabilisation dans le vent à la navigation autonome*, Ph.D. thesis, LAAS-CNRS, 2006.

[10] Ta, D. A., Fantoni, I., and Lozano, R., "Modeling and control of a convertible mini-UAV," *Proceedings of the 18th IFAC World Congress*, 2011, pp. 1492–1497.

[11] Hrishikeshavan, V., Bogdanowicz, C., and Chopra, I., "Experimental Investigation of Performance of a Wing-Propeller System for a Quad-Rotor-Biplane Micro Air Vehicle," *54th AIAA/ASME/ASCE/AHS/ASC Structures, Structural Dynamics, and Materials Conference*, AIAA, Boston, Massachusetts, April 2013.

[12] Ostermann, T., Holsten, J., Dobrev, Y., and Moormann, D., "Control concept of a tilt-wing UAV during low speed manoeuvring," *Proceeding of the 28th International Congress of the Aeronautical Sciences: ICAS Brisbane, Australia*, 2012.

[13] Phung, D.-K. and Morin, P., "Modeling and Energy Evaluation of Small Convertible UAVs," *Workshop on Research, Education and Development of Unmanned Aerial Systems*, Vol. 2, Compiegne, France, Nov. 2013, pp. 212–219.

[14] Phung, D.-K. and Morin, P., "An Approach for Modeling, Design, and Energy Evaluation of Small Convertible Aerial Vehicles," *AIAA Modeling and Simulation Technologies Conference*, June 2014.

[15] Phung, D.-K. and Morin, P., "Control of a New Convertible UAV With a Minimal Sensor Suite," *IEEE Conference on Decision and Control*, Dec. 2014, pp. 229–235.

[16] Green, W. and Oh, P., "A fixed-wing aircraft for hovering in caves, tunnels, and buildings," *American Control Conference*, June 2006.

[17] Frank, A., McGrew, J., Valenti, M., Levine, D., and How, J. P., *Hover, transition, and level flight control design for a single-propeller indoor airplane*, Defense Technical Information Center, 2007.

[18] Pucci, D., *Towards a unified approach for the control of aerial vehicles*, Ph.D. thesis, Université de Nice-Sophia Antipolis and "Sapienza" Universita di Roma, 2013.

[19] "U.S. Federal Aviation Administration - Pilot's Handbook of Aeronautical Knowledge," 2008.

[20] Basset, P.-M., Tremolet, A., and Lefbvre, T., "Rotary Wings UAVs presizing: Past and present methodological approaches at Onera," *Onera Aerospace Lab*, 2014.

[21] Hua, M. D., *Contributions au contrôle automatique de véhicules aériens*, Ph.D. thesis, Université de Nice Sophia-Antipolis, 2009.

[22] "U.S. Federal Aviation Administration - Helicopter Flying Handbook," 2012.

[23] Newman, S., *Foundations of Helicopter Flight*, A Butterworth-Heinemann Title, April 1994.

[24] Alvissalim, M., Zaman, B., Hafizh, Z., Ma'sum, M., Jati, G., Jatmiko, W., and Mursanto, P., "Swarm quadrotor robots for telecommunication network coverage area expansion in disaster area," *SICE Annual Conference*, Aug. 2012, pp. 2256–2261.

[25] Jaimes, A., Kota, S., and Gomez, J., "An approach to surveillance an area using swarm of fixed wing and quad-rotor unmanned aerial vehicles UAV(s)," *IEEE International Conference on System of Systems Engineering*, June 2008, pp. 1–6.

[26] Kushleyev, A., Mellinger, D., Powers, C., and Kumar, V., "Towards a swarm of agile micro quadrotors," *Autonomous Robots*, Vol. 35, No. 4, Nov. 2013, pp. 287–300.

[27] Ryll, M., Bulthoff, H. H., and Giordano, P. R., "Modeling and control of a quadrotor UAV with tilting propellers," *IEEE International Conference on Robotics and Automation*, 2012, pp. 4606–4613.

[28] Senkul, F. and Altug, E., "Modeling and control of a novel tilt - roll rotor quadrotor UAV," *International Conference on Unmanned Aircraft Systems*, 2013, pp. 1071–1076.

[29] McKenna, J. T., "One Step Beyond," *Rotor & Wing*, 2007, pp. 54.

[30] Bhanja C., A., Kulhare, A., and Raina, G., "A generalized control method for a Tilt-rotor UAV stabilization," *2012 IEEE International Conference on Cyber Technology in Automation, Control, and Intelligent Systems (CYBER)*, May 2012, pp. 309–314.

[31] Basset, P.-M. and Cuzieux, F., "CREATION – Note Technique – Convertibles et Combinés: éléments pour l'estimation analytique de leur performance," Onera report NT 3/18466 DCSD, June 2013.

[32] Kubo, D., Muraoka, K., and Okada, N., "High Angle of Attack Flight Characteristics of a Wing-in-Propeller-Slipstream Aircraft," *Proceedings of ICAS2010*, 2010.

[33] Cetinsoy, E., Dikyar, S., Hancer, C., Oner, K., Sirimoglu, E., Unel, M., and Aksit, M., "Design and construction of a novel quad tilt-wing UAV," *Mechatronics*, Vol. 22, No. 6, Sept. 2012, pp. 723–745.

[34] Kubo, D., Muraoka, K., and Suzuki, S., "Vertical Takeoff and Landing Technology Research Using Small Experimental Unmanned Aircraft," *International Conference on Intelligent Unmanned Systems*, 2011.

[35] Shkarayev, S., Moschetta, J.-M., and Bataille, B., "Aerodynamic design of VTOL micro air vehicles," *Proc. of the MAV07 International Conference, France*, 2007.

[36] Leishman, J. G., *Principles of Helicopter Aerodynamics*, Cambridge University Press, April 2006.

[37] Driessens, S. and Pounds, P., "Towards a more efficient quadrotor configuration," *2013 IEEE/RSJ International Conference on Intelligent Robots and Systems (IROS)*, Nov. 2013, pp. 1386–1392.

[38] Brandt, J. B. and Selig, M. S., "Propeller Performance Data at Low Reynolds Numbers," *49th AIAA Aerospace Sciences Meeting*, 2011, pp. 2011–1255.

[39] Tennekes, H., *The simple science of flight: from insects to jumbo jets*, MIT Press, Cambridge, Mass., 2009.

[40] Aleksandrov, D. and Penkov, I., "Energy Consumption of Mini UAV Helicopters with Different Number of Rotors," *11th International Symposium - Topical Problems in the Field of Electrical and Power Engineering*, 2012, pp. 259–262.

[41] Moschetta, J.-M., "Introduction to innovative micro air vehicles configurations: key challenges, breakthroughs and trade-offs," Oct. 2014, Aerial Robotics, Onera, Toulouse, France.

[42] Stepniewski, W. Z. and Keys, C. N., *Rotary-Wing Aerodynamics*, Dover Publ., 1979.

[43] Bramwell, A. R. S., Done, G. T. S., and Balmford, D., *Bramwell's Helicopter Dynamics*, AIAA, 2nd ed., Jan. 2001.

[44] Johnson, W., *Helicopter Theory*, Courier Dover Publications, Oct. 1994.

[45] Pucci, D., "Flight dynamics and control in relation to stall," *American Control Conference*, 2012, pp. 118–124.

[46] Johnson, W., *Rotorcraft Aeromechanics*, Cambridge University Press, April 2013.

[47] Martin, P. and Salaun, E., "The true role of accelerometer feedback in quadrotor control," *IEEE International Conference on Robotics and Automation*, 2010, pp. 1623–1629.

[48] Anderson, J., *Fundamentals of Aerodynamics*, McGraw-Hill Education, Feb. 2010.

[49] Drela, M., "XFoil Subsonic Airfoil Development System, http://web.mit.edu/drela/Public/web/xfoil/," 2008.

[50] Moffitt, B., Bradley, T., Parekh, D. E., and Mavris, D., "Validation of vortex propeller theory for UAV design with uncertainty analysis," *46th AIAA Aerospace Sciences Meeting and Exhibit*, 2008, pp. 2008–406.

[51] Merchant M. P., "Propeller Performance Measurement For Low Reynolds Number UAV Applications," Master thesis, Wichita State University, 2004.

[52] Brandt, J. B. and Selig, M. S., "UIUC Propeller Data Site, http://www.ae.illinois.edu/m-selig/props/propDB.html," 2012.

[53] Landing Products, "APC Propeller Performance Data," 2013.

[54] Schenk, H., "PropCalc - Propeller Calculator Software, http://www.drivecalc.de/PropCalc/index.html," 2012.

[55] Pucci, D., Hamel, T., Morin, P., and Samson, C., "Nonlinear Control of PVTOL Vehicles subjected to Drag and Lift," *IEEE Decision and Control and European Control Conference*, 2011, pp. 6177–6183.

[56] Sheldahl, R. E. and Klimas, P. C., "Aerodynamic Characteristics of Seven Symmetrical Airfoil Sections Through 180-Degree Angle of Attack for Use in Aerodynamic Analysis of Vertical Axis Wind Turbines," Tech. Rep. SAND-80-2114, Sandia National Labs., Albuquerque, NM (USA), March 1981.

[57] Hua, M.-D., Hamel, T., Morin, P., and Samson, C., "A Control Approach for Thrust-Propelled Underactuated Vehicles and its Application to VTOL Drones," *IEEE Transactions on Automatic Control*, Vol. 54, No. 8, Aug. 2009, pp. 1837–1853.

[58] Stevens, B. L. and Lewis., F. L., *Aircraft control and simulation*, Wiley, Hoboken, NJ, 2nd ed., 2003.

[59] Shamma, J. S., *Analysis and design of gain scheduled control systems*, Ph.D. thesis, Massachusetts Institute of Technology, 1988.

[60] Kadmiry, B. and Driankov, D., "A fuzzy gain-scheduler for the attitude control of an unmanned helicopter," *IEEE Transactions on Fuzzy Systems*, Vol. 12, No. 4, 2004, pp. 502–515.

[61] Lane, S. H. and Stengel, R., "Flight Control Design using Nonlinear Inverse Dynamics," *American Control Conference, 1986*, June 1986, pp. 587–596.

[62] Wang, Q. and Stengel, R., "Robust nonlinear flight control of a high-performance aircraft," *IEEE Transactions on Control Systems Technology*, Vol. 13, No. 1, Jan. 2005, pp. 15–26.

[63] Sobolic, F. M., "Agile flight control techniques for a fixed-wing aircraft," Master thesis, Massachusetts Institute of Technology, 2009.

[64] Hua, M.-D., Hamel, T., Morin, P., and Samson, C., "Introduction to feedback control of underactuated VTOL vehicles: A review of basic control design ideas and principles," *IEEE Control Systems*, Vol. 33, No. 1, Feb. 2013, pp. 61–75.

[65] Bouabdallah, S., Noth, A., and Siegwart, R., "PID vs LQ Control Techniques Applied to an Indoor Micro Quadrotor," *Intelligent Robots and Systems*, 2004, pp. 2451–2456.

[66] Benallegue, A., Belaidi, A., and Mokhtari, A., "Polynomial linear quadratic gaussian and sliding mode observer for a quadrotor unmanned aerial vehicle," *Journal of Robotics and Mechatronics*, Vol. 17, No. 3, 2006, pp. 483–495.

[67] Takahashi, M. D., "Synthesis and evaluation of an H_2 control law for a hovering helicopter," *AIAA Journal of Guidance, Control, and Dynamics*, Vol. 16, No. 3, 1993, pp. 579–584.

[68] Mammar, S. and Duc, G., "Loop Shaping H_∞ design applied to the robust stabilization of an helicopter," *IEEE Conference on Control Applications*, 1992, pp. 806–811.

[69] Luo, C.-C., Liu, R.-F., Yang, C.-D., and Chang, Y.-H., "Helicopter H_∞ control design with robust flying quality," *Aerospace Science and Technology*, Vol. 7, No. 2, 2003, pp. 159–169.

[70] Morin, P. and Samson, C., "Control with transverse functions and a single generator of underactuated mechanical systems," *2006 45th IEEE Conference on Decision and Control*, Dec. 2006, pp. 6110–6115.

[71] Hua, M.-D., Morin, P., and Samson, C., "Balanced-force-control of underactuated thrust-propelled vehicles," *2007 46th IEEE Conference on Decision and Control*, Dec. 2007, pp. 6435–6441.

[72] Dreier, M., *Introduction to Helicopter and Tiltrotor Flight Simulation*, AIAA, Reston, Va., March 2007.

[73] Naldi, R. and Marconi, L., "Optimal transition maneuvers for a class of V/STOL aircraft," *Automatica*, Vol. 47, 2011, pp. 870–879.

[74] Naldi, R. and Marconi, L., "Robust control of transition maneuvers for a class of V/STOL aircraft," *Automatica*, Vol. 49, No. 6, June 2013, pp. 1693–1704.

[75] Casau, P., Cabecinhas, D., and Silvestre, C., "Hybrid Control Strategy for the Autonomous Transition Flight of a Fixed-Wing Aircraft," *IEEE Transactions on Control Systems Technology*, Vol. 21, No. 6, Nov. 2013, pp. 2194–2211.

[76] Itasse, M., Moschetta, J.-M., Ameho, Y., and Carr, R., "Equilibrium Transition Study for a Hybrid MAV," *International Journal of Micro Air Vehicles*, Vol. 3, No. 4, Dec. 2011, pp. 229–246.

[77] Guenard, N., Hamel, T., and Moreau, V., "Dynamic modeling and intuitive control strategy for an "X4-flyer"," *IEEE International Conference on Control and Automation*, Vol. 1, 2005, pp. 141–146.

[78] Hamel, T. and Mahony, R., "Attitude estimation on SO[3] based on direct inertial measurements," *IEEE International Conference on Robotics and Automation*, May 2006, pp. 2170–2175.

[79] Mahony, R., Hamel, T., and Pflimlin, J.-M., "Nonlinear complementary filters on the special orthogonal group," *IEEE Transactions on Automatic Control*, Vol. 53, No. 5, 2008, pp. 1203–1218.

[80] Gracey, W., "Summary of methods of measuring the angle of attack on aircraft," Tech. Rep. 4351, NASA Technical Note, 1958.

[81] Whitmore, S. A., Moes, T. R., and Larson, T. J., "Preliminary results from a subsonic high angle-of-attack flush air-data sensing (HI-FADS) system: design, calibration, and flight test evaluation," Tech. Rep. 101713, NASA Technical Memorandum, 1990.

[82] Samy, I., Postlethwaite, I., and Gu, D., "Subsonic Tests of a Flush Air Data Sensing System Applied to a Fixed-Wing Micro Air Vehicle," *Journal of Intelligent and Robotic Systems*, Vol. 54, No. 1-3, 2009, pp. 275–295.

[83] *U.S. Department of Defense Handbook MIL-HDBK-1797 - Flying Qualities of Piloted Aircraft*, 1997.

[84] Theys, B., Dimitriadis, G., Andrianne, T., Hendrick, P., and De Schutter, J., "Wind Tunnel Testing of a VTOL MAV Propeller in Tilted Operating Mode," *International Conference on Unmanned Aircraft Systems*, 2014, pp. 1064–1072.

Appendix A

Detailed Calculation of Propellers Parameters

The calculations below use the following relationships:

$$\int_0^{2\pi} \sin^2 \Psi \, \mathrm{d}\Psi = \pi \tag{A.1}$$

$$\int_0^{2\pi} \sin \Psi \, \mathrm{d}\Psi = \int_0^{2\pi} \sin^3 \Psi \, \mathrm{d}\Psi = 0 \tag{A.2}$$

Substituting Eq. (2.42) into Eq. (2.44), we obtain:

$$\begin{aligned} T &= \frac{N_P}{2\pi} \int_0^R \int_0^{2\pi} \frac{1}{2} \rho |U|^2 c_P(\bar{r}) \Big[C_{LP}(\alpha_P, \bar{r}) \cos\varphi - C_{DP}(\alpha_P, \bar{r}) \sin\varphi \Big] \, \mathrm{d}\Psi \mathrm{d}r \\ &= \frac{N_P}{4\pi} \rho R \int_0^1 \int_0^{2\pi} |U|^2 c_P(\bar{r}) \Big[C_{LP}(\alpha_P, \bar{r}) \cos\varphi - C_{DP}(\alpha_P, \bar{r}) \sin\varphi \Big] \, \mathrm{d}\Psi \mathrm{d}\bar{r} \end{aligned} \tag{A.3}$$

$$\begin{aligned} Q &= \frac{N_P}{2\pi} \int_0^R \int_0^{2\pi} \frac{1}{2} \rho |U|^2 c_P(\bar{r}) r \Big[C_{LP}(\alpha_P, \bar{r}) \sin\varphi + C_{DP}(\alpha_P, \bar{r}) \cos\varphi \Big] \mathrm{d}\Psi \mathrm{d}r \\ &= \frac{N_P}{4\pi} \rho R^2 \int_0^1 \int_0^{2\pi} |U|^2 c_P(\bar{r}) \bar{r} \Big[C_{LP}(\alpha_P, \bar{r}) \sin\varphi + C_{DP}(\alpha_P, \bar{r}) \cos\varphi \Big] \mathrm{d}\Psi \mathrm{d}\bar{r} \end{aligned} \tag{A.4}$$

$$\begin{aligned} H &= \frac{N_P}{2\pi} \int_0^R \int_0^{2\pi} \frac{1}{2} \rho |U|^2 c_P(\bar{r}) \sin\Psi \Big[C_{LP}(\alpha_P, \bar{r}) \sin\varphi + C_{DP}(\alpha_P, \bar{r}) \cos\varphi \Big] \mathrm{d}\Psi \mathrm{d}r \\ &= \frac{N_P \rho R}{4\pi} \int_0^1 \int_0^{2\pi} |U|^2 c_P(\bar{r}) \sin\Psi \Big[C_{LP}(\alpha_P, \bar{r}) \sin\varphi + C_{DP}(\alpha_P, \bar{r}) \cos\varphi \Big] \mathrm{d}\Psi \mathrm{d}\bar{r} \end{aligned} \tag{A.5}$$

Note that the term $\sin\Psi$ appears in the expression of in-plane drag force H since H is the integration of $\mathrm{d}H$ along the line parallel to $\boldsymbol{j}$ in figure 2.8 (the integration of $\mathrm{d}H$ along the line parallel to $\boldsymbol{i}$ is zero due to flow symmetry).

Using the simplified assumptions in section 2.2.3 the simplified thrust expression is:

$$\begin{aligned}
T &= \frac{N_P \rho c_P R \nu_T^2}{4\pi} \int_0^1 \int_0^{2\pi} (\bar{r} + \bar{\nu}_2 \sin\Psi)^2 (C_{L0} + a\alpha_P)\, \mathrm{d}\Psi \mathrm{d}\bar{r} \\
&= \frac{N_P \rho c_P R \nu_T^2}{4\pi} \int_0^1 \int_0^{2\pi} (C_{L0} + a\theta_P)(\bar{r} + \bar{\nu}_2 \sin\Psi)^2 - a\bar{\nu}_{3,\mathrm{ind}} (\bar{r} + \bar{\nu}_2 \sin\Psi)\, \mathrm{d}\Psi \mathrm{d}\bar{r} \\
&= \frac{N_P \rho c_P R \nu_T^2}{4\pi} \int_0^1 \int_0^{2\pi} \left[C_{Lt} \bar{\nu}_2^2 \sin^2\Psi + (2C_{Lt}\bar{r}\bar{\nu}_2 - a\bar{\nu}_{3,\mathrm{ind}}\bar{\nu}_2) \sin\Psi + (C_{Lt}\bar{r}^2 - a\bar{\nu}_{3,\mathrm{ind}}\bar{r}) \right] \mathrm{d}\Psi \mathrm{d}\bar{r} \\
&= \frac{N_P \rho c_P R \nu_T^2}{4\pi} \int_0^1 \left[\pi C_{Lt} \bar{\nu}_2^2 + 2\pi (C_{Lt}\bar{r}^2 - a\bar{\nu}_{3,\mathrm{ind}}\bar{r}) \right] \mathrm{d}\bar{r} \\
&= \frac{N_P \rho c_P R \nu_T^2}{4} \left[C_{Lt} \left(\frac{2}{3} + \bar{\nu}_2^2 \right) - a\bar{\nu}_{3,\mathrm{ind}} \right]
\end{aligned} \tag{A.6}$$

Before simplifying Q and H, we need to calculate this term:

$$\begin{aligned}
C_{LD} &= C_{LP}(\alpha_P) \sin\varphi + C_{DP}(\alpha_P) \cos\varphi \\
&= (C_{L0} + a\alpha_P)\varphi + (b_0 + b_1\alpha_P + b_2\alpha_P^2) \\
&= C_{L0} \frac{\bar{\nu}_{3,\mathrm{ind}}}{\bar{r} + \bar{\nu}_2 \sin\Psi} + b_0 + \left(a \frac{\bar{\nu}_{3,\mathrm{ind}}}{\bar{r} + \bar{\nu}_2 \sin\Psi} + b_1 \right) \left(\theta_P - \frac{\bar{\nu}_{3,\mathrm{ind}}}{\bar{r} + \bar{\nu}_2 \sin\Psi} \right) + b_2 \left(\theta_P - \frac{\bar{\nu}_{3,\mathrm{ind}}}{\bar{r} + \bar{\nu}_2 \sin\Psi} \right)^2 \\
&= \frac{(b_0 + b_1\theta_P + b_2\theta_P^2)(\bar{r} + \bar{\nu}_2 \sin\Psi)^2 + \bar{\nu}_{3,\mathrm{ind}}(C_{L0} + a\theta_P - b_1 - 2b_2\theta_P)(\bar{r} + \bar{\nu}_2 \sin\Psi) + (b_2 - a)\bar{\nu}_{3,\mathrm{ind}}^2}{(\bar{r} + \bar{\nu}_2 \sin\Psi)^2} \\
&= \frac{\beta_2 (\bar{r} + \bar{\nu}_2 \sin\Psi)^2 + \beta_1 \bar{\nu}_{3,\mathrm{ind}} (\bar{r} + \bar{\nu}_2 \sin\Psi) + \beta_0 \bar{\nu}_{3,\mathrm{ind}}^2}{(\bar{r} + \bar{\nu}_2 \sin\Psi)^2} \\
&= \frac{\beta_2 \bar{\nu}_2^2 \sin^2\Psi + (2\beta_2 \bar{r}\bar{\nu}_2 + \beta_1 \bar{\nu}_{3,\mathrm{ind}}\bar{\nu}_2) \sin\Psi + \beta_2 \bar{r}^2 + \beta_1 \bar{\nu}_{3,\mathrm{ind}}\bar{r} + \beta_0 \bar{\nu}_{3,\mathrm{ind}}^2}{(\bar{r} + \bar{\nu}_2 \sin\Psi)^2}
\end{aligned} \tag{A.7}$$

Substituting Eq. (A.7) into Eq. (A.4) we have:

$$\begin{aligned}
Q &= \frac{N_P}{4\pi} \rho R^2 \nu_T^2 \int_0^1 \int_0^{2\pi} c_P \bar{r} \left[\beta_2 \bar{\nu}_2^2 \sin^2\Psi + (2\beta_2 \bar{r}\bar{\nu}_2 + \beta_1 \bar{\nu}_{3,\mathrm{ind}}\bar{\nu}_2) \sin\Psi + \beta_2 \bar{r}^2 + \beta_1 \bar{\nu}_{3,\mathrm{ind}}\bar{r} + \beta_0 \bar{\nu}_{3,\mathrm{ind}}^2 \right] \mathrm{d}\Psi \mathrm{d}\bar{r} \\
&= \frac{N_P \rho R^2 c_P \nu_T^2}{4\pi} \int_0^1 \left[\pi\beta_2 \bar{\nu}_2^2 + 2\pi (\beta_2 \bar{r}^2 + \beta_1 \bar{\nu}_{3,\mathrm{ind}}\bar{r} + \beta_0 \bar{\nu}_{3,\mathrm{ind}}^2) \right] \bar{r} \mathrm{d}\bar{r} \\
&= \frac{N_P \rho R^2 c_P \nu_T^2}{4} \left[\bar{\nu}_{3,\mathrm{ind}} \left(\frac{2}{3}\beta_1 + \beta_0 \bar{\nu}_{3,\mathrm{ind}} \right) + \frac{\beta_2}{2} (1 + \bar{\nu}_2^2) \right]
\end{aligned} \tag{A.8}$$

Substituting Eq. (A.7) into Eq. (A.5) we have:

$$\begin{aligned}
H &= \frac{N_P}{4\pi} \rho R \nu_T^2 \int_0^1 \int_0^{2\pi} c_P \sin\Psi \left[\beta_2 \bar{\nu}_2^2 \sin^2\Psi + (2\beta_2 \bar{r}\bar{\nu}_2 + \beta_1 \bar{\nu}_{3,\mathrm{ind}}\bar{\nu}_2) \sin\Psi + \beta_2 \bar{r}^2 + \beta_1 \bar{\nu}_{3,\mathrm{ind}}\bar{r} + \beta_0 \bar{\nu}_{3,\mathrm{ind}}^2 \right] \mathrm{d}\Psi \mathrm{d}\bar{r} \\
&= \frac{N_P \rho R c_P \nu_T^2}{4\pi} \int_0^1 \pi (2\beta_2 \bar{r}\bar{\nu}_2 + \beta_1 \bar{\nu}_{3,\mathrm{ind}}\bar{\nu}_2) \mathrm{d}\bar{r} \\
&= \frac{N_P \rho R c_P \nu_T^2}{4} \bar{\nu}_2 (\beta_1 \bar{\nu}_{3,\mathrm{ind}} + \beta_2)
\end{aligned} \tag{A.9}$$

Now we develop the relations between different representations of thrust and torque coefficients. From Eq. (2.65), Eq. (2.69), and Eq. (3.28), one can easily deduce the following relation:

$$\kappa_T = \frac{1}{2} \rho A R^2 C_T = \frac{1}{4} \rho A R^2 s \left(\frac{2}{3} C_{Lt} - a\bar{\nu}_{3,\mathrm{ind}} \right) \tag{A.10}$$

Similarly, Eq. (2.67), Eq. (2.72), and Eq. (3.28) yield:

$$\kappa_Q = \frac{1}{2}\rho A R^3 C_Q = \frac{1}{4}\rho A R^3 s \left[\bar{\nu}_{3,\text{ind}} \left(\frac{2}{3}\beta_1 + \beta_0 \bar{\nu}_{3,\text{ind}}\right) + \frac{\beta_2}{2}\right] \tag{A.11}$$

It can be seen that κ_T and κ_Q depend on the normalized total flow perpendicular to the propeller disk $\bar{\nu}_{3,\text{ind}}$. In practice, for simple estimates to be used in the controller, these coefficients are measured using a static test bench as in appendix B.

Appendix B

Static Test Bench

Propeller thrust and torque are measured by a simple test bench. The schematic diagrams of the test bench are shown in figure B.1 and figure B.2. The propeller and the motor are mounted on a bar that can rotate freely around a pivot point. Due to symmetric arrangement, the scale reading is equal to the propeller thrust.

As for the torque measurement in figure B.2, when the propeller spins, there is a reactive torque $\boldsymbol{Q}$ acting at the pivot point. The magnitude of this torque can be easily calculated from $Q = L \times F$ where L is the distance from the rotor axis to the pivot point and F is the scale reading. The propeller speed ϖ can be measured manually by a tachometer. Knowing ϖ, T, Q, the thrust constant κ_T and torque constant κ_Q can be easily calculated from Eq. (3.28). Similarly, the thrust coefficient C_T and torque/power coefficients $C_Q = C_P$ can be deduced from Eq. (2.65) and Eq. (2.67). The actual experimental setup is shown in figure B.3. The scale is Sartorius AY6000 with maximum weight 6 kg and precision 1 g. The optical tachometer is Voltcraft DT-20LK which can measure from 2 to 99,999 RPM and have resolution $\pm 0.05\%$.

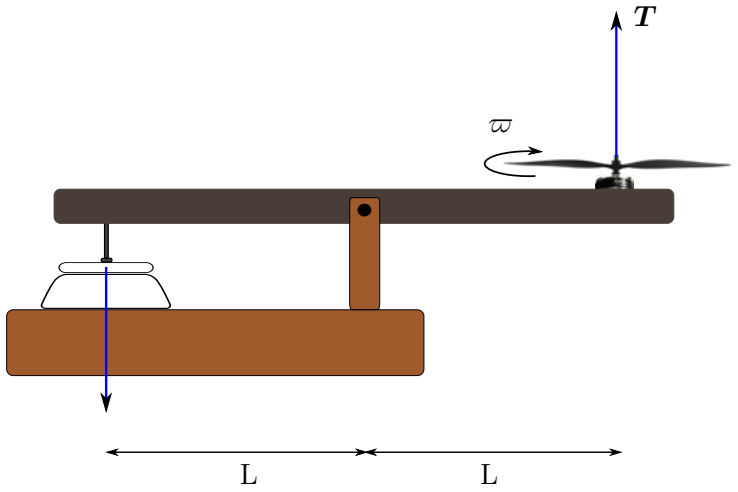

Figure B.1: Schematic of test bench for thrust measurement

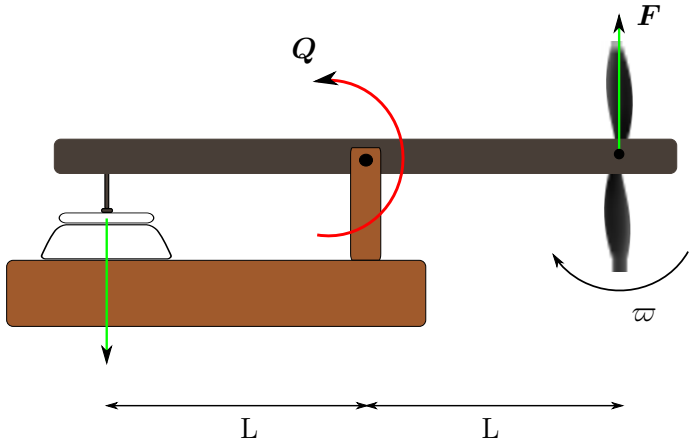

Figure B.2: Schematic of test bench for torque measurement

Figure B.3: Experimental setup of our static test bench for torque measurement

Appendix C

Parameters for Simulation

The parameters for the simulation in chapter 2 and chapter 3 are the same as the parameters for the physical convertible UAV model in section 4.2, except that the simulated model uses APC SlowFlyer 11×4.7 propellers with the following parameters:

- number of propellers $N = 4$,
- number of blades per propeller $N_P = 2$,
- propeller radius $R = 0.1397$ m,
- propeller area $A = \pi R^2 = 0.061$ m^2,
- mean chord of a propeller blade at 75% radius $c_P = 0.028$ m,
- solidity of the propeller $s = N_P c_P R/A = 0.127$,
- pitch angle at 75% radius of the propeller blade $\theta_P = 0.1794$ rad,
- blade aerodynamic coefficients $[C_{L0}, a, b_0, b_1, b_2] = [0.48, 4.53, 0.02, 0.02, 2.21]$,
- constants for thrust and torque are: $\kappa_T = 1.9 \times 10^{-5}$ and $\kappa_Q = 3.8 \times 10^{-7}$.

The total mass of the UAV is $m = 3.2$ kg. The aerodynamic parameters of NACA0018 wing(s) as derived based on [56] (see chapter 2):

- drag constant $c_1 = 0.0128$,
- average lift constant $c_2 = 0.9595$,
- high lift constant $c_{2T} = 2.6749$,
- reference Reynolds number $\mathrm{Re}_{\mathrm{ref}} = 160000$,
- Reynolds number exponential constant $\mathrm{Re}_{\mathrm{exp}} = 0.3$,
- reference angle where the stall starts $\alpha_{0\mathrm{ref}} = 12^\circ$.

The standard constants are:

- air density $\rho = 1.225$ kg/m^3,
- air viscosity $\mu_{\mathrm{vis}} = 1.789 \times 10^{-5}$,

- gravity constant $g = 9.8$ m/s^2.

The parasite drag coefficient is $c_{\text{para}} = 0.4$ and the effective parasite drag area is $\Sigma_{\text{para}} = 0.1$ m^2. The propeller motor efficiency is assumed to be $\eta_M = 0.7$. In reality, this efficiency depends on torque and rotational speed. The modeling and testing of the electric motors will be considered in the near future.

Appendix D

Inertia Calculation

The objective of this section is to estimate the moments of inertia of the convertible UAV. Refer to figure 4.11 for the top-view schematic of the UAV.

We suppose that all the mass distributes on the propellers' plane, i.e., the mass distribution along the thrust axis is neglected. We also assume that the UAV is composed of the following elements, each with homogeneous mass distribution:

- four motors, with coordinates $x_1 = \pm\ell_1, x_2 = \pm\ell_2$ and mass of each motor m_1;
- two bars parallel to $\boldsymbol{i}$, with coordinates $x_1 \in [-\ell_2, \ell_2], x_2 = \pm\ell_1$ and mass m_2;
- two bars parallel to $\boldsymbol{j}$, with coordinates $x_1 = \pm\ell_3, x_2 \in [-\ell_1, \ell_1]$ and mass m_3;
- one rectangular plate, with coordinates $x_1 \in [-\ell_3, \ell_3], x_2 \in [-\ell_1, \ell_1]$ and mass m_4;
- one rectangular battery, with coordinates $x_1 \in [-\ell_5, \ell_5], x_2 \in [-\ell_4, \ell_4]$ and mass m_5;
- two external bars parallel to $\boldsymbol{j}$, with coordinates $x_1 = \pm\ell_7, x_2 \in [-\ell_6, \ell_6]$ and mass m_6;
- two wings parallel to $\boldsymbol{i}$, with coordinates $x_1 \in [-\ell_7, \ell_7], x_2 = \pm\ell_6$ and mass m_7;

The moment of inertia of these elements is calculated as follows:

Each motor (considered as a point mass):

$$J_{11} = m_1\ell_1^2$$
$$J_{22} = m_1\ell_2^2$$

where J_{11} and J_{22} are the principle moments of inertia around $\boldsymbol{i}$ and $\boldsymbol{j}$, respectively.

Each bar parallel to $\boldsymbol{i}$: with ρ_l the linear mass density (unit kg/m),

$$J_{11} = \int_{-\ell_2}^{\ell_2} \ell_1^2 \, \rho_l \mathrm{d}x_1 = 2\rho_l\ell_2\ell_1^2 = m_2\ell_1^2$$
$$J_{22} = \int_{-\ell_2}^{\ell_2} x_1^2 \, \rho_l \mathrm{d}x_1 = 2\rho_l\frac{\ell_2^3}{3} = m_2\frac{\ell_2^2}{3}$$

Each bar parallel to $\boldsymbol{j}$:

$$J_{11} = \int_{-\ell_1}^{\ell_1} x_2^2 \, \rho_l \mathrm{d}x_2 = 2\rho_l \frac{\ell_1^3}{3} = m_3 \frac{\ell_1^2}{3}$$
$$J_{22} = \int_{-\ell_1}^{\ell_1} \ell_3^2 \, \rho_l \mathrm{d}x_2 = 2\rho_l \ell_1 \ell_3^2 = m_3 \ell_3^2$$

Rectangular plate: with ρ_s the surface mass density (unit kg/m^2),

$$J_{11} = \int_{-\ell_1}^{\ell_1} \int_{-\ell_3}^{\ell_3} x_2^2 \, \rho_s \mathrm{d}x_1 \mathrm{d}x_2 = 2\rho_s \ell_3 \int_{-\ell_1}^{\ell_1} x_2^2 \, \mathrm{d}x_2 = 4\rho_s \ell_3 \frac{\ell_1^3}{3} = m_4 \frac{\ell_1^2}{3}$$
$$J_{22} = m_4 \frac{\ell_3^2}{3}$$

Battery:

$$J_{11} = m_5 \frac{\ell_4^2}{3}$$
$$J_{22} = m_5 \frac{\ell_5^2}{3}$$

Each external bar parallel with $\boldsymbol{j}$:

$$J_{11} = m_6 \frac{\ell_6^2}{3}$$
$$J_{22} = m_6 \ell_7^2$$

Each wing parallel to $\boldsymbol{i}$:

$$J_{11} = m_7 \ell_6^2$$
$$J_{22} = m_7 \frac{\ell_7^2}{3}$$

By summing all above moments of inertia, we obtain the total moments of inertia of the UAV:

$$J_{11} = 4m_1\ell_1^2 + 2m_2\ell_1^2 + 2m_3\frac{\ell_1^2}{3} + m_4\frac{\ell_1^2}{3} + m_5\frac{\ell_4^2}{3} + 2m_6\frac{\ell_6^2}{3} + 2m_7\ell_6^2$$
$$J_{22} = 4m_1\ell_2^2 + 2m_2\frac{\ell_2^2}{3} + 2m_3\ell_3^2 + m_4\frac{\ell_3^2}{3} + m_5\frac{\ell_5^2}{3} + 2m_6\ell_7^2 + 2m_7\frac{\ell_7^2}{3}$$

The moment of inertia around $\boldsymbol{k}$ is simply the sum of the two previous moments of inertia:

$$J_{33} = J_{11} + J_{22}$$

D.1 Numerical Evaluation

The geometric parameters are:

$$2\ell_1 = 0.5,\ 2\ell_2 = 0.55,\ 2\ell_3 = 0.15,\ 2\ell_4 = 0.15,\ 2\ell_5 = 0.08,\ 2\ell_6 = 1.44,\ 2\ell_7 = 0.74 \qquad \text{(D.1)}$$

where we consider the battery (0.5 kg) dimension. The masses are:

- The motors (T-Motor 4008) with propellers (13-inch Graupner) with mass 0.134 kg.
- The bars parallel to $\boldsymbol{i}$ are made of glass fiber. With all the connecting parts (screws, nuts, etc.), the estimated mass is 0.18 kg.
- The bars parallel to $\boldsymbol{j}$ are considered to be part of the rectangular plate.
- The rectangular plate with mass 1.27 kg.
- The battery with mass 0.3 kg or 0.5 kg depending on the model.
- The external bars are made of carbon fiber. Each bar and the connecting parts have approximate mass of 0.1 kg.
- Each wing (including servo) has mass of about 0.15 kg

In summary, with the battery 0.5 kg we have:

$$m_1 = 0.134,\ m_2 = 0.18,\ m_3 = 0,\ m_4 = 1.27,\ m_5 = 0.5,\ m_6 = 0.1,\ m_7 = 0.15 \tag{D.2}$$

We verified that the battery impact on the moment of inertia is negligible. Finally, the total moments of inertia are (unit: kg m^2):

$$J_{11} = 0.273,\ J_{22} = 0.093,\ J_{33} = 0.366 \tag{D.3}$$

In the case without the wings, one has:

$$J_{11} = 0.083,\ J_{22} = 0.052,\ J_{33} = 0.135$$

Appendix E

Proof of Proposition 1

The proof is given for $v_{a,2} > 0$. The case $v_{a,2} < 0$ is completely similar.

First, since v_a is assumed to be constant, $\xi(v_a)$ and α^* are also constant. Note also, from (2.78) and (3.55), that

$$k_p(\zeta, \xi(v_a)) = g_1^{-1}\left(g_2(\xi(v_a))\cot(\alpha)\right) h(\alpha)\sin(\alpha) \tag{E.1}$$

Let $\tilde{\alpha} = \alpha - \alpha^*$. Then $\dot{\tilde{\alpha}} = \dot{\alpha} = -\dot{\zeta}$ and it follows from (2.78), (3.51), (3.56), and (E.1) that

$$\begin{array}{rcl} J_A\ddot{\tilde{\alpha}} & = & (g_1^{-1}(g_2(\xi(v_a))\cot(\alpha)) - |v_a|^2)h(\alpha)\sin\alpha + k_v(\zeta, \xi(v_a))\dot{\zeta} \\ & = & (g_1^{-1}(g_2(\xi(v_a))\cot(\alpha)) - |v_a|^2)h(\alpha)\sin\alpha - k_v(\pi - \alpha - \xi(v_a), \xi(v_a))\dot{\tilde{\alpha}} \end{array} \tag{E.2}$$

The equilibrium points of the above equation are defined by the relation

$$(g_1^{-1}(g_2(\xi)\cot(\alpha)) - |v_a|^2)h(\alpha)\sin\alpha = 0$$

Since by assumption h is a strictly positive function, this is equivalent to

$$g_1^{-1}(g_2(\xi(v_a))\cot(\alpha))\sin\alpha = |v_a|^2\sin\alpha \tag{E.3}$$

We claim that $\alpha = 0, \pi$ are not solutions to the above equation. Indeed, it follows from (3.54) in Assumption 1 that

$$\lim_{\tau \to +\infty} \frac{g_1^{-1}(\tau)}{\tau} = \frac{1}{b} > 0$$

Thus,

$$\lim_{\alpha \to 0} g_1^{-1}(g_2(\xi(v_a))\cot(\alpha))\sin\alpha \quad = \quad \lim_{\alpha \to 0} \frac{g_2(\xi(v_a))}{b}\cot(\alpha)\sin\alpha \quad = \quad \frac{g_2(\xi(v_a))}{b} \quad \neq \quad 0 \tag{E.4}$$

which implies that $\alpha = 0, \pi$ are not solutions to (E.3). The equilibrium points are thus given by the solutions of

$$g_1^{-1}(g_2(\xi(v_a))\cot(\alpha)) = |v_a|^2 \tag{E.5}$$

This condition is equivalent to $g_2(\xi(v_a))\cot(\alpha) = g_1(|v_a|^2)$. From (3.53), this implies that $\alpha = \alpha^*$ or $\alpha = \alpha^* + \pi$. Thus α^* is an equilibrium point of (E.2).

Since v_a is constant, Eq. (E.2) is autonomous and the stability of $\alpha = \alpha^*$ can be studied from the linearized equation. Since g_1 is a class $\mathcal{K}_\infty$ function (and thus strictly increasing), and the function $\cot\alpha$ is strictly decreasing, one easily verifies that the linearized system is asymptotically stable. Since there are only two equilibrium points, the domain of convergence is necessarily $(\alpha^* - \pi, \alpha^* + \pi)$. This concludes the proof. ∎

Appendix F

Proof of Proposition 2

The aerodynamic forces are composed of the parasite drag $\boldsymbol{D}$ acting at the center of mass, the aerodynamic force $\boldsymbol{F_{a\to A}}$ acting on the front wing and the aerodynamic force $\boldsymbol{F_{a\to C}}$ acting on the back wing. The aerodynamic torque is thus

$$\boldsymbol{\Gamma_a} = \Gamma_a \boldsymbol{i} = L\boldsymbol{j} \times (\boldsymbol{F_{a\to A}} - \boldsymbol{F_{a\to C}}) \tag{F.1}$$

From the expressions of lift and drag forces in Eq. (2.79),

$$\boldsymbol{F_{a\to A}} = k_a |\boldsymbol{v_{a,A}}| c_L(\alpha_A, \mathrm{Re}_A) \boldsymbol{v}_{\boldsymbol{a,A}}^{\perp} - k_a |\boldsymbol{v_{a,A}}| c_D(\alpha_A, \mathrm{Re}_A) \boldsymbol{v_{a,A}}$$

Since by assumption $\boldsymbol{v_{a,A}} = \boldsymbol{v} = v_2 \boldsymbol{j_0}$, this yields

$$\boldsymbol{F_{a\to A}} = -k_a |v|^2 \big(c_L(\alpha_A, \mathrm{Re}_A) \boldsymbol{k_0} + c_D(\alpha_A, \mathrm{Re}_A) \boldsymbol{j_0} \big)$$

This implies that

$$L\boldsymbol{j} \times \boldsymbol{F_{a\to A}} = -Lk_a |v|^2 \big(c_L(\alpha_A, \mathrm{Re}_A) \cos\theta - c_D(\alpha_A, \mathrm{Re}_A) \sin\theta \big) \boldsymbol{i} \tag{F.2}$$

Similarly,

$$\boldsymbol{F_{a\to C}} = k_a \big| \boldsymbol{v} - \varepsilon |\boldsymbol{v}| \boldsymbol{k} \big| c_L(\alpha_C, \mathrm{Re}_C) (\boldsymbol{v} - \varepsilon |\boldsymbol{v}| \boldsymbol{k})^{\perp} - k_a \big| \boldsymbol{v} - \varepsilon |\boldsymbol{v}| \boldsymbol{k} \big| c_D(\alpha_C, \mathrm{Re}_C) (\boldsymbol{v} - \varepsilon |\boldsymbol{v}| \boldsymbol{k})$$

Noting that

$$(\boldsymbol{v} - \varepsilon |\boldsymbol{v}| \boldsymbol{k})^{\perp} = \boldsymbol{v}^{\perp} - \varepsilon |\boldsymbol{v}| \boldsymbol{k}^{\perp} = -|v| \boldsymbol{k_0} - \varepsilon |v| \boldsymbol{j}$$

we obtain after a few calculations that

$$L\boldsymbol{j} \times \boldsymbol{F_{a\to C}} = -Lk_a |v| \big| \boldsymbol{v} - \varepsilon |\boldsymbol{v}| \boldsymbol{k} \big| \big(c_L(\alpha_C, \mathrm{Re}_C) \cos\theta - c_D(\alpha_C, \mathrm{Re}_C)(\varepsilon + \sin\theta) \big) \boldsymbol{i}$$

in which

$$\begin{aligned} \big| \boldsymbol{v} - \varepsilon |\boldsymbol{v}| \boldsymbol{k} \big| &= \big| |v| \boldsymbol{j_0} - \varepsilon |v| (\cos\theta \, \boldsymbol{k_0} - \sin\theta \, \boldsymbol{j_0}) \big| \\ &= |v| \big| (1 + \varepsilon \sin\theta) \, \boldsymbol{j_0} - \varepsilon \cos\theta \, \boldsymbol{k_0} \big| \\ &\approx |v| \big(1 + \varepsilon \sin\theta + O^2(\varepsilon) \big) \end{aligned}$$

where $O^2(x)$ denotes terms of order two at least. Therefore, the above expression of $L\boldsymbol{j} \times \boldsymbol{F_{a\to C}}$ can be written as

$$L\boldsymbol{j} \times \boldsymbol{F_{a\to C}} = -Lk_a |v|^2 \big(1 + \varepsilon \sin\theta + O^2(\varepsilon) \big) \big(c_L(\alpha_C, \mathrm{Re}_C) \cos\theta - c_D(\alpha_C, \mathrm{Re}_C)(\varepsilon + \sin\theta) \big) \boldsymbol{i} \tag{F.3}$$

We deduce from (F.1), (F.2), and (F.3) that

$$\begin{aligned}\Gamma_a = \quad -Lk_a|v|^2\Big[&\big(c_L(\alpha_A,\mathrm{Re}_A)-c_L(\alpha_C,\mathrm{Re}_C)\big)\cos\theta-\big(c_D(\alpha_A,\mathrm{Re}_A)-c_D(\alpha_C,\mathrm{Re}_C)\big)\sin\theta\\ &-\varepsilon\sin\theta\big(c_L(\alpha_C,\mathrm{Re}_C)\cos\theta-c_D(\alpha_C,\mathrm{Re}_C)\sin\theta\big)-\varepsilon c_D(\alpha_C,\mathrm{Re}_C)+O^2(\varepsilon)\Big]\end{aligned}$$

With the assumption of small angles of attack (and neglecting the dependence of aerodynamic characteristics on the Reynolds number), we have

$$\begin{aligned}c_L(\alpha_A,\mathrm{Re}_A)-c_L(\alpha_C,\mathrm{Re}_C)&=\frac{\partial c_L}{\partial\alpha}(\alpha_C,\mathrm{Re}_C)(\alpha_A-\alpha_C)+O^2(\alpha_A-\alpha_C)\\ c_D(\alpha_A,\mathrm{Re}_A)-c_D(\alpha_C,\mathrm{Re}_C)&=\frac{\partial c_D}{\partial\alpha}(\alpha_C,\mathrm{Re}_C)(\alpha_A-\alpha_C)+O^2(\alpha_A-\alpha_C)\end{aligned}$$

Thus, Γ_a can be written as:

$$\begin{aligned}\Gamma_a \quad = \quad &-Lk_a|v|^2\cos\theta\left[\frac{\partial c_L}{\partial\alpha}(\alpha_C,\mathrm{Re}_C)(\alpha_A-\alpha_C)+O^2(\alpha_A-\alpha_C)\right]\\ &+Lk_a|v|^2\sin\theta\left[\frac{\partial c_D}{\partial\alpha}(\alpha_C,\mathrm{Re}_C)(\alpha_A-\alpha_C)+O^2(\alpha_A-\alpha_C)\right]\\ &+Lk_a|v|^2\sin\theta\left[\varepsilon\big(c_L(\alpha_C,\mathrm{Re}_C)\cos\theta-c_D(\alpha_C,\mathrm{Re}_C)\sin\theta\big)\right]\\ &+Lk_a|v|^2\varepsilon c_D(\alpha_C,\mathrm{Re}_C)-Lk_a|v|^2O^2(\varepsilon)\end{aligned}$$

This concludes the proof. ∎

Abstract

The family of aircraft essentially consists of two classes of systems: fixed-wing and VTOL (Vertical Take-Off and Landing) aircraft. Due to their streamline shapes inducing high lift/drag ratio, fixed-wing airplanes are efficient in cruising flight. However, most of them require runways or catapult/net systems for take-off and landing. As for VTOL aircraft, thanks to their hover ability, they are particularly suitable for many applications including observation and structures inspection, but their efficiency in horizontal flight is generally mediocre. There is therefore an interest in designing so-called "convertible" vehicles, that combine the advantages of these two types of aircraft: efficient cruising flight and VTOL capability. This thesis is devoted to the conception, modeling, and control of such a convertible mini-UAV (Unmanned Aerial Vehicle).

The main contributions of this work are threefold. Firstly, we design a novel UAV structure by adding to each side of a quadrotor one wing that can rotate around an axis belonging to the propellers' plane. Our prototype has many advantages over existing convertible structures: simple mechanical concept since inspired by a classical quadrotor, flexibility for selecting different components (wings, propellers) and payload placement, flexibility for the control design, etc. Secondly, we provide an energy modeling of this type of convertible UAVs, taking into account their characteristics as compared to full-scale helicopters (large variation of aerodynamic forces, performance degradation at low Reynolds number, etc.). This modeling relies on momentum and blade element theories for the propellers and an aerodynamic coefficient model for full range of angle of attack for the wings. The ultimate objective is to optimize the wings' inclination with respect to the propellers' plane so as to achieve energy-efficient flight. In addition, the impact of various parameters (choice of propellers, wings' area, mass of UAV) is analyzed. The energy modeling provides useful guidelines for UAV presizing and control design - which is also the third contribution of this thesis. The degrees of freedom of the wings permit the decoupling between propellers and wings' orientations. This greatly enhances the control flexibility as compared to traditional aircraft. Relying on this feature, several control approaches are proposed. In particular, using a specific geometrical design, we show that an efficient control of our UAV can be obtained without air-velocity measurements. This strategy is well suited to small aerial vehicles for which such measurements are difficult to acquire. Simulation results confirm the soundness of our control design even in the presence of strong and varying wind.

En route to validate the theory, a mechanical prototype of the UAV was constructed in our laboratory and preliminary flight tests were performed. This is reported in the last chapter of the thesis.

Keywords: VTOL UAV, Convertible UAV, Energy Modeling, Aerodynamics, Feedback Control

Résumé

La famille des véhicules aériens est essentiellement constituée de deux classes de systèmes: les voilures-fixes et les systèmes à décollage et atterrissage vertical (VTOL en anglais, pour "Vertical Take-Off and Landing"). En raison de leur forme profilée, induisant un rapport portance/traînée élevé, les voilures-fixes ont l'avantage d'une bonne efficacité énergétique. Cependant, la plupart d'entre eux nécessitent des pistes ou des systèmes catapulte/filet pour le décollage et l'atterrissage. Quant aux VTOL, grâce à leur capacité au vol stationnaire, ils sont particulièrement bien adaptés aux applications d'observation et d'inspection de structures, mais leur efficacité énergétique en vol "de croisière" est généralement médiocre. Il y a donc un intérêt à concevoir des véhicules appelés "convertibles", qui combinent les avantages de ces deux types de structures : bonne efficacité énergétique en vol de croisière et capacité au vol stationnaire. Cette thèse est consacrée à la conception, la modélisation et la commande d'un tel mini-drone convertible.

Les principales contributions de ce travail comportent trois volets. Tout d'abord, nous concevons une nouvelle structure de drone en ajoutant de chaque côté d'un quadrirotor une aile qui peut pivoter autour d'un axe appartenant au plan des hélices. Notre prototype a de nombreux avantages par rapport aux structures convertibles existantes: conception mécanique simple car dérivée d'un quadrirotor classique, flexibilité pour le montage de différents composants (ailes, hélices) et le placement de la charge utile, flexibilité de la conception de commande, etc. Deuxièmement, nous proposons une modélisation énergétique de ce type de drone convertible, en tenant compte de ses caractéristiques par rapport aux hélicoptères avec pilote à bord (grande variation des forces aérodynamiques, dégradation des performances à faible nombre de Reynolds, etc.). Cette modélisation s'appuie sur les théories de la quantité de mouvement et de l'élément de pale pour les hélices et un modèle de coefficient aérodynamique couvrant la gamme complète des angles d'attaque pour les ailes. L'objectif ultime est d'optimiser l'inclinaison des ailes par rapport au plan des hélices afin d'obtenir la meilleure efficacité énergétique. En outre, l'impact de divers paramètres (choix des hélices, des aile(s), masse de drone) est analysé. La modélisation énergétique fournit des informations utiles pour la conception mécanique et la conception de la commande; ce dernier aspect constituant la troisième contribution de cette thèse. Les degrés de liberté des ailes permettent le découplage entre les orientations des hélices et celle des ailes. Cela augmente considérablement les possibilités de contrôle par rapport aux aéronefs traditionnels. S'appuyant sur cette caractéristique, plusieurs approches de contrôle sont proposées. En particulier, en utilisant une conception géométrique spécifique, nous montrons qu'un contrôle efficace peut être obtenu sans mesures de la vitesse air. Cette stratégie est bien adaptée aux petits véhicules aériens pour lesquels ces mesures sont difficiles à acquérir. Les résultats de simulation confortent cette stratégie de contrôle, même en présence de vent fort et variable.

Afin de valider la théorie, un prototype mécanique du drone a été construit dans notre laboratoire et des essais en vol préliminaires ont été effectués. Ces aspects sont décrits dans le dernier chapitre de la thèse.

Mots-clés: Véhicule à décollage et atterrissage vertical, Drone convertible, Modélisation énergétique, Aérodynamique, Commande par retour d'état